Numerical Simulation of Stagnation Point Transpiration Cooling in Non-Equilibrium Hypersonic Flow

Samuel D. Brody

New College

A thesis submitted for the degree of
Doctor of Philosophy

Supervised by
Dr. Luca di Mare and Dr. Matthew McGilvray

Department of Engineering Science
University of Oxford

Trinity Term, 2025

Dedicated to all my teachers

Declaration

This thesis, except where stated, is my own work and describes my own research. The views expressed in this thesis are those of the author and do not reflect the official policy or position of the United States Air Force, Department of Defense, or the U.S. Government.

Samuel D. Brody

Acknowledgements

This research would not have been possible without the generous support of the Marshall Commission and the United States Air Force. My time pursuing it would not have so enjoyable without the board of directors of the Osney One Cookie Conglomerate alongside me.

I am deeply grateful to my supervisors, Luca di Mare and Matthew McGilvray, for their patient guidance, for generously sharing their seemingly unlimited knowledge, and for their trust in me.

Thank you to Jon Brody, Ben Brody, and Leelou Lambolez for reading and critiquing a draft of this thesis.

Whether near or far, I thank my family, friends, and loved ones who have given me unwavering and undeserved patience, encouragement, and joy. They achieved the impossible in making England a sunny place.

To everyone who has offered advice, support, ideas, or just a smile along the way, thank you!

Abstract

Hypersonic flight is an essential component of strategic defense and planetary exploration missions. Recent advances in physical understanding, material technology, and design practice have opened new possibilities both in defense and commercial applications and have led to a resurgence of interest in hypersonic technologies. Aerodynamic heating still presents the primary technical challenge in hypersonic flight. Traditionally, vehicles mitigate large heat loads with blunt leading edges and sometimes ablative thermal protection, accepting reduced aerodynamic performance. Achieving the performance and maneuverability required for sustained hypersonic flight necessitates sharp leading edges, making the management of their thermal loads critical for vehicle feasibility. A sharp leading edge results in a reduced shock standoff distance, leading to a thinner shock layer and reduced drag, but also to increased surface heat flux, which needs an effective and durable mitigation strategy. The costs and technical challenges of flight testing necessitate the use of computational modeling. However, thermochemistry in the hypersonic regime is difficult to analyze and model. Thus, developing accurate computational means to analyze relevant technologies will provide vehicle designers with the information required to achieve mission objectives.

The goal of this project is to develop a computationally accurate and inexpensive numerical methodology for modeling transpiration cooling (TC) on stagnation points, which will experience the highest heat loads. This method should incorporate the following phenomena: non-equilibrium thermochemistry, wall catalycity, and species transport to and inside the porous medium. Detailed temperature profiles and species concentrations in the shock layer and within the porous medium can be evaluated, with variations in these profiles and in stagnation heat and mass transfer computed as functions of flight altitude, speed, leading edge radius, and coolant flow rate and composition.

The pursuit of this goal can be divided into three elements: 1) an accurate thermochemical model suitable for gas mixtures with general molecular weights; 2) a numerical solution method capable of representing the stagnation line from the shock layer to the flow within the porous medium; and finally 3) a comprehensive study of conditions at the stagnation point of a TC cooled tip resulting in improved correlations. Improvements in the thermochemical modeling are introduced through the evaluation of collision integrals using the Stockmayer potential for polar species, such as NO, CO, CN, and CH. The accurate evaluation of transport properties for atmospheres containing polar species makes the present work relevant to atmospheric entry problems on Mars/Jupiter as well as to active cooling systems that may introduce such species into flow around a hypersonic vehicle. The TC solver developed as part of this work is capable of accurately modeling stagnation line flows with low computational cost. The solution method retains the full detail of the thermochemical model along the entire length of the stagnation line, including in the porous medium. The solver has been validated for both non-blowing and blowing applications. Results are presented on the comparison of coolant effectiveness for a generic

test case. Finally, surface properties, catalycity and treatment of the wall temperature are studied to understand their impact on stagnation line profile, surface heat flux, and surface species concentration. These investigations allowed for the development of correlations for heat and mass Stanton number reduction.

This research aimed to develop a computationally accurate and efficient numerical solver capable of modeling transpiration cooling specifically at stagnation points under conditions of thermochemical non-equilibrium and to leverage this tool for a detailed characterization of the TC problem across a wide operational parameter space. The work explicitly addressed key physical phenomena central to hypersonic flows with mass injection, including the complexities of non-equilibrium thermochemistry and multicomponent transport properties.

List of publications

Primary author

- Samuel D. Brody, Justin Clarke, Matthew McGilvray, and Luca di Mare. "Collision Integrals and Orbiting Analysis for Polar Species Using the Stockmayer Potential," Journal of Thermophysics and Heat Transfer (2025). doi:10.2514/1.T7112
- Samuel Brody, Kin Sing Lau, Justin Clarke, Matthew McGilvray and Di Mare Luca. "Numerical Simulation of Transpiration Cooling on Stagnation Line in Thermochemical Non-Equilibrium," AIAA 2024-0648. AIAA SCITECH 2024 Forum. January 2024.

Contributing author

- J. Clarke, S. Brody, J. Steer, M. McGilvray, L. Di Mare, "Quasi-one-dimensional non-equilibrium method for shock tube and stagnation line flows," Physics of Fluids 1 September 2024; 36 (9): 096140. https://doi.org/10.1063/5.0218676

Table of contents

List of figures

List of tables

Glossary

$A_{f,r}$	=	forward reaction Arrhenius constant for reaction r
$A_{b,r}$	=	backward reaction Arrhenius constant for reaction r
a	=	Millikan-White empirical parameter
b	=	Millikan-White empirical parameter
a_∞	=	ambient speed of sound
B_h	=	blowing parameter
B_m	=	mass blowing parameter
b	=	impact parameter; nose-tip radius
b_0	=	orbiting impact parameter
D_{ij}	=	mixture coefficient of diffusion for species i and j
e_v	=	specific vibrational energy
F	=	blowing ratio
H	=	total enthalpy
H_v	=	volumetric heat transfer coefficient
$h_{v,s}$	=	specific vibrational energy of species s
h_w	=	specific enthalpy
k	=	conductivity; Boltzmann Constant, 1.380649e-23 J/K
$k_{b,r}$	=	backward reaction rate constant for reaction r
k_D	=	Darcy coefficient
k_F	=	Forchheimer coefficient
$k_{f,r}$	=	forward reaction rate constant for reaction r
M	=	Mach number; molecular weight
m	=	average molecular weight of the mixture
n	=	number density
p	=	pressure
R	=	Reynolds number
$R_{f,r}$	=	forward reaction rate for reaction r
$R_{b,r}$	=	backward reaction rate for reaction r
r	=	radial intermolecular separation
St	=	heat Stanton number
St_m	=	mass Stanton number
T	=	temperature
$T_{f,r}$	=	forward reaction activation temperature for reaction r
$T_{b,r}$	=	backward reaction activation temperature for reaction r
$\vec{u}$	=	velocity vector
V_∞	=	freestream velocity

$\dot{w}$ = mass production rate
y = molar concentration
α = Darcy penalization control
$\alpha^{j,r}$ = stoichiometric coefficient of reactant j in reaction r
$\beta^{j,r}$ = stoichiometric coefficient of product j in reaction r
δ = polarity term; shock standoff distance; domain widths
δ_{max} = maximum polarity term for a given collision pair
ϵ = emissivity
ϵ_n = porosity in flow direction
ε_0 = dispersion energy
$\varepsilon_{i,j}$ = dispersion energy for binary collision pair of species i and j
γ = specific heat ratio
μ = dipole moment; viscosity; reduced molecular weight
ϕ = azimuthal angle between two particles, deg
σ = rigid sphere diameter
σ_{SB} = Stefan-Boltzmann constant
σ_v = effective vibrational relaxation cross section
τ = viscosity tensor
τ_v = vibrational relaxation time
θ = characteristic temperature
$\theta_{1,2}$ = angle of inclination of dipole 1 and 2, deg
φ = intermolecular potential function
ζ = orientation-dependent polarity function
$\Omega_{ij}^{(l,s)*}$ = collision integral, $\mathring{\text{A}}^2$
$Q^{(l)}$ = integral cross section

Subscripts

1,2 = 1st and 2nd species in a collision pair
e = electronic
ev = electrovibrational
inj = injectant
p = porous region
s = species; solid
t = translational; total
tr = trans-rotational
v = vibrational
w = wall
∞ = freestream

Superscripts

$\sim$ = dimensional value
* = non-dimensional value

Chapter 1
Introduction

"[T]he hypersonic regime is defined as the realm of speed wherein the physics of flows is dominated by aerodynamic heating. This heating is far more intense than at speeds that are merely supersonic..."

T.A. Heppenheimer [11]

1.1 Historical context

Extreme speeds result in extreme temperatures. Extreme temperatures require protection (should survival be a priority). This domain of extreme speeds and temperatures is the hypersonic regime, where the ratio of the velocity ahead of the vehicle (V_∞) to the ambient speed of sound (a_∞), the Mach number, is much greater than one:

$$M_\infty = \frac{V_\infty}{a_\infty} \gg 1 \tag{1.1}$$

Hypersonic flow is often distinguished from standard supersonic flow theory at Mach 5 and aligns with the following characteristics: thin shock layers, negligible viscous-inviscid interactions, non-negligible entropy layers, high heat transfer, and low-density [12]. High heat transfer comes from the large deceleration across the shock wave in front of the vehicle, producing extreme temperatures close to the body. As speeds increase, large heat transfer to vehicles necessitates dedicated thermal protection systems (TPS) to shield vehicles and maintain structural integrity during operation.

The first instance of human-produced hypersonic flight came from the German V-2 rocket during World War II. Although the term "hypersonics" did not appear until 1946 (courtesy of Caltech aerodynamicist Hsue-she Tsien), the German V-2 rocket achieved a flight speed of Mach 5 (often described as the crossover from the supersonic to hypersonic flight regimes) [11]. The first human to experience hypersonic flight was Yuri Gagarin in 1961. The X-15 was the first self-propelled and piloted hypersonic vehicle. In 1967 United States Air Force pilot Pete Knight flew the X-15 at 4520 miles per hour (2.02 km/s), or equivalently Mach 6.7 at 58,400 meters above sea level [12], an air speed record that still stands. Throughout this two decade period after the hypersonic regime was first described, it became clear that while challenges arose from more traditional areas of vehicle design such as lift and drag characteristics, stability, and propulsion, the most significant came from extreme temperatures. As early as 1954, Von Karman noted that the "temperature barrier" for vehicles returning from space would present a more significant challenge than the sonic barrier [13]. The decades following the advent of hypersonic flight witnessed an explosion in productive research in the

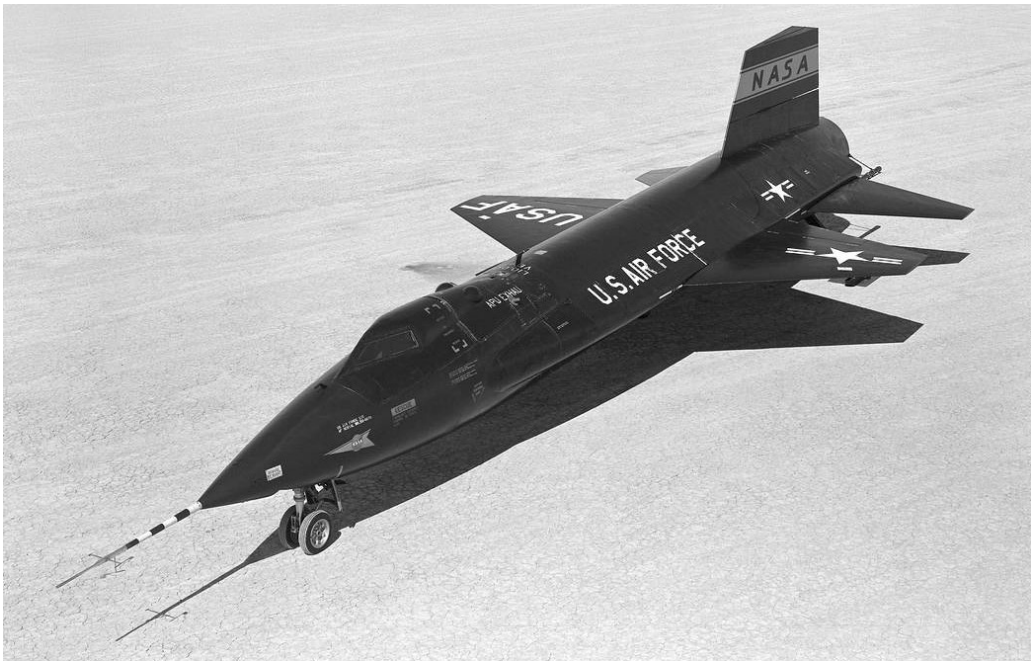

Figure 1.1: X-15 hypersonic research vehicle, ship #1, taken from NASA archives

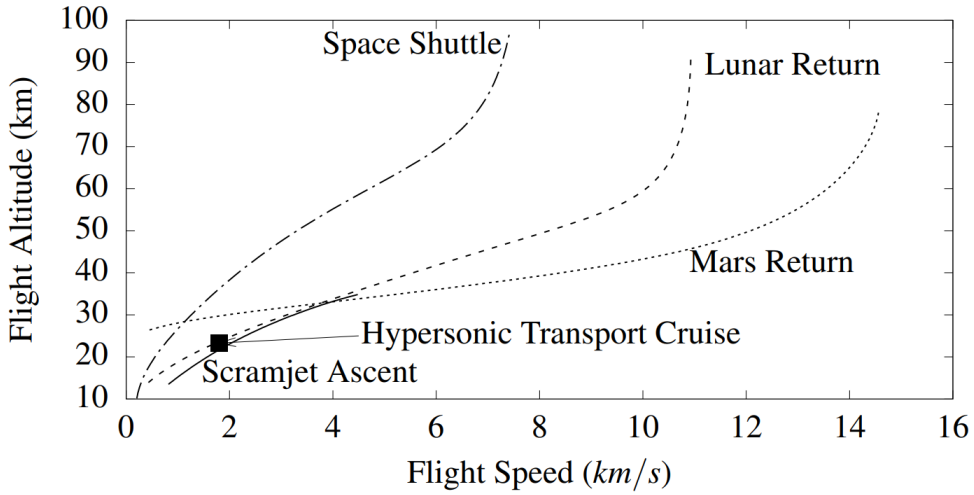

Figure 1.2: Hypersonic vehicle altitude-speed trajectories through Earth's atmosphere, taken from Satchell [1]

field, developing the basis for the thermochemical and aerodynamic description of hypersonic flight that stands today.

Interest in hypersonic vehicles has grown in recent decades, especially with the increase of commercial, military, and space exploration applications. Figure 1.2 displays the variety of mission flight trajectories requiring hypersonic vehicles. Special focus has been devoted to transatmospheric vehicles (TAVs) that are characterized by longer sustained flight accelerating through various atmospheric regions to orbital speeds [14]. These vehicles experience even higher heat loads than simple atmospheric

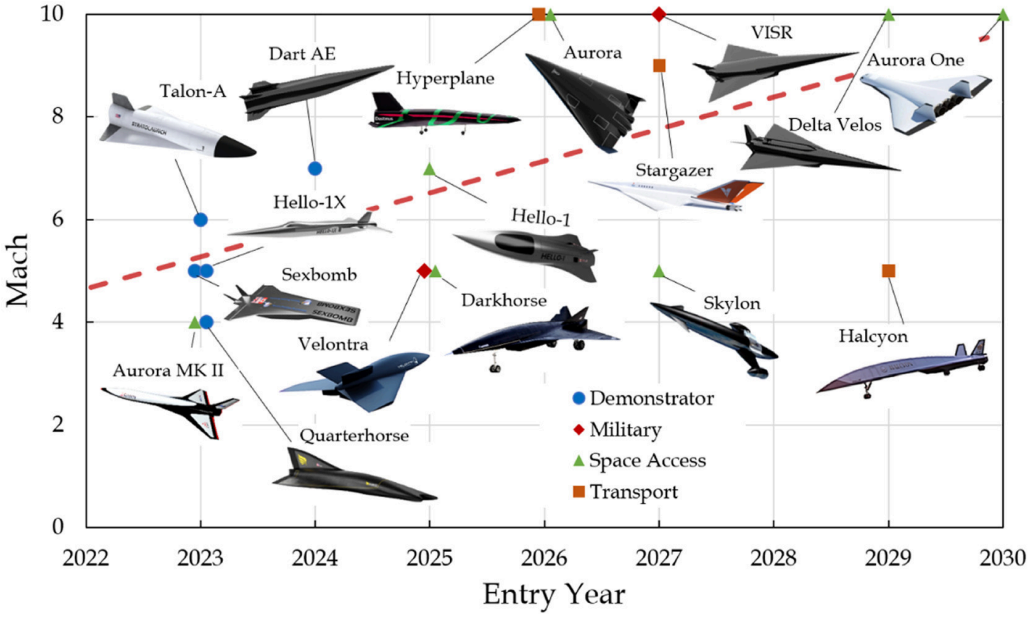

Figure 1.3: Hypersonic vehicles under recent development (dashed line is trend of increasing Mach), taken from Pollock and Wild [2]

entry bodies, with equilibrium stagnation temperatures in excess of 3500 Kelvin [15]. Large-scale efforts to develop stable hypersonic flight began in the 1960's with the X-15 and continued to gain attention and funding through the 1980's with the National Aerospace Plane Program (NASP). Unfortunately, the program was cancelled before a prototype of its demonstration vehicle, the X-30, could be built [11]. Figure 1.3 displays hypersonic vehicles under development in the current decade, along with their trend of increasing operational Mach number. Applications for hypersonic vehicles are far-reaching, extending beyond the military-industrial complex that was their impetus. Commercialization of space, space exploration, and commercial and passenger travel through high atmosphere all stand to benefit from the development of reliable and inexpensive hypersonic flight vehicles.

Traditionally, thermal management for hypersonic flight has relied on blunt leading edges to reduce heat loads and ablative thermal protection systems (TPS) to handle extreme temperatures [11, 14, 16]. However, extended flight times required for the acceleration and reentry phases of more modern missions require the use of low-drag geometries [15, 17, 18]. Santos [19] showed that, at the expense of increased stagnation line heating, reducing leading edge bluntness improves the lift-to-drag ratio for a waverider design hypersonic vehicle. A very low shock standoff distance (or an attached shock at the leading edge) reduces pressure leakage from the lower surface to the upper surface of the vehicle. Higher angles of incidence increase this pressure leakage, implying the greater need for sharp leading edges on missions requiring maneuverability. Sharp leading edge vehicles further present challenges for traditional ablative thermal management. Ablative shields are not shape-stable, eroding over time and thus altering aerodynamic properties.

As leading edges get smaller in high-speed low-density applications, thermochemical phenomena

begin to significantly affect hypersonic flows and their interaction with flight vehicles. At hypersonic speeds, a strong shock wave forms ahead of the vehicle, rapidly converting the air's kinetic energy into thermal energy. This initial heating primarily excites the translational motion of gas particles. However, energy is also stored in the particles' internal modes (rotation, vibration, and electronic), and chemical reactions can occur. Molecular particles may dissociate into constituent elements and then even ionize. The transfer of energy to these internal modes (relaxation processes) and the progress of chemical reactions do not happen instantaneously compared to the speed of the airflow. Unlike lower-speed flight where these processes are nearly instantaneous, the finite timescales in hypersonic flow mean the air behind the shock does not immediately reach a state of thermal and chemical equilibrium. This results in regions of non-equilibrium, where the distribution of energy among molecular modes and the chemical composition are still evolving, adding complexity to the flow physics. The structure and location of the shock, the characteristics of the shock layer, the surface heat flux, and the surface chemical composition cannot be accurately evaluated in these regimes without accounting for non-equilibrium effects. There would be value in a stagnation line analysis that investigates these relevant thermochemical phenomena in a compact and efficient formulation.

1.2 Motivation

The primary challenge in the hypersonic regime, acknowledged in 1954 by Von Karman [13] as the "temperature barrier," is the extreme aerodynamic heating experienced by vehicles.

The increasing interest in and development of hypersonic capabilities for applications ranging from commercial spaceflight to advanced defense systems necessitate overcoming this thermal challenge. The drive for improved aerodynamic performance, such as higher lift-to-drag ratios essential for maneuverability and range, often leads to vehicle designs incorporating sharp leading edges. While beneficial aerodynamically, these sharper geometries significantly increase stagnation point heat flux compared to blunter designs, exacerbating the thermal problem.

High-speed, low-density environments encountered by hypersonic vehicles, especially at sharp leading edges, introduce significant thermochemical non-equilibrium effects. The timescales for chemical reactions and internal energy relaxation can become comparable to the flow timescales, meaning the gas is not in thermal or chemical equilibrium. Accurate modeling of the shock layer composition, energy distribution, and surface heat transfer in these regimes requires accounting for these non-equilibrium phenomena. Models or analyses that assume equilibrium for the thermal or chemical state can lead to significant errors in the prediction of the flow field and surface conditions.

Given the extreme heat loads and the limitations of passive high-temperature materials alone, advanced thermal protection systems are indispensable. While ablative TPS have been widely used (e.g., on many NASA reentry vehicles), they are non-reusable and can alter vehicle geometry. Alternatively, transpiration cooling, which involves injecting a coolant gas through a porous surface, offers potential

advantages including reusability, adaptability to varying heat loads, and preservation of leading edge shape.

However, mass injection into the hypersonic shock layer adds another layer of difficulty. The interaction between the injected coolant and the high-enthalpy, potentially non-equilibrium shock layer is complex. Specifically, the mixing process, heat and mass transfer near the wall, the impact of multi-component diffusion (especially with injectants dissimilar to the shock layer mixture), and surface conditions must be accurately modeled.

Therefore, there is value in a robust computational tool capable of accurately modeling active thermal protection systems like transpiration cooling under the challenging conditions of hypersonic flight, specifically accounting for:

- Non-equilibrium thermochemistry within the shock layer and near-wall region.
- Extreme stagnation point heating associated with high speeds and sharp leading edges.
- The interaction of injected mass with a high-enthalpy, multi-species flow.
- Surface effects such as catalycity and wall temperature and injection via porous flow.

The work undertaken in this DPhil focuses on developing and applying such a tool. By incorporating rigorous multi-component non-equilibrium thermochemistry and extending traditional stagnation line flow theory, this research aims to provide an efficient and versatile numerical tool to rapidly assess the performance of transpiration cooling systems across a wide range of freestream conditions, vehicle geometries, injectant species, and surface properties. This provides a valuable contribution towards enabling the next generation of hypersonic vehicles. The following sections introduce the foundational concepts necessary to contextualize the research objectives pursued in this thesis.

1.3 Non-equilibrium hypersonic aerothermodynamics

A thermochemical model must be chosen for the analysis of flow properties and ideally should accurately describe the dominant features of the flight regime of interest. The quick deceleration of the flow behind a normal shock results in an increase in enthalpy, and thus large temperature increases. Excitation of internal energy modes and chemical reactions occurring on timescales similar to that of fluid translation results in regions of thermochemical non-equilibrium. Figure 1.4 displays the velocity/altitude parameter space for the Apollo mission trajectory along with the relevant chemical effects. With decreasing leading edge radius, the regions of non-equilibrium would extend to lower altitude and slower velocities, indicating the necessity of analyzing modern hypersonic technologies in the context of non-equilibrium phenomena.

In the non-equilibrium state, energy is not evenly distributed, meaning different molecular energy modes effectively exist at different temperatures. To capture this, multi-temperature (MT) models are employed, assigning distinct temperatures to groups of energy modes. The most common simplification

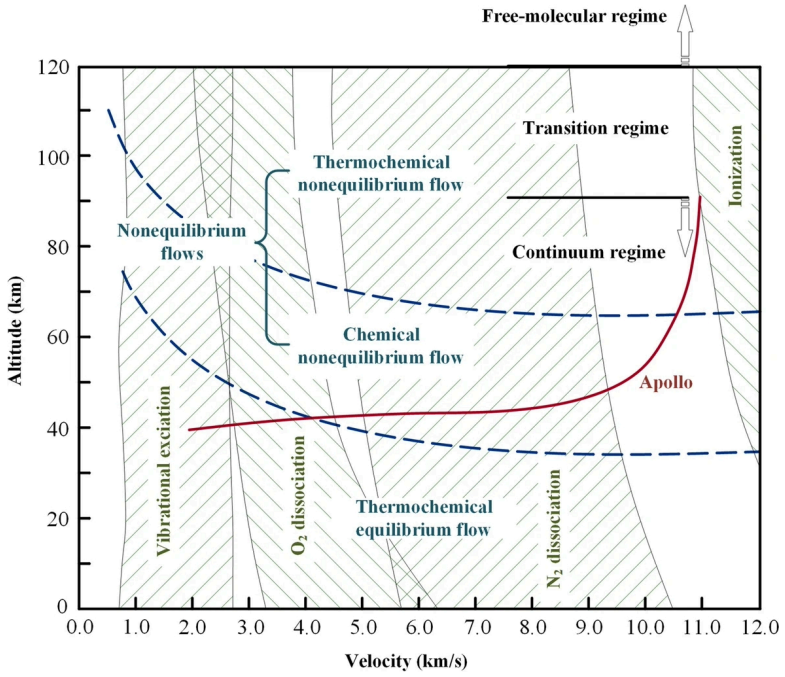

Figure 1.4: Flight stagnation air chemistry for velocity/altitude parameter space with Apollo reentry trajectory, taken from Zhang *et al.* [3]

is the two-temperature model. Prominent examples include models by Park [20, 21] and the Modified Marrone and Treanor (MMT) model [22]. Both assume translational and rotational modes are in equilibrium at one temperature and vibrational and electronic modes are in equilibrium at a separate temperature. Park's two-temperature model is widely used and relies heavily on shock tube experiments. More recently, efforts like the MMT model have sought to inform these two-temperature frameworks with parameters derived from state-resolved simulations using ab-initio quantum chemistry. However, generating such detailed models for complete atmospheres is computationally intensive and challenging, requiring billions of collision simulations [23]. Therefore, this thesis utilizes thermochemical models based on Park's framework [21, 24, 25], as for many applications, more complex models are either not available or are not significantly different [26, 27]. Further, the addition of foreign gas injectants (and the extension to different atmospheres) precludes the use of the MMT model, which is tuned for specific chemical systems.

An alternative strategy to the multi-temperature approach is state-to-state (StS) modeling. With this approach, each internal energy state (vibrational, rotational, electronic) of each species is considered separately. Thus, while a multi-temperature model describes the internal energy states of chemical species in bulk terms, state-resolved calculations require a mass continuity equation for each "pseudo-species." MT methods assume Boltzmann distributions at a given temperature, but collisions in high-energy environments can result in significant departures of internal energy states from these equilibrium distributions [5]. Resulting StS models for air can incorporate upward of 100 species and 10,000 reactions [28]. Further, developing the rates for these models is computationally expensive

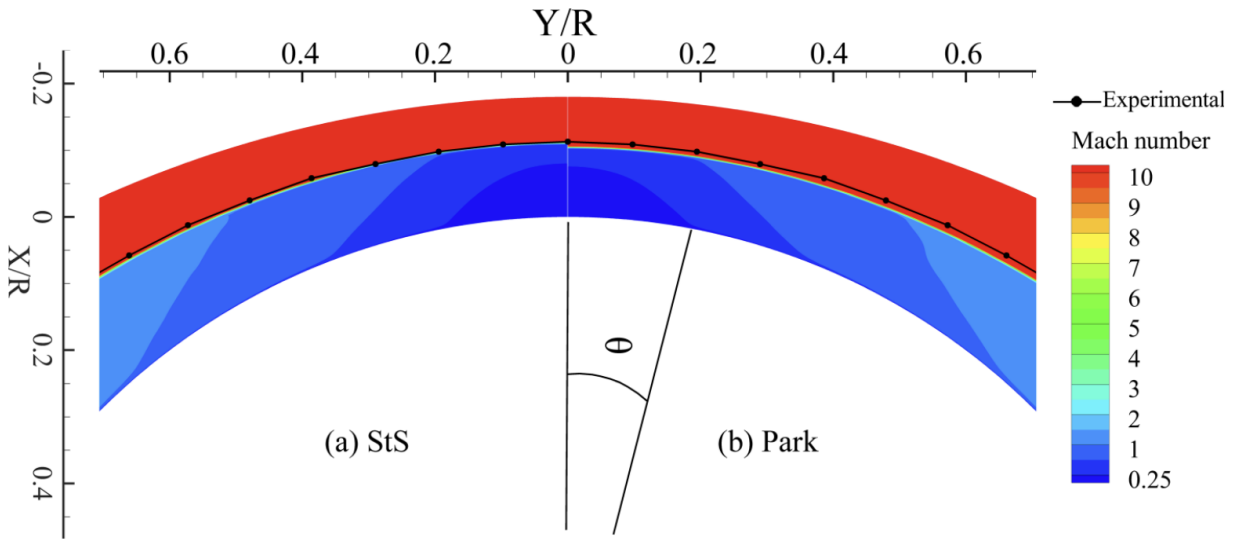

Figure 1.5: Numerical results using State-to-State and Park thermochemical models compared to experimental results by Nonaka *et al.* [4], taken from work by Colonna *et al.* [5]

and experimentally challenging. Capitelli *et al.* [29] provide a useful description of these models, and several sources display their application [28, 30, 5, 31, 32]. While StS modeling is receiving increased attention as computing power expands, two-temperature modeling remains the standard thermochemical solution for the majority of hypersonic applications (especially when considering diverse multi-component mixtures). Figure 1.5 displays the fairly accurate ability of Park's model in recreating velocity profiles and shock standoff distance, relative to a StS model, for experimental results from Nonaka *et al.* [4]

1.4 Stagnation point heating

Heat transfer is generally most concentrated at the leading edge stagnation point, as the shock is strongest and closest at this point, resulting in the steepest temperature gradient. This makes stagnation heat flux a key consideration in the design and analysis of hypersonic vehicles, particularly for sharp leading edges where thermal loads are most severe.

Understanding the flow along the stagnation line (from freestream conditions, through the shock, and to the vehicle wall) is essential for predicting the resulting heat flux. From the vehicle frame of reference, as the freestream gas approaches, it undergoes rapid deceleration through a shock wave, leading to a sharp increase in both temperature and pressure. This process results in a corresponding increase in static enthalpy. In hypersonic flows, real gas effects such as dissociation and ionization must also be considered, as they significantly influence the thermal and chemical behavior of the flow.

Heat transfer occurs as a result of spatial temperature differences which induce thermal energy exchange. Heat transfer can be broken into three primary components: conductive heat transfer,

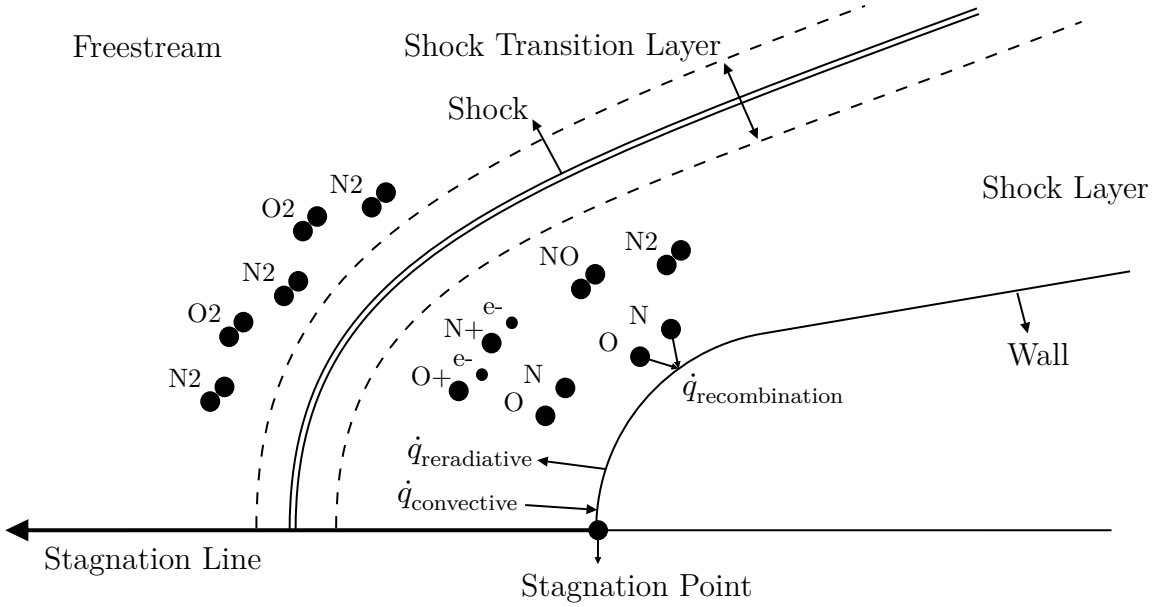

Figure 1.6: Schematic of flow domain for hypersonic leading edge, adapted from Rocher [6]

convective heat transfer, and radiative heat transfer [33]. The relative magnitudes of these modes depend on flight conditions, shock layer composition, vehicle geometry, and material properties. A detailed understanding of these components is essential for accurate prediction and mitigation of thermal loads.

Conduction is the transfer of energy by adjacent particles due to their physical interaction. Convection is the transfer of energy made possible by motion, either the random motion of particles (diffusion) or the bulk motion of the fluid (advection). It should be noted that in the context of stagnation point heat transfer, the cumulative heat transfer resulting from the motion of the fluid colliding with the vehicle is often described as the convective heat transfer (as in Figure 1.6). Finally, radiation is the transfer of energy by emission of particles holding thermal energy. While not a transfer of thermal energy, accurate modelling of the thermal environment at the stagnation point must include viscous dissipation, or the work done by shear forces. This heat generation results from the velocity gradient near the surface which induces frictional forces. In turn, the work required to overcome the shear stress is converted into internal energy.

Real gas effects influence all modes of heat transfer. At high temperatures, molecular dissociation occurs as energy stored in molecules becomes sufficient to break chemical bonds. As the flow cools downstream of the shock, recombination reactions become more prevalent, releasing energy in the process. When these recombination reactions occur near or at the surface, they contribute to the heat flux to the material through convection. Changing chemical composition and temperature gradients in the shock layer lead to variations in transport properties, which in turn affects surface heat conduction from the fluid. This effect is further intensified by the catalytic properties of the surface material, which can

enhance the rate of recombination reactions. The interplay between dissociation and recombination is particularly important in hypersonic flows, where chemical reactions significantly influence the thermal environment. Figure 1.6 provides a schematic representation of the flow domain for a hypersonic leading edge, illustrating the key regions where thermal and chemical processes occur. Accurate analysis of freestream conditions, shock-induced changes, and shock layer behavior is required to determine the heat flux at the stagnation point. Radiative heat transfer becomes significant at extremely high velocities, typically above 9 km/s for air [34, 35]. At these speeds, the excitation of particles—intensified by the shock process—leads to the emission of electromagnetic radiation as particles relax to more stable energy states. While radiative heat flux is negligible at lower velocities, it can dominate the total heat flux in extreme hypersonic flight. Reradiative heat transfer, usually defined by the Stefan-Boltzmann equation, represents the loss of heat from the vehicle's surface to the freestream via thermal radiation. Unlike radiation of the gas plasma to the surface, this cooling mechanism can be significant at lower hypersonic velocities, so long as the surface temperatures is significantly higher than the freestream.

For stagnation point heating in the context of the hypersonic flows considered in this thesis, the conductive and diffusive components of heat transfer dominate. Advection and radiation are negligible due to low or outward (for mass injection) bulk velocities and freestream velocities below 9 km/s, respectively. Stagnation heat transfer for these conditions has been extensively studied, with notable contributions from Sutton and Graves [36], Fay and Riddell [37], and Brandis and Johnston [38], who developed correlations to predict heat flux under various entry conditions. These correlations have been verified by experiment [39, 40, 41, 42]. For Earth and Mars entries, these correlations provide valuable insights into the role of convective heating in thermal protection system design. When using these correlations, it should be understood that they do not account for mass injection, and only the correlation by Brandis and Johnston [38] accounts for radiative heating and non-equilibrium effects. They are, however, worthwhile in displaying the general trend of stagnation line heating and its dependence on vehicle geometry at the leading edge.

1.5 Thermal protection and transpiration cooling

The flight characteristics of hypersonic vehicles result in extreme heat loads that cannot be sustained by surface materials alone [11]. Even Ultra-High-Temperature-Ceramics (UHTC) are not effective alone, as they are susceptible to oxidation, which may reduce the melting temperature by half [43]. Thermal Protection Systems must be implemented in the design of such vehicles. Further, the increased drive for high-atmosphere and space flight, especially recurring and inexpensive space flight, increases the importance of developing TPS that are effective and durable. TPS comprise three categories, as shown in Figure 1.7: passive, semi-passive, and active.

Passive thermal protection emphasizes the use of insulation and material selection over energy consuming equipment or systems. Examples of passive TPS include heat sinks, insulation, or the straightforward use of a highly temperature-resistant material to absorb heat and obstruct heat flux to

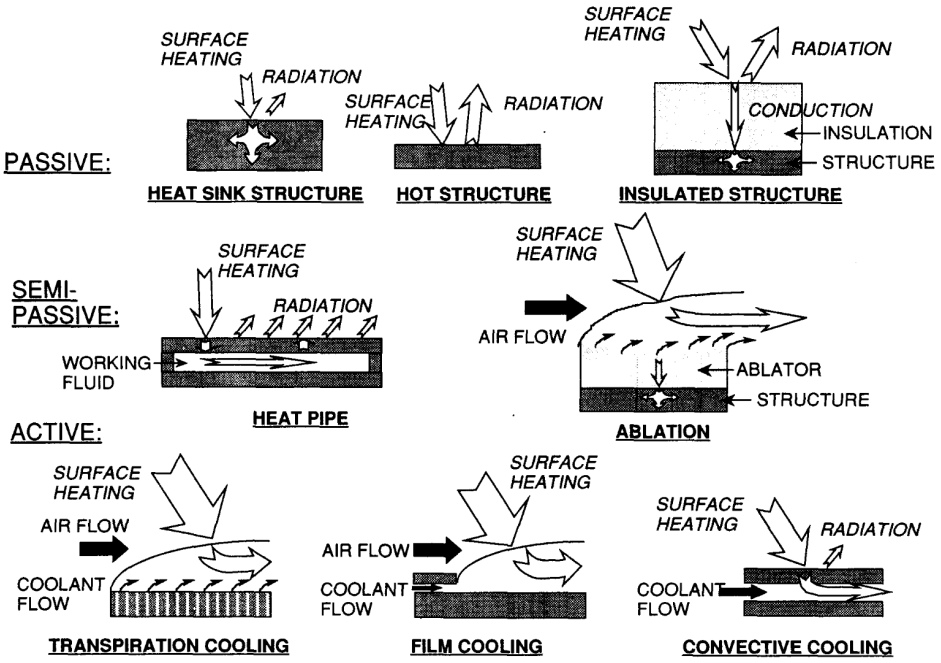

Figure 1.7: Thermal protection system concepts, taken from Kelly and Blosser [7]

the internal components of a vehicle. These TPS have the benefit of simplicity but often are limited in overall cooling effectiveness and adaptability to shifting mission requirements. Semi-passive TPS, most commonly in the form of ablatives, have been most prevalent for hypersonic vehicle design. Implemented as ablative heat shields in hypersonic vehicles such as the X-15, semi-passive TPS offer effective cooling at the expense of re-usability and shape resistance. In this cooling system, the ablating surface material enters the flow around the vehicle in a liquid or gas state, thus absorbing heat through phase change and transporting heat away from the surface through mass injection [15]. Unfortunately, ablative systems suffer from two large drawbacks. Ablatives are single-use and mission restrictive for both time and flight path, meaning the skin of the vehicle generally requires complete refurbishment between flights. Secondly, ablatives are not shape-stable, thus increasing leading edge bluntness throughout the time of flight. As mentioned above, this can have detrimental effects to the aerodynamic performance. In addition to leading edges blunting, ablative cooling applied to sharp leading edge may result in drag-increasing protuberances due to localized heating [44]. Finally, surface roughness increases through time of flight may prematurely transition the boundary layer (especially for sharp leading edges), leading to increases in heating due to turbulent flow [45].

Active Thermal Protection Systems require energy consuming infrastructure within a vehicle. Like ablative cooling, traditional active cooling systems rely on mass injection. Transpiration and film cooling are the most common implementation of active systems, with general schematics of their implementation in Figure 1.8. Generally, film cooling operates through the injection of individual streams of gas or liquid that create a cool layer over the surface of the vehicle. Transpiration cooling,

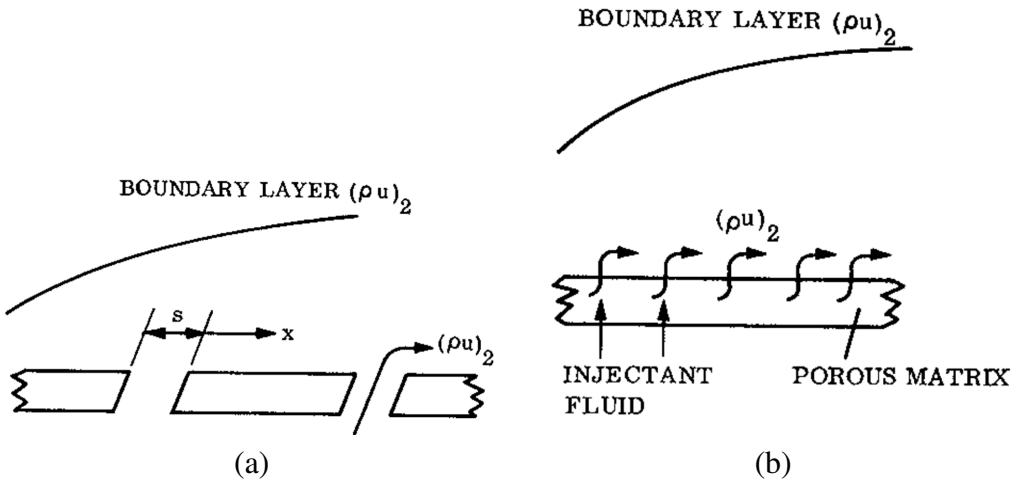

Figure 1.8: Schematic diagram of (a) film and (b) transpiration cooling systems, taken from Laganelli [8]

on the other hand, results from the injection of a gas or liquid through a porous structure on the surface, generally resulting in a more uniform effect on the boundary layer and requiring lower injection rates [8]. While being more technically challenging to implement, transpiration cooling has been shown to be more effective relative to film cooling [8, 46]. Further, transpiration cooling better preserves boundary layer stability aft of injection and may reduce skin friction drag [47]. Boundary layer stability is important, as increases in heating due to disrupted boundary layers could offset cooling benefits from mass injection [48]. Active cooling systems are complex, requiring internal infrastructure and adding risk to reliability. However, these systems are highly adaptable relative to other TPS, due to control over injection rates and injectant compositions. Further these systems are re-usable, with only the refilling of injectant reservoirs between flights.

1.6 Research contribution

The research presented in this thesis attempts to further demonstrate and characterize the application of transpiration cooling on hypersonic stagnation points in thermochemical non-equilibrium. The development of a novel numerical method constituted the core effort, requiring significant work on both the solver architecture and the expansion of the underlying thermochemistry library and database to support rigorous non-equilibrium transport property calculations. The aims of the thesis can be further split into three main objectives. The first objective relates to thermochemical modeling of the complex flows investigated, while the remaining two objectives correspond to the development and application of a numerical solver capable of modeling transpiration cooling. The objectives are as follows:

- Expand the thermochemistry database and library (OCEAN) maintained by the Oxford Thermofluids Institute Numerical Analysis group to be able to perform all evaluations necessary

for modeling the transpiration cooling (TC) problem, specifically focusing on polar species collisions.

- Develop a numerical method that accurately describes stagnation line flow with mass injection across free stream conditions, atmosphere, injectant, and surface material and properties.
- Deploy the developed tool for the characterization of the transpiration cooling problem across the large operational parameter space.

1.7 Outline of thesis

This thesis comprises six chapters, including the current introductory chapter. This work follows the integrated thesis format. Thus, after a review of the literature presented in Chapter 2, Chapters 3, 4, and 5 present the research contributions of the thesis in the format of self-contained journal papers. The remainder of the thesis is organized into the following sections:

- Chapter 2 - Literature Review: this chapter includes a description and background on the important concepts relevant to the current and future areas of focus.
- Chapter 3 - Collision Integrals and Orbiting Analysis for Polar Species Using the Stockmayer Potential: this chapter includes published work on the investigation of the Stockmayer Potential as a means for evaluating transport properties of polar molecules.
- Chapter 4 - Numerical Simulation of Transpiration Cooling on Stagnation Line in Thermochemical Non-Equilibrium: this chapter presents work undertaken for the development and validation of a transpiration cooling solver. This work has been submitted for review.
- Chapter 5 - Transpiration Cooled Stagnation Point in Non-Equilibrium Hypersonic Flow: this chapter presents work employing the numerical solver for a parametric characterization of transpiration cooling. This work has been prepared for submission.
- Chapter 6 - Conclusions and future work: this chapter briefly reiterates the contributions made and outlines the opportunities for future work.

Chapter 2
Literature review

"Hypersonic flows differ from supersonic flows in that hypersonic flows involve high temperatures. The interaction between the fluid flow and the high temperature phenomena defines the domain of aerothermodynamics."

Chul Park [20]

2.1 Introduction

This literature review provides the foundational context for the thesis by surveying key topics in high-temperature gas dynamics and hypersonic aerothermodynamics. It begins with an overview of thermochemical modeling, emphasizing the treatment of non-equilibrium effects, chemical kinetics, and the calculation of transport properties in multi-component gas mixtures. The review then examines the simulation of stagnation line flows, highlighting the challenges of modeling coupled fluid dynamics and thermochemistry near hypersonic stagnation points. Finally, it discusses the principles and applications of transpiration cooling, focusing on its role in thermal protection systems for hypersonic vehicles and the complexities introduced by mass injection into high-enthalpy boundary layers.

2.2 Thermochemical modeling

Hypersonic flight is complicated by non-equilibrium thermochemistry. Extreme reduction in velocity through the shock (due to the collision of the freestream air with the vehicle) results in the conversion of kinetic energy into thermal motion of particles. This is witnessed by the bulk increase in temperature across a shock. However, this energy is stored exclusively in the random motion of particles, as opposed to a distribution between translation and the internal modes of energy: rotational, vibrational, and electronic. Collisions between particles allow for the redistribution, or relaxation, of energy bound in internal modes of particles throughout the mixture, eventually resulting in a new equilibrium temperature, where all internal modes exist at a uniform temperature. The nature of this excitation and relaxation to equilibrium behind a shock wave is displayed in Figure 2.1. While chemical reaction rates and thermal excitation progress at well-defined temperatures and pressures, the timescales are generally orders of magnitude smaller than the translational timescales of the fluid. In other words, chemical reactions and relaxation processes occur so quickly that fluids can be described as in equilibrium everywhere, and shocks can be considered as instantaneous flow discontinuities precipitating well-defined impacts on bulk fluid properties. However, for the freestream conditions and leading edge

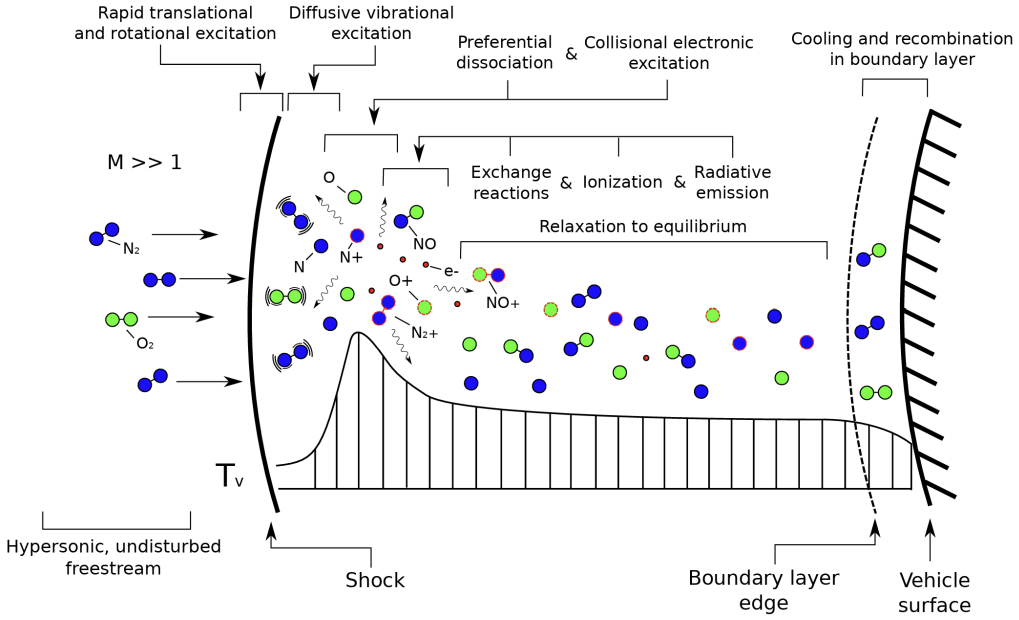

Figure 2.1: Schematic of thermochemical non-equilibrium in hypersonic flows, taken from Potter [9]

geometries considered in this thesis, chemical reactions and thermal excitation occur on timescales similar in magnitude to fluid velocities, resulting in regions of non-equilibrium for both the chemical composition and thermal energy modes. Thermal non-equilibrium arises from differences in the energy held in each of the modes of a plasma. In reality, each particle is described by its own translational, electronic, rotational, and vibrational modes, as applicable (e.g. atoms do not vibrate). In practice, particles of the same species can be treated as thermally uniform, with thermal non-equilibrium being principally described by the bulk difference in energy held in each mode [49]. Further, several sources indicate that the quick equilibration between the translational and rotational energy modes and the significant coupling between the vibrational and electronic modes allow for a simplification into a two temperature model [50, 49, 20]. This is the basis for the model presented by Park [21], where energy modes are coupled in the translational/rotational temperature and the electronic/vibrational temperature. Chemical non-equilibrium arises when chemical reaction rates occur at the same order of magnitude as other timescales, such as the translational velocity of the fluid.

Non-equilibrium is always present where flow discontinuities arise. However, at low speeds and high densities, discontinuities such as shocks are so thin relative to characteristic lengths that the region of non-equilibrium is negligible. It is important to accurately model non-equilibrium phenomena for higher speed and lower density flows. This is especially true when characteristic lengths are small enough such that the non-equilibrium region is relatively large.

Thermochemical modeling requires description of the chemical reaction scheme. This includes all reaction channels and their rates, third body efficiencies, preferential dissociation, and ionization and dissociation energies. A multi-temperature model requires description of the relaxation between modes. In the case of a two-temperature model, this is principally described by the vibrational relaxation rates.

Lastly, collisions and exchange of energy resulting from collisions must be described. Collision cross sections and integrals are used for this purpose.

To account for thermal non-equilibrium, Park has presented a two-temperature model [20]. In this model, the rotational and translational mode temperatures of heavy (non-electron) particles are assumed equal. The vibrational temperature of heavy particles, the translational temperature of electrons, and the electronic excitation of atoms and molecules are governed by a second temperature. This is due to the fast energy transfer between the vibrational motion of heavy particles and the translational motion of electrons as well as the relaxation of low-lying electronic states of species with ground electronic states [51, 52]. In chemical equilibrium, the flow is considered to be steady-state with respect to reactions, meaning forward and backward reactions rates are equal. Widely used thermochemistry models such as NASA's CEA employ this assumption [53]. However, for a non-equilibrium gas, different forward and backward rates will control reactions. Arrhenius forms of reactions with their forward and backward rate coefficients are therefore required [54, 55]. Two common databases for these rates come from Park [20] and the combined efforts of Blottner [56] and Dunn and Kang [57].

2.2.1 Transport Properties

The transport properties of a gas, either defined in the mixture sense or individually for multi-component definitions, describe the ability of the fluid to transfer mass, momentum, and energy within itself. The Boltzmann transport equation describes these macroscopic effects by defining a velocity distribution function based on the microscopic movement and collisions of particles. Due to the inherent complexity of the collision term in the Boltzmann equation, determining these properties requires approximation methods like Chapman-Enskog Theory, as described by Hirschfelder *et al.* [58]. The Chapman-Enskog method simplifies the Boltzmann equation by considering small deviations (representing macroscopic gradients) from a local equilibrium distribution function. These deviations are represented using expansions of Sonine polynomials. Hirschfelder *et al.* [58] note that good approximations of the full coefficients can be had using only the first term in the Sonine polynomial expansion. Substituting these expansions into the equation leads to a system of linear equations. Expressions for transport properties then rely on collision integrals, which appear as coefficients in the equations for the Sonine expansions. These integrals quantify the average effect of molecular collisions and depend on the intermolecular potential (the forces between particles) and temperature. They represent how effectively collisions cause mixing and transfer momentum or energy. Definitions are provided in Appendix A.

Equipped with collision integrals, transport properties for a given fluid state can be evaluated. For most applications, including equilibrium models such as NASA's CEA solver [53], the mixing rules developed by Yos [59] and expanded by Gupta [55] are employed. Wilke [60] and Gordon and McBride [53] present similar mixing rules which were assessed by Palmer and Wright [61] to halve the computational cost relative to a full multi-component "rigorous" method, as presented by Hirschfelder *et al.* [58]. While computationally efficient, these evaluations can be inaccurate, with non-negligible

error in viscosity arising at temperatures above 10,000 K for air, where ionization effects begin to dominate [61]. In addition, work by Magin and Degrez [62] presents a conjugate gradient method that allows for rigorous evaluation with lower computational cost than the Gupta [55] and Wilke [60] mixing rules. Thus, it is worthwhile to pursue the most rigorous multi-component method possible when considering high-temperature non-equilibrium phenomena. From several resources [58, 63, 36, 64], rigorous formulations implementing Park's two temperature model can be employed. Murphy presented an implementation of a multi-component rigorous method [65]. The methods for calculating transport properties in this work were validated against Murphy's work. Further, Murphy presented a comparison between the viscosity of 11 species air, as computed with his rigorous method and Gupta's mixing rule. Again, the methods used in this work align nicely with Murphy's. Full definitions of the transport properties are presented in Appendix A.

2.2.2 Chemical-kinetic parameters

Reaction Rates

Chemical reactions govern the transformation of chemical species, converting reactants into products. The rate of a chemical reaction is directly proportional to the product of the concentrations of the reactants, each raised to the power of its stoichiometric coefficient in a balanced chemical equation.

For a generic chemical reaction, reactants combine to form products [55]:

$$\sum_{i=1} \alpha_{i,r} X_i \underset{k_{f,r}}{\overset{k_{b,r}}{\rightleftharpoons}} \sum_{i=1} \beta_{i,r} X_i \tag{2.1}$$

Here, X_i represents species i, and the coefficients $\beta_{i,r}$ and $\alpha_{i,r}$ are the stoichiometric coefficient of species i in the products and reactants, respectively, of reaction r. The reaction can proceed in both the forward direction, converting reactants to products at a rate governed by the forward rate constant $k_{f,r}$, and the backward direction, converting products back to reactants at a rate governed by the backward rate constant $k_{b,r}$. The net rate of change for each species is determined by the balance between these forward and backward reaction rates.

Moss [66] presented the rate of production of species i through NR reactions as:

$$\dot{w}_i = M_i \sum_{r=1}^{NR} (\beta_{i,r} - \alpha_{i,r})(R_{f,r} - R_{b,r}) \tag{2.2}$$

The value M_i is the molar mass of species i. The values $R_{f,r}$ and $R_{b,r}$ are the forward and backward reaction rates of reaction r.

Reaction rates and coefficients generally take the following form from Gnoffo's work [54].

$$R_{f,r} = k_{f,r} \prod_{j=1}^{NR} (n_j \rho)^{\alpha^{j,r}} \tag{2.3}$$

$$R_{b,r} = k_{b,r} \prod_{j=1}^{NR} (n_j \rho)^{\beta^{j,r}} \tag{2.4}$$

where the forward and backward rate constants are defined:

$$k_{f,r} = A_{f,r} T^{\alpha_{f,r}} \exp(-\frac{T_{f,r}}{T}) \tag{2.5}$$

$$k_{b,r} = A_{b,r} T^{\alpha_{b,r}} \exp(-\frac{T_{b,r}}{T}) \tag{2.6}$$

Here, $A_{f,r}$ and $A_{b,r}$ are the Arrhenius constants for the forward and backward reactions, respectively. The exponents $\alpha_{f,r}$ and $\alpha_{b,r}$ are the temperature exponents, while $T_{f,r}$ and $T_{b,r}$ are the activation temperatures for the forward and backward reactions, respectively. When considering chemical non-equilibrium, backwards reaction rates can be determined using equilibrium constants defined through the minimization of the Gibbs free energy [67].

In Park's model, forward reaction rates are evaluated at a specified controlling temperature, whereas the backward reaction rates are evaluated at the translational temperature. The controlling temperature for dissociation reactions is the geometric mean of the electrovibrational and transrotational temperature, $(T_{tr}T_v)^{0.5}$. The transrotational temperature is used for most other reactions that do not include electrons as reactions or products. Electron-impact ionization reactions employ the electrovibrational temperature. Dissociation reactions generally include third bodies, which do not undergo chemical change, but instead facilitate the dissociation of a molecule. In a reaction set (or a given atmosphere), certain species facilitate dissociation reactions with varying efficiencies. These third body efficiencies are defined based on the varying activation energy of the reaction for a given third body.

Marrone and Treanor [68] developed a model that accounted for varying likelihood of molecular dissociation based on vibrational state. Dissociation is more likely among molecules with higher vibrational energy levels. Park [21] incorporated this idea in evaluating dissociation reactions at a "controlling temperature". Under the preferential dissociation model, dissociating molecules carry a disproportionately large share of the total vibrational energy. Thus, the average vibrational energy loss for a dissociating particle should be larger than the average vibrational energy of the system. Sharma *et al.* [69] determined an empirical factor of 30% of the dissociation energy to be removed from the vibrational energy budget. Using results from state-to-state modeling, Kim and Jo [25] presented parameters that vary with temperature for each dissociation reaction. The vibrational energy preference ratio is shown to decrease with rising temperature.

Common reaction sets for two-temperature models come from Park [21] and the modified Marronne-Treanor model presented by Chaudhry [23]. Reaction sets for other atmospheres are presented by a variety of sources, such as those by Park [24] for Mars, Gokcen [70] for Titan, and Leibowitz and Kuo [71] for Saturn and Jupiter.

Relaxation parameters

While chemical reactions rates can be used to define the chemical excitation of a fluid, further parameters are required to model the excitation and relaxation of energy modes. For two-temperature models,

the pioneering work of Millikan and White [50] provides a framework for assessing relaxation rates, built on Landau-Teller theory [72]. The following empirical equation defines vibrational relaxation times, τ_v, for binary collision pairs based on their reduced molecular weight and the characteristic temperature (representing the resistance to energy transfer) of the oscillator:

$$p\tau_v = e^{a(T^{-1/3}-b)-18.42} \tag{2.7}$$

$$a = 0.00116\mu^{0.5}\theta^{1.333} \tag{2.8}$$

$$b = 0.015\mu^{0.15} \tag{2.9}$$

Alternatively, values for a and b can be determined from experiment or simulation [21, 24, 73, 25]. The standard Millikan-White relaxation scheme does not preserve agreement with experimental results at high temperatures. Park [21] presented a high-temperature correction to better align with data over 8,000 K. Kim and Jo [25] further developed this work, presenting high-temperature corrections for all binary collision pairs of interest for high-temperature air.

Park found that at high temperatures (above 8,000 K in air), the Millikan and White formula resulted in relaxation times far too low. This is due to the finiteness of the elastic collision cross sections which limit relaxation rates. There is a limit to how effectively particles can transfer energy during a collision which is not accounted for in the Millikan and White formulation. At very high temperatures, relaxation is not limited by the probability of significant energy transfer, but instead solely by the collision frequency. The collision frequency is proportional to the number density of particles and the collision cross section, which approaches a limit with increasing temperature. The Park correction accounts for this limit through an effective elastic collision cross section. Park's high temperature correction increases the relaxation time as follows:

$$\tau_{v,corrected} = \tau_v + (n_t\sigma_v\sqrt{8kT/\pi M})^-1 \tag{2.10}$$

$$\sigma_v = \sigma_v'(50000/T)^2 \tag{2.11}$$

where n_t is the total number of colliding particles and M is the average molecular weight of the mixture. The variable σ_v is the effective vibrational relaxation cross section, and σ_v' is determined by best fit to experimental data [21, 24].

Kim and Jo [25] expanded Park's two-temperature 11 species air model. State-resolved master equations calculations and the quasi-classical trajectory method were employed to determine vibrational relaxation times for air species collision pairs. Modified values for a, b, along with temperature-dependent formulations for σ_v. These new values aligned well with legacy shock-tube experimental values as well as newer state-resolved calculations. In general, relaxation times for the Kim and Jo model diverge from the Park high-temperature correction at temperatures above 8,000 K, but differences are not drastic until temperatures reach 20,000 K.

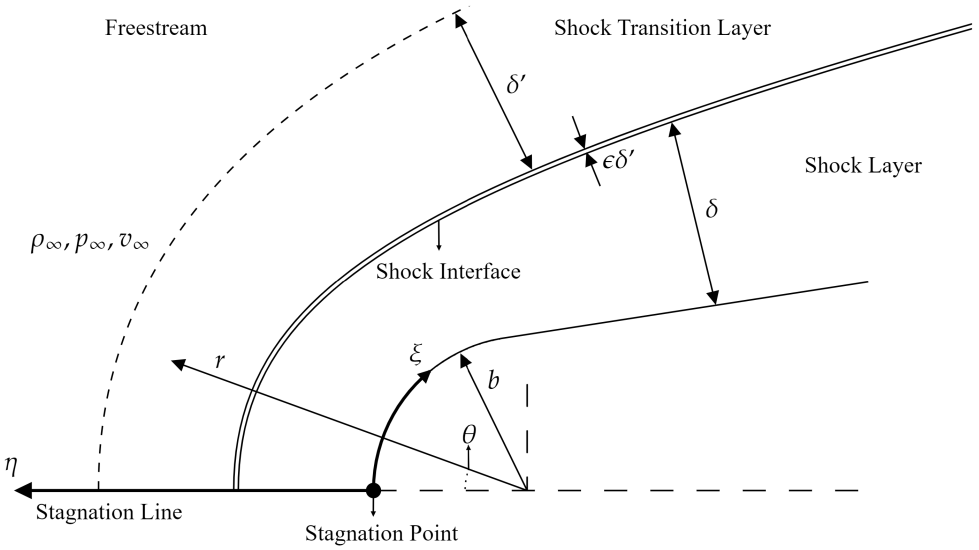

Figure 2.2: Two-layer flow domain and surface coordinates as employed by Cheng [10]

2.3 Simulation of stagnation line flow

The accurate simulation of flow phenomena in the stagnation region of bodies subjected to high-speeds is important for the design and analysis of hypersonic vehicles and atmospheric re-entry bodies. This region is characterized by the complex interaction of a detached shock wave, viscous effects, and high-temperature chemical phenomena.

The stagnation line heating problem was first rigorously investigated in 1936 by Homann [74], offering the classical analysis of a steady incompressible flow around a surface of revolution in proximity to the stagnation point. Lighthill [75] provides a solution for the inviscid incompressible high-speed flow around a sphere, assuming a concentric shock structure to the sphere.

Herring [76] expanded on the works of Homman and Lighthill, presenting a set of equations to define the hypersonic flow around a sphere at the stagnation point. Recognizing that the region between the detached shock wave and the body surface could, under certain conditions, be approximated as a boundary layer, Herring developed a method based on simplifying the Navier-Stokes equations. The explicit incorporation of the tangential pressure gradient, derived from the conditions in the inviscid flow behind the shock, was a notable feature that coupled the boundary layer solution to the outer flow field and influenced the calculated velocity profiles and, consequently, quantities like shock standoff distance and heat transfer.

Boundary layer theory is, however, limited at low Reynolds number, where the shock wave and the viscous layer become merged or strongly interact. Cheng [10] developed a two-layer viscous shock layer model for the blunt-body problem in hypersonic flow. This model splits the flow into two layers, as displayed in Figure 2.2: the inner viscous shock layer and the outer shock-transition layer. Cheng's model retained pressure variation across the shock layer, unlike the classical boundary-layer assumption,

and employed modified Rankine-Hugoniot relations to evaluate the shock transition zone. Furthermore, Cheng's work initiated the incorporation of high-temperature effects by including non-equilibrium dissociation with a simplified single dissociation-recombination kinetic model. Earlier work by Fay and Riddell [37] had also incorporated dissociated air. Building upon the foundation of viscous shock layer theory, Blottner [56] investigated the viscous shock layer specifically at the stagnation point and employed a seven-species air model with finite reaction rates and more accurate thermodynamic and transport properties. These methods treated the shock, or shock transition zone, as a discontinuity at the outer edge of the shock layer and did not resolve the internal structure of the shock wave itself. They rely, at least partially in the case of Cheng, on simplifying transformations that result in systems of ordinary differential equations.

Achieving a complete simulation of the flow problem, including the resolution of the structure of the shock wave itself, which is a region of significant non-equilibrium in hypersonic flows, requires solving the full conservation equations (species continuity, momentum, and energy). For these conditions, the shock transition region is of non-negligible thickness relative to the length scales of the vehicle, and the flow can be assumed laminar [47]. For accurately capturing high-temperature non-equilibrium phenomena, the governing equations for two-temperature non-equilibrium conditions can be found in works such as that by Gnoffo *et al.* [54]. These full equations, solved numerically from the uniform free stream through the shock and shock layer to the body surface, represent a more complete approach to modeling stagnation line flows and the associated heating problem, capturing the complex interplay of viscous stresses, heat transfer, and chemical and thermal non-equilibrium within the entire flow field. For many supersonic and hypersonic flow problems, the Navier-Stokes equations can be simplified using the Parabolized Navier-Stokes (PNS) approximation. This technique exploits the dominance of the flow in a primary direction (e.g., along the stagnation line or along the body surface) and allows for efficient space-marching numerical solutions of a system of partial differential equations.

When considering numerical simulations of these complex flows, the boundary conditions applied at the body surface are important for determining the heat transfer to the vehicle. Standard wall boundary conditions include the no-slip condition for velocity (setting tangential and normal velocity components to zero relative to the wall), thermal conditions such as a fixed wall temperature (isothermal wall) or zero heat flux (adiabatic wall), and conditions for species concentrations. A critical aspect of these wall boundary conditions in high-enthalpy flows is the wall catalycity. Wall catalycity refers to the ability of the surface material to promote or inhibit surface chemical reactions. A non-catalytic wall does not facilitate surface reactions; dissociated species reaching the wall do not recombine and instead diffuse back into the flow (or into a porous section). A fully catalytic wall, conversely, instantly catalyzes the recombination of all dissociated species that reach the surface, driving the species concentrations at the wall towards their equilibrium values at the wall temperature and pressure. Materials used in hypersonic vehicle thermal protection systems fall somewhere between these two extremes and are characterized by finite catalytic recombination rates. In stagnation line simulations, wall catalycity is incorporated either through explicit species concentration conditions or finite rate chemistry [77, 78, 79, 80]. The

latter provides increased flexibility through the provision of either catalytic efficiency ratios or rate constants which can be selected to mimic true material properties.

Several recent studies have considered the stagnation line problem numerically, with varying degrees of complexity. Two-dimensional and three-dimensional treatments benefit from the applicability to more complex problems but can be computationally expensive [27, 80, 25]. Chen and Sun [81] developed a one-dimensional solver, but it determines shock standoff distance via correlation [82] and employs simplifying assumptions for transport properties and thermochemistry. Other one-dimensional methods investigate state-resolved thermochemistry [83, 84, 85], increasing fidelity at the cost of computational expense and limiting the number of species. They often make simplifying assumptions for the flow field, such as thin shock [83], single temperature [86, 87], or low-species flows [84, 83]. While these methods capture many complex phenomena, they still face challenges and may leave gaps for transpiration cooling applications, such as the inclusion of mass injection through the wall or the robust handling of multicomponent diffusion effects under all conditions.

2.3.1 Porous injection

Transpiration cooling requires the transport of an injectant through a porous material. Advantages over film cooling through slots or channels come from the uniform spread of coolant over the surface and the lower momentum of coolant injectant at any given location on the surface (reducing the risk of substantial effects on the boundary layer). Darcy's law is traditionally used to model the pressure change across a porous section [88]. In 1856, Henry Darcy investigated the water supply of Dijon and discovered a relationship between the flow rate and pressure difference across a porous substrate [89].

$$u = -\frac{K_D}{\mu}\frac{\delta p}{\delta x} \tag{2.12}$$

where K_D, often called the Darcy coefficient is defined by the nature of the medium and is independent of the fluid characteristics. While Darcy's law was determined empirically through experiment, it has since been derived as a special case of the Navier-Stokes equations using the method of volume averaging [90]. When inertial effects are large, at high Reynolds numbers, the additional Forchheimer term is included to describe the pressure gradient [88]:

$$-\frac{\delta p}{\delta x} = \frac{\mu}{K_D}u + \frac{\rho}{K_F}u^2 \tag{2.13}$$

The term K_F is a form-drag constant, named after the work of Philipp Forchheimer [91]. Darcy's equation alone holds so long as the surface drag due to friction is much larger than the form drag due to flow recirculation. Typically, this is true when the flow velocity is low, or when the pore-diameter Reynolds number is below the order of 1 to 10 [92, 93]. Further, for thin porous sections, the importance of modeling non-linear pressure behavior decreases.

Several strategies exist for modeling non-porous/porous flow interactions, including simply imposing material boundary conditions, coupling of the Navier-Stokes and Darcy equations, or the

modification of the Navier-Stokes equations via penalization [94, 95, 96, 97, 98, 99, 100]. Direct Navier-Stokes solutions which resolve to pore length-scales are also possible but are very computationally expensive [101, 102]. In applications for ablatives and material response, coupled domain methodologies are often used to link shock layer and material response solutions via interface boundary conditions [103, 104, 105, 106]. A universal methodology which provides a more robust treatment of the fluid-material interface has been presented by Weng and Martin [107] and since expanded for more complex applications [108, 109, 110].

Cimolin and Discacciati [111] present a useful methodology for the application of standard flow equations throughout a domain partially occupied by a porous medium. This is accomplished by enforcing a given formulation of the Navier-Stokes equations throughout the domain, with the addition of appropriate penalization terms within the porous subdomain. These penalization terms can be defined to enforce the standard Darcy-Forchheimer pressure gradient. This allows for the numerical solution of fluid properties within a single domain, as opposed to the brute application of boundary conditions at the wall surface or the costly separation of domains into two coupled solutions. This penalization method is based on work by Brinkman [112]. The presented analysis considers the challenge of defining interface conditions applicable to both the first order differential Darcy equation and the second order differential Navier-Stokes equations. Brinkman suggests a modification to the Darcy equation to include an additional viscous term:

$$-\frac{\delta p}{\delta x} = \frac{\mu}{K_D} u - \mu \nabla \cdot (\nabla u) \tag{2.14}$$

When ignoring inertial terms in the Navier-Stokes equations, the Brinkman equation simplifies to Darcy's law when $K_D \to 0$ and the Navier-Stokes equations when $K_D \to \infty$. Brinkman notes that the viscosity in the added term may need to be modified when the porosity is significantly less than one. The modification of the viscosity is based on the geometry of the porous material and can be very challenging to determine [113]. Often, this "effective" viscosity is ignored for pragmatic reasons due to challenges in determining appropriate values for a given material [114, 115, 116, 88]. Nield and Bejan [88] present further modification the Brinkman equation to include a Forchheimer term:

$$-\frac{\delta p}{\delta x} = \frac{\mu}{K_D} u + \frac{C_F}{K_D^{1/2}} |u| u - \mu \nabla \cdot (\nabla u) \tag{2.15}$$

Cimolin and Disciacciati [111] then include the inertial terms of the Navier-Stokes equations. As mentioned above, it should be noted that the exclusion of a modified "effective" viscosity has only been proven rigorously for highly porous materials [116] but is applied pragmatically for the applications considered in this thesis. Additionally, the inertial connective term that has been re-introduced would not suitably model inertial terms due to its disappearance in steady, compressible, one-dimensional flow [111]. This latter simplification is thus valid when inertial effects are negligible. When considering a standard formulation of the Navier-Stokes equations (as presented by Gnoffo *et al.*), the momentum equation can be modified to include the appropriate resistance term. A further complication of including

a porous region is the treatment of the fluid-solid interaction. Hermann *et al.* [117] present a solution incorporating physical properties of the porous material to model fluid-solid heat exchange and solid conduction. Alongside the Darcy-Forchheimer penalization terms in the momentum equation, the fluid-solid exchange term must then be included in the total energy equation, resulting in a modified form of the Navier-Stokes equations.

$$0 = -\nabla \cdot (\rho_s \vec{u}) - \nabla \cdot (\rho_s D_s \nabla y_s) + \dot{w}_s \tag{2.16}$$

$$0 = -\nabla \cdot (\rho \vec{u} \otimes \vec{u}) - \nabla p + \nabla \cdot \tau - \alpha \left(\frac{\mu}{K_D} \vec{u} + \frac{\rho}{K_F} |\vec{u}| \vec{u} \right) \tag{2.17}$$

$$0 = -\nabla \cdot (\rho e_v \vec{u}) + \nabla \cdot ((k_e + k_v) \nabla T_v) + \nabla \cdot \left(\sum_{s=1}^{n_s} h_{v,s} (\rho_s D_s \nabla y_s) \right) - p_e \nabla \cdot \vec{u} - Q \tag{2.18}$$

$$0 = -\nabla \cdot (\rho H \vec{u}) + \nabla \cdot q_c + \nabla \cdot q_d + \nabla \cdot (\tau \cdot \vec{u}) - H_v (T_s - T_t) \tag{2.19}$$

$$0 = k_s (1 - \varepsilon) \nabla \cdot (\frac{\partial T_s}{\partial y}) + H_v (T_s - T_t) \tag{2.20}$$

The coefficient α is thus non-zero for grid cells within the porous subregion. The set of equations models the fluid flow and its interaction with the porous medium via Darcy resistance and fluid-solid energy exchange. It should be noted that an assumption that the porous material is strongly orthotropic allows for a simplification of the porous flow in only the radial direction. This removes any tangential loss terms. Finally, while the frictional resistance term will result in additional heat flux, the slow velocities inside the porous block and moderate permeabilities means this heat flux addition will be small for the applications considered in this thesis.

2.4 Transpiration Cooling

Transpiration cooling (TC) is a thermal management technique that involves injecting a coolant gas through a porous surface. The ability of this process to protect a vehicle is generally described via three main mechanisms. Firstly, as the cold injectant flows through the porous structure, it removes heat from the vehicle via convection. Secondly, the injected gas displaces the hot shock layer gases adjacent to the surface, thereby reducing the near-wall thermal gradient and the conductive heat flux to the wall. Finally, the injectant impedes the transport of reactive species from the shock layer to the surface, mitigating heat flux contributions from near-wall chemical reactions. This inhibition of species transport is also crucial for protecting surface materials, particularly those susceptible to degradation like oxidation in the case of ultrahigh temperature ceramics (UHTCs), which are otherwise promising alternatives to traditional metals due to their high melting points. Consequently, the effectiveness of a transpiration cooling system hinges on its capacity to simultaneously reduce heat and mass transfer to the wall. Figure 2.3 illustrates the flow domain schematic for a transpiration cooled leading edge, highlighting these three cooling mechanisms.

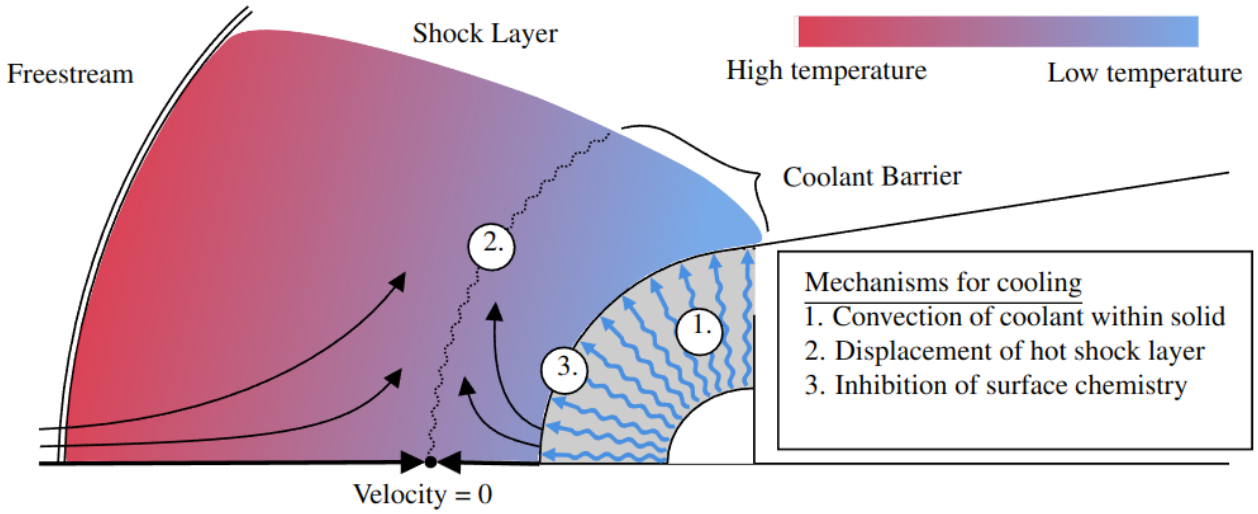

Figure 2.3: Schematic of transpiration cooling with mechanisms for cooling, adapted from Chapter 5

Transpiration cooling research began in the 1940's with Rannie's [118] analytical study of a laminar, transpired sublayer. In 1954, Eckert and Livingood [46] showed the relative benefits of transpiration cooling over film cooling in the context of aircraft engines (later confirmed by Laganelli [8]). Experimental research carried out through the next two decades furthered the phenomenological understanding of mass injection on skin friction, heat transfer, boundary layer transition, shock standoff distance, etc. [119, 120, 121, 122, 123, 124]. In 1966, Woodruff and Lorenz [120] investigated transpiration cooling applied to the hypersonic regime, considering foreign gas injection into a hypersonic boundary layer.

Limits for coolant injectant rate present a fundamental question to the application of TC, with Yoshikawa [125] demonstrating the boundary layer blowoff effect resulting from excessive blowing. This has the effect of blunting the leading edge. Experimental work has further concluded that cooling effectiveness is not consistent at extreme blowing parameters [126, 127] and encourages boundary layer transition aft of injection [128, 129]. Conversely, relatively low blowing ratios may result in recession of the stagnation point inside the porous section, resulting in a similar blunting effect [125]. Meroney and Giedt [121] studied transpiration cooling on a flat plate with a partially dissociated freestream gas, determining that multicomponent transport properties impact heat flux with blowing, further confirming similar conclusions by Libby and Pierucchi [130] and Hearne *et al.* [131]. Howe and Sheaffer [132] studied both forced and natural mass addition for speeds between 10 and 15 km/s, finding characterizations of flow field structures with mass addition for partially dissociated and ionized plasmas in equilibrium and noting that mixture transport property evaluations are valid only when the mixing species are all similar. Specifically, this work found that blowing ratio determined injectant concentration at the wall while Reynolds number controlled the region of diffusion into the shock layer.

More recent studies have introduced more complexity in solution methods, geometries, flow

regimes, and scale. Riabov [133] presented a direct simulation Monte-Carlo (DSMC) technique to study transitional flows over spheres, specifically for rarefied gases. Results confirmed historical trends in near-continuum flow. Meinert *et al.* presented experimental and numerical results investigating the impact of injection on cooling and boundary layer flow [134]. Further studies investigated the effect of mass injection on shock interactions [135, 136], scramjet performance [137, 138], and joint cooling systems [139]. Significant research has been done to study transpiration cooling applied to engine turbines [140, 141, 142, 143]. Recent studies focus on the use of transpiration cooling on flat plates, with special interest in the impact of injection on the boundary layer and aft injection region [138, 144, 145, 146].

Non-equilibrium and multicomponent phenomena with injection

The mixing of cool injectant gas with a dissociated and thermally excited shock layer mixture may result in thermochemical non-equilibrium near the vehicle surface. Further, dissociation and mixing with an injectant gas may result in complex multi-component diffusion phenomena. Often, mixture assumptions are made to simplify the analysis of the shock layer, as done by Lees [147]. This allows for the treatment of the gas mixture with an average molecular weight and specific heat capacity, which in turn reduces the interaction of an injected gas with the shock layer to a binary problem. However, this method is not valid when considering injectants dissimilar from the shock layer mixture, when interested in the effect of individual species, or when the shock layer is appreciably reactive [36]. Thus, it may be important to consider the effect of non-equilibrium and multi-component diffusion when investigating the cooling effectiveness of transpiration cooling.

Hearne *et al.* [131] presented results for an Apollo style trajectory, indicating non-equilibrium gas mixtures resulted in higher wall temperatures relative to an equilibrium analysis and an appreciably thicker shock standoff distance. More recently, Zhang *et al.* [148] and Yi *et al.* [149] considered non-equilibrium for injection on a flat plate and within a channel, respectively. Yi *et al.* [149] specifically employed a coupled two-domain methodology that allows for explicit modeling of the porous flow.

Foreign injectants

Of particular interest in transpiration cooling research is the effect of employing foreign coolants, particularly light gases. Early work by Mickley [150] highlighted the significant influence of molecular weight on mass injection performance. Subsequent analytical investigations, such as those conducted by Hartnett and Liu [151], utilized correlations based on molecular weight to effectively describe experimental results across a range of gas combinations, Mach numbers, and temperature conditions.

Generally, the cooling performance of an injectant is strongly dictated by its thermophysical properties, principally diffusivity and specific heat capacity, both of which are influenced by molecular weight and by binary collision behavior. A wide range of studies suggest that lower molecular weight

injectants outperform heavier gases for cooling applications [143, 152, 153, 144, 146, 154, 155, 156]. The importance of high specific heat capacity is notably demonstrated by the exceptionally high cooling performance achievable with water injection, as discussed by Van Foreest *et al.* [157]. Consequently, a combination of low molecular weight and high heat capacity is generally considered optimal for achieving high cooling effectiveness. Hearne [131] summarized injectant effectiveness based on composition: "The effectiveness of an injected species depends upon its energy storage capacity and its ability to move quickly into the hot outer portions of the boundary layer. The former is characterized by the specific heat and the latter by the molecular weight of the injectant."

However, the use of light gases as injectants is not without potential disadvantages, particularly concerning flow stability and downstream effects. For example, in the context of film cooling for rocket nozzle walls, Keller *et al.* [154] observed that the injection of light gases such as helium were more prone to inducing flow instability due to boundary layer deformation. Furthermore, experimental studies comparing different injectants have shown varied outcomes depending on the specific application and flow regime. Gülhan and Braun [158], for instance, found that compared to air, helium injection resulted in a smaller region of cooling protection downstream of the porous sample. Their work indicated that helium could potentially lead to a greater increase in aerothermal heating, which they attributed to effects like boundary layer transition. Additionally, Glass *et al.* [159] indicated low blowing with hydrogen may increase heat flux due to combustion in the boundary layer.

Oxidation

A further benefit of transpiration cooling is its ability to limit transport of freestream species to the surface of a vehicle. As noted by Henline [160], surface reactions, heavily influenced by the reactivity of the vehicle surface, may contribute significantly to the overall surface heat flux. Additionally, surface reactions are important for oxidation effects, where the recombination of atomic oxygen at the surface can result in degradation of the surface material and its ability to protect internal vehicle components [161, 162, 43]. Rocher *et al.* [163] and Mills and Wortman [164] presented results on mass transfer reduction with injection for a range of freestream conditions and injectants.

Stagnation point injection

This thesis is specifically interested in characterizing mass injection at the stagnation point of a sphere. Table 2.1 outlines investigations of transpiration cooled stagnation points, along with their applicability to elements of the transpiration cooling problem. Only the work of Howe and Sheaffer [132] explicitly considered a catalytic wall condition, while other sources implicitly considered surface reactivity either due to physical material properties in experiments or ablative species in simulations. These sources are thus marked with a "$\sim$" symbol. It should be noted that the work of Marvin and Pope [165] presented results with surface reactivity and foreign injectants only in the experimental section.

Table 2.1: Summary of Methods and Modeling Considerations Across Studies

Source	Method	MC Non-eq	Radius	W. Temp	Catalycity	Injectant
Swann & Pittman (1962) [166]	Numerical	×	×	✓	∼	×
Howe & Sheafffer (1964) [132]	Numerical	×	✓	✓	✓	✓
Marvin & Pope (1967) [165]	Analytical/experimental	×	✓	✓	∼	∼
Yoshikawa (1967) [125]	Analytical/numerical	×	✓	✓	×	✓
Pappas & Lee (1970) [124]	Experimental	n/a	×	×	∼	✓
Mills & Wortman (1972) [164]	Numerical	×	×	✓	×	✓
Kaattari & Field (1978) [129]	Experimental	n/a	✓	×	∼	×
Sreekanth & Reddy (1997) [167]	Numerical	×	×	∼	×	×
Thompson & Gnoffo (2008) [168]	Numerical	✓	×	✓	×	×
Rocher *et al.* (2022) [163]	Semi-analytical	×	✓	✓	×	✓
Naved *et al.* (2023) [169]	Experimental	n/a	×	×	∼	✓

2.4.1 Correlations for mass injection

The effectiveness of transpiration cooling is most commonly quantified by its ability to reduce convective heat and mass transfer to the wall. Several studies have sought to correlate this reduction using non-dimensional parameters, enabling comparison across different flow conditions and injectant properties. Early efforts for correlations sought to assess transpiration cooling effectiveness based on its ability to reduce surface temperature [170, 155]. It is useful to investigate transpiration cooling in the context of correlations. Cooling effectiveness is most commonly described through the use of non-dimensional values. A foundational parameter is the blowing ratio, F, which normalizes the injected mass flux by the freestream mass flux:

$$F = \frac{\rho_{inj} u_{inj}}{\rho_\infty u_\infty} \tag{2.21}$$

The heat transfer Stanton number, St, is the surface heat flux, $\dot{q}_w$ normalized by the external flow enthalpy flux.

$$St = \frac{\dot{q}_w}{\rho_\infty u_\infty (H_0 - h_w)} \tag{2.22}$$

$$H_0 = h_\infty + \frac{1}{2} u_\infty^2 \tag{2.23}$$

The blowing parameter, B_h, is then defined as [171]:

$$B_h = \frac{F}{St_0} \tag{2.24}$$

Initial efforts, such as thin film theory by Mickley [150] and Moffat and Kays [122], described cooling as the result of a surface film generated by the injectant. Kays and Crawford [172] extended this to film cooling, leading to the classic correlation:

$$\frac{St}{St_0} = \frac{B_h}{e^{B_h} - 1} \tag{2.25}$$

Moyer and Rindall [173] investigated the problem in chemically reacting laminar and turbulent boundary layers and amended the correlation:

$$\frac{St}{St_0} = \frac{2\lambda B_h}{e^{2\lambda B_h} - 1} \tag{2.26}$$

where λ is set to 0.4 for turbulent boundary layers and 0.5 for laminar turbulent layers. Thompson and Gnoffo [168] later applied this form to stagnation points, adjusting λ to a value of 1. Swann and Pittman [166] investigated air injection into an equilibrium air shock layer (now for stagnation points), establishing the following correlation employing a quadratic expression.

$$\frac{St}{St_0} = 1 - 0.724B_h + 0.13B_h^2 \tag{2.27}$$

Marvin and Pope [165] verified experimentally and analytically the correlation from Swann and Pittman [166] for both frozen and reacting shock layers. Their work demonstrated that heat flux reduction at the wall is governed by the low-temperature transport properties near the wall, with the high-temperature shock layer having less influence on the near-wall temperature gradient. They further applied their analysis to the Martian atmosphere, finding that while convective heating increased relative to a nitrogen based atmosphere, heat flux reduction via mass injection was consistent. Marvin and Pope [165] considered foreign injectants under the assumption of near-wall frozen chemistry. Extending prior work at low temperatures, and assuming the injected gas will have little chemical interaction with the shock layer, they proposed the following scaling for molecular weight:

$$B_h = \left(\frac{M_\infty}{M_{inj}}\right)^n \frac{F}{St_0} \tag{2.28}$$

The exponent n is determined empirically, with Marvin and Pope citing a range between 0.25 and 0.4. A main limitation of this work is the evaluation of the shock layer with mixture properties. For higher enthalpy, smaller radius applications, the assumptions of equal diffusivity of component species may fail to accurately capture heat flux reduction.

Yoshikawa [125] pursued a shock layer theory approach, building on the work of Marvin and Pope across a variety of gases. The distribution of the mass flow is assumed independent of heat transfer, allowing the energy equation to be decoupled from the mass and momentum conservation equations. The resulting linearized energy equation allowed for simple evaluation of convective heat reduction

due to mass addition.

$$\frac{St}{St_0} = \left(\frac{\delta}{\delta_0}\gamma^{B_h/B_*}\right)^{0.5} \frac{exp\left(-(1/\pi)\left(\frac{\delta}{\delta_0}\right)\gamma^{B_h/B_*}B_h^2\right)}{1+erf\left((1/\pi)\left(\frac{\delta}{\delta_0}\right)\gamma^{B_h/B_*}\right)^{0.5}B_h} \tag{2.29}$$

$$B_* = 1.59\sqrt{\frac{M_{inj}}{M_{air}}} \tag{2.30}$$

$$\gamma = \sqrt{\frac{M_\infty}{M_{inj}}}N_{inj} \tag{2.31}$$

$$\frac{\delta}{\delta_0} = 1 + \sqrt{\frac{\rho_\infty}{\rho_s}\frac{M_\infty}{M_{inj}}}St_0 B_h \tag{2.32}$$

Here, differences in performance of injectant is determined from the work of Marvin and Pope and incorporates only a difference in the molecular weight of the injectant.

Mass transfer reduction is also of interest, particularly for limiting the transport of reactive species to the surface. Mills and Wortman [164] and Rocher *et al.* [163] developed correlations for the mass Stanton number, St_m. The former provided correlations for both heat and mass transfer reduction, incorporating the effects of injectant molecular weight and specific heat:

$$\frac{St}{St_0} = \frac{a_h B_h}{e^{a_h B_h}-1} \tag{2.33}$$

$$a_h = 1.3\left(\frac{M_\infty}{M_{inj}}\right)^{1/3}\left(\frac{C_{p,inj}}{2.5\mathcal{R}/M_{inj}}\right)^{1/2} \tag{2.34}$$

$$\frac{St_m}{St_{m0}} = \frac{a_m B_m}{e^{a_m B_m}-1} \tag{2.35}$$

$$a_m = 1.65\left(\frac{M_\infty}{M_{inj}}\right)^{5/6} \tag{2.36}$$

Rocher *et al.* [163] employed a self-similar boundary layer analysis, developing a correlation which was shown to be equivalent to the wall concentration of the injectant.

$$\frac{St_m}{St_{m0}} = \frac{\lambda B_m}{e^{\lambda B_m}-1} \tag{2.37}$$

$$\lambda = \left(\frac{\mu_e T_w}{\mu T_e}\right)^{0.5} Sc_w^{0.6} 2.52\rho_e \left(\frac{M_{ext}D_{ext,ext}}{M_{inj}D_{inj,ext}}\right)_w^{0.75} \tag{2.38}$$

While these historical correlations provide valuable engineering guidance, they are generally limited by assumptions of equilibrium and simplified mixing rules for transport properties. It would be useful to understand the importance of rigorous multi-component transport property calculations (especially for dissimilar injectants) and non-equilibrium conditions, as discussed in the introduction.

2.5 Opportunity for contributions

The preceding sections have outlined robust research contributing to the understanding of transpiration cooling applied as a thermal protection system to hypersonic stagnation points. The main opportunities to contribute to the current state of the art are the explicit modeling and analysis of complexities that arise from diverse near wall gas mixtures. Non-equilibrium thermochemistry and multi-component transport properties (which require accurate descriptions for binary collision behavior) are important when considering sharp leading edges and injectants dissimilar from the freestream gas mixture. It would be especially useful to investigate the effect of conductivity and diffusion on cooling behavior in the context of multicomponent gas mixtures and foreign injectants. While multidimensional universal solvers provide robust treatment of both the shock layer and the material response, there is still value in a lower-order method capable of modeling the important physical features independent of explicit vehicle geometry. The definition and implementation of a unified treatment of shock layer stagnation flow with porous injection and appropriate surface conditions (such as surface catalycity and solid temperature) remain active areas of research critical for predictive simulations.

Chapter 3
Collision Integrals and Orbiting Analysis for Polar Species Using the Stockmayer Potential

3.1 Foreword

Accurate modeling of non-equilibrium flows and the complex mixing introduced by mass injection requires robust thermochemical data and transport property calculations. The OCEAN library, developed by the Numerical Analysis Group at the Oxford Thermofluids Institute, provides a strong foundation for evaluating transport properties of two-temperature gas mixtures using rigorous kinetic theory. While many solvers compute transport properties using mixing rules and polynomial fits, OCEAN provides the benefit of more rigorous evaluations and the accompanying derivatives for directly building system Jacobian matrices. The research presented in this chapter leveraged and expanded OCEAN.

Typically, the contributions of polar species to plasma transport properties are evaluated using spherical phenomenological potential functions or, more recently, with ab-initio computations. This research addressed a gap in the thermochemical modeling literature by investigating the binary interactions of polar species using a methodology that specifically accounted for molecular polarity. It is important to understand how to accurately model the near wall mixing interactions in the context of transpiration cooling. Non-equilibrium flows and small radii result in shock layer compositions approaching the wall that may have large concentrations of minor species (relative to equilibrium compositions). For air, this is notably NO. For Mars, this is notably CO. In the context of pyrolysis gases or more complex injectants, this could be other polar species such as CN and CH. These species can impact transport properties when present in large concentrations. This work explored using the non-spherical Stockmayer potential function to model polar-polar collisions and developed a methodology to analyze the orbiting boundary's asymptotic behavior at low energies.

This research, contributing to the fundamental understanding and modeling of transport properties in complex gas mixtures, was published in the Journal of Thermophysics and Heat Transfer (April 2025).

3.2 Statement of authorship

- Title of the paper: *Collision Integrals and Orbiting Analysis for Polar Species Using the Stockmayer Potential*
- Publication status: Published

- Publication details: Samuel D. Brody, Justin Clarke, Matthew McGilvray, and Luca di Mare, "Collision Integrals and Orbiting Analysis for Polar Species Using the Stockmayer Potential," Journal of Thermophysics and Heat Transfer (2025). doi:10.2514/1.T7112

Table 3.1: Statement of Authorship

Author	**Contribution**	**Percentage (%)**
Samuel D. Brody	Conception	40
	Writing	90
	Code Development	60
	Data Acquisition	100
	Analysis and Interpretation	70
Justin Clarke	Code Development	20
Matthew McGilvray	Supervision	20
	Critical Revision	40
Luca di Mare	Conception	60
	Writing	10
	Code Development	20
	Analysis and Interpretation	30
	Supervision	80
	Critical Revision	60

3.3 Manuscript

Collision Integrals and Orbiting Analysis for Polar Species Using the Stockmayer Potential

Samuel D. Brody *, Justin Clarke †, Matthew McGilvray ‡ Luca di Mare §
Oxford Thermofluids Institute, University of Oxford, Oxford, Oxfordshire, OX1 2JD, United Kingdom

Polar species appear in several planetary entry problems, in both the shock heated gas and its interaction with the ablative heat shield or other active cooling systems. Typically, the contributions of polar species to plasma transport properties are evaluated using spherical phenomenological potential functions or, more recently, with ab-initio computations. Limited consideration has been given to the use of non-spherical potential functions for polar species. The Stockmayer potential is a Lennard-Jones potential function, modified to account for polar interactions. In this paper, the Stockmayer potential is used to compute collision integrals for NO, CN, CO, and CH. Additionally, a methodology applicable to potential functions similar in form to the Lennard-Jones potential is developed to determine scaling laws which describe the asymptotic behavior of the orbiting boundary at low energies. The use of the non-spherical Stockmayer potential function preserves agreement with the Lennard Jones potential at moderate to high temperatures (above 5,000 K) when potential parameters are selected consistently. This indicates that the polarity of species at these temperatures do not strongly impact transport properties.

Nomenclature

b	=	impact parameter
b_0	=	orbiting impact parameter
k	=	Boltzmann Constant, 1.380649e-23 J/K
l	=	first constant for collision integral
M	=	molecular weight
$Q^{(l)}$	=	integral cross section
r	=	radial intermolecular separation
s	=	second constant for collision integral

*DPhil Candidate, Department of Engineering Science. Electronic mail: samuel.brody@new.ox.ac.uk
†DPhil Candidate, Department of Engineering Science.
‡Professor, Department of Engineering Science.
§Associate Professor, Department of Engineering Science.

T = Temperature, K

δ = polarity term

δ_{max} = maximum polarity term for a given collision pair

ε_0 = dispersion energy

ζ = orientation-dependent polarity function

$\theta_{1,2}$ = angle of inclination of dipole 1 and 2, deg

μ = dipole moment, Debye

σ = rigid sphere diameter

ϕ = azimuthal angle between two particles, deg

φ = intermolecular potential function

$\Omega_{ij}^{(l,s)*}$ = collision integral, Å^2

Subscripts

1,2 = 1st and 2nd species in a collision pair

Superscripts

$\sim$ = dimensional value

* = non-dimensional value

I. Introduction

Collision integrals are required for the computation of transport properties in gas mixtures. For a multi-species gas, such as those encountered in atmospheric entry and sustained hypersonic flight problems, collision integrals for all interacting species pairs must be computed. Atmospheric entry and sustained flight conditions involving species such as NO, CO, and CN are particularly problematic due to the high levels of radiation emitted within these mixtures. Specific entry conditions for particles result in differing deflection scenarios. Relative to traditional potential functions, accounting for polarity requires better characterization of collisions due to the impact of changing dipole orientation. Work by Mason and Monchick [1, 2] presented a framework for the use of the Stockmayer potential, but only for generic dipole moment separations. Itean et al. [3] tabulated values for Earth species at temperatures below 1200 K. Little effort has been made to implement this work for individual binary interactions at moderate to high temperatures, accounting for the full range of possible entry orientations. Current literature focuses primarily on ab-initio or density functional theory solution schemes when data is available or spherical potential functions which still only afford a partial representation of polar species [4–15]. Wright et al. have published very useful resources for collision integrals for both Earth [16] and Mars and Venus [17] entry problems. However, spherical potentials are used for polar species.

This paper presents a solution approach specific to the polar species present in atmospheric entry or in active cooling

systems. Basic definitions for computing collision integrals are presented in Section II. Orbiting conditions are discussed in Section III. Section IV describes the assessment of collision integrals and specifically the determination of potential parameters. Results and conclusions are presented in Sections V and VI, respectively. The notation of Hirschfelder et al. [18] and Monchick and Mason [1] is followed throughout.

II. Orientation-Averaged Collision Integrals

The Stockmayer potential function is a modified form of the Lennard-Jones (LJ) potential, with the addition of a long-range term accounting for the polarity of the species involved in the collision. Most potential functions, including the traditional LJ potential, assume nonpolar molecules and are thus spherical. For some scenarios, however, polarity may have an important impact on intermolecular interactions. This is especially applicable in regimes where dissociation results in the creation of multiple polar species, or where ablation or mass injection introduce such species into flows. The polarity of a molecule is defined by its embedded electric dipole moment, μ, which quantifies the separation of positive and negative electrical charges in a molecule. A polar molecule exhibits this separation of charge but has no charge overall. For a collision between two polar molecules, the deflection angle will depend appreciably on the orientation of the dipoles of each molecule during their interaction.

The Stockmayer potential is defined as follows:

$$\tilde{\varphi}(\tilde{r}, \mu_1, \mu_2, \zeta) = 4\varepsilon_0 \left[\left(\frac{\sigma}{\tilde{r}} \right)^{12} - \left(\frac{\sigma}{\tilde{r}} \right)^{6} \right] - \left(\frac{\mu_1 \mu_2}{\tilde{r}^3} \right) \zeta \tag{1}$$

where $\zeta = 2cos(\theta_1)cos(\theta_2) - sin(\theta_1)sin(\theta_2)cos(\phi)$. The subscripts 1 and 2 indicate the two colliding molecules. The variable $\tilde{r}$ represents the dimensional distance between the colliding molecules, and ε_0 and σ are constants for a given collision pair, corresponding to the minimum intermolecular potential energy and separation distance for zero potential energy, respectively. The variable σ is also called the equivalent rigid sphere diameter. The angles θ_1, θ_2, and ϕ define the orientation of the colliding species, as displayed in Figure 1. The Stockmayer potential can be defined in non-dimensional terms, as done by Monchick and Mason [1] to follow the non-dimensional solution scheme presented by Hirschfelder et al. [18]. The potential, $\tilde{\varphi}$, is normalized by ε_0, and $\tilde{r}$ is normalized by σ.

$$\varphi(r, \delta) = 4 \left[\left(\frac{1}{r^{12}} \right) - \left(\frac{1}{r^6} \right) + \delta \left(\frac{1}{r^3} \right) \right] \tag{2}$$

where $\delta = (1/4)\mu_1 \mu_2 \zeta$. It should also be noted that by this definition, a positive value of δ corresponds to a repulsive dipole configuration, resulting in an additional long range repulsive term.

Chapman-Enskog theory can be used to determine the transport properties of a gas mixture in terms of the collision

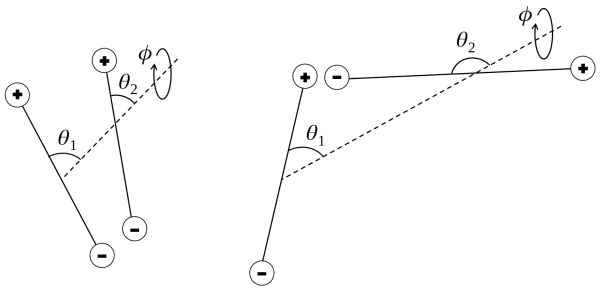

(a) (b)

Fig. 1 Intermolecular interaction for (a) neutral interaction and (b) highly attractive "head-to-tail" interaction

integrals $\Omega^{(l,s)}$ for binary interactions [18]. The collision integrals are defined as

$$\Omega_{ij}^{(l,s)*}(T^*,\delta) = \frac{2}{(s+1)!T^{*s+2}}\int_0^\infty x^{2s+3}e^{-x^2}Q^{(l)}(T^*,\delta)dx \tag{3}$$

where $T^* = kT/\varepsilon_0$, and k is the Boltzmann constant. The variables l and s specify the transport property being evaluated. The quantity $Q^{(l)}$ is the integral cross section, which is evaluated as

$$Q^{(l)}(\varepsilon,\delta) = \frac{2}{\left[1-\frac{1}{2}\frac{1+(-1)^l}{1+l}\right]}\int_0^\infty (1-\cos^l\chi(\varepsilon,b,\delta))bdb \tag{4}$$

where b is the impact parameter, i.e. the minimum distance between the trajectories in absence of any interaction. Finally, the deflection angle χ is evaluated by the following integral:

$$\chi(\varepsilon,b,\delta) = \pi - 2b\int_{r_c}^\infty \frac{dr}{r^2F(b,\varepsilon,r,\delta)^{\frac{1}{2}}} \tag{5}$$

Where F is a function of impact parameter, kinetic energy, intermolecular separation, and polarity parameter, respectively, defined by:

$$F(b,\varepsilon,r,\delta) = 1 - \frac{\varphi(r,\delta)}{\varepsilon} - \frac{b^2}{r^2} \tag{6}$$

The integrand of equation 5 represents the deflection angle as evaluated from the classical mechanics two-body problem represented with respect to the center of mass of the two interacting particles. The lower limit of the integral, r_c, is the distance of closest approach, which is the largest root of the equation $F(b,\varepsilon,r,\delta) = 0$.

The deflection angle is averaged over all possible values of the collision parameter b to obtain the cross section of interest. The collision integral is finally obtained averaging the cross sections over all possible values of relative kinetic energy between the interacting particles.

Equation 3 defines collision integrals for a fixed relative orientation (δ) and temperature (T^*). Due to the complexity

of the problem, it is impossible to analytically determine the given orientation for an intermolecular collision. Thus, a numerical approach must be defined. Earlier attempts to evaluate transport properties using the Stockmayer potential opted for a set value of $\zeta = 2$, corresponding to a head-to-tail configuration [19]. However, this maximum attractive orientation does not dominate an intermolecular interaction. It is likely that the deflection angle primarily depends on the "entry" interaction at the distance of closest approach. In this range, which dominates the integrand of Equation 5, orientation is likely relatively stable [5]. Thus, it is reasonable to evaluate the deflection angle at one relative orientation, rather than accounting for changes throughout a collision trajectory [1].

With the inclusion of the fixed-relative orientation, the cross sections and collision integrals are computed as averages across all possible orientations. Monchick and Mason [1] attribute equal weight to all orientations, as there is no indication that a more complex weighting system would be more realistic. Given this assumption, the orientation-averaged collision integral can be defined:

$$\langle \Omega_{ij}^{(l,s)}(T^*) \rangle = \frac{1}{8\pi} \int_{-1}^{1} \int_{-1}^{1} \int_{0}^{2\pi} \Omega_{ij}^{(l,s)*}(T^*, \delta) d\phi d(cos(\theta_1)) d(cos(\theta_2)) \tag{7}$$

As noted by Mason and Monchick [1], five-point Gaussian integration is suitable for the accurate evaluation of these integrals and has been implemented in this study. In the case of collisions between differing species, i and j, binary definitions must be applied for the rigid sphere diameter, σ, and the potential minimum, ε_0. These combination rules are the standard implementation [2, 13, 14, 20, 21], but other rules could easily be implemented. They are defined along with the non-dimensional forms of the temperature and dipole moment [2, 18].

$$\sigma_{ij} = \frac{1}{2}(\sigma_i + \sigma_j) \tag{8}$$

$$\varepsilon_{ij} = (\varepsilon_{0_i} \varepsilon_{0_j})^{\frac{1}{2}} \tag{9}$$

$$T^* = \frac{kT}{\varepsilon_{ij}} \tag{10}$$

$$\mu = \frac{\mu'}{(\varepsilon_{ij} \sigma_{ij}^3)^{\frac{1}{2}}} \tag{11}$$

III. Orbiting

Intermolecular interactions result in three possible types of collision [18], shown schematically in Figure 2. It is useful to discuss these scenarios in relation to the function $F(b, \varepsilon, r, \delta)$. Collisions can be characterized graphically using roots to the function or as the intersections of the curves of energy-scaled potential function and of the function $1 - b^2/r^2$. The first two collision types are the limiting cases of possible collision behavior. First, grazing collisions result from dominating attractive forces, at relatively high impact parameters and energies. This occurs when the

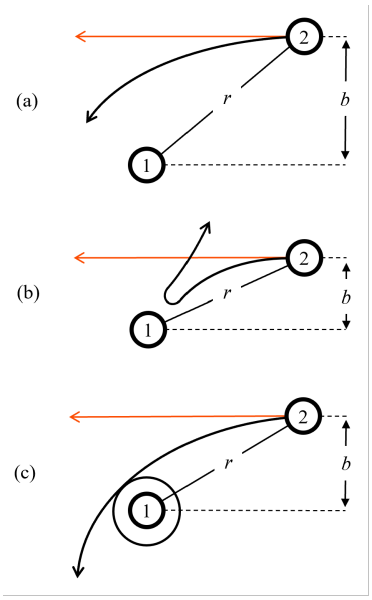

Fig. 2 Intermolecular interaction from the frame of reference of particle 1 for (a) grazing collision, (b) head-on collision, and (c) orbiting collision

function $F(b, \varepsilon, r, \delta)$ is monotonic, as shown in subplot (a) of Figure 3. Second, "head-on" collisions, where the repulsive forces dominate, generally occur at lower impact parameters. Displayed in Figure 3, the function $F(b, \varepsilon, r, \delta)$ has a local minimum which is not simultaneously a root for collisions of this type. Finally, between these two collisions, the opportunity for orbiting arises, when a balance exists between the attractive and repulsive forces. Decreasing from high energy (where only grazing collisions are possible), orbiting first occurs at the "critical" case. Here, the root is an inflection point, and a tangency condition between the partitioned curve is their only intersection, as shown in subplot (c) of Figure 3. As displayed in subplot (d) of Figure 3, the generic form of orbiting conditions below the critical energy corresponds to a root coinciding instead with a local minimum of $F(b, \varepsilon, r, \delta)$. The tangency condition is now the intersection at larger intermolecular separation. These conditions are met by moderate impact parameters and negative, or only small positive, values of δ.

Orbiting presents challenges in the evaluation of the collision cross section, with such conditions manifesting as a singularity in the integration of the cross section due to rapid oscillation in the $cos(\chi)$ term. Collision integrals are typically evaluated numerically. To overcome the inefficiency that arises from orbiting, integration for the collision cross section is split at the orbiting impact parameter, b_0 [22]:

$$Q^{(l)} = \frac{2}{\left[1 - \frac{1}{2}\frac{1+(-1)^l}{1+l}\right]} \times \left(\int_0^{b_0} (1 - \cos^l \chi) b db + \int_{b_0}^{\infty} (1 - \cos^l \chi) b db \right) \tag{12}$$

It should be noted that orbiting conditions are constrained by a maximum relative kinetic energy. However, the

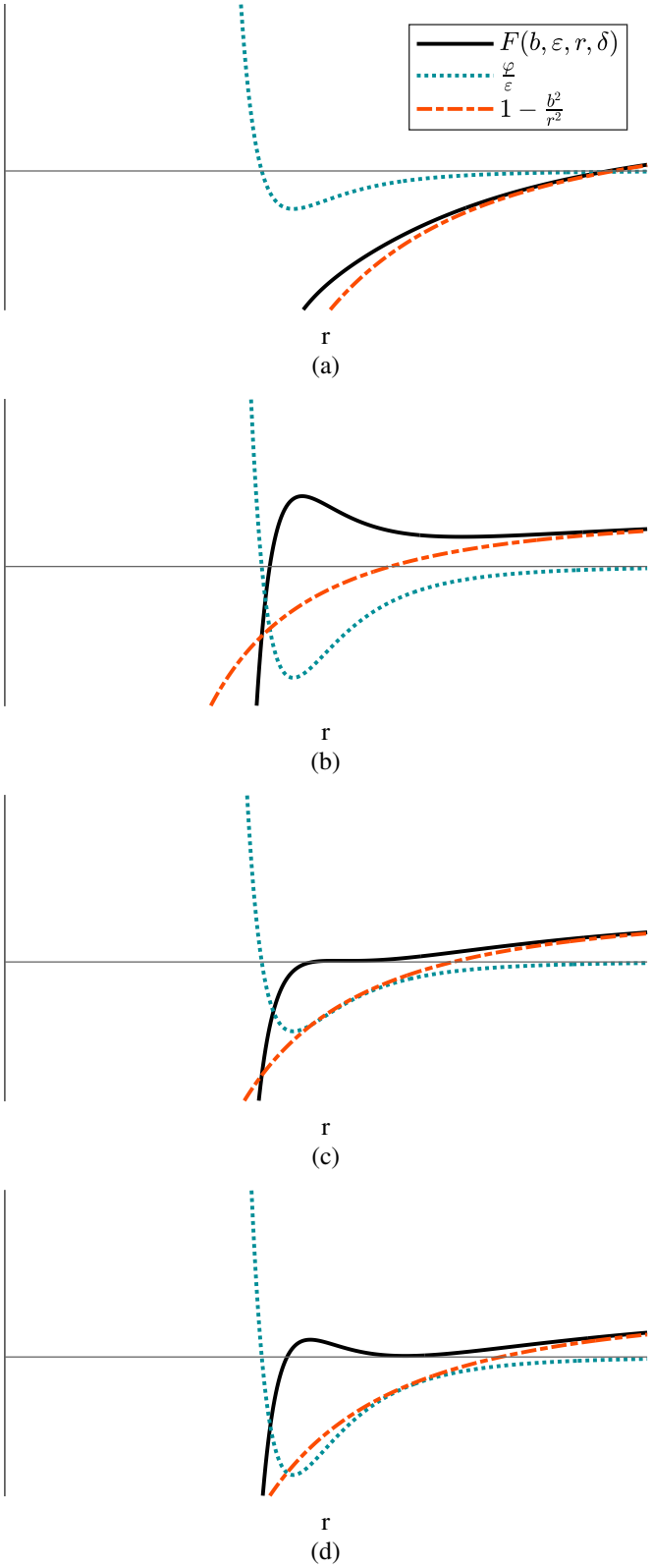

Fig. 3 Plots of $F(b,\varepsilon,r,\delta)$ for (a) grazing collision (non-orbiting), (b) head-on collision (non-orbiting), (c) critical orbiting collision, and (d) generic orbiting collision

existence of closely-packed oscillations of the deflection angle at higher energies can introduce similar inefficiency in numerical evaluations. Thus, a similar splitting of the cross section integral at the impact parameter corresponding to the locus of minima of $F(b, \varepsilon, r, \delta)$ is employed. With the possibility of orbiting, it becomes important to define an orbiting boundary and a method for determining orbiting conditions in order to compute the integral efficiently (by splitting). It is therefore useful to explore the asymptotic behavior of the orbiting boundary across a wide range of realistic impact parameters.

A. Orbiting Conditions

Orbiting conditions (and locus of minima conditions) can be represented by curves in the (b, ε) parameter space and are used for the selection of b_0 in Equation 12. The definition of these curves begins with the solution of critical orbiting parameters. Critical orbiting parameters are the highest energy orbiting conditions, defined as the solution to the following system of equations:

$$F(b, \varepsilon, r, \delta) = 1 - \frac{\varphi(r, \delta)}{\varepsilon} - \frac{b^2}{r^2} = 0 \tag{13}$$

$$\frac{\partial F}{\partial r}(b, \varepsilon, r, \delta) = 0 \tag{14}$$

$$\frac{\partial^2 F}{\partial r^2}(b, \varepsilon, r, \delta) = 0 \tag{15}$$

Generalized orbiting conditions below this maximum ε are determined with the same first two constraints, with the orbiting branch selected with a relaxed third constraint of $\partial^2 F/\partial r^2 > 0$. It is necessary to determine the upper orbiting boundary, i.e. the highest energy where the splitting in Equation 12 occurs. From this critical orbiting boundary, a tangent function can be determined which allows for the use of a continuation algorithm along the surface defined by the first two constraints. This follows from the understanding that the third constraint, defining a line, must lie along the intersection of these two surfaces.

Two notes must be made for the implementation of a continuation algorithm to define an orbiting curve for a given value of δ. First, the curve must be defined at energies above and below the critical orbiting energy. Energies above correspond to the locus of minima conditions, determined by reversing the inequality of the third constraint. Values of the critical orbiting energy correspond to the equality of the single and double roots that can be found in from the first constraint ($F = 0$). From the critical energy, the double and single roots diverge, with one growing while the other shrinks. Because two particles will approach from large distances, only the scenarios corresponding to the larger double root (which satisfies the second constraint) will precipitate orbiting. Thus, a continuation algorithm must enforce a search in the direction of increasing radial distance and decreasing energy to define the singularity branch of the orbiting curve. Second, when searching at energies above the critical orbiting energy, the double root no longer exists. Thus, the locus of minima branch is defined by the location of the single root from the $F = 0$ constraint.

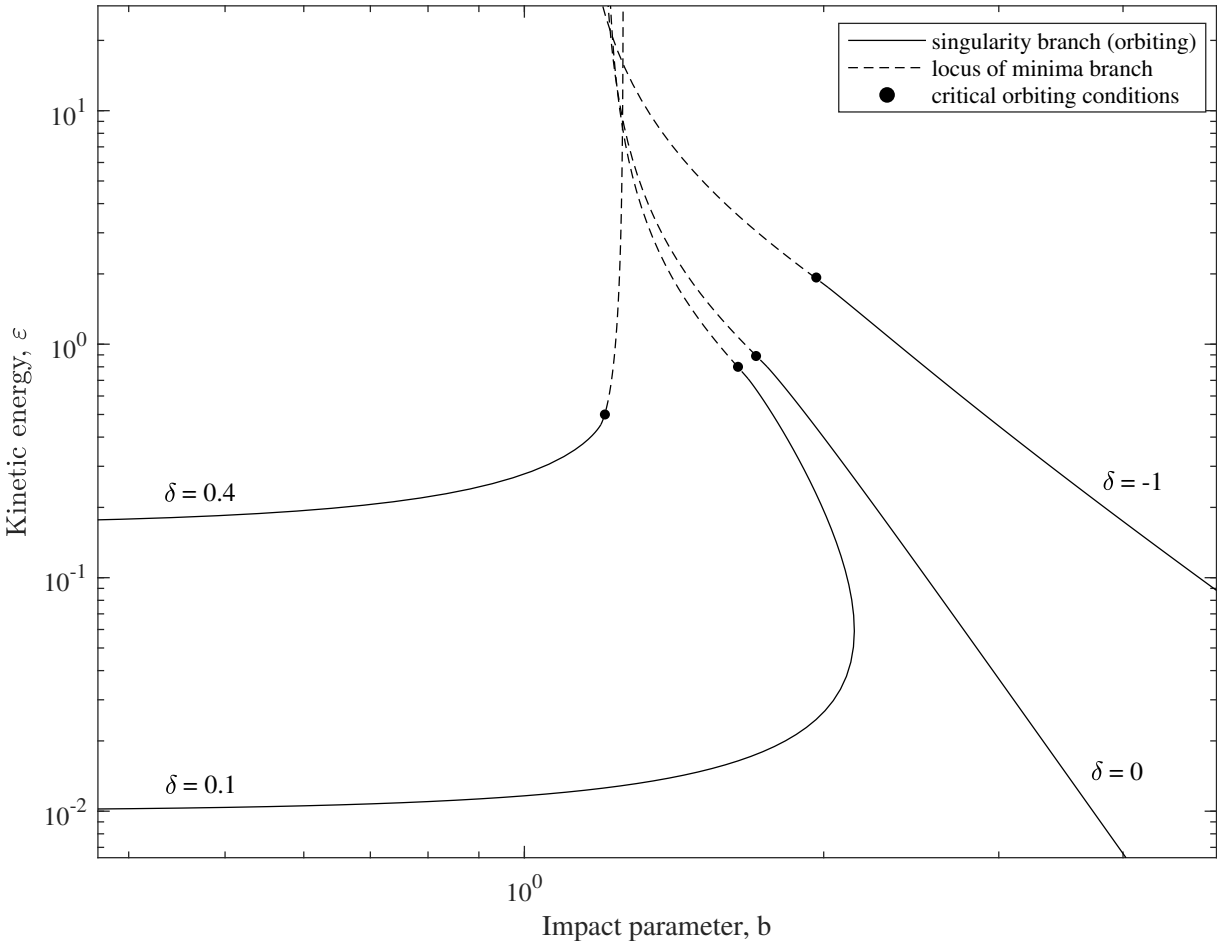

Fig. 4 Orbiting curves for varying values of δ

B. Orbiting Surface

For the Lennard-Jones potential, only one orbiting curve is required. However, when implementing the orientation-averaged collision integral solution scheme for the Stockmayer potential, a large range of δ values must be considered to account for all possible collision orientations. Thus, the orbiting curve solution process becomes untenable, requiring the numerically taxing creation of an orbiting curve for every possible value of δ. Several of these curves are displayed in Figure 4.

The complexity can be reduced if orbiting curves can be scaled in a form independent of δ. The relationship across varying δ can be assessed through an order of magnitude analysis of the orbiting conditions. It should be noted that this analysis applies to any spherical potential modified to incorporate a third long range term which requires a fourth integration step, whether to account for orientation or another parameter. Noting the potential function can be generically expressed using only the first term of the expansion (ignoring the long-range repulsive region) and the

Stockmayer term, the two orbiting constraints are cast as follows:

$$\text{Constraint 1: } F \approx 1 - \frac{4}{\varepsilon r^m} - \frac{4\delta}{\varepsilon r^3} - \frac{b^2}{r^2} = 0 \tag{16}$$

$$\text{Constraint 2: } \frac{\partial F}{\partial r} \approx \frac{4m}{\varepsilon r^{m+1}} + \frac{12\delta}{\varepsilon r^4} + \frac{2b^2}{r^3} = 0 \tag{17}$$

Ignoring the $1/r^m$ term at relatively high intermolecular separation and substituting Equation 16 into Equation 17, the resulting relation appears:

$$\frac{-2\delta}{\varepsilon r^3} \propto 1 \quad \text{or} \quad r \propto \left(\frac{-2\delta}{\varepsilon}\right)^{\frac{1}{3}} \tag{18}$$

Substituting into the first constraint, the slope for all δ at relatively large separation is defined with the following relation:

$$b \propto \left(\frac{\delta}{\varepsilon}\right)^{\frac{1}{3}} \tag{19}$$

Consider the two constraints for the $\delta = 0$ case.

$$F \approx 1 - \frac{4}{\varepsilon r^m} - \frac{b^2}{r^2} = 0 \tag{20}$$

$$\frac{\partial F}{\partial r} \approx \frac{4m}{\varepsilon r^{m+1}} + \frac{2b^2}{r^3} = 0 \tag{21}$$

Multiplying the second constraint through by r and eliminating the b^2/r^2 terms by subtraction results:

$$r \propto \varepsilon^{\frac{-1}{m}} \tag{22}$$

Upon substitution back into the first constraint, the scaling law which collapses orbiting curves onto the $\delta = 0$ curves appears:

$$b \propto \varepsilon^{\frac{-1}{m}} \tag{23}$$

Looking now at the cases for end behavior, consider orbiting curves where $\delta > 0$ when impact parameter goes to zero.

$$F \approx 1 - \frac{4}{\varepsilon r^m} - \frac{4\delta}{\varepsilon r^3} = 0 \tag{24}$$

$$\frac{\partial F}{\partial r} \approx \frac{4m}{\varepsilon r^{m+1}} + \frac{12\delta}{\varepsilon r^4} = 0 \tag{25}$$

Eliminating the $1/r^3$ term, the following relation results:

$$r \propto \varepsilon^{\frac{-1}{m}} \tag{26}$$

Substituting back into the first constraint, a scaling law for end behavior $\delta > 0$ curves is obtained:

$$\varepsilon \propto \delta^2 \tag{27}$$

Now consider orbiting curves where $\delta < 0$ when impact parameter grows.

$$F \approx 1 - \frac{4}{\varepsilon r^m} - \frac{4\delta}{\varepsilon r^3} - \frac{b^2}{r^2} = 0 \tag{28}$$

$$\frac{\partial F}{\partial r} \approx \frac{4m}{\varepsilon r^{m+1}} + \frac{12\delta}{\varepsilon r^4} + \frac{2b^2}{r^3} = 0 \tag{29}$$

Using the relation from Equation 19 substituted into both constraints and multiplying the second constraint through by r, the following arises:

$$\frac{4}{\varepsilon r^m} \propto -\frac{b^2}{r^2} \tag{30}$$

$$\frac{4m}{\varepsilon r^m} \propto -\frac{2b^2}{r^2} \tag{31}$$

Subtracting the two equations and understanding that m is a constant, the b^2/r^2 term is reduced to a constant. Thus, the same logic can be applied as for the $b = 0$ case, only now where the b^2/r^2 term is combined with the scalar 1, resulting in the scaling law for end behavior for $\delta < 0$.

$$\varepsilon \propto \delta^2 \tag{32}$$

The nature of these curves can be described through a variety of power law relationships as shown in Figures 5 and 6. Because the orbiting curves mimic each other in form, a subset of curves can be used to create an orbiting surface. It is clear that an orbiting surface can be defined across the necessary range of impact parameters, energies, and polarity constants. Two boundaries of this orbiting surface exist. First, a linear boundary exists across the δ range such that beyond certain corresponding energies, no positive impact parameter will result in orbiting. These are the critical orbiting parameters that correspond to the boundary between the singularity and locus of minima branches on the orbiting curve. Second, orbiting curves for positive values of δ where orbiting is still possible trend to the $b = 0$ axis, resulting in an additional boundary. Only values of δ up to $\sqrt{8/27}$ can result in orbiting conditions [1]. This is because, as the additional long-range repulsive term (corresponding to positive δ values) grows, the depth of the potential energy

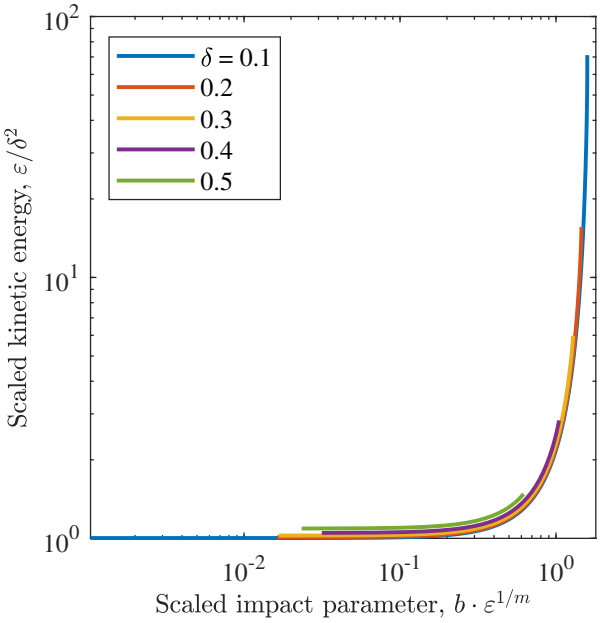

Fig. 5 Scaled Orbiting Curves for positive values of δ for $m = 6$

"well" diminishes, limiting and finally removing the opportunity for orbiting. The limits of this region are easily defined by continuation from the critical orbiting parameters to the orbiting parameters for zero impact parameter. To constrain the orbiting surface further, polarity parameters and impact parameters were investigated at physically realistic values, with special attention to the lower values of impact parameter, where orbiting is generally more likely [18].

This surface can be used as the basis for determining splitting conditions, with interpolated values used as an initial guess for the solution to the system of equations. In this work, Delaunay triangulation was used to define a surface from a suitable range of orbiting curves, and a jump-and-walk scheme was used for the interpolation [23]. Greater refinement is used in the region around critical orbiting parameters as well as at lower energies where impact parameter varies more drastically.

The result of this orbiting surface investigation is a clear understanding of its smooth nature. This simplifies the numerical implementation. Only a few orbiting curves must be defined at the beginning of the solution process, and orbiting conditions can be discovered by interpolation and quickly refined solution throughout the solution process.

IV. Assessment of Collision Integrals

The preceding sections outline the framework for evaluating collision integrals based on the non-spherical Stockmayer Potential. The presence of polar species for many applications may warrant a non-spherical potential. However, polarity complicates the analysis of orbiting. Evaluating the integral cross section, or specifically the singularity of this integral, requires an accurate characterization of orbiting conditions. Analytical power laws derived from the form of the chosen

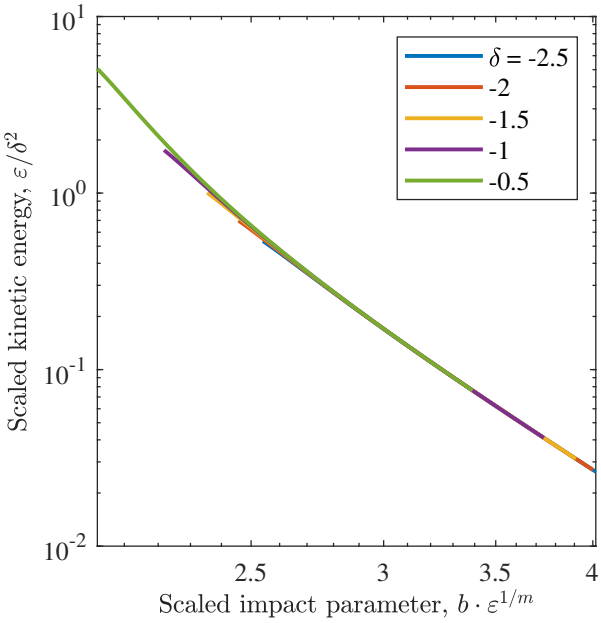

Fig. 6 Scaled Orbiting Curves for negative values of δ for $m = 6$

potential function provides an understanding of the asymptotic behavior of binary collisions. These power laws enable the creation of an orbiting surface from only a few (in the case of this work, 20) generic orbiting curves. Orbiting curves are assessed by continuation from critical orbiting conditions using newton iterations. Interpolated values from the orbiting surface serve as an initial guess for orbiting conditions, which are then refined. In this way, the solution scheme does not require the creation of an orbiting curve for every orientation, or even for every collision pair. Other methods could be employed to treat the singularity for the collision cross section integral. Colonna and Laricchiuta [24] provide a very efficient numerical method. The creation of an orbiting surface is less numerically efficient but allows for the study of the asymptotic behavior of orbiting. With orbiting appropriately characterized, non-dimensional collision integrals can then be assessed for specific collision pairs. Gauss-Laguerre integration is used for improper integrals, and 5 point Gauss-Legendre integration is used for proper integrals, including the last round of integration across orientation. This mirrors the implementation by Mason and Monchick [1]. Thus, the benefit of the proposed method is not in increased numerical efficiency but in increased procedural efficiency, as the number of orbiting curves required for a set of collision pairs is reduced.

A. Potential Parameters

A significant practical challenge to assessing dimensional collision integrals is the selection of potential parameters. As outlined above, these parameters are used to cast a non-dimensional solution process. The potential minimum, ε_0 (generally presented as the ratio with the Boltzmann constant, k), and the equivalent rigid sphere diameter, σ, are specific

to the employed potential function. The rigid sphere diameter has a larger effect on collision integrals than the potential minimum. Neither parameter affects the shape of the collision integral curve as a function of temperature; they only scale the collision integral or temperature. Potential parameters are generally obtained from transport properties at low temperatures, where experimental data or ab initio results exist. Otherwise, estimates for transport properties must be used. Other methods employ Density Functional Theory [8] or inversion of reduced collision integrals [6] to determine potentials and their parameters. For some applications, 2nd virial coefficients are used but may provide significantly varying results [25, 26] when applied to transport properties evaluations. Thus, collision integrals generically match transport properties at low temperatures, and extrapolation to higher temperatures is not easily validated. The Lennard Jones potential is the most well-studied potential function. A significant literature exists for fitting potential parameters and analyzing the use of this potential to model observed transport properties [18, 21, 27–29]. For the present study of polarity's effect on transport properties, any spherical potential function form could have been chosen and modified. The existence of previous generic work for validation as well the large amount of historical research for the LJ potential made its modified form a desirable choice.

V. Results and Discussion

Collision integrals for the species of interest have been computed and reported in Tables 1 and 2. Potential parameters are chosen to match experimental data or ab-initio results when available. Otherwise, predicted viscosity values between 1000 K and 5000 K from Svehla [21] are used to fit potential parameters. For the case of interactions where at least one low-polarity species (NO and CO), the potential parameters do not vary from Lennard Jones parameters fit to the same data. For collisions involving these species, the maximum value of δ, defined as $\delta_{max} = 0.5\mu_1\mu_2$, remains on the order of 0.1 or less. For interactions between the highly polar species (CN and CH), potential parameters differ appreciably from Lennard Jones parameters fit to the same data. Maximum values of δ for these interaction pairs can exceed 2.5.

As is common for collision integral data [16, 17], tabulations for the $\Omega^{1,1}$ and $\Omega^{2,2}$ are provided, with the ability to derive other necessary collision integral data from these two sets. Additionally, tabulations of the collision integral ratios B* and C*, used in the definition of transport properties such a thermal conductivity and diffusivity, are provided in the Appendix in Tables 3 and 4. Figure 7 displays the variance between Stockmayer produced collision integrals with those evaluated using the un-modified Lennard Jones potential. Significant differences mainly occur at temperatures below 1000 K, indicating polarity only affects collision behavior at low temperatures. When standard Lennard Jones parameters are used, values at high temperature match regardless of polarity. Adjusting potential parameters to match viscosity data even at low temperatures results in only small shifts to the high-temperature values. Non-dimensional tabulations of the computed collision integrals are provided in Tables 5 and 6 of the Appendix, which can be transformed with the introduction of new potential parameters. However, non-dimensional collision integrals for the Stockmayer potential correspond to a collision pair specific δ_{max}, attained from the non-dimensional definition of the dipole moment.

Table 1 Collision integral $\Omega^{1,1}$ (Å^2) with potential parameters

	Species Pair									
	CH-CH	CN-CH	CN-CN	CO-CH	CO-CN	CO-CO	NO-CH	NO-CN	NO-CO	NO-NO
ε/k(K)	75.00	80.78	87.00	83.87	90.34	93.80	94.87	102.18	106.09	120.00
σ(Å)	3.30	3.55	3.79	3.48	3.73	3.67	3.38	3.63	3.57	3.47
T(K)										
300	15.613	16.206	17.127	11.073	12.897	12.586	10.820	12.649	12.294	12.048
500	11.728	12.588	13.695	9.905	11.503	11.206	9.597	11.187	10.868	10.557
600	10.727	11.656	12.826	9.568	11.104	10.817	9.252	10.779	10.471	10.150
1000	8.819	9.845	11.054	8.760	10.155	9.894	8.442	9.824	9.549	9.222
2000	7.263	8.324	9.514	7.846	9.092	8.857	7.550	8.782	8.537	8.230
4000	6.301	7.312	8.420	7.045	8.164	7.954	6.778	7.884	7.665	7.387
5000	6.057	7.041	8.117	6.805	7.886	7.683	6.546	7.615	7.404	7.136
6000	5.872	6.832	7.882	6.613	7.665	7.467	6.363	7.402	7.197	6.937
8000	5.599	6.523	7.530	6.321	7.327	7.139	6.082	7.077	6.881	6.633
10000	5.401	6.295	7.271	6.103	7.074	6.892	5.872	6.833	6.644	6.405
15000	5.066	5.907	6.824	5.723	6.634	6.464	5.507	6.408	6.232	6.009
20000	4.848	5.646	6.524	5.466	6.336	6.174	5.261	6.122	5.953	5.741

Table 2 Collision integral $\Omega^{2,2}$ (Å^2) with potential parameters

	Species Pair									
	CH-CH	CN-CH	CN-CN	CO-CH	CO-CN	CO-CO	NO-CH	NO-CN	NO-CO	NO-NO
ε/k(K)	75.00	80.78	87.00	83.87	90.34	93.80	94.87	102.18	106.09	120.00
σ(Å)	3.30	3.55	3.79	3.48	3.73	3.67	3.38	3.63	3.57	3.47
T(K)										
300	17.614	18.332	19.357	12.137	14.125	13.765	11.855	13.847	13.442	13.168
500	13.371	14.198	15.362	10.919	12.665	12.334	10.563	12.298	11.940	11.578
600	12.263	13.163	14.359	10.576	12.260	11.937	10.210	11.880	11.535	11.161
1000	9.932	11.011	12.319	9.751	11.293	10.995	9.383	10.908	10.594	10.214
2000	8.102	9.282	10.598	8.800	10.190	9.923	8.458	9.831	9.552	9.197
4000	7.055	8.189	9.423	7.944	9.201	8.962	7.636	8.878	8.629	8.309
5000	6.800	7.906	9.107	7.683	8.900	8.669	7.386	8.588	8.348	8.039
6000	6.610	7.690	8.863	7.475	8.659	8.435	7.187	8.357	8.124	7.824
8000	6.334	7.372	8.502	7.155	8.290	8.075	6.880	8.002	7.779	7.494
10000	6.135	7.140	8.236	6.914	8.011	7.805	6.649	7.734	7.519	7.245
15000	5.793	6.740	7.778	6.492	7.524	7.331	6.246	7.266	7.064	6.808
20000	5.562	6.467	7.465	6.206	7.193	7.008	5.972	6.947	6.755	6.511

Thus, values must be interpolated from generic tabulations for a variety of δ_{max} to estimate dimensional collision integrals for given parameters. Tables 5 and 6 provide tabulations for values of δ_{max} greater than those presented

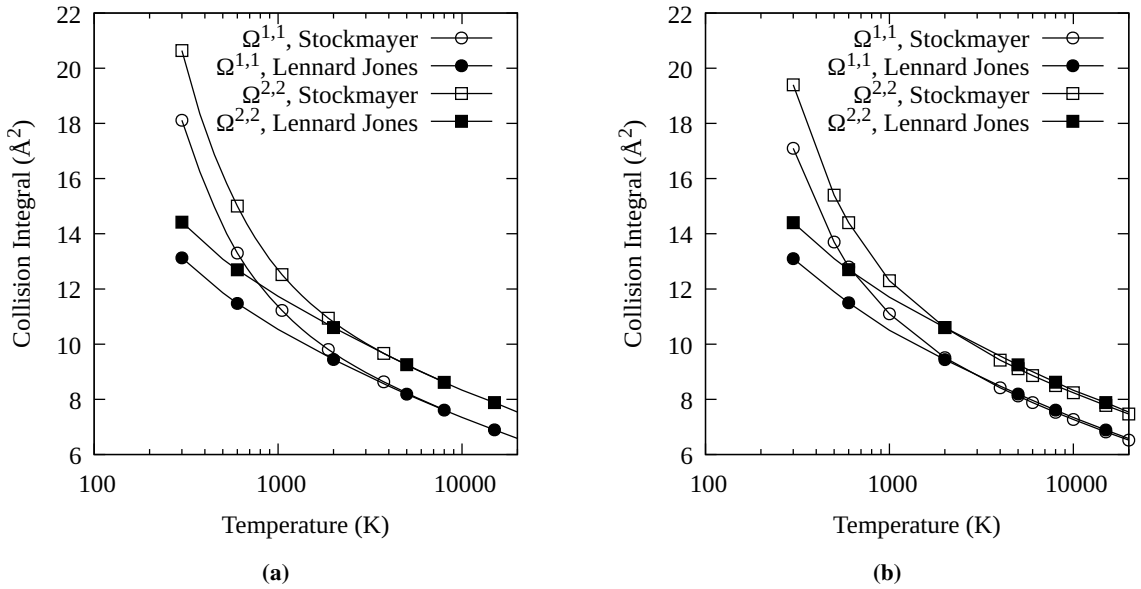

Fig. 7 Collision Integrals for CN-CN collision pair with (a) Lennard Jones potential parameters and (b) potential parameters fit to Svehla [21] viscosity predictions for 1000-5000 K

by Mason and Monchick [1] or Itean et al. [3]. Values for dipole moments are taken from the NIST Computational Chemistry Comparison and Benchmark DataBase (CCCBDB) [30]. Only electronic ground states have been considered in this study.

Figure 8 displays the NO component of viscosity relative to temperature for a standard Earth atmosphere entry condition. Viscosity is evaluated for an equilibrium post-shock condition using rigorous kinetic theory. The specific formulation employed is provided in the Appendix, and results differ exclusively in the collision integrals employed for polar species interactions. Potential parameters were fit to the experimental data presented by Ellis and Raw [31] and Clifford et al. [32]. The dataset from Itean et al. dataset is masked by the experimental data points. Results from Abbaspour et al. [6], using the inversion of reduced viscosity collision integrals at zero pressure, match well, indicating more robust methods would behave similarly with the addition of a polarity term. The same consistency remained for carbon monoxide tabulations [7]. Evaluation of viscosity using the Lennard Jones potential is omitted, as values never differed by more than 0.2% across the temperature range. Figure 9 displays the same results for a highly polar molecule, presenting the CN component of viscosity relative to temperature for a standard Mars atmosphere entry condition. Potential parameters are again fit to low temperature values, in this case the predicted values of Svehla [21]. Even for highly polar species, the difference between the Lennard Jones potential and Stockmayer potential is small, never exceeding 5% at temperatures above 1000 K. Thus, it is apparent that polarity does not affect transport properties at high temperatures when potential parameters are selected consistently. Differences at high temperatures between the Stockmayer potential and tabulations from Bzowski et al. [14] or Riabov [13] are then a result of differences

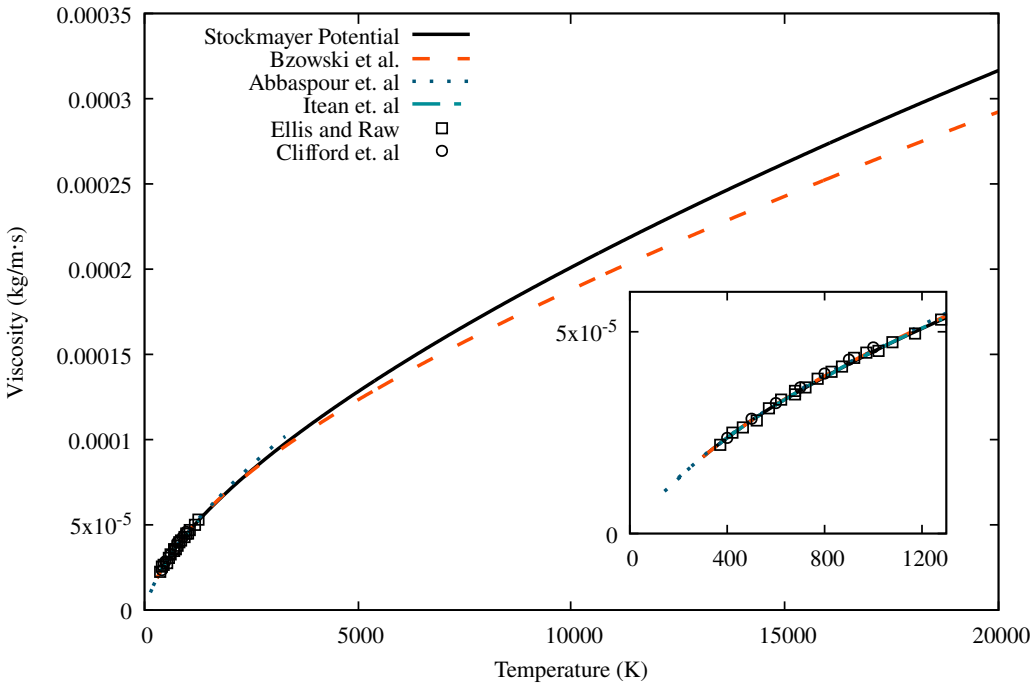

Fig. 8 NO component of viscosity versus temperature for Earth atmosphere at 10 kPa

in the spherical representation of collisions. Thus, for temperatures of interest to atmospheric entry or hypersonic flight vehicles likely to result in the presence of polar species, modelling polarity does not appreciably affect transport properties, relative to an unmodified spherical counterpart where potential parameters are determined consistently. This extends to Martian and other planetary entry problems as well as a range of foreign mass injectant cooling technologies. At low temperatures, the shape of the potential and its long range behavior, including polarity, determine behavior. However, polarity does not contribute to the collision integrals at higher temperatures because it scales with the long-range r^{-3} term and is therefore masked by the spherical terms (generally of order r^{-6} or below depending on the potential function). Because a similar situation would arise with most potentials, it is likely that the addition of polar terms does not affect high temperature collision integrals.

VI. Conclusions

A calculation method for orientation-averaged collision integrals has been presented which effectively incorporates the large parameter space for orbiting. This methodology may be useful for the implementation of other potential functions (that incorporate an additional integration across collision integrals) or even observed collision potential energy surfaces. The Lennard Jones potential provided a test case for the addition of a polarity term. There exist phenomenological and experimentally-based potential functions developed as improvements to the Lennard Jones potential [6, 7, 12–14, 33]. Similar to the Lennard Jones potential, the inclusion of a polar term to these alternative

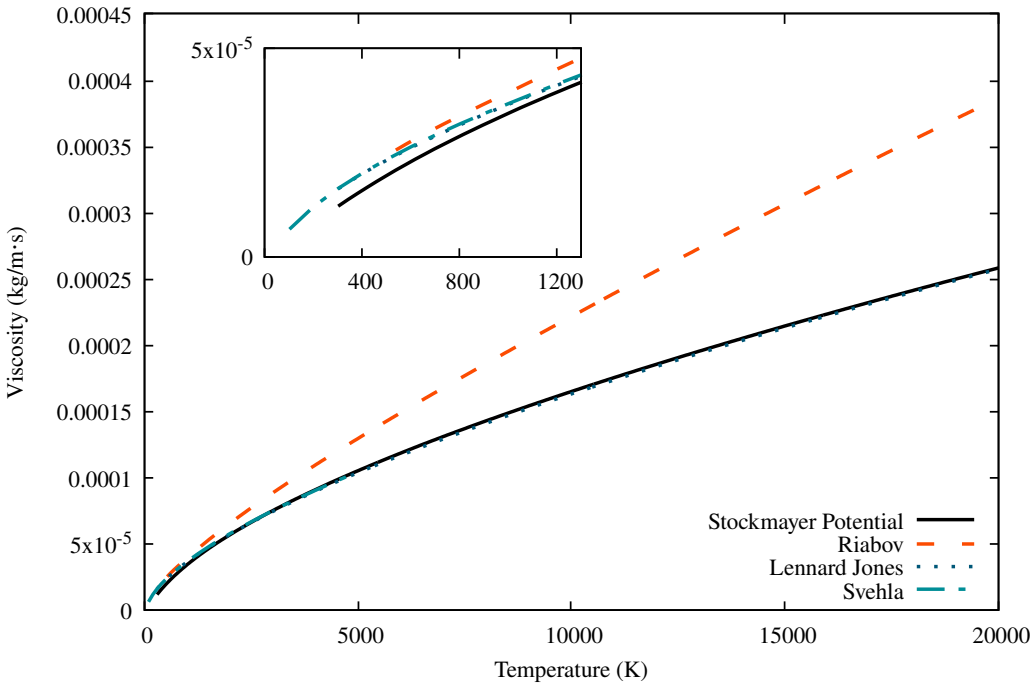

Fig. 9 CN component of viscosity versus temperature for Martian atmosphere at 10 kPa

potential functions would likely not affect transport property evaluations at high temperatures, as long as parameters were determined consistently. Thus, where available, more robust phenomenological potentials should be used. Otherwise, the LJ potential with standard potential parameters can be employed.

As the diversity of atmospheres under investigation for entry problems and mass injection grows, accurately modeling specific binary interactions warrants increased focus. The importance of this pursuit is further increased in scenarios of high thermo-chemical non-equilibrium which may result in large concentrations of diverse species in a broad range of temperatures [34, 35]. In this paper, polarity was investigated. Real potentials for polar molecules are multipoles, with a spherical portion followed by a long-range dipole term. However, the inner part of the potential determines the collision behavior at high temperature, with its shape dominated almost exclusively by the spherical part of the potential. Thus, when polar species such as NO, CN, CO, and CH are introduced into flows, at moderate to high temperatures, the use of spherical potential functions for the tabulation of collision integrals is likely sufficient. The more physically realistic Stockmayer potential is shown to match the Lennard Jones potential in the evaluation of transport properties, when potential parameters are fit to match the same viscosity data. This remains true even for highly polar species with dipole moments greater than 2.0 Debye. A library of collision integrals which incorporates physically realistic binary interaction modelling is worthwhile in the pursuit of accurate thermochemical modelling for diverse problem sets. The results of this study indicate that spherical potential functions validated against similar non-polar collision pairs can be accurately employed for polar species.

Appendix: Supplementary Definitions and Tabulations

A. Evaluation of Transport Properties

Hirschfelder et al. [18] present a rigorous method for the evaluation of viscosity, conductivity, electrical conductivity, and diffusion of gas mixtures. The coefficient for pure viscosity and the first approximation for a binary mixture are defined:

$$[\eta_i]_1 = 2.6693 \times 10^{-8} \frac{\sqrt{MT}}{\sigma^2 \Omega^{(2,2)*}(T^*)} \tag{33}$$

$$[\eta_{ij}]_1 = 2.6693 \times 10^{-8} \frac{\sqrt{2M_1M_2T/(M_1+M_2)}}{\sigma_{ij}^2 \Omega^{(2,2)*}(T_{12}^*)} \tag{34}$$

From these terms, the rigorous definition for viscosity of multicomponent gas mixtures is:

$$[\eta_{mix}]_1 = -\frac{\begin{vmatrix} H_{11} & H_{12} & H_{13} & \cdots & H_{1n} & x_1 \\ H_{12} & H_{22} & H_{23} & \cdots & H_{2n} & x_2 \\ H_{13} & H_{23} & H_{33} & \cdots & H_{3n} & x_3 \\ . & . & . & & . & . \\ . & . & . & & . & . \\ . & . & . & & . & . \\ H_{1n} & H_{2n} & H_{3n} & \cdots & H_{nn} & x_n \\ x_1 & x_2 & x_3 & \cdots & x_n & 0 \end{vmatrix}}{\begin{vmatrix} H_{11} & H_{12} & H_{13} & \cdots & H_{1n} \\ H_{12} & H_{22} & H_{23} & \cdots & H_{2n} \\ H_{13} & H_{23} & H_{33} & \cdots & H_{3n} \\ . & . & . & & . \\ . & . & . & & . \\ . & . & . & & . \\ H_{1n} & H_{2n} & H_{3n} & \cdots & H_{nn} \end{vmatrix}} \tag{35}$$

$$H_{ii} = \frac{x_i^2}{[\eta_i]_1} + \sum_{k=1}^{n} \frac{2x_i x_k}{[\eta_i k]_1} \frac{M_i M_k}{(M_i + M_k)^2} \left[\frac{5}{3A_{ik}^*} + \frac{M_k}{M_i} \right], \quad k \neq i \tag{36}$$

$$H_{ij} = -\frac{2x_i x_j}{[\eta_{ij}]_1} \frac{M_i M_j}{(M_i + M_j)^2} \left[\frac{5}{3A_{ij}^*} - 1 \right], \quad i \neq j \tag{37}$$

$$A_{ij}^* = \frac{\Omega_{ij}^{(2,2)*}}{\Omega_{ij}^{(1,1)*}} \tag{38}$$

Definitions for thermal conductivity, electrical conductivity, and diffusion are similar in form and for brevity will not be presented here. If rigorous definitions are not required, the method provided by Yos et al. [36], which implements mixing rules for collision integrals, can be utilized.

B. Additional Collision Integral Tabulations

Table 3 Collision integral ratio B* (-) with potential parameters

	Species Pair									
	CH-CH	CN-CH	CN-CN	CO-CH	CO-CN	CO-CO	NO-CH	NO-CN	NO-CO	NO-NO
ε/k(K)	75.00	80.78	87.00	83.87	90.34	93.80	94.87	102.18	106.09	120.00
σ(Å)	3.30	3.55	3.79	3.48	3.73	3.67	3.38	3.63	3.57	3.47
T(K)										
300	1.222	1.195	1.171	1.099	1.100	1.100	1.103	1.104	1.104	1.108
500	1.164	1.143	1.128	1.093	1.093	1.093	1.094	1.094	1.094	1.095
600	1.150	1.131	1.119	1.092	1.092	1.092	1.093	1.093	1.093	1.094
1000	1.122	1.109	1.103	1.093	1.093	1.092	1.093	1.093	1.092	1.092
2000	1.102	1.098	1.096	1.094	1.094	1.094	1.094	1.094	1.094	1.093
4000	1.095	1.095	1.095	1.096	1.096	1.096	1.096	1.096	1.096	1.095
5000	1.095	1.095	1.095	1.097	1.097	1.096	1.096	1.096	1.096	1.096
6000	1.094	1.095	1.095	1.097	1.097	1.097	1.097	1.097	1.097	1.096
8000	1.094	1.095	1.095	1.098	1.098	1.097	1.097	1.097	1.097	1.097
10000	1.094	1.095	1.095	1.098	1.098	1.098	1.098	1.098	1.098	1.097
15000	1.094	1.096	1.096	1.099	1.099	1.099	1.099	1.098	1.098	1.098
20000	1.096	1.097	1.097	1.099	1.099	1.099	1.099	1.099	1.099	1.099

Acknowledgments

Samuel Brody gratefully acknowledges the Marshall Commission for financial support as well as the U.S. Air Force for their support of this effort. Justin Clarke gratefully acknowledges the Rhodes Trust for financial support. The authors have no conflicts to disclose.

Table 4 Collision integral ratio C* (-) with potential parameters

	Species Pair									
	CH-CH	CN-CH	CN-CN	CO-CH	CO-CN	CO-CO	NO-CH	NO-CN	NO-CO	NO-NO
ε/k(K)	75.00	80.78	87.00	83.87	90.34	93.80	94.87	102.18	106.09	120.00
σ(Å)	3.30	3.55	3.79	3.48	3.73	3.67	3.38	3.63	3.57	3.47
T(K)										
300	0.794	0.814	0.833	0.917	0.915	0.913	0.910	0.908	0.907	0.900
500	0.835	0.855	0.874	0.935	0.933	0.933	0.931	0.929	0.930	0.925
600	0.852	0.871	0.888	0.939	0.938	0.938	0.936	0.934	0.935	0.931
1000	0.888	0.904	0.916	0.945	0.945	0.945	0.944	0.944	0.943	0.942
2000	0.922	0.931	0.937	0.948	0.948	0.948	0.948	0.948	0.948	0.947
4000	0.939	0.943	0.945	0.948	0.948	0.948	0.948	0.948	0.948	0.948
5000	0.942	0.944	0.946	0.948	0.948	0.948	0.948	0.948	0.948	0.948
6000	0.944	0.946	0.947	0.948	0.948	0.948	0.948	0.948	0.948	0.948
8000	0.946	0.947	0.947	0.948	0.948	0.948	0.948	0.948	0.948	0.948
10000	0.947	0.947	0.948	0.947	0.947	0.947	0.947	0.948	0.948	0.948
15000	0.948	0.948	0.948	0.947	0.947	0.947	0.947	0.947	0.947	0.947
20000	0.949	0.948	0.948	0.947	0.947	0.947	0.947	0.947	0.947	0.947

Table 5 Reduced collision integral $\Omega^{1,1}$ (*)

	Species Pair									
	CH-CH	CN-CH	CN-CN	CO-CH	CO-CN	CO-CO	NO-CH	NO-CN	NO-CO	NO-NO
δ_{max}	4.589	3.413	2.576	0.287	0.216	0.018	0.366	0.274	0.023	0.029
T^*										
1	6.223	4.335	2.923	1.445	1.445	1.445	1.445	1.445	1.445	1.442
1.2	5.388	3.650	2.584	1.319	1.319	1.319	1.320	1.319	1.319	1.319
1.4	4.924	3.368	2.347	1.230	1.230	1.230	1.231	1.230	1.230	1.232
1.6	4.487	2.998	2.142	1.165	1.164	1.165	1.166	1.165	1.165	1.169
1.8	4.156	2.825	1.984	1.124	1.123	1.130	1.128	1.122	1.136	1.118
2	3.883	2.624	1.850	1.077	1.077	1.077	1.077	1.077	1.077	1.077
2.5	3.334	2.289	1.606	1.003	1.003	1.003	1.003	1.003	1.003	1.000
3	2.946	1.985	1.441	0.951	0.951	0.951	0.951	0.951	0.951	0.950
3.5	2.665	1.790	1.312	0.913	0.913	0.913	0.913	0.913	0.913	0.913
4	2.373	1.632	1.218	0.884	0.884	0.884	0.885	0.884	0.884	0.885
5	2.020	1.418	1.093	0.842	0.842	0.842	0.842	0.842	0.842	0.843
6	1.798	1.286	1.007	0.812	0.812	0.812	0.813	0.812	0.812	0.813
7	1.645	1.164	0.942	0.790	0.790	0.790	0.790	0.790	0.790	0.790
8	1.488	1.086	0.895	0.771	0.771	0.771	0.771	0.771	0.771	0.771
9	1.383	1.016	0.859	0.756	0.756	0.756	0.756	0.756	0.756	0.756
10	1.290	0.967	0.830	0.742	0.742	0.742	0.742	0.742	0.742	0.742
12	1.151	0.894	0.787	0.720	0.720	0.720	0.721	0.720	0.720	0.720
14	1.063	0.846	0.755	0.703	0.703	0.703	0.703	0.703	0.703	0.703
16	0.988	0.806	0.729	0.688	0.688	0.688	0.688	0.688	0.688	0.688
18	0.934	0.775	0.708	0.675	0.675	0.675	0.675	0.675	0.675	0.675
20	0.887	0.748	0.692	0.664	0.664	0.664	0.664	0.664	0.664	0.664
25	0.805	0.698	0.659	0.642	0.642	0.642	0.642	0.642	0.642	0.642
30	0.746	0.663	0.636	0.624	0.624	0.624	0.624	0.624	0.624	0.624
35	0.704	0.639	0.618	0.609	0.609	0.609	0.609	0.609	0.609	0.609
40	0.672	0.620	0.604	0.596	0.596	0.596	0.596	0.596	0.596	0.596
50	0.626	0.592	0.581	0.576	0.576	0.576	0.576	0.576	0.576	0.576
75	0.566	0.548	0.543	0.541	0.541	0.541	0.541	0.541	0.541	0.541
100	0.533	0.521	0.518	0.517	0.517	0.517	0.517	0.517	0.517	0.517

Table 6 Reduced collision integral $\Omega^{2,2}$ (*)

	Species Pair									
	CH-CH	CN-CH	CN-CN	CO-CH	CO-CN	CO-CO	NO-CH	NO-CN	NO-CO	NO-NO
δ_{max}	4.589	3.413	2.576	0.287	0.216	0.018	0.366	0.274	0.023	0.029
T^*										
1	6.591	4.559	3.234	1.591	1.591	1.591	1.592	1.591	1.591	1.592
1.2	5.858	4.043	2.883	1.458	1.458	1.457	1.458	1.458	1.457	1.456
1.4	5.304	3.670	2.619	1.358	1.358	1.357	1.358	1.358	1.357	1.356
1.6	4.882	3.346	2.400	1.281	1.281	1.281	1.282	1.281	1.281	1.280
1.8	4.449	3.079	2.218	1.226	1.226	1.226	1.224	1.226	1.225	1.221
2	4.192	2.865	2.085	1.175	1.175	1.175	1.176	1.175	1.175	1.176
2.5	3.603	2.467	1.815	1.093	1.093	1.093	1.093	1.093	1.093	1.094
3	3.137	2.185	1.622	1.039	1.039	1.039	1.039	1.039	1.039	1.039
3.5	2.827	2.008	1.495	1.000	1.000	1.000	1.000	1.000	1.000	1.000
4	2.611	1.844	1.388	0.970	0.970	0.970	0.970	0.970	0.970	0.970
5	2.299	1.617	1.234	0.927	0.927	0.927	0.927	0.927	0.927	0.927
6	2.052	1.453	1.135	0.896	0.896	0.896	0.896	0.896	0.896	0.896
7	1.857	1.339	1.064	0.873	0.873	0.873	0.873	0.873	0.873	0.873
8	1.732	1.251	1.009	0.854	0.854	0.854	0.854	0.854	0.854	0.854
9	1.616	1.179	0.966	0.838	0.838	0.838	0.838	0.838	0.838	0.838
10	1.514	1.120	0.932	0.824	0.824	0.824	0.824	0.824	0.824	0.824
12	1.362	1.027	0.880	0.802	0.802	0.802	0.802	0.802	0.802	0.802
14	1.244	0.959	0.842	0.784	0.784	0.784	0.784	0.784	0.784	0.784
16	1.152	0.908	0.814	0.768	0.768	0.768	0.768	0.768	0.768	0.768
18	1.080	0.869	0.791	0.755	0.755	0.755	0.755	0.755	0.755	0.755
20	1.020	0.838	0.772	0.744	0.744	0.744	0.744	0.744	0.744	0.744
25	0.910	0.780	0.736	0.720	0.720	0.720	0.720	0.720	0.720	0.720
30	0.839	0.741	0.710	0.701	0.701	0.701	0.701	0.701	0.701	0.701
35	0.788	0.713	0.690	0.685	0.685	0.685	0.685	0.685	0.685	0.685
40	0.751	0.692	0.675	0.672	0.672	0.672	0.672	0.672	0.672	0.672
50	0.700	0.661	0.650	0.650	0.650	0.650	0.650	0.650	0.650	0.650
75	0.634	0.616	0.611	0.611	0.611	0.611	0.611	0.611	0.611	0.611
100	0.601	0.589	0.586	0.585	0.585	0.585	0.585	0.585	0.585	0.585

References

[1] Monchick, L., and Mason, E. A., "Transport Properties of Polar Gases," *The Journal of Chemical Physics*, Vol. 35, No. 5, 1961, pp. 1676–1697. https://doi.org/10.1063/1.1732130.

[2] Monchick, L., and Mason, E. A., "Transport Properties of Polar-Gas Mixtures," *The Journal of Chemical Physics*, Vol. 36, No. 10, 1962, pp. 2746–2757. https://doi.org/10.1063/1.1732363.

[3] Itean, E. C., Glueck, A. R., and Svehla, R. A., "Collision Integrals for a modified Stockmayer Potential," Tech. Rep. NASA TN D-481, National Aeronautics and Space Administration, 1961.

[4] Stallcop, J., Partridge, H., and Levin, E., "Effective potential energies and transport cross sections for interactions of hydrogen and nitrogen," *Physical Review A - Atomic, Molecular, and Optical Physics*, Vol. 62, 2000. https://doi.org/10.1103/PhysRevA.62.062709.

[5] Stallcop, J. R., Partridge, H., and Levin, E., "Effective potential energies and transport cross sections for atom-molecule interactions of nitrogen and oxygen," *Physical Review A - Atomic, Molecular, and Optical Physics*, Vol. 64, 2001. https://doi.org/10.1103/PhysRevA.64.042722.

[6] Abbaspour, M., Goharshadi, E. K., and Emampour, J. S., "Determination of potential energy functions and calculation transport properties of oxygen and nitric oxide via the inversion of reduced viscosity collision integrals at zero pressure," *Chemical Physics*, Vol. 326, No. 2, 2006, pp. 620–630. https://doi.org/https://doi.org/10.1016/j.chemphys.2006.03.028.

[7] Abbaspour, M., and Goharshadi, E. K., "Determination of potential energy functions of CO–CO, CO2–CO2, and N2O–N2O and calculation of their transport properties," *Chemical Physics*, Vol. 330, No. 1, 2006, pp. 313–325. https://doi.org/https://doi.org/10.1016/j.chemphys.2006.09.003.

[8] Lee, J. W., Nilson, R. H., Templeton, J. A., Griffiths, S. K., Kung, A., and Wong, B. M., "Comparison of Molecular Dynamics with Classical Density Functional and Poisson–Boltzmann Theories of the Electric Double Layer in Nanochannels," *Journal of Chemical Theory and Computation*, Vol. 8, No. 6, 2012, pp. 2012–2022. https://doi.org/10.1021/ct3001156.

[9] Laricchiuta, A., D'Angola, A., Pirani, F., Pietanza, L. D., Capitelli, M., and Colonna, G., "Thermodynamic and transport properties of reacting air including ablated species," *Hypersonic Meteoroid Entry Physics*, 2053-2563, IOP Publishing, 2019, pp. 14–1 to 14–21. https://doi.org/10.1088/2053-2563/aae894ch14.

[10] Capitelli, M., Giordano, D., Gorse, C., and Longo, S., "Collision Integrals of High-Temperature Air Species," *Journal of Thermophysics and Heat Transfer*, Vol. 14, 2000, pp. 259–268. https://doi.org/10.2514/2.6517.

[11] Colonna, G., D'angola, A., Laricchiuta, A., Bruno, D., and Capitelli, M., "Analytical Expressions of Thermodynamic and Transport Properties of the Martian Atmosphere in a Wide Temperature and Pressure Range," *Plasma Chemistry and Plasma Processing*, Vol. 33, 2013, p. 401. https://doi.org/10.1007/s11090-012-9418-4.

[12] Laricchiuta, A., Bruno, D., Capitelli, M., Catalfamo, C., Celiberto, R., Colonna, G., Diomede, P., Giordano, D., Gorse, C., Longo, S., Pagano, D., and Pirani, F., "High temperature Mars atmosphere. Part I: Transport cross sections," *European Physical Journal D*, Vol. 54, 2009, pp. 607–612. https://doi.org/10.1140/epjd/e2009-00192-7.

[13] Riabov, V., "Approximate Calculation of Transport Coefficients of Earth and Mars Atmospheric Dissociating Gases," *Journal of Thermophysics and Heat Transfer*, Vol. 10, 1996, pp. 209–216. https://doi.org/10.2514/3.777.

[14] Bzowski, J., Kestin, J., Mason, E. A., and Uribe, F. J., "Equilibrium and Transport Properties of Gas Mixtures at Low Density: Eleven Polyatomic Gases and Five Noble Gases," *Journal of Physical and Chemical Reference Data*, Vol. 19, No. 5, 1990, pp. 1179–1232. https://doi.org/10.1063/1.555867.

[15] Weaver, A. B., Kulakhmetov, M., and Alexeenko, A. A., "Consistent Atomic Oxygen Model for Direct Simulation Monte Carlo Below 1000 Kelvin," *Journal of Thermophysics and Heat Transfer*, Vol. 30, No. 3, 2016, pp. 689–694. https://doi.org/10.2514/1.T4780.

[16] Wright, M., Bose, D., Palmer, G., and Levin, E., "Recommended Collision Integrals for Transport Property Computations Part 1: Air Species," *Aiaa Journal - AIAA J*, Vol. 43, 2005. https://doi.org/10.2514/1.16713.

[17] Wright, M. J., Hwang, H. H., and Schwenke, D. W., "Recommended Collision Integrals for Transport Property Computations Part II: Mars and Venus Entries," *AIAA Journal*, Vol. 45, No. 1, 2007, pp. 281–288. https://doi.org/10.2514/1.24523.

[18] Hirschfelder, J. O., Curtiss, C. F., and Bird, R. B., *Molecular Theory of Gases and Liquids*, John Wiley & Sons, Inc., New York, 1954.

[19] Krieger, F. J., *The Viscosity of Polar Gases*, RAND Corporation, Santa Monica, CA, 1951. https://doi.org/10.7249/RM646.

[20] Bellemans, A., and Magin, T., "Calculation of collision integrals for ablation species," *8th European Conference on Aerodynamics for Space Vehicles, Lisbon, Portugal*, Vol. 85, 2015, pp. 107–171.

[21] Svehla, R. A., "Estimated Viscosities and Thermal Conductivities of Gases at High Temperatures," Tech. Rep. NASA TR R-132, National Aeronautics and Space Administration, 1962.

[22] Smith, F. J., and Munn, R. J., "Automatic Calculation of the Transport Collision Integrals with Tables for the Morse Potential," *The Journal of Chemical Physics*, Vol. 41, No. 11, 1964, pp. 3560–3568. https://doi.org/10.1063/1.1725768.

[23] Wang, F., and di Mare, L., "Hybrid meshing using constrained Delaunay triangulation for viscous flow simulations," *International Journal for Numerical Methods in Engineering*, Vol. 108, No. 13, 2016, pp. 1667–1685. https://doi.org/https://doi.org/10.1002/nme.5272.

[24] Colonna, G., and Laricchiuta, A., "General numerical algorithm for classical collision integral calculation," *Computer Physics Communications*, Vol. 178, No. 11, 2008, pp. 809–816. https://doi.org/https://doi.org/10.1016/j.cpc.2008.01.039.

[25] Leeuwen, M. E. V., "Derivation of Stockmayer potential parameters for polar fluids," *Fluid Phase Equilibria*, Vol. 99, 1994, pp. 1–18. https://doi.org/10.1016/0378-3812(94)80018-9.

[26] Mamedov, B. A., and Somuncu, E., "Boyle Temperature and Boyle Volume of Refrigeration Gases," *Journal of Thermophysics and Heat Transfer*, Vol. 34, No. 3, 2020, pp. 601–604. https://doi.org/10.2514/1.T5944.

[27] Mourits, F. M., and Rummens, F. H. A., "A critical evaluation of Lennard–Jones and Stockmayer potential parameters and of some correlation methods," *Canadian Journal of Chemistry*, Vol. 55, No. 16, 1977, pp. 3007–3020. https://doi.org/10.1139/v77-418.

[28] Park, C., Jaffe, R. L., and Partridge, H., "Chemical-Kinetic Parameters of Hyperbolic Earth Entry," *Journal of Thermophysics and Heat Transfer*, Vol. 15, No. 1, 2001, pp. 76–90. https://doi.org/10.2514/2.6582.

[29] Kee, R. J., Rupley, F. M., Miller, J. A., Coltrin, M. E., Grcar, J. F., Meeks, E., Moffat, H. K., Lutz, A. E., Dixon-Lewis, G., Smooke, M. D., Warnatz, J., Evans, G. H., Larson, R. S., Mitchell, R. E., Petzold, L. R., Reynolds, W. C., Caracotsios, M., Stewart, W. E., Glarborg, P., Wang, C., and Adigun, O., *TRANSPORT: A SOFTWARE PACKAGE FOR THE EVALUATION OF GAS-PHASE, MULTICOMPONENT TRANSPORT PROPERTIES*, Reaction Design, San Diego, CA, 2000. URL www.ReactionDesign.com.

[30] National Institute of Standards and Technology, "NIST Computational Chemistry Comparison and Benchmark Database," , 2022. Data retrieved from NIST Standard Reference Database Number 101, https://cccbdb.nist.gov/introx.asp.

[31] Ellis, C. P., and Raw, C. J. G., "High-Temperature Gas Viscosities. II. Nitrogen, Nitric Oxide, Boron Trifluoride, Silicon Tetrafluoride, and Sulfur Hexafluoride," *The Journal of Chemical Physics*, Vol. 30, No. 2, 1959, pp. 574–576. https://doi.org/10.1063/1.1729989.

[32] Clifford, A. A., Gray, P., and Scott, A. C., "Viscosities of gaseous nitric oxide, nitrous oxide and sulphur dioxide at high temperatures," *Journal of the Chemical Society, Faraday Transactions 1: Physical Chemistry in Condensed Phases*, Vol. 77, 1981, pp. 997–1001. https://doi.org/10.1039/F19817700997.

[33] Laricchiuta, A., Colonna, G., Bruno, D., Celiberto, R., Gorse, C., Pirani, F., and Capitelli, M., "Classical transport collision integrals for a Lennard-Jones like phenomenological model potential," *Chemical Physics Letters*, Vol. 445, No. 4, 2007, pp. 133–139. https://doi.org/https://doi.org/10.1016/j.cplett.2007.07.097.

[34] Fertig, M., Dohr, A., and Fruhauf, H.-H., "Transport Coefficients for High-Temperature Nonequilibrium Air Flows," *Journal of Thermophysics and Heat Transfer*, Vol. 15, No. 2, 2001, pp. 148–156. https://doi.org/10.2514/2.6603.

[35] Preci, A., and Auweter-Kurtz, M., "Sensitivity Analysis of Nonequilibrium Martian Entry Flow to Chemical and Thermal Modeling," *Journal of Thermophysics and Heat Transfer*, Vol. 31, No. 2, 2017, pp. 378–389. https://doi.org/10.2514/1.T4846.

[36] Yos, J. M., "Transport properties of nitrogen, hydrogen, oxygen, and air to 30,000 K," Tech. Rep. RAD TM-63-7, AVCO CORP WILMINGTON MA RESEARCH AND ADVANCED DEVELOPMENT DIV, 1963.

Chapter 4
Numerical Simulation of Transpiration Cooling on Stagnation Line in Thermochemical Non-Equilibrium

4.1 Foreword

The second contribution of this thesis is the development of a novel quasi-one-dimensional numerical method specifically designed for simulating transpiration cooling at hypersonic stagnation points. The resulting solver was built with a modular approach, allowing it to accurately model various physical phenomena and offering flexibility in configuration to match different problems or compare against literature.

The solver is capable of simulating stagnation line flows in thermochemical equilibrium or two-temperature non-equilibrium, with or without mass injection of various compositions. It supports a range of wall boundary conditions, including catalytic/non-catalytic and isothermal/non-isothermal surfaces. It offers a choice of shock treatment through either the resolution of the shock structure or the implementation of a Rankine-Hugoniot shock boundary condition. The architecture allows for the integration of different thermochemical models from literature (including non-Earth atmospheres). Despite its structural simplicity, the solver accurately captures the essential features of stagnation line flows, such as surface heat flux, wall composition, shock standoff distance, and profiles for temperature, pressure, and species concentrations. This makes the tool well-suited for efficient parametric studies and engineering applications.

Investigation of specific aspects of transpiration cooling was facilitated by the development of a novel methodology. This is especially true in the aim of large parameters sweeps for generic transpiration cooling applications. Existing stagnation line methods omitted treatment of the porous medium and/or non-equilibrium thermochemistry. Available CFD tools are computationally expensive and incur the disadvantage of unnecessary geometry selection. Building on work from Chapter 3, further implementations of rigorous thermochemical modeling pushed the results to higher accuracy. Thus, developing a solver allowed for the advancement in stagnation line solution methods with porous flows as well as the physical investigations of transpiration cooling made in this and the following chapter.

Preliminary aspects of this solver development were presented at the SciTech Forum 2024 conference. The completed work is presented in this report as a manuscript submitted for review to the

Journal of Thermophysics and Heat Transfer.

4.2 Statement of authorship

- Title of the paper: *Numerical Simulation of Transpiration Cooling on Stagnation Line in Thermochemical Non-Equilibrium*
- Publication status: Submitted for Publication
- Publication details: Samuel D. Brody, Justin Clarke, Kin Sing Lau, Matthew McGilvray, and Luca di Mare, "Numerical Simulation of Transpiration Cooling on Stagnation Line in Thermochemical Non-Equilibrium."

Table 4.1: Statement of Authorship

Author	**Contribution**	**Percentage (%)**
Samuel D. Brody	Conception	30
	Writing	90
	Code Development	50
	Data Acquisition	100
	Analysis and Interpretation	60
	Thermochemical Validation	40
	Critical Revision	10
Justin Clarke	Code Development	15
	Thermochemical validation	60
Kin Sing Lau	Code Development	10
Matthew McGilvray	Conception	20
	Analysis and Interpretation	20
	Supervision	30
	Critical Revision	40
Luca di Mare	Conception	50
	Writing	10
	Code Development	25
	Analysis and Interpretation	30
	Supervision	70
	Critical Revision	60

4.3 Manuscript

Numerical Simulation of Transpiration Cooling on Stagnation Line in Thermochemical Non-Equilibrium

Samuel Brody *, Justin Clarke †, Kin Sing Lau ‡, Matthew McGilvary § Luca Di Mare ¶
Oxford Thermofluids Institute, University of Oxford, Oxford, Oxfordshire, OX1 2JD

Sharp leading edges offer aerodynamic and observability advantages in hypersonic flight. The reduction in standoff distance resulting from the adoption of sharp edges, however, results in increased convective heating that needs to be managed. Transpiration cooling is an attractive option in terms of aerothermal performance, reusability and complexity. In this study, a method is presented for the numerical simulation of transpiration cooling at the stagnation point of sharp leading edges or tips. The method is suited to both equilibrium and non-equilibrium flow and is based on Cheng's stagnation line theory. The method explicitly represents coolant flow through the porous medium. Detailed temperature profiles and mass fractions in the shock layer and within the porous medium are computed. The sensitivity of these profiles to coolant flow rate and nature, wall thermal boundary conditions, and catalytic activity is studied. The ability of different coolant mixtures to limit the transport of reactive species to the surface is assessed. It is found that low molecular weight injectants provide better shielding of the surface at moderate to high blowing. At low blowing, low molecular weight injectants are less effective because of the increased diffusivity of shock layer species through the injectant. The effect of wall catalycity is found to be rather localized and of secondary importance to thermal boundary condition and blowing rate.

Nomenclature

B_h = blowing parameter

B_m = mass blowing parameter

b = nose-tip radius

D = diffusivity

e_v = specific vibrational energy

F = blowing ratio

*DPhil Candidate, Department of Engineering Science, Oxford Thermofluids Institute, University of Oxford.
†DPhil Candidate, Department of Engineering Science, Oxford Thermofluids Institute, University of Oxford.
‡MEng, Department of Engineering Science, Oxford Thermofluids Institute, University of Oxford.
§Professor, Oxford Thermofluids Institute, Department of Engineering Science, University of Oxford.
¶Associate Professor, Oxford Thermofluids Institute, Department of Engineering Science, University of Oxford.

H = total enthalpy

$h_{v,s}$ = specific vibrational energy of species s

h_w = specific enthalpy

H_v = volumetric heat transfer coefficient

k_D = Darcy coefficient

k_e = electronic component of thermal conductivity

k_v = vibrational component of thermal conductivity

p = pressure

R = Reynolds number

St_h = Stanton number

St_m = mass Stanton number

T = temperature (K)

$\vec{u}$ = velocity vector

$\dot{w}$ = mass production rate

y = molar concentration

α = Darcy penalization control

δ = shock standoff distance, domain widths

ϵ = emissivity

ϵ_n = porosity in flow direction

μ = viscosity

ρ = density

σ_{SB} = Stefan-Boltzmann constant

τ = viscosity tensor

Subscripts

s = species, solid

e = electronic

ev = electrovibrational

v = vibrational

t = translational

tr = trans-rotational

p = porous region

w = wall

∞ = freestream

I. Introduction

Hypersonic flight has received increased attention in recent years for both civil and defense applications. In both contexts, considerations of aerodynamic performance and maneuverability for slender vehicles indicate that sharp leading edges are advantageous. A sharp leading edge results in a reduced standoff distance, leading to a larger thermal gradient and increased surface convective heat flux. This heat flux can be well over 1 MW/m^2, requiring an active cooling technology rather than passive reradiation. Ablative layers are not a feasible mitigation strategy for sharp leading edges, because they are not reusable and invariably result in a radius of curvature that grows during flight, thereby negating the advantages of the initial choice of a sharp geometry.

Transpiration cooling (TC) has been presented as a favorable compromise between effectiveness and system complexity. TC operates through injection of coolant through a porous patch of the surface that requires cooling. TC cools the surface by 1) convection of a relatively cold coolant through the porous layer; 2) displacing the hot external stream in proximity of the surface and reducing the temperature gradient; 3) inhibiting surface reactions which contribute to the overall heat flux through catalytic heating [1]; 4) favorably altering near wall transport properties. According to the selection of the coolant mixture, TC can also be beneficial as an oxidation management method, as it can displace oxygen away from the surface. TC requires the provision of a feed system that needs to be compatible with the limited amount of space available behind the surface to be cooled. Typically, this can be achieved by concealing a plenum behind the edge to be cooled and moving the plumbing where thermo-mechanical and spatial arrangement constraints are less taxing. The performance of a TC system depends on the hydraulic properties of the porous layer, the coolant mass flux density, and its feed conditions.

An ideal system should operate with the lowest possible plenum pressure to reduce stress and with the lowest possible coolant flow rate. To minimize tank storage, it is desirable that the cooled surface be uniformly covered by the coolant stream. However, it is undesirable to inject excess coolant. While drag has been shown to change only slightly [2], risk of boundary layer blowoff may reduce the aerodynamic advantages of a sharp leading edge. Performance data on transpiration cooling devices in hypersonic environments have been obtained for a range of applications, including stagnation line heating [1]. Testing of cooling devices is however limited in scope because of the difficulty of either achieving realistic freestream enthalpies or Reynolds numbers or of obtaining data at realistic surface temperatures in transient facilities. Further, the large expense of flight tests is often prohibitive. Therefore, there is an acute need for engineering tools to perform accurate but expeditious calculations on transpiration cooling systems, their performance, and their effect on downstream aerodynamics.

Engineering calculations of transpiration cooling systems should be able to predict the pressure margin/mass flow

rate characteristics of the system as well as the heat flux and surface temperature reduction as functions of coolant mass flow rate, flight speed and attitude, altitude, and coolant composition. These data should be made available in a time compatible with design iterations and in presence of incomplete data on the vehicle geometry. The numerical prediction of transpiration cooling performance in a hypersonic environment is however complicated by: partially dissociated and ionized plasma, thermal and chemical non-equilibrium, surface catalysis, and radiation from the surface. Additionally, in a transpiration cooling simulation, the flow through the porous medium also needs to be modelled. This further complicates the simulation task, because it requires the coupling of the high-subsonic (and further upstream supersonic) shock layer with a nearly incompressible flow domain within the porous block and with a conduction problem through the block material. It is clear that the complete numerical simulation of a transpiration cooled vehicle is a formidable challenge. This challenge, however, is not strictly needed for engineering calculations, because the heat flux (and presumably the coolant consumption rate) scale with the condition at the stagnation point/line where a vehicle experiences the most intense heating. As an example, correlations for surface concentrations have been presented by Rocher *et al.* [3] using self-similar boundary layer solutions with equilibrium chemistry and injection boundary conditions, without addressing the details of mass, momentum and energy transport within the porous layer.

Efficient methods for calculation in proximity of stagnation points/lines have been known for several years. Stagnation line theory developed by Blottner [4] as a continuation of Cheng's thin shock layer work [5] can be harnessed to characterize the local geometry of a sharp leading edge vehicle. Thus, the combination of computational expediency with physical realism within the area in proximity of the stagnation point provides the framework for an accurate engineering tool for the application of transpiration cooling to hypersonic sharp leading edges.

The contribution of this paper is the calculation of the entire shock layer and porous medium thickness in condition of thermochemical non-equilibrium, including wall catalysis and diffusion of shock layer species into the wall. The solver is very efficient due to the simplification of the complex TC problem, while maintaining accuracy to the most prominent aspects of the problem. The paper is organized into four additional sections. Section II describes the formulation of the method. Section III presents verification and validation of the solver against correlations and previous results from simulations and experiments. Section IV presents results on the following topics:

- sensitivity of surface heat flux and compositions for a specific flight altitude and speed for a variety of coolant injection rates and compositions
- detailed profiles of species and temperatures through the stagnation line for the selected case
- sensitivity of temperature and compositions for catalytic and non-catalytic surface conditions and isothermal and transient surface conditions

Section V presents conclusions on the results and discussion of pathways for future work.

II. Methodology

A. Parabolized Navier Stokes

The method presented in this paper employs the parabolized Navier Stokes (PNS) equations due to their ability to preserve the full thermochemical model at a low computational cost. This paper considers continuum flow regimes likely experienced by hypersonic vehicles: low free-stream density and high flight velocity. In these regimes, shock transition occurs over a layer of non-negligible thickness, and Reynolds numbers remain low enough to allow an assumption of laminar flow in the regions of interest around the stagnation point. The presentation by Gnoffo *et al.* [6] of the conservation equations for hypersonic flows in thermochemical non-equilibrium is used as the basis for the governing equations employed in this paper. Further details can be found in the work of Clarke *et al.* [7]

$$0 = -\nabla \cdot (\rho_s \vec{u}) - \nabla \cdot (\rho_s D_s \nabla y_s) + \dot{w}_s \tag{1}$$

$$0 = -\nabla \cdot (\rho \vec{u} \otimes \vec{u}) - \nabla p + \nabla \cdot \tau - \alpha \frac{\mu}{K_D} \vec{u} \tag{2}$$

$$0 = -\nabla \cdot (\rho e_v \vec{u}) + \nabla \cdot ((k_e + k_v) \nabla T_v) + \nabla \cdot \left(\sum_{s=1}^{n_s} h_{v,s} (\rho_s D_s \nabla y_s) \right) - p_e \nabla \cdot \vec{u} - S - Q_{rad} \tag{3}$$

$$0 = -\nabla \cdot (\rho H \vec{u}) + \nabla \cdot q_c + \nabla \cdot q_d + \nabla \cdot (\tau \cdot \vec{u}) - Q_{rad} - H_v (T_s - T_t) \tag{4}$$

The mass production rate, $\dot{w}_s$, the source terms, S, and radiation loss term, Q_{rad}, are taken directly from Gnoffo *et al.*. The conductive heat flux, q_c, and diffusive enthalpy flux, q_d, are defined using Fourier's law and Fick's law with multicomponent diffusional mass flux, respectively. The viscous stress term τ is defined:

$$\boldsymbol{\tau} = \mu \left(\nabla \boldsymbol{u} + (\nabla \boldsymbol{u})^T - \frac{2}{3} (\nabla \cdot \boldsymbol{u}) \right) \tag{5}$$

A Darcy penalization has been included in the momentum equation as the final term [8]. Often, a Forchheimer term is added to model non-linear pressure differences due to inertial effects in porous flows with larger Reynolds numbers. The low flow velocities, small width of the porous media, and small pore diameter allow this term to be ignored for the cases considered in this study [9]. In addition, the material is assumed to be strong orthotropic, which simplifies the flow in the porous section to only the radial direction. The constant α is zero when in the freestream and shock layer and one in the porous medium. The coefficient k_D is a material property term describing the permeability of the porous medium. This property can be attained through experiment or predicted based on pore size and geometry [10]. Further, a solid energy equation is required, comprising a conduction term and a solid-fluid heat exchange term [11]. The latter is also included in the total energy equation.

$$0 = k_s (1 - \varepsilon) \nabla \cdot \left(\frac{\partial T_s}{\partial y} \right) + H_v (T_s - T_t) \tag{6}$$

For the purpose of this study, the governing equations are cast in spherical coordinates but could similarly be employed in cylindrical coordinates for applications to leading edges. Application of Cheng's stagnation line theory requires the evaluation of the tangential pressure gradient prevailing on the stagnation line downstream of the shock. The pressure gradient is evaluated from a linearized Rankine-Hugoniot problem with frozen flow properties. The full set of equations is integrated from the freestream, through the shock, shock layer, and porous section, to the plenum surface. If needed, the integration can start immediately downstream of the shock, in which case the Rankine-Hugoniot relations with frozen properties are used to evaluate the post-shock state.

B. Stagnation Line Problem with Transpiration Cooling

The flow along the stagnation line can be determined independently of the flow around the rest of the body. The surface geometry only appears in the stagnation line equations through the radius of curvature of the surface and, for hypersonic flows, through the radius of curvature of the shock. Homann [12] presented a solution for the stagnation line in a viscous flow as a separation of variables problem, exploiting the known shape of the wall and of the stagnation streamline. Herring [13] presented a derivation for the equations ruling the flow near the stagnation point over a spherical cap based on a trigonometric expansion around the center-line.

In the present work, the stagnation line and a small volume of gas surrounding it are idealized as a one-dimensional streamtube. For the purpose of representing the transpiring leading edge, the flow path is extended into the porous medium as depicted in Figure 1. The porous medium is treated as a homogeneous and possibly anisotropic phase characterized by a porosity, a permeability, and a wet area per unit volume. Within the porous medium, an additional conservation equation is solved, which represents the energy balance for the solid phase.

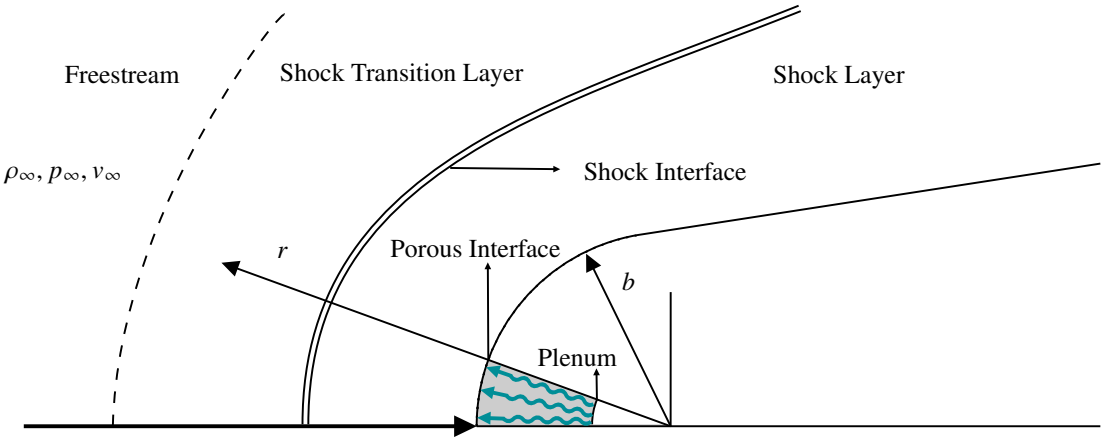

Fig. 1 Schematic of flow domain for transpiration cooled leading edge stagnation line

Herring's derivation is adapted to the case of a non-equilibrium, two temperature plasma. The resulting theory incorporates Fay and Riddell's [14] solution for the stagnation line problem and is structurally similar to Blottner's

[4] theory, but dispenses with the use of a streamfunction. Because the momentum equation remains unchanged for a two temperature model, Herring's approximation for the relation between shock strength, curvature, and tangential pressure gradient holds rigorously for an infinitely thin shock. Additionally, the derivation is modified to account for a shock layer of finite thickness compared to the body leading edge radius. The formulation and implementation of the non-equilibrium model follows Clarke *et al.* [7]. For high-speed scenarios, a significant portion of the overall cooling may come passively through reradiation, as defined below:

$$\dot{q}_{rad} = \varepsilon\sigma_{SB}(T_s - T_\infty)^4 \tag{7}$$

This passive cooling can be hindered by oxidation, emphasizing the importance of decreasing surface transport of oxidizing species [15]. The porous medium is modelled as non-radiative, and the shock layer is treated as optically thin.

The wall is treated as fully catalytic for ions and can be treated as fully catalytic or non-catalytic for neutral species. Catalycity of ions is assumed by enforcing mole fractions of zero for charged species [16]. This allows for a thermal equilibrium condition at the wall. Catalycity of neutral species is enforced with the incorporation of wall reactions, whose rates are large enough to enforce equilibrium at the wall temperature. Due to the porosity of the wall, a portion of the atomic species do not impact the wall and thus diffuse and advect into the porous block. The porous medium is assumed to be non-catalytic, which likely does not appreciably affect the flow. The majority of surface chemistry would occur at or just below the outer wall, especially for non-zero blowing cases where the open region of the porous block is mostly filled with injectant. The method allows nitric oxide to exist at the wall. This is chosen for simplicity and the ability to adapt to a finite-rate catalycity by defining specific recombination rates for each reaction, as opposed to enforcing a boundary condition at the wall.

C. Thermochemical Model

The fluid is modeled as a partially dissociated and partially ionized non-equilibrium plasma with two temperatures, following Park [17]. An 11-species air model plus injectant (argon, helium, or already included nitrogen) is employed. Chemical rates are evaluated using mass action laws. Preferential dissociation is accounted for by using a combination of translational and electrovibrational temperature when evaluating reaction constants for the forward reactions. Backward reaction rates are obtained from the forward rates and equilibrium constants evaluated at the translational temperature. Thermal relaxation is modelled using Millikan and White's correlations [18] with high temperature corrections from Park [19] or from Kim and Jo [20] (when noted). Reaction source terms for the electrovibrational energy are evaluated using tabulated species dissociation energies. Transport properties are determined through Chapman-Enskog Theory, as presented by Hirschfelder *et al.* [21] but are adapted to the two-temperature framework. Collision integrals for heavy species interactions are evaluated at the translational temperature. Collision integrals for electron-heavy and

electron-electron interactions are evaluated at the electrovibrational temperature. In computing transport properties, binary property terms are computed at the translational temperature for interactions involving only heavy particles, while the electrovibrational temperature is used for interactions involving electrons. For the purpose of computations, the model is implemented in a software library developed at the University of Oxford, OCEAN (Oxford Chemical Equilibrium Analysis and Non-equilibrium). The library allows the evaluation of relaxation and reaction rates from any combination of sources. This arrangement allows, as an example, both Park models [19, 22] or Kim and Jo's model [20] to be used without modifications to the solution methods. The library also computes collision integrals using a range of potential functions best suited for each species interaction. Tabulated collision integrals from literature can also be imported. Mixture transport properties can be evaluated from the binary transport properties either by rigorous application of the Chapman-Enskog first order expansion [21] or by using a variety of mixing rules, such as those proposed by Yos [23], and implemented in the work of Gupta *et al.* [24] and Gnoffo *et al.* [6]. Results validating the implementation of the thermochemical model and transport properties are presented in the work of Clarke *et al.* [7]. For the purpose of the transpiration cooling calculations presented in Section IV, the full multicomponent transport property formulation is used, on account of the need to accurately represent species and temperatures profiles through the shock. This is particularly important for helium cases due to the large difference in molecular weight between the coolant and the free-stream species. Table 3, included in the appendix, provide Park's [19] reactions and reaction rate coefficients for a standard 11-species air model (with helium [25] and argon [26] added for use as injectants). A more detailed description of the formulation and validation of transport property evaluations is included in the appendix.

D. Numerical Method

The one-dimensional computational domain is divided in cells. The conservation equations are discretized following a finite volume approach. Boundary conditions are applied at the freestream with pressure, temperature, and chemical composition as well as at the plenum, where coolant mass flow rate (or plenum pressure for a real system), temperature, and composition are assigned. Simulations begin by assigning the freestream condition to the freestream and shock transition layer cells and the Rankine-Hugoniot post-shock condition for the cells in the shock layer and porous block. Simulations can also begin from previously converged grids. Because of the wide range of Mach numbers encountered along the streamline, care is needed in the coupling of the pressure and normal velocity fields. This coupling can be accomplished in a number of ways. The strategy chosen in the present work is to stagger the position of the discrete normal velocity variables and the other scalar fields, following the approach of Harlow and Welch [27]. In the present method the normal velocities are associated to the cell boundaries, and all other variables are stored at cell centers. Physical interfaces, e.g. the porous block surface, are located at cell boundaries. The variable arrangement is shown diagrammatically in Figure 2.

Differently from stagnation line solutions by Blottner [4], Herring [13] and Cheng [5], the present solutions are

characterized by changes in flow direction. While the shock layer gas travel from the freestream towards the vehicle surface, the injected coolant travels from the plenum wall towards the shock. As blowing increases, the interface between the shock layer gas and the coolant (where the radial velocity is zero) moves away from the wall and into the shock layer. The position of the stagnation point is determined as part of the solution. The discretization of the convective derivatives in Equations 1-6 requires upwind derivatives for numerical stability. Upwinding is purely convective and is based on the sign of the normal velocity only. Variable flow direction presents challenges to numerical stability, as the Newton-Raphson method in this solver generally employs first-order finite differencing. Thus, the system of equations must be discretized and solved using differencing schemes that preserve upwinding regardless of flow direction. The discretization method results in a large system of algebraic equations of the type $F(\vec{q}) = \vec{0}$. F is the residual of the discrete version of Equations 1-6. The vector $\vec{q}$ is the solution vector, including gas states throughout the shock layer and the porous block and the solid temperatures. The equations are solved by Newton-Raphson iterations. The Newton iterations require inversion of the residual Jacobian matrix. This matrix is block tridiagonal:

$$\begin{bmatrix} \mathbf{a_{1,2}} & \mathbf{a_{1,3}} & \mathbf{0} & \dots & \mathbf{0} \\ \mathbf{a_{2,1}} & \mathbf{a_{2,2}} & \mathbf{a_{2,3}} & \mathbf{0} & \vdots \\ \mathbf{0} & \ddots & \ddots & \ddots & \mathbf{0} \\ \vdots & \mathbf{0} & \mathbf{a_{n-1,1}} & \mathbf{a_{n-1,2}} & \mathbf{a_{n-1,3}} \\ \mathbf{0} & \dots & \mathbf{0} & \mathbf{a_{n,1}} & \mathbf{a_{n,2}} \end{bmatrix} d \begin{bmatrix} \vec{q}_1 \\ \vec{q}_2 \\ \vdots \\ \vec{q}_{n-1} \\ \vec{q}_n \end{bmatrix} = \begin{bmatrix} \vec{r}_1 \\ \vec{r}_2 \\ \vdots \\ \vec{r}_{n-1} \\ \vec{r}_n \end{bmatrix} \tag{8}$$

where,

$$\mathbf{a_{i,1}} = \frac{\partial \vec{r}_i}{\partial \vec{q}_{i-1}} \tag{9}$$

$$\mathbf{a_{i,2}} = \frac{\partial \vec{r}_i}{\partial \vec{q}_i} \tag{10}$$

$$\mathbf{a_{i,3}} = \frac{\partial \vec{r}_i}{\partial \vec{q}_{i+1}} \tag{11}$$

The Newton iterations are started from an approximate solution obtained using Rankine-Hugoniot relations with frozen thermochemistry.

The solution procedure described above needs to be supplemented with special treatments for the determination of the shock standoff distance and for the representation of the absorbed state on the porous block surface. The shock standoff distance is not known *a-priori* but is determined by the tangential momentum balance. In the numerical

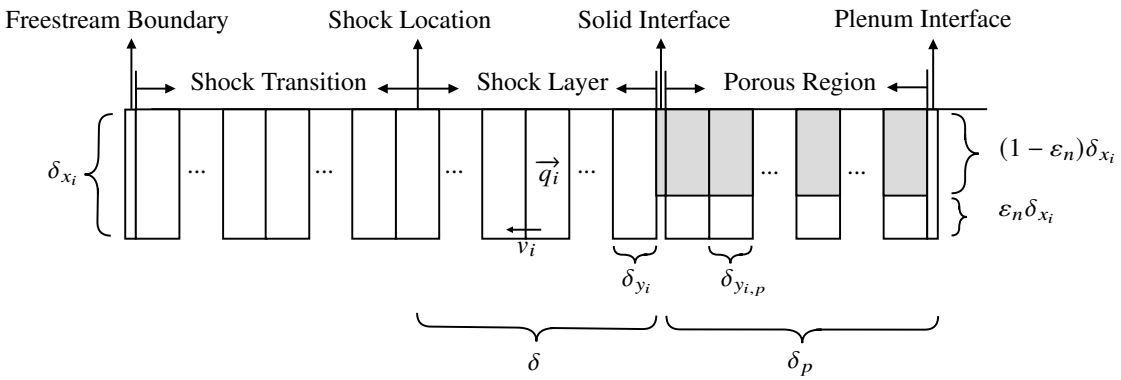

Fig. 2 Unified domain using staggered grid for numerical method

solution, the standoff distance δ appears as a scaling factor in the grid size and the metric coefficients, as well as in the expression of the tangential pressure gradient driving the tangential flow. The standoff distance can be determined by requiring that a given fraction of the static pressure rise through the shock is realized at a selected grid point. This condition appears as an additional equation to be added to the set of discrete equations 1-6.

In order to represent discontinuous behavior at the interface, a zero thickness solid cell is used to carry fluxes between the last fluid cell and solid portion of the first porous cell as well as enforce interface conditions. The resulting equation added to the system generates an additional dependency for the adjacent cells on either side of the interface. This cell would therefore disrupt the tridiagonal scheme, requiring 5 diagonals due to the dependence of the surrounding cells on three additional cells, instead of two. Schur complements allow for the solution of additional equations introduced by the standoff distance and the absorbed state, and therefore provide a computationally convenient mechanism for the resolution of the second complication. Thus, the resulting system of equations can be expressed using a block tridiagonal Jacobian matrix coupled with a Schur complement scheme to handle the two interfaces, which represents the system solved in this study:

$$\left[\begin{array}{c|c} \mathbf{A} & \mathbf{S_3} \\ \hline \mathbf{S_1} & \mathbf{S_2} \end{array}\right] d \left[\begin{array}{c} \vec{q}_1 \\ \vec{q}_2 \\ \vdots \\ \vec{q}_{n-1} \\ \vec{q}_n \\ \hline \delta \\ \vec{q}_w \end{array}\right] = \left[\begin{array}{c} \vec{r}_1 \\ \vec{r}_2 \\ \vdots \\ \vec{r}_{n-1} \\ \vec{r}_n \\ \hline r_\delta \\ \vec{r}_w \end{array}\right] \tag{12}$$

The tridiagonal matrix with Schur complements can be expressed more completely as:

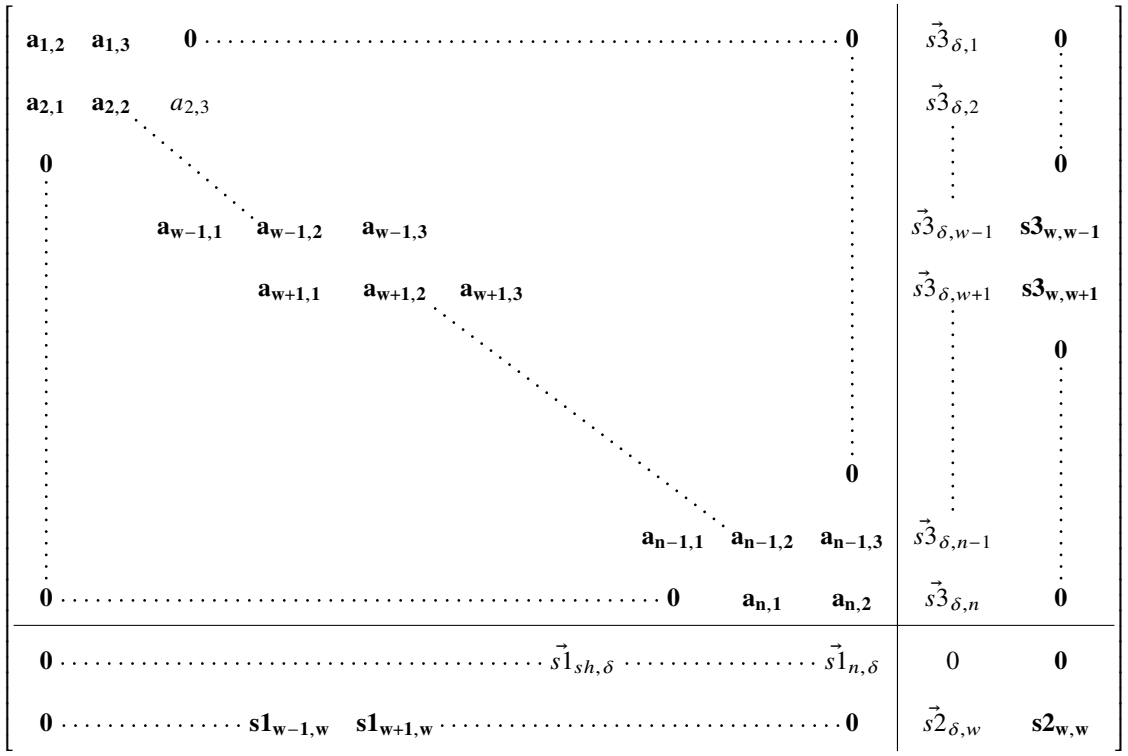

Entries to the block matrices employing the Schur complement are defined:

$$\mathbf{s1_{i,w}} = \frac{\partial \vec{r}_w}{\partial \vec{q}_i} \tag{13}$$

$$\vec{s3}_{\delta,i} = \frac{\partial \vec{r}_i}{\partial \delta} \tag{14}$$

$$\mathbf{s3_{w,i}} = \frac{\partial \vec{r}_i}{\partial \vec{q}_w} \tag{15}$$

$$\vec{s2}_{\delta,w} = \frac{\partial \vec{r}_w}{\partial \delta} \tag{16}$$

$$\mathbf{s2_{w,w}} = \frac{\partial \vec{r}_w}{\partial \vec{q}_w} \tag{17}$$

In the current work, Jacobian matrices for fluxes, source terms, and metric coefficients are evaluated symbolically and assembled contextually with the evaluation of the residuals. The linearization of each term in the discrete equations is verified by numerical differentiation. It should be noted that $s1_{n-1,\delta}$ and $s1_{n,\delta}$ are populated with the boundary condition that the post-shock pressure is equal to half of the far-field pressure, where cell $n+1$ is a no-height cell describing the free-stream conditions.

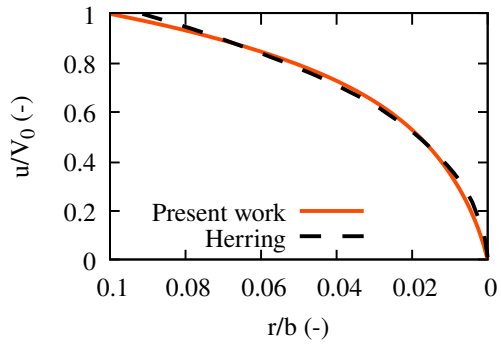

Fig. 3 Tangential velocity profile for M_∞ = 15.27, R_∞ = 5030 with comparison to Herring [13]

III. Validation and Verification

The stagnation line solver combines three elements: unified numerical domain for modeling from freestream to porous section, non-equilibrium stagnation flows, and mass injection. Each element is verified to prove the correctness of its formulation and implementation.

A. Numerical Verification

Viscous fluxes are evaluated through the shock, and shock thickness was previously validated in the work of Clarke *et al.* [7] against the analytical solution presented by Morduchow and Libby [28]. The shock structure and tangential velocity profile through the shock layer are validated by comparison with the analytical results by Herring [13]. The validation is based on comparison of the shock standoff distance and the velocity profiles within the shock layer, as shown in Figure 3. The geometry is a spherical cap, and the solution does not resolve through the shock, instead enforcing the post-shock Rankine-Hugoniot conditions.

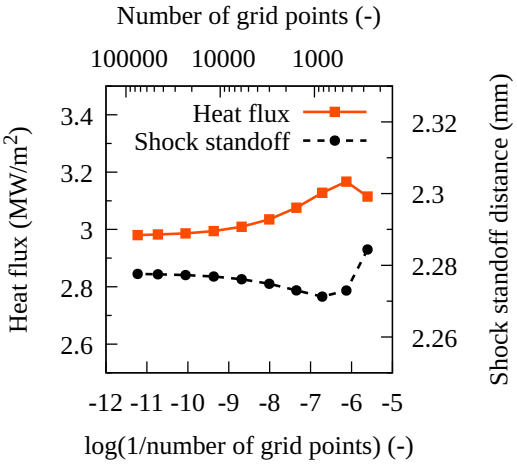

Fig. 4 Convergence history for stagnation heat flux and shock standoff distance for 40 km, 4 km/s, 25 mm nose radius test case with N2 injection

Refinement is performed selectively. If neighboring points differ by more than the determined refinement criteria, a new point is added in between via interpolation. The refinement criteria is determined by first determining the maximum range for each state variable and then setting a limit for the maximum neighboring discrepancy relative to the range. Figure 4 displays the convergence history for heat flux and shock standoff distance. These are the limiting convergence features, as they exist at discontinuities in the domain. Convergence of the shock structure and thus profiles can be found in the work of Clarke *et al.* [7]. While flux values across cells are generally very sensitive to grid spacing, convergence within the range of reasonable confidence (0.1%) is easily met on for grids whose profiles are refined to less than 0.01% difference between adjacent cells, which is the order of compression required to fully capture the shock structure.

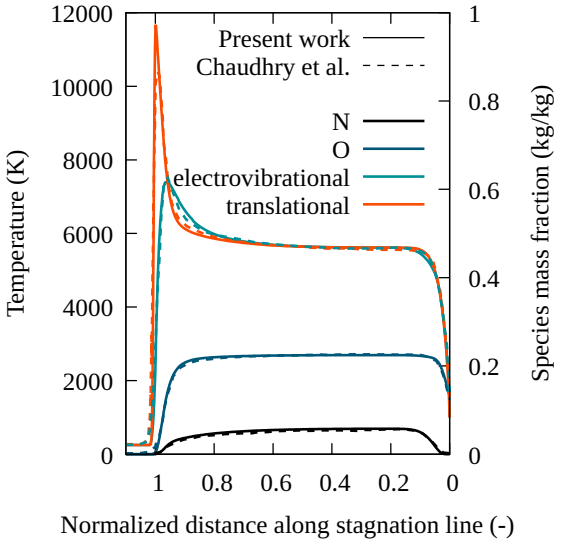

Fig. 5 Temperature and mass fraction profiles on stagnation line for 40 km, 5 km/s, 100 mm radius with comparison to Chaudhry *et al.* [29]

B. Physical Validation

Work by Chaudhry *et al.* [29] provides a similar case, generated by the US3D solver, to the conditions of interest in this paper. This case is 40 km and 5 km/s with a nose radius of 100 mm and 1,000 K isothermal wall. Figure 5 displays temperature and atomic element profiles. The wall catalycity is validated with simulations from Yang *et al.* [30]. The simulations have a 5.732 km/s free-stream velocity, 38 mm nose radius, and 300 K isothermal wall. They were generated by the SHOCK2D solver [31]. The thermochemical model presented by Kim and Jo [20] is used. Mass fraction profiles for a non-catalytic (NC) and fully catalytic (FC) wall conditions appear in Figure 6.

In order to be confident in the solver across the full range of conditions where non-equilibrium modeling may be useful, a high-altitude and high-speed case was investigated. Again employing the thermochemical model of Kim *et al.* [20], the RAM C-II geometry for a 65 km and 7.651 km/s test condition is considered. This case allowed for validation

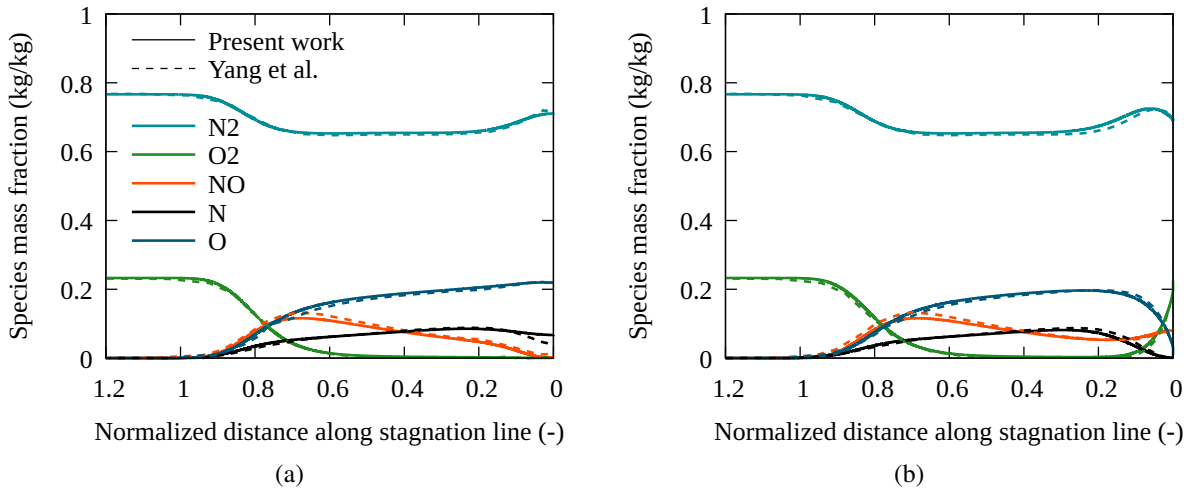

Fig. 6 Mass fraction profiles on stagnation line for 178.93 Pa, 545 K, 5.732 km/s, 38 mm radius with non-catalytic (a) and full catalytic (b) wall condition with comparison to Yang *et al.* [30]

of a significantly dissociated shock layer and thick shock. Figure 7 shows the temperature profiles and mass fraction profiles for the major species.

Along with stagnation line profiles, surface heat flux and shock standoff distance are shown for validation in Table 1. All simulations for these cases are isothermal. Experimental results from Nonaka *et al.* [32] match well.

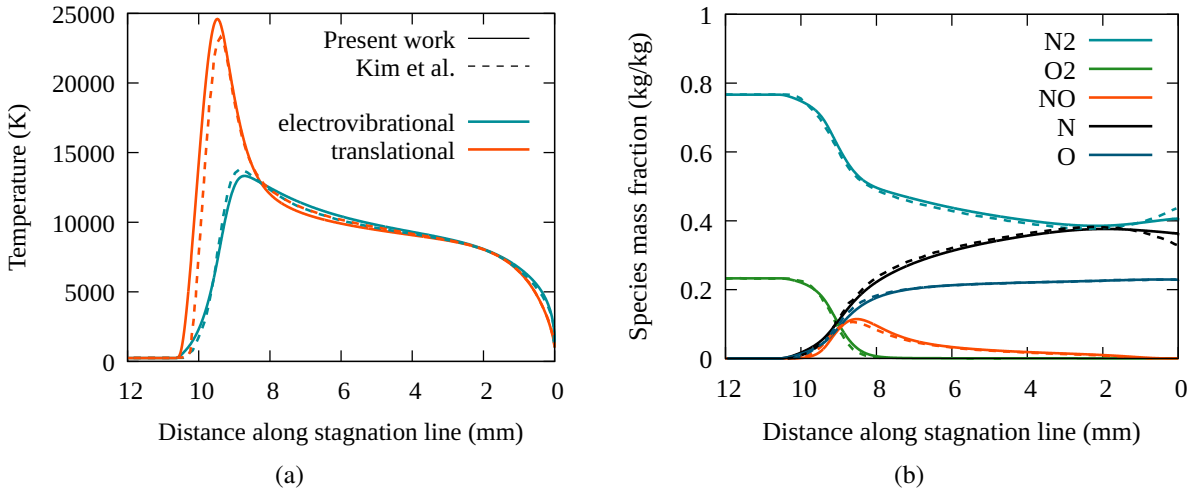

Fig. 7 Temperature (a) Mass fraction (b) profiles on stagnation line for 61 km, 7.65 km/s, 152.4 mm radius with comparison to Kim *et al.* [20]

C. Validation of Transpiration Cooling

To validate the implementation of mass injection into the solver, results in 11-species air for a Mach 7 test case (151 Pa, 42.2 K, 915 m/s, and 25 mm nose radius) with nitrogen injection were compared against the Yoshikawa correlation

Table 1 Comparison of shock standoff distance, δ (mm) and heat flux $\dot{q_w}$ (MW/m^2)

Source	Condition					$\dot{q_w}$ (MW/m^2)		δ (mm)	
	P (Pa)	T (K)	u (m/s)	R (m)	T_w (K)	Source	Present	Source	Present
[29]	287	250	5.0	100.0	1000	3.28	3.45	7.40	7.08
[30]	179	545	5.732	38.0	300 (NC)	5.51	5.15	3.39	3.12
[30]	179	545	5.732	38.0	300 (FC)	8.43	8.45	-	-
[20]	17.7	243	7.652	152.4	1000	-	-	9.88	10.02
[32]	4850	293	3.490	7.0	4000	-	-	0.77	0.73

[33] and experimental data from Naved *et al.* [34], from which the specific test parameters and material properties were taken. The material is porous alumina with a porosity of 0.39 and a Darcy coefficient K_D of 3.04e-15 m^2. Traditionally, transpiration cooling is assessed by the ability of mass injection to reduce surface Stanton number. The blowing ratio, F, normalizes the injected mass flux against the freestream mass flux. The blowing parameter, B_h, normalizes the blowing ratio by the zero-blowing Stanton number.

$$F = \frac{\rho_{inj} u_{inj}}{\rho_\infty u_\infty} \tag{18}$$

$$B_h = \frac{F}{St_{h0}} \tag{19}$$

The heat transfer Stanton number, St_h, is the convective heat flux, $\dot{q}_w$, normalized by the external flow enthalpy flux.

$$St_h = \frac{\dot{q}_w}{\rho_\infty u_\infty (H_0 - h_w)} \tag{20}$$

$$H_0 = h_\infty + \frac{1}{2} u_\infty^2 \tag{21}$$

$$\tag{22}$$

When Stanton number and blowing ratio are normalized by the non-blowing Stanton number, St_{h0}, they provide a useful description of cooling effectiveness. Figure 8 displays the results of the validation. The numerical results of this work align closely with both the correlation and experimental results.

A similar definition to heat Stanton number can be made for surface mass flux. As heat Stanton number compares the wall heat flux to the freestream enthalpy flux, mass Stanton number compares the wall diffusive flux of the injectant to a reference freestream flux. Thus, mass Stanton number reduction describes the ability of the injectant to act as a diffusive barrier to the transport of shock layer species to the wall.

$$B_m = \frac{F}{St_{m0}} \tag{23}$$

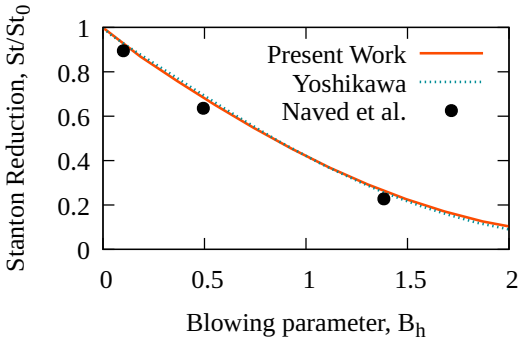

Fig. 8 Stanton number reduction versus blowing parameter with N2 injection for 151 Pa, 42.2 K, 915 m/s, and 25 mm nose radius with isothermal (T_w = 300 K) and non-catalytic wall compared with Yoshikawa [33] and Naved *et al.* [34]

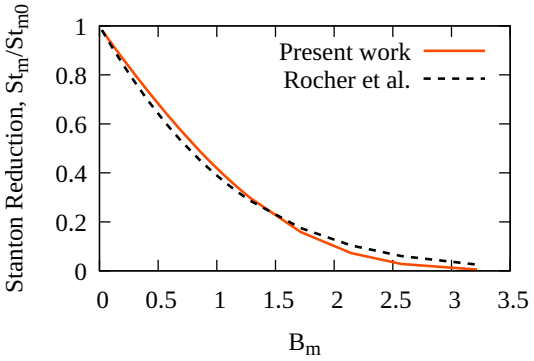

Fig. 9 Mass Stanton number reduction versus mass blowing parameter with nitrogen injection for 151 Pa, 42.2 K, 915 m/s, and 25 mm nose radius with isothermal (T_w = 300 K) and non-catalytic wall compared with Rocher et al. [3]

$$St_m = \frac{\rho_s D_s \nabla y_{inj}}{\rho_\infty u_\infty \Delta y_{inj,w-\infty}} \tag{24}$$

The definition of mass Stanton number with the injectant simplifies the description of transport of shock layer species to the wall, as the net diffusive flux of the shock layer species must equal that of the injectant. Figure 9 presents mass Stanton number reduction with comparison to a correlation from Rocher et al. [3], with the overall trend matching well. The same validation case from Naved *et al.* is selected in order to compare with the correlation at perfect gas conditions, where differences in the thermochemical models used is not relevant. It should be noted that this semi-analytical correlation was derived using self-similar analysis of equilibrium flows and assumes fixed transport properties near the wall. The ability of the current solver to evaluate multicomponent transport properties throughout the profile likely produces the differences with the correlation, which is built on bulk transport properties. Further comparison to the Rocher correlation will be discussed in more detail in the Results section.

The solver appears applicable to 11-species air for hypersonic flight test cases in the equilibrium regime for mass injection. Experimental data, and therefore empirical correlations, have not yet been published in a form that would allow for the direct validation of this solver in the non-equilibrium regime. However, the validation of the two-temperature thermochemical model for non-blowing, non-equilibrium cases alongside the validation of the solver in equilibrium gives confidence in the solver's applicability to non-equilibrium flight test cases.

IV. Results

Results have been obtained for various injectants across a range of blowing ratios. A specific case has been investigated that represents a generic hypersonic mission profile point relevant to transpiration cooling implementations. The test case employs material properties for porous alumina, and an altitude and freestream velocity of 40 km and 4 km/s are chosen. While porous alumina is likely not a viable material for flight vehicles, it is chosen here for consistency with the validation test case [34]. Shock standoff distance for this condition is approximately 10% of the nose tip radius (25 mm for the selected case). Given the standoff distance and post-shock velocity relevant to this case, non-equilibrium thermochemistry must be considered within the shock layer. Results explicitly model the unified domain from freestream to plenum wall. Figure 10 displays the full two-temperature stagnation profile as well as the full concentration profile for no blowing and moderate blowing with helium. Profiles capture the shock structure, post-shock thermochemical relaxation processes, and near-wall non-equilibrium. The uneven cooling between energy modes is the result of low excitation in the injectant. Thus, the diffusion of cool, unexcited injectant results in a corresponding region of non-equilibrium near the wall. It should be noted that while mass injection appreciably alters the shock standoff-distance, the introduction of the injectant into the shock layer has only local, near-wall effects. The temperature and species profiles in the immediate post-shock region are offset but otherwise similar when compared to the non-blowing case. This confirms previous conclusions that stagnation mass injection can be characterized mainly

from near-wall properties and overall shock geometry [33, 35, 36]. Small levels of ionization do occur in the shock layer but do not appreciably affect the overall profile.

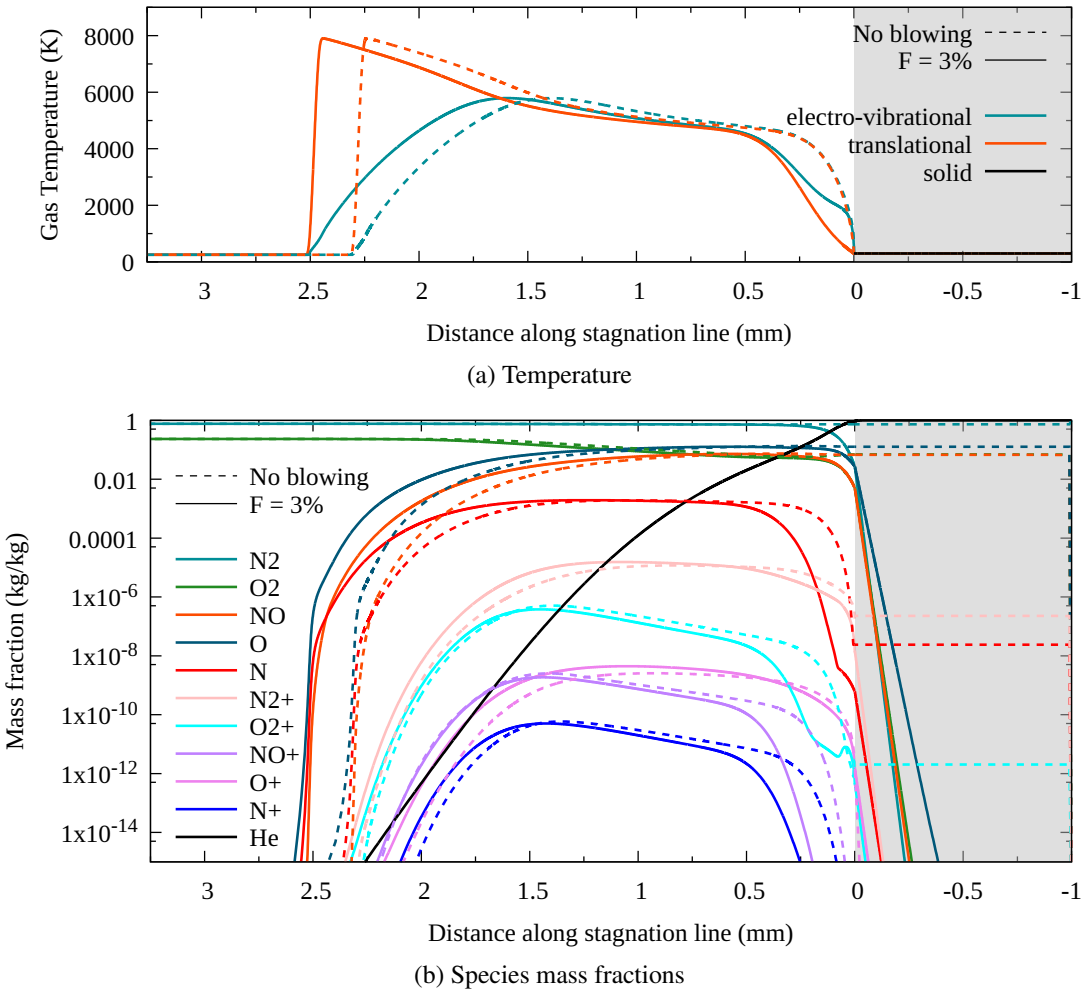

(a) Temperature

(b) Species mass fractions

Fig. 10 Temperature and species profiles with no blowing and helium injection at $F = 3\%$ for 40 km, 4 km/s test case with isothermal (T_w = 300 K) and non-catalytic wall

A. Comparison of injectants

Detailed profiles for the surface temperature and surface mass fraction of atomic oxygen are presented in Figures 11 and 12. The wall is assumed to be non-catalytic and isothermal at 300 K for these simulations. The material is made impermeable for the non-blowing cases. The surface mass fraction is defined as the percentage of atomic oxygen by mass relative to the fluid solution. While for this case the mass fraction never exceeds roughly 0.1, even very small proportions of oxygen will result in heat flux due to surface recombination. As expected, helium outperforms argon and nitrogen for temperature reduction. The trend is more complicated for the inhibition of species transport to the surface. At low blowing, helium underperforms relative to the heavier injectants. The trend reverses at moderate to high blowing

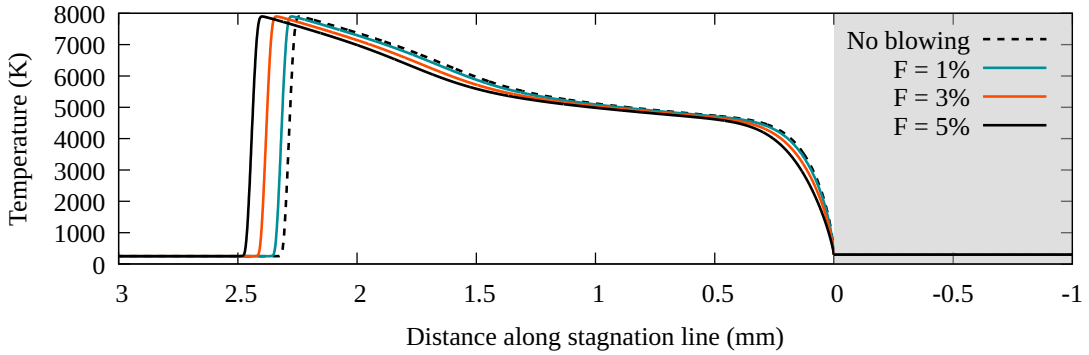

(a) Argon

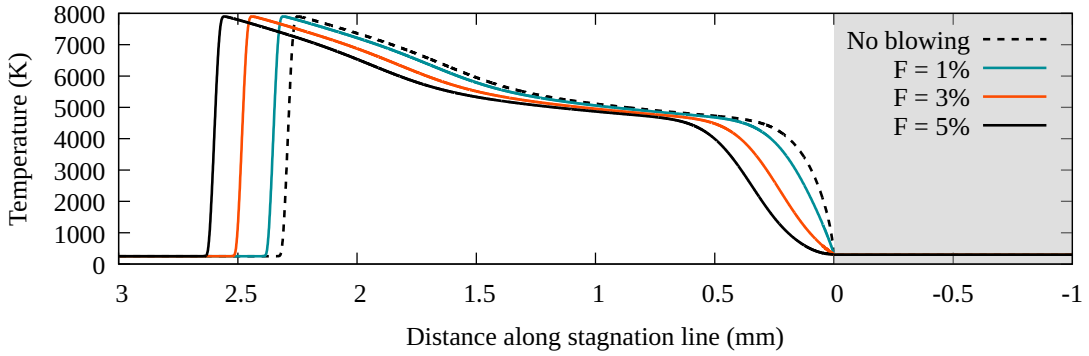

(b) Helium

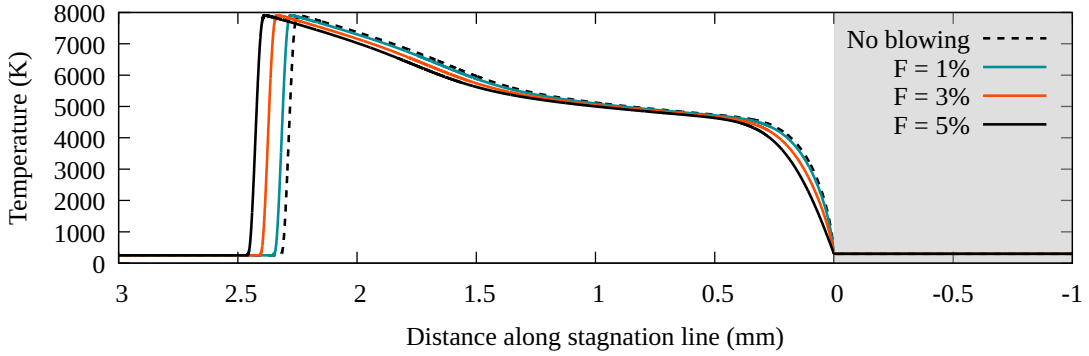

(c) Nitrogen

Fig. 11 Translational temperature profiles for varying blowing ratio and injectant for 40 km, 4 km/s, 25 mm radius test case with isothermal (T_w = 300 K) and non-catalytic wall

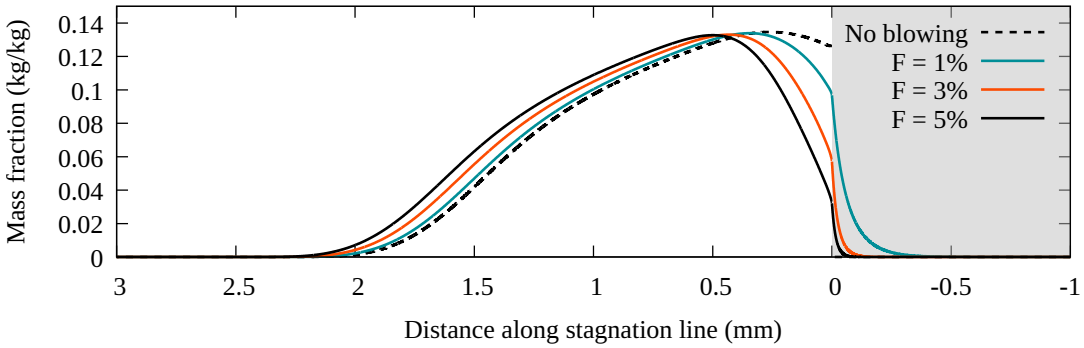

(a) Argon

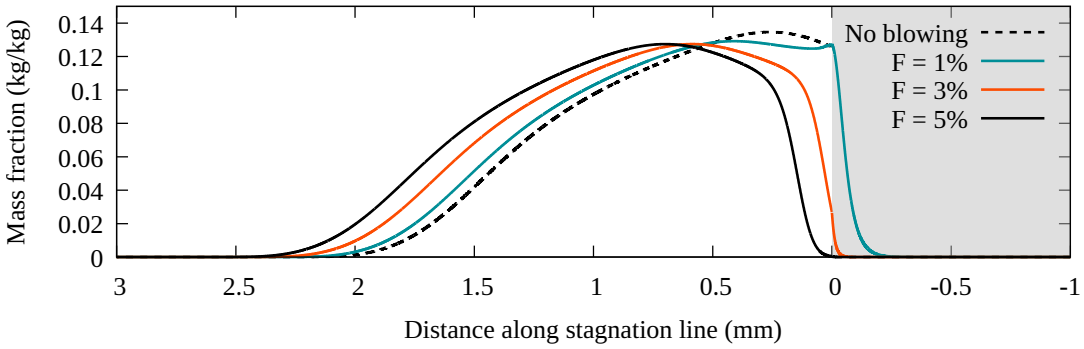

(b) Helium

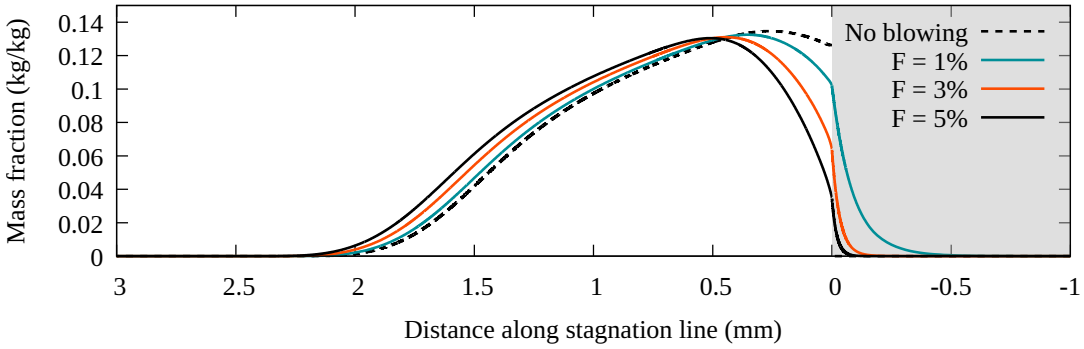

(c) Nitrogen

Fig. 12 Atomic oxygen mass fraction profiles for varying blowing ratio and injectant for 40 km, 4 km/s, 25 mm nose radius test case with isothermal (T_w = 300 K) and non-catalytic wall

rates. This is likely related to the much lower molecular weight of helium, which results in a larger diffusivity. At low blowing, atomic oxygen diffuses more easily to the wall amid lighter helium. At high blowing, the ability of helium to diffuse further into the shock layer than the heavier injectant generates a larger and more effective coolant barrier. Figure 13 displays surface heat flux reduction, mass fraction reduction, and shock standoff distance growth across the three injectant candidates. While argon and nitrogen exhibit similar performance, nitrogen resulted in reduced heat flux and standoff distance relative to argon, but increased transport of atomic oxygen to the surface. Again, this effect is likely the result of differences in diffusivity related to nitrogen's lighter molar mass. The effect could also come from nitrogen's contribution to the reaction channel as a more effective third body in oxygen dissociation.

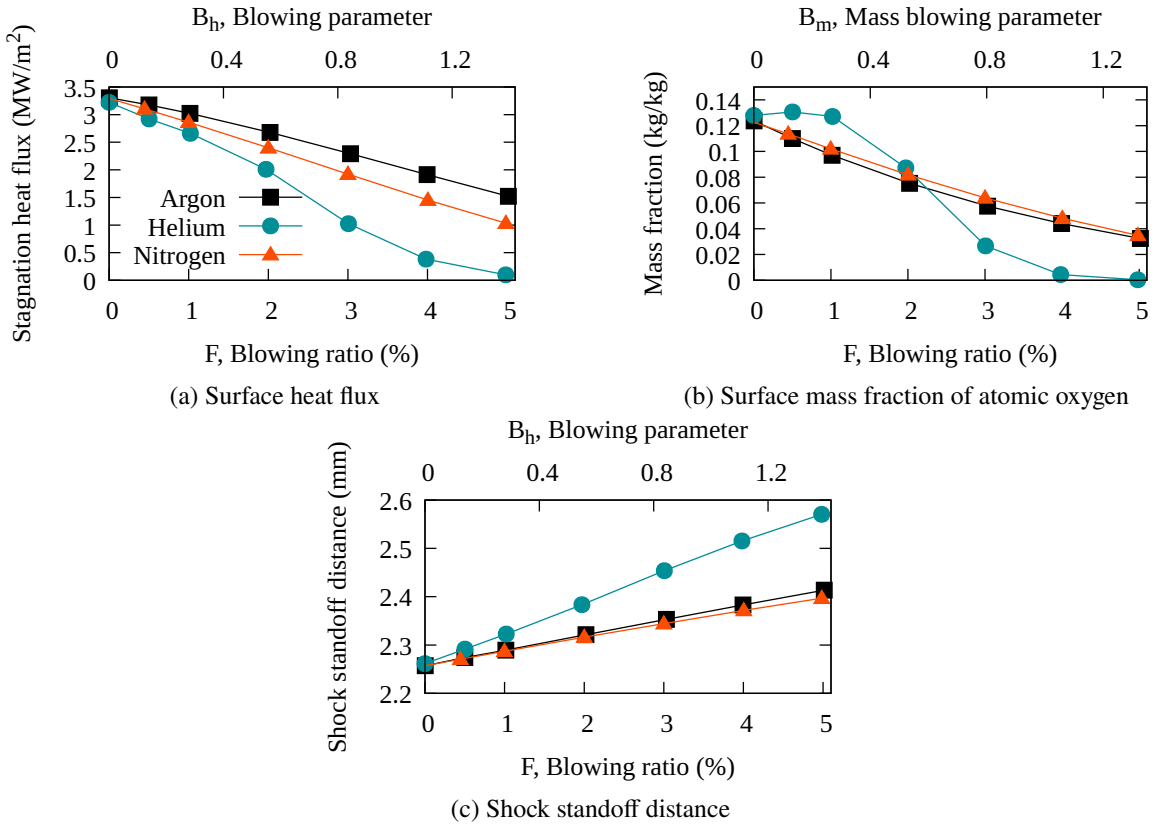

(a) Surface heat flux

(b) Surface mass fraction of atomic oxygen

(c) Shock standoff distance

Fig. 13 Variation of surface heat flux, concentration of atomic oxygen, and shock standoff distance relative to blowing ratio for 40 km, 4 km/s, 25 mm nose radius test case

For consistent flight conditions, the injectant composition and the modifications it induces in the structure of the shock layer determine the variations in heat flux. Mass flux is often used to characterize cooling performance, as it can be used to determine requirements for coolant infrastructure and storage and is easily determined in experimental studies. Swann and Pittman [37] determined a quadratic correlation for the injection of air into air. Correlations from Yoshikawa [33] and Marvin and Pope [35] verified the quadratic from Swann and Pittman and expanded to foreign gas injection. Scaling laws employing molecular weight directly with mass flux have been previously investigated elsewhere for film

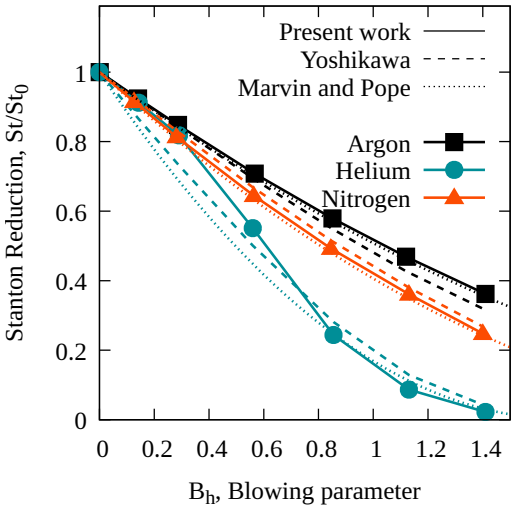

Fig. 14 Stanton number reduction versus blowing ratio for various injectants compared with Yoshikawa correlation [33] and Marvin and Pope correlation [35] for 40 km, 4 km/s, 25 mm nose radius test case

cooling and transpiration cooling [3, 35, 36, 38–40]. Exponents of power laws are generally determined empirically. The scaling law of $(M_{inj}/M_{\infty})^{0.25}$ from Marvin and Pope [35] is commonly used. Figure 14 presents a comparison between all injectants for surface Stanton number reduction. Correlations from Yoshikawa [33] and Marvin and Pope [35] are also presented. Both accurately capture the overall trend but fail to capture the inflection in helium's cooling effectiveness.

Rocher et al. [3] used a semi-analytical approach using film theory to determine a correlation for mass Stanton number reduction for self-similar equilibrium flows. This correlation is not applicable to the cases presented here, as a non-equilibrium shock layer will cease to be self-similar. Further, the use of bulk transport properties becomes less suitable as the near-wall chemistry becomes more relevant to the flow. Figure 15 displays the underprediction of mass Stanton number reduction by the correlation. This likely results from the greater ability of the injectant to diffuse through the lighter dissociated fluid near the wall. Further differences arise from the ability of the current method to model differing near-wall compositions of the shock layer species, which change with blowing and alter transport properties at the wall.

B. Effect of nose radius

Nose radius accounts for the major geometry effects for stagnation heating. Effective radius allows for investigation of non-hemispherical leading tip geometries [41]. For a given flight velocity and altitude, altering nose radius alters the total number of mean free paths across the length of the shock layer. A very large nose radius results in equilibrium flow approaching the near wall region. A very small nose radius may result in a frozen post-shock plasma interacting with the

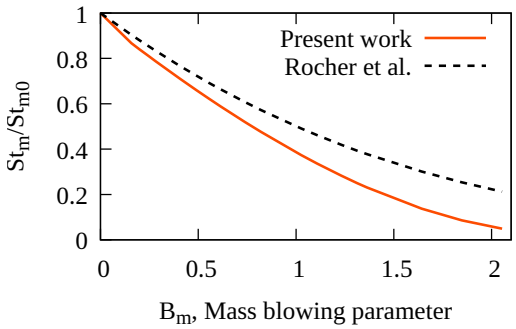

Fig. 15 Mass stanton number reduction versus mass blowing ratio for nitrogen injection compared with correlation from Rocher et al. [3] for 40 km, 4 km/s, 25 mm nose radius test case

wall. Figure 16 displays the normalized stagnation profile for varying nose tip radius. The wide range of radii provide examples of frozen, non-equilibrium, and equilibrium shock layers from smallest to largest respectively. Relative thickening of the shock with decreasing radius necessitates explicitly modeling shock structure. The larger mass fraction of atomic oxygen at the wall for the 25 mm test case as compared to the larger 250 mm test case is likely the result of the larger thermal gradient at the wall and the smaller absolute region of decreased temperature approaching the cold wall.

C. Comparison of Wall Conditions

The solver employs variable wall conditions for catalycity and solid temperature. Figures 17 and 18 display the near-wall species profiles and temperature profiles, respectively, for a low and high blowing case for each wall condition. Table 2 provides the resulting surface properties. For these tests, nitrogen was employed as the injectant, with the flight conditions used throughout the study. The wall boundary condition does not largely affect the shock standoff distance and overall form of the shock layer. Thus, while Figures 17 and 18 show near-wall conditions, the overall profiles between all wall conditions do not differ greatly from the profile shown in subplot (c) of Figures 11 and 12, except near the wall. The presence of local thermal non-equilibrium can be seen, most notably for the isothermal and high-blowing cases. This is due to the interaction between the low-temperature gas exiting the wall and the electrovibrationally excited gas from the shock layer. The feature exists to some degree for all high-blowing cases, as the diffusion of low-temperature injectant plays a large role in the near wall temperature profile. While there does exist a non-equilibrium in the non-isothermal cases, its magnitude is much smaller, as the solid is allowed to heat up which in turn excites the nearby gas before it reaches the wall exit.

Further, as the non-catalytic surface temperature is allowed to rise by 1988 K and 511 K for the low and high blowing cases, respectively, both the near-surface chemistry and surface heat flux are appreciably changed. The isothermal wall results in larger heat fluxes for both catalytic and non-catalytic cases. Transient facilities may therefore overpredict catalytic heating when using a cold test model. The same behavior is observed between the isothermal and

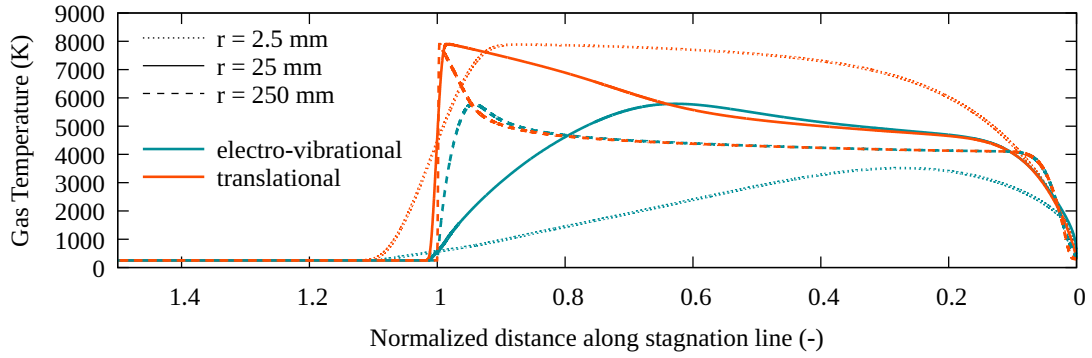

(a) Temperature

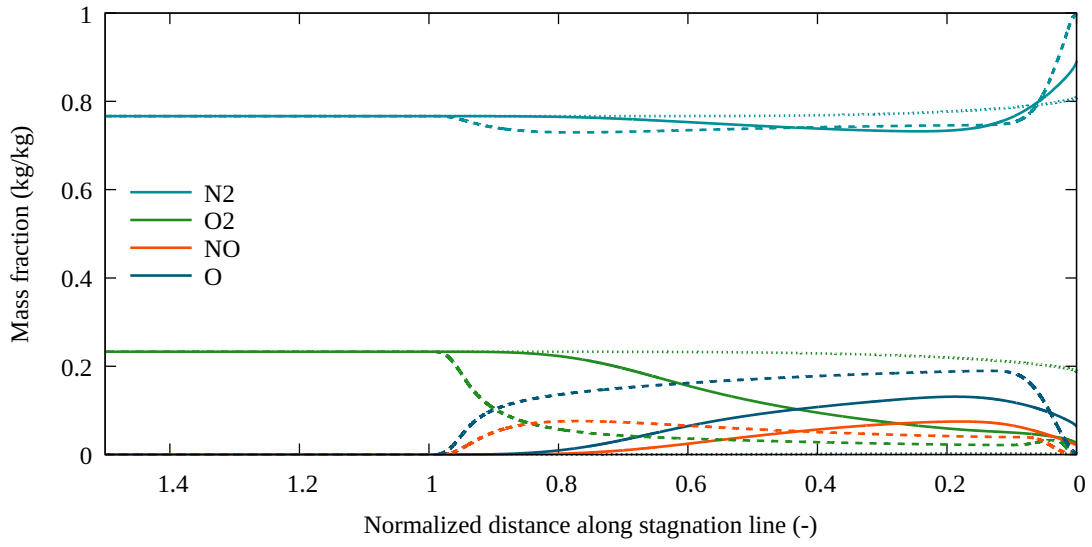

(b) Species mass fractions

Fig. 16 Temperature and species profiles with varying radius for nitrogen injection at $F = 3\%$ for 40 km, 4 km/s test case with isothermal (T_w = 300 K) and non-catalytic wall

Table 2 Surface properties for various wall conditions for 40 km, 4 km/s, 25 mm nose radius test case

	T_w (K)		$x_{O,w}$ (kg/kg)		$\dot{q_w}$ (MW/m$_2$)	
Blowing ratio, F	0.5	5.0	0.5	5.0	0.5	5.0
Wall condition						
Isothermal, non-catalytic (I-NC)	300	300	1.12E-01	3.48E-02	3.08	1.03
Non-isothermal, non-catalytic (NI-NC)	2287	811	1.12E-01	3.37E-02	1.84	0.93
Isothermal, catalytic (I-C)	300	300	6.71E-03	3.75E-03	4.37	1.20
Non-isothermal, catalytic (NI-C)	2539	1117	3.91E-02	1.04E-02	2.56	1.00

non-isothermal cases, with the catalytic wall increasing surface heat flux. Surface heat flux increases by 34% and 15% for isothermal cases and by 32% and 7% for non-isothermal cases when enforcing a catalytic wall condition relative to the non-catalytic condition. This indicates the contribution of catalytic heating is largely dependent on surface temperature. The low blowing isothermal cases are very similar in their hydrodynamic thermal load characteristics, so the difference can be largely attributed to the increased heat flux resulting from the recombination of a 10% atomic oxygen mass fraction condition as the surface. Unsurprisingly, high blowing limits the impact of the wall condition, confirming the benefit of TC in the protection against unfavorable wall properties.

Due to the porosity of the surface and the diffusive capacity of the fluid, even instantaneous reactions at the wall do not result in equilibrium compositions at the wall. For a non-isothermal wall, the effect on surface chemistry is smaller, as the higher surface temperature would result in a smaller correction to the equilibrium composition. The effect of the diffusive barrier is most visible for the isothermal and catalytic case. The equilibrium composition would be the same, but higher blowing decreases the surface mass fraction by 56%. While the non-catalytic cases show similar surface concentrations of atomic oxygen, the diffusion of oxygen into the surface is much greater for the non-isothermal case. Again, this feature shrinks for high blowing cases (for both catalytic and non-catalytic surface conditions), indicating that mass injection diminishes the impact of surface physical characteristics.

V. Conclusions

This paper presents a quasi-one-dimensional non-equilibrium stagnation line method with coupling between external flow and flow permeating through a porous leading edge. The method is capable of modeling detailed transport properties, kinetics, wall catalycity, and thermal balance. The method reproduces stagnation profiles, surface heat flux, and shock standoff distance in non-equilibrium flow, as previously presented by two-dimensional simulations across a range of flight and wall boundary conditions. Further, validation of transpiration cooling has been presented relative to Stanton number reduction correlations and experimental data.

Results from this study present detailed profiles of species concentrations and temperatures, which are computed based on full multi-component transport properties. Specifically, the sensitivity of these profiles, stagnation heat flux,

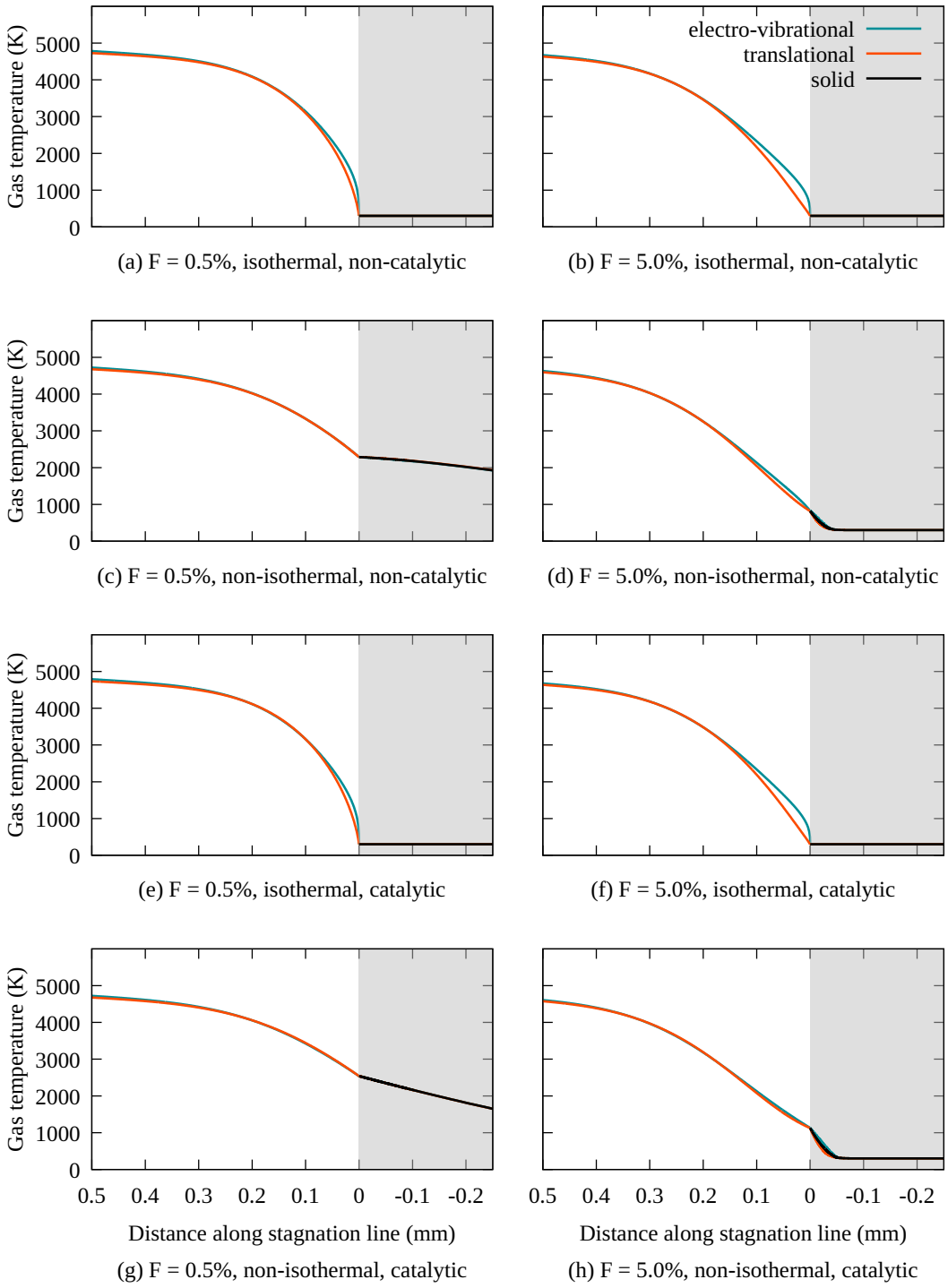

(a) F = 0.5%, isothermal, non-catalytic

(b) F = 5.0%, isothermal, non-catalytic

(c) F = 0.5%, non-isothermal, non-catalytic

(d) F = 5.0%, non-isothermal, non-catalytic

(e) F = 0.5%, isothermal, catalytic

(f) F = 5.0%, isothermal, catalytic

(g) F = 0.5%, non-isothermal, catalytic

(h) F = 5.0%, non-isothermal, catalytic

Fig. 17 Temperature profiles for nitrogen injectant for various wall conditions at low and high blowing

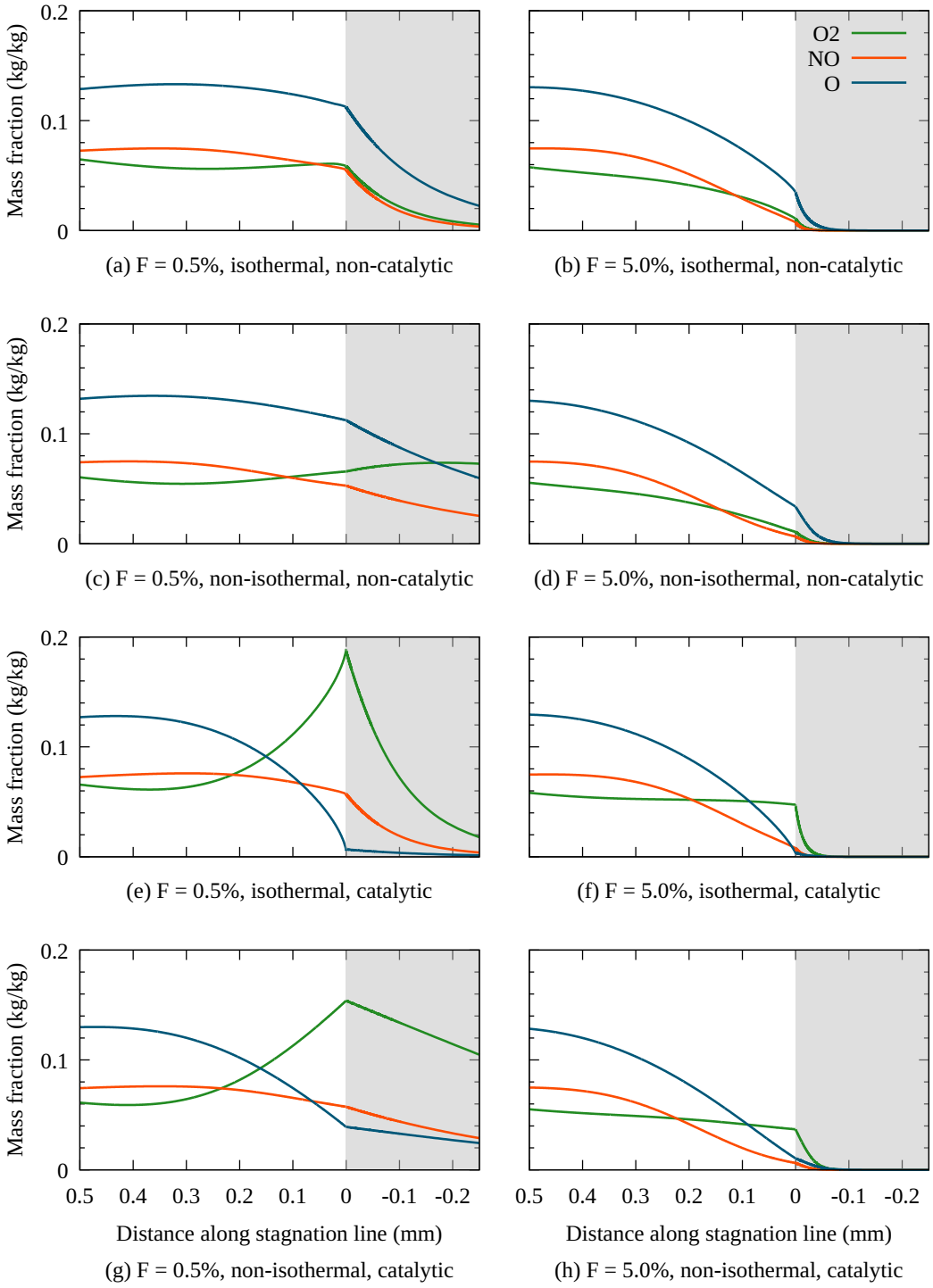

(a) F = 0.5%, isothermal, non-catalytic
(b) F = 5.0%, isothermal, non-catalytic
(c) F = 0.5%, non-isothermal, non-catalytic
(d) F = 5.0%, non-isothermal, non-catalytic
(e) F = 0.5%, isothermal, catalytic
(f) F = 5.0%, isothermal, catalytic
(g) F = 0.5%, non-isothermal, catalytic
(h) F = 5.0%, non-isothermal, catalytic

Fig. 18 Species profiles for nitrogen injectant for various wall conditions at low and high blowing

and surface concentration relative to injectant composition and rate and wall boundary condition is shown. The results show previously undocumented behavior of the species concentrations near the surface, as the solver explicitly solves the flow equations throughout the porous medium. Results show that cooling performance is primarily dependent on injectant molecular weight, at similar injectant mass flux. Injectants of low molecular weight, e.g. Helium, are more effective at shielding the wall from shock-layer species at moderate to high blowing rates. However, low molecular weight injectants are less effective at low blowing rates, as species from the shock layer diffuse faster through the lighter injectant.

Finally, results are presented for varying wall catalycity and thermal boundary conditions. Wall catalytic activity does not significantly affect the efficacy of the injectant at higher blowing rates, because atomic and ionic species are displaced away from the surface. The same is true for thermal wall conditions, as colder coolant inhibits chemical processes near the wall. At low blowing rates, wall features have a larger, but localized, effect on the shock layer.

The method presented in this work provides a numerically efficient and physically accurate means of modeling the entire domain of interest for transpiration cooling applications to stagnation points. Characterization of coolant effectiveness relative to mass flux can be performed comprehensively with varying coolants, leading edge radii, and solid material properties as well as across a wide range of flight velocities and altitudes.

Appendix

A. Transport properties

Often, transport properties are computed using the mixing rules presented by Yos [23], as implemented in the work of Gupta *et al.* [24] and Gnoffo *et al.* [6]. These mixing rules offer low computational costs. However, as shown by Palmer and Wright [42], accuracy decreases significantly at temperatures above roughly 10,000 Kelvin for air. Wilke [43] and Gordon and McBride [44] present similar mixing rules which were assessed by Palmer and Wright [42] to halve the computational cost relative to a full multi-component rigorous method, as presented by Hirschfelder *et al.* [21]. While computationally efficient, these evaluations can be inaccurate, with non-negligible error arising at temperatures above 10,000 K for air, where ionization effects begin to dominate. From several resources [21, 45, 46], rigorous formulations implementing Park's two temperature model can be employed. Murphy presented an implementation of a multi-component rigorous method [47]. The methods for calculating transport properties in this work were validated against Murphy's work, with results presented in Figures 19-21. Further, Murphy presented a comparison between the viscosity of 11 species air, as computed with his rigorous method and Gupta's mixing rule. Again, the methods used in this work align nicely with Murphy's, as shown in Figure 22.

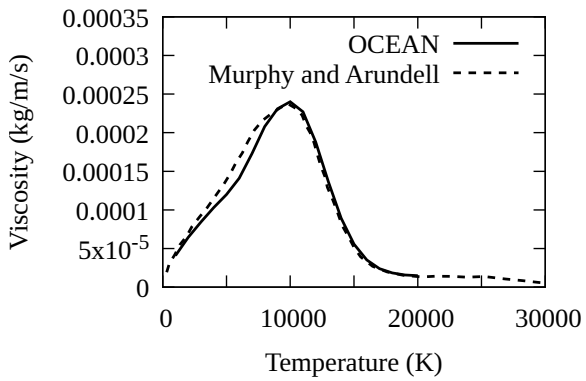

Fig. 19 Viscosity of nitrogen compared with data from Murphy and Arundell [47]

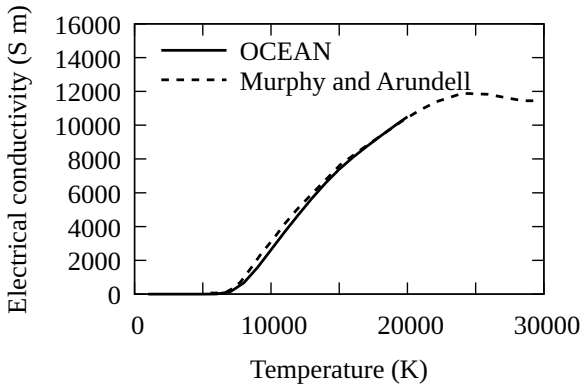

Fig. 20 Electrical conductivity of nitrogen compared with data from Murphy and Arundell [47]

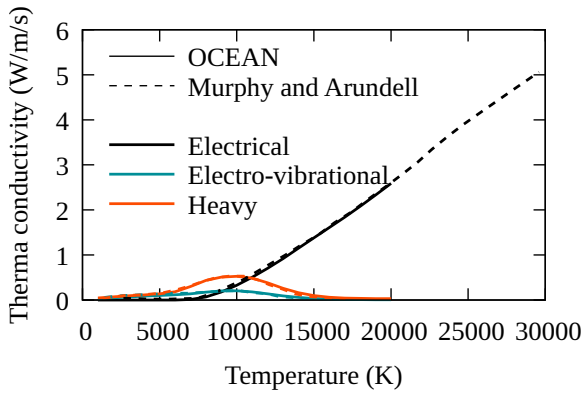

Fig. 21 Thermal conductivity components of nitrogen compared with data from Murphy and Arundell [47]

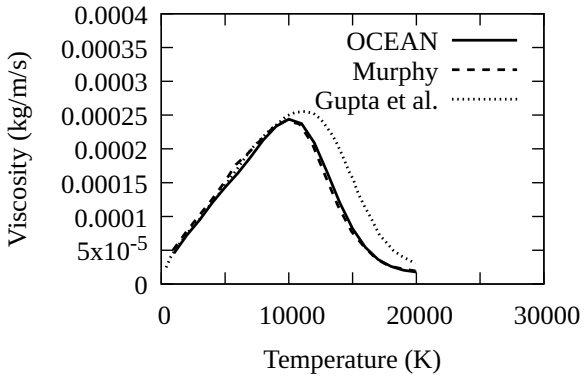

Fig. 22 Viscosity of air compared with data from Murphy [48] and Gupta *et al.* [24]

B. Chemical Model Reactions and Rates

Acknowledgments

Samuel Brody gratefully acknowledges the Marshall Commission for financial support as well as the U.S. Air Force for their support of this effort. Justin Clarke gratefully acknowledges the Rhodes Trust for financial support.

Table 3 Chemical Reactions from Park [19] with inert gas ionization

		$k_{f,r} = A_{f,r} T^{\alpha_{f,r}} e^{-T_{f,r}/T_{av}}$		
Reaction Number	Reaction	$A_{f,r}$	$\alpha_{f,r}$	$T_{f,r}$
1	$N_2 + M_2 \rightleftharpoons 2N + M_2$	7.00×10^{21}	-1.6	1.132×10^5
2	$O_2 + M_1 \rightleftharpoons 2O + M_1$	2.00×10^{21}	-1.5	5.95×10^4
3	$NO + M_3 \rightleftharpoons N + O + M_3$	5.00×10^{15}	0.0	7.45×10^4
4	$N_2 + e^- \rightleftharpoons 2N + e^-$	1.20×10^{25}	-1.6	1.132×10^5
5	$NO + O \rightleftharpoons O_2 + N$	8.40×10^{12}	0.0	1.945×10^4
6	$N_2 + O \rightleftharpoons NO + N$	6.40×10^{17}	-1.0	3.84×10^4
7	$N + O \rightleftharpoons NO^+ + e^-$	8.80×10^{08}	1.0	3.19×10^4
8	$O + O \rightleftharpoons {O_2}^+ + e^-$	7.10×10^{02}	2.7	8.06×10^4
9	$N + N \rightleftharpoons {N_2}^+ + e^-$	4.40×10^{07}	1.5	6.75×10^4
10	$O + NO^+ \rightleftharpoons O_2 + N^+$	1.00×10^{12}	0.5	7.72×10^4
11	$N_2 + N^+ \rightleftharpoons N + {N_2}^+$	1.00×10^{12}	0.5	1.22×10^4
12	${O_2}^+ + N \rightleftharpoons N^+ + O_2$	8.70×10^{13}	0.14	2.86×10^4
13	$O^+ + NO \rightleftharpoons N^+ + O_2$	1.40×10^5	1.9	2.66×10^4
14	${O_2}^+ + N_2 \rightleftharpoons {N_2}^+ + O_2$	9.90×10^{12}	0.0	4.07×10^4
15	$O + {O_2}^+ \rightleftharpoons O_2 + O^+$	4.00×10^{12}	-0.09	1.80×10^4
16	$NO^+ + N \rightleftharpoons O^+ + N_2$	3.40×10^{13}	-1.08	1.28×10^4
17	$NO^+ + O_2 \rightleftharpoons {O_2}^+ + NO$	2.40×10^{13}	0.41	3.26×10^4
18	$NO^+ + O \rightleftharpoons {O_2}^+ + N$	7.20×10^{12}	0.29	4.86×10^4
19	$O^+ + N_2 \rightleftharpoons {N_2}^+ + O$	9.10×10^{11}	0.036	2.28×10^4
20	$NO^+ + N \rightleftharpoons {N_2}^+ + O$	7.20×10^{13}	0.0	3.55×10^5
21	$O + e^- \rightleftharpoons O^+ + e^- + e^-$	3.90×10^{33}	-3.78	1.585×10^5
22	$N + e^- \rightleftharpoons N^+ + e^- + e^-$	2.50×10^{34}	-3.82	1.686×10^5
	Inert gas ionization			
23 [26]	$Ar + e^- \rightleftharpoons Ar^+ + e^- + e^-$	2.5×10^{34}	-3.82	1.817×10^5
24 [25]	$He + e^- \rightleftharpoons He^+ + e^- + e^-$	3.33×10^{20}	0.5	2.852×10^5

References

[1] Ewenz Rocher, M., Hermann, T., McGilvray, M., Grossman, M., and Vandeperre, L., "Measuring the Concentration of Freestream Species on a Hypersonic Transpiration-Cooled Stagnation Point," *Journal of Spacecraft and Rockets*, Vol. 59, No. 4, 2022, pp. 1380–1387. https://doi.org/10.2514/1.A35283.

[2] Ravichandran, R., Doherty, L. J., McGilvray, M., Damm, K., and Gollan, R., *Aerodynamic Effects and Heat Flux Augmentation of a Transpiration Cooled Hypersonic Sharp Leading Edge*, 2023. https://doi.org/10.2514/6.2023-0437.c1.

[3] Rocher, M. E., Hermann, T., McGilvray, M., and Gollan, R., "Correlation for Species Concentration on a Hypersonic Stagnation Point with Mass Injection," *AIAA Journal*, Vol. 60, 2022, pp. 2798–2809. https://doi.org/10.2514/1.J061159.

[4] Blottner, F., "Viscous Shock layer at the Stagnation Point with Nonequilibrium Air Chemistry," *AIAA Journal*, Vol. 7, 1969, pp. 2281–2288. https://doi.org/10.2514/3.5528.

[5] Cheng, H., "The Blunt-Body Problem in Hypersonic Flow at Low Reynolds Numbers," , No. AF-1285-A-10, 1963.

[6] Gnoffo, P. A., Gupta, R. N., and Shinn, J. L., "Conservation equations and physical models for hypersonic air flows in thermal and chemical nonequilibrium," Tech. Rep. NASA TP 2867, 1989.

[7] Clarke, J., Brody, S., Steer, J., McGilvray, M., and Di Mare, L., "Quasi-one-dimensional non-equilibrium method for shock tube and stagnation line flows," *Physics of Fluids*, Vol. 36, No. 9, 2024. https://doi.org/10.1063/5.0218676.

[8] Cimolin, F., and Discacciati, M., "Navier–Stokes/Forchheimer models for filtration through porous media," *Applied Numerical Mathematics*, Vol. 72, 2013, pp. 205–224. https://doi.org/10.1016/j.apnum.2013.07.001.

[9] Nield, D. A., Bejan, A., et al., *Convection in porous media*, Vol. 3, Springer, 2006.

[10] Erugn, S., "Fluid Flow through Packed Columns," *Chemical Engineering Progress*, Vol. 48, 1952, pp. 89–94.

[11] Hermann, T. A., McGilvray, M., Ifti, H. S., Hufgard, F., and Loehle, S., *Fluid-Solid Heat Exchange in Porous Media for Transpiration Cooling Systems*, 2023. https://doi.org/0.2514/6.2019-0537.

[12] Homann, F., "Einfluß großer zähigkeit bei strömung um zylinder," *Forschung auf dem Gebiet des Ingenieurwesens A*, Vol. 7, No. 1, 1936, pp. 1–10.

[13] Herring, T. K., "The boundary layer near the stagnation point in hypersonic flow past a sphere," *Journal of Fluid Mechanics*, Vol. 7, 1960, pp. 257–272. https://doi.org/10.1017/S002211206000147X.

[14] Fay, J. A., and Riddell, F. R., "Theory of Stagnation Point Heat Transfer in Dissociated Air," *Journal of the Aerospace Sciences*, Vol. 25, No. 2, 1958, pp. 73–85. https://doi.org/10.2514/8.7517.

[15] Parthasarathy, T., Rapp, R., Opeka, M., and Kerans, R., "A model for the oxidation of ZrB2, HfB2 and TiB2," *Acta Materialia*, Vol. 55, No. 17, 2007, pp. 5999–6010. https://doi.org/10.1016/j.actamat.2007.07.027.

[16] Scott, C. D., "Wall catalytic recombination and boundary conditions in nonequilibrium hypersonic flows—with applications," *Advances in Hypersonics: Modeling Hypersonic Flows*, Springer, 1992, pp. 176–250. https://doi.org/10.1007/978-1-4612-0371-1_6.

[17] Park, C., *Nonequilbrium Hypersonic Aerothermodynamics*, John Wiley & Sons, Inc., 1990.

[18] Millikan, R. C., and White, D. R., "Systematics of Vibrational Relaxation," *The Journal of Chemical Physics*, Vol. 39, No. 12, 1963, pp. 3209–3213. https://doi.org/10.1063/1.1734182.

[19] Park, C., "Review of chemical-kinetic problems of future NASA missions. I - Earth entries," *Journal of Thermophysics and Heat Transfer*, Vol. 7, No. 3, 1993, pp. 385–398. https://doi.org/10.2514/3.431.

[20] Kim, J. G., and Jo, S. M., "Modification of chemical-kinetic parameters for 11-air species in re-entry flows," *International Journal of Heat and Mass Transfer*, Vol. 169, 2021, p. 120950. https://doi.org/https://doi.org/10.1016/j.ijheatmasstransfer.2021.120950.

[21] Hirschfelder, J. O., Curtiss, C. F., and Bird, R. B., *Molecular Theory of Gases and Liquids*, John Wiley & Sons, Inc., 1954.

[22] Park, C., Jaffe, R. L., and Partridge, H., "Chemical-Kinetic Parameters of Hyperbolic Earth Entry," *Journal of Thermophysics and Heat Transfer*, Vol. 15, No. 1, 2001, pp. 76–90. https://doi.org/10.2514/2.6582.

[23] Yos, J. M., "Transport properties of nitrogen, hydrogen, oxygen, and air to 30,000 K," Tech. Rep. RAD-TM-63-7, AVCO CORP WILMINGTON MA RESEARCH AND ADVANCED DEVELOPMENT DIV, 1963.

[24] Gupta, R. N., Yos, J. M., and Thompson, R. A., "A review of reaction rates and thermodynamic and transport properties for the 11-species air model for chemical and thermal nonequilibrium calculations to 30000 K," Tech. Rep. NASA RP-1232, NASA, 1989.

[25] Leibowitz, L. P., and Kuo, T.-J., "Ionizational Nonequilibrium Heating During Outer Planetary Entries," *AIAA Journal*, Vol. 14, No. 9, 1976, pp. 1324–1329. https://doi.org/10.2514/3.61465.

[26] Gokcen, T., "N2-CH4-Ar Chemical Kinetic Model for Simulations of Atmospheric Entry to Titan," *Journal of Thermophysics and Heat Transfer*, Vol. 21, No. 1, 2007, pp. 9–18. https://doi.org/10.2514/1.22095.

[27] Harlow, F. H., and Welch, J. E., "Numerical Calculation of Time-Dependent Viscous Incompressible Flow of Fluid with Free Surface," *The Physics of Fluids*, Vol. 8, No. 12, 1965, pp. 2182–2189. https://doi.org/10.1063/1.1761178.

[28] Morduchow, M., and Libby, P. A., "On a Complete Solution of the One-Dimensional Flow Equations of a Viscous, Heat-Conducting, Compressible Gas," *Journal of the Aeronautical Sciences*, Vol. 16, No. 11, 1949, pp. 674–684. https://doi.org/10.2514/8.11882.

[29] Chaudhry, R. S., Boyd, I. D., and Candler, G. V., *Vehicle-Scale Simulations of Hypersonic Flows using the MMT Chemical Kinetics Model*, 2020. https://doi.org/10.2514/6.2020-3272.

[30] Yang, Y., Lee, S., and Kim, J. G., "Influence of catalytic wall on the effective radius of a blunt body geometry in a nonequilibrium hypersonic flow," *Case Studies in Thermal Engineering*, Vol. 35, 2022, p. 102085. https://doi.org/https://doi.org/10.1016/j.csite.2022.102085.

[31] Kim, J. G., and Park, G., "Thermochemical nonequilibrium parameter modification of oxygen for a two-temperature model," *Physics of Fluids*, Vol. 30, No. 1, 2018, p. 016101. https://doi.org/10.1063/1.4996799.

[32] Nonaka, S., Mizuno, H., Takayama, K., and Park, C., "Measurement of Shock Standoff Distance for Sphere in Ballistic Range," *Journal of Thermophysics and Heat Transfer*, Vol. 14, No. 2, 2000, pp. 225–229. https://doi.org/10.2514/2.6512.

[33] Yoshikawa, K. K., "Linearized Theory of Stagnation Point Heat and Mass Transfer at Hypersonic Speeds," Tech. Rep. NASA TN D-5246, 1969.

[34] Naved, I., Hermann, T., McGilvray, M., Ewenz Rocher, M., Hambidge, C., Doherty, L., Le Page, L., Grossman, M., and Vandeperre, L., "Heat Transfer Measurements of a Transpiration-Cooled Stagnation Point in Transient Hypersonic Flow," *Journal of Thermophysics and Heat Transfer*, Vol. 37, No. 2, 2023, pp. 296–308. https://doi.org/10.2514/1.T6610.

[35] Marvin, J. G., and Pope, R. B., "Laminar convective heating and ablation in the Mars atmosphere." *AIAA Journal*, Vol. 5, No. 2, 1967, pp. 240–248. https://doi.org/10.2514/3.3948.

[36] Kays, W. M., Crawford, M. E., and Weigand, B., *Convective heat and mass transfer*, Vol. 2, McGraw-Hill New York, 1980.

[37] Swann, R. T., and Pittman, C. M., *Numerical analysis of the transient response of advanced thermal protection systems for atmospheric entry*, National Aeronautics and Space Administration, 1962.

[38] Mickley, H., *Heat, mass, and momentum transfer for flow over a flat plate with blowing or suction*, Vol. 3208, National Advisory Committee for Aeronautics, 1954.

[39] Tauber, M. E., "A review of high-speed, convective, heat-transfer computation methods," 1989.

[40] Pappas, C. C., and Lee, G., "Heat transfer and pressure on a hypersonic blunt cone with mass addition," *AIAA Journal*, Vol. 8, No. 5, 1970, pp. 954–956. https://doi.org/10.2514/3.5801.

[41] Zoby, E. V., and Sullivan, E. M., "Effects of Corner Radius on Stagnation-Point Velocity Gradients on Blunt Axisymmetric Bodies," *Journal of Spacecraft and Rockets*, Vol. 3, No. 10, 1966, pp. 1567–1567. https://doi.org/10.2514/3.59538.

[42] Palmer, G. E., and Wright, M. J., "Comparison of methods to compute high-temperature gas viscosity," *Journal of Thermophysics and Heat Transfer*, Vol. 17, 2003, pp. 232–239. https://doi.org/10.2514/2.6756.

[43] Wilke, C. R., "A viscosity equation for gas mixtures," *The Journal of Chemical Physics*, Vol. 18, No. 4, 1950, pp. 517–519.

[44] Gordon, S., and McBride, B. J., "Computer Program for Calculation of Complex Chemical Equilibrium," Tech. Rep. NASA-RP-1311, 1994.

[45] Muckenfuss, C., and Curtiss, C. F., "Thermal conductivity of multicomponent gas mixtures," *The Journal of Chemical Physics*, Vol. 29, 1958, pp. 1273–1277. https://doi.org/10.1063/1.1744709.

[46] Capitelli, M., Colonna, G., Gorse, C., and D'angola, A., "Transport properties of high temperature air in local thermodynamic equilibrium," *The European Physical Journal D - Atomic, Molecular, Optical and Plasma Physics*, Vol. 11, 2000, pp. 279–289. https://doi.org/10.1007/s100530070094.

[47] Murphy, A. B., and Arundell, C. J., "Transport Coefficients of Argon, Nitrogen, Oxygen, Argon-Nitrogen, and Argon-Oxygen Plasmas," *Plasma Chemistry and Plasma Processing*, Vol. 14, 1994. https://doi.org/10.1007/BF01570207.

[48] Murphy, A. B., "Transport Coefficients of Air, Argon-Air, Nitrogen-Air, and Oxygen-Air Plasmas," *Plasma Chemistry and Plasma Processing*, Vol. 15, 1995. https://doi.org/10.1007/BF01459700.

Chapter 5
Transpiration Cooled Stagnation Point in Non-Equilibrium Hypersonic Flow

5.1 Foreword

The efficient nature of the method, presented in the previous chapter, enabled the exploration of the transpiration cooling problem across a large parameter space. This application of the tool constitutes the third major objective of this thesis. The computational speed, allowing for tens of simulations per day, facilitates extensive parametric studies investigating the influence of varying freestream conditions, injectant properties (composition, mass flux), and surface characteristics on cooling performance and surface chemistry.

A significant aspect of this application is the characterization of surface chemical composition and transport properties under mass injection, which is crucial for assessing material compatibility and degradation. The data generated from these studies was employed in an effort to validate and develop predictive engineering correlations, such as those presented by Yoshikawa [125] or Marvin and Pope [165]. These results not only provide useful approximations for vehicle design and experimental planning but also deepen the physical understanding of the dominant processes governing stagnation point flows with active mass injection. Further, the investigation of thermochemical modeling and its impact on flow features is continued from Chapter 3 in the consideration of transport properties (which rely on collision integrals). Finally, extension to the Mars atmosphere (and the large concentration of CO for certain conditions) displays the importance of accurately capturing polar collision behavior.

5.2 Statement of authorship

- Title of the paper: *Transpiration Cooled Stagnation Point in Non-Equilibrium Hypersonic Flow*
- Publication status: Unpublished and unsubmitted work written in a manuscript style
- Publication details: Samuel D. Brody, Justin Clarke, Claudio Rapisarda, Matthew McGilvray, and Luca di Mare, “Characterization of Transpiration Cooled Stagnation Point in Non-Equilibrium Hypersonic Flow.”

Table 5.1: Statement of Authorship

Author	**Contribution**	**Percentage (%)**
Samuel D. Brody	Conception	50
	Writing	100
	Code Development	80
	Data Acquisition	100
	Analysis and Interpretation	70
	Thermochemical Validation	50
Justin Clarke	Code Development	5
	Thermochemical Validation	10
Claudio Rapisarda	Thermochemical validation	40
Matthew McGilvray	Conception	20
	Analysis and Interpretation	5
	Supervision	40
	Critical Revision	50
Luca di Mare	Conception	30
	Writing	10
	Code Development	15
	Analysis and Interpretation	25
	Supervision	60
	Critical Revision	50

5.3 Manuscript

Transpiration Cooled Stagnation Point in Non-Equilibrium Hypersonic Flows

Samuel Brody *, Justin Clarke †, Claudio Rapisarda ‡, Matthew McGilvary §, Luca Di Mare ¶
Oxford Thermofluids Institute, University of Oxford, Oxford, Oxfordshire, OX1 2JD

Extreme heat loads during flight constrain the design of hypersonic vehicles. Further, certain missions necessitate the use of sharp leading edges, which enhance aerodynamic performance. Sharp leading edges decrease the shock standoff distance, which increases temperature gradient and thus surface heat flux. Additionally, reduced standoff distance introduces non-equilibrium phenomena into the near-surface gas mixture, which may result in high catalytic heating. Transpiration cooling is a method for reducing surface heat loads, preventing oxidative damage, and maintaining leading edge geometry during flight, while also providing reusability. This paper investigates the application of transpiration cooling to stagnation points in hypersonic flight, across a wide parameter space. Results are generated from a stagnation line solver, applying Park two-temperature non-equilibrium thermochemistry and rigorous multicomponent evaluations for transport properties. This study explores a range of freestream altitudes and velocities, leading edge radii, injectants, and surface properties. Correlations for both heat and mass Stanton numbers are presented and compared to existing correlations. Injectants similar to the shock layer gas align with correlations established with equilibrium assumptions and mixture definitions for transport properties. However, wall catalycity, wall temperature, and dissimilar injectants modify the cooling behavior. These effects are due to alterations in near wall mixing that can only be captured with non-equilibrium thermochemistry and multicomponent transport properties.

Nomenclature

B_h	=	blowing parameter
B_m	=	mass blowing parameter
b	=	nose-tip radius
c_1, c_2	=	coefficients for Eq. 21

*DPhil Candidate, Department of Engineering Science, Oxford Thermofluids Institute, University of Oxford.
†DPhil Candidate, Department of Engineering Science, Oxford Thermofluids Institute, University of Oxford.
‡DPhil Candidate, Department of Engineering Science, Oxford Thermofluids Institute, University of Oxford.
§Professor, Oxford Thermofluids Institute, Department of Engineering Science, University of Oxford.
¶Associate Professor, Oxford Thermofluids Institute, Department of Engineering Science, University of Oxford.

D_{ij} = mixture coefficient of diffusion for species i and j

$\mathscr{D}_{ij}$ = binary coefficient of diffusion for species i and j

$D'_{i,mix}$ = effective coefficient of diffusion for species i into a gas mixture

e_v = specific vibrational energy

F = blowing ratio

H = total enthalpy

$h_{v,s}$ = specific vibrational energy of species s

h_w = specific enthalpy

H_v = volumetric heat transfer coefficient

k = conductivity; Boltzmann Constant, 1.380649e-23 J/K

k_D = Darcy coefficient

k_e = electronic component of thermal conductivity

k_s = solid conductivity

k_v = vibrational component of thermal conductivity

M = molecular weight

p = pressure

R = Reynolds number

St = Stanton number

St_m = mass Stanton number

T = temperature (K)

$\vec{u}$ = velocity vector

$\dot{w}$ = mass production rate

y = molar concentration

α = Darcy penalization control

δ = shock standoff distance, domain widths

ϵ = emissivity

$\varepsilon_{i,j}$ = dispersion energy for binary collision pair of species i and j

ϵ_n = porosity in flow direction

μ = viscosity

ρ = density

$\sigma_{i,j}$ = rigid sphere diameter for binary collision pair of species i and j

σ_{SB} = Stefan-Boltzmann constant

τ = viscosity tensor

$\Omega_{ij}^{(l,s)*}$ = collision integral, $\mathring{A}^2$

Subscripts

inj = injectant

e = electronic

ev = electrovibrational

p = porous region

s = species

t = translational

tr = trans-rotational

v = vibrational

w = wall

∞ = freestream

I. Introduction

Applications to planetary exploration, space tourism, global supply chain and travel, and defense merit the continued study of hypersonic flight. The primary challenge in the hypersonic regime is the extreme heat loads experienced during flight. Sharp leading edges (on the order of 1 mm), often required for aerodynamic performance, exacerbate the heating problem by reducing the shock standoff distance, increasing surface heat flux, and introducing non-equilibrium phenomena to the near surface gas mixture. Transpiration cooling (TC) offers an effective solution to mitigate surface heat and mass transfer which is both shape-resistant and reusable. TC operates by the injection of a gas through a porous structure on the vehicle surface and provides cooling, generally described via three primary mechanisms. First, the cold injectant gas convects heat from the vehicle as it travels through the porous substructure. Second, the injectant displaces the hot shock layer gas near the surface, reducing the conductive heat flux to the wall through the reduction of the near-wall thermal gradient. Third, the injectant inhibits the transport of shock layer species to the wall, reducing the heat flux due to chemical reactions near the wall. A fourth mechanism, often overlooked, is the alteration of near wall transport properties, which will be investigated in this study. The transport of shock layer species has further implications for material degradation. Ultrahigh temperature ceramics (UHTCs) offer promising performance over traditional metallic materials with high melting temperatures (thus, large radiative cooling capacities) but are susceptible to oxidation [1]. Thus, the effectiveness of a transpiration cooling system is dependent on its ability to both reduce wall heat transfer and inhibit mass transfer. Figure 1 displays a schematic of the flow domain for a transpiration cooled leading edge, with the three mechanisms for cooling highlighted.

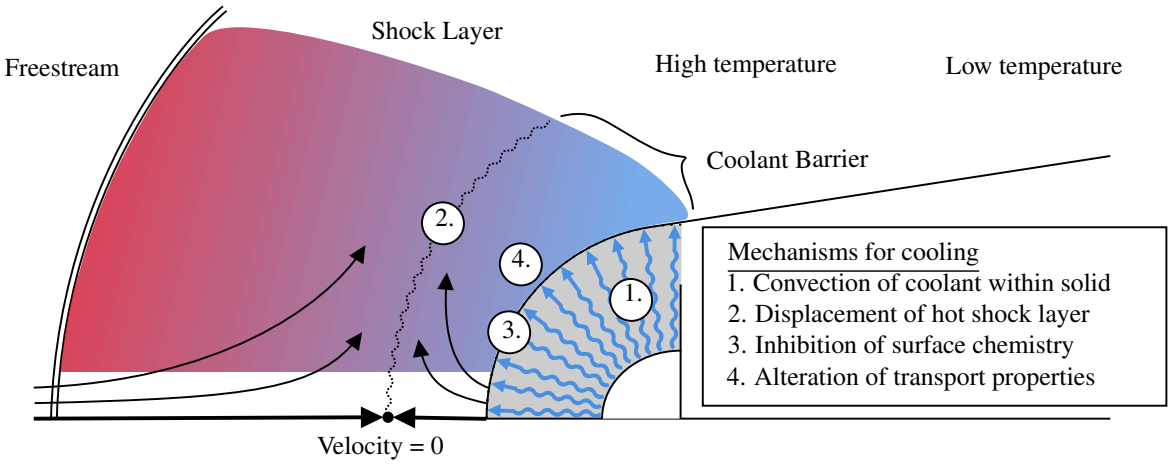

Fig. 1 Schematic of flow domain for transpiration cooled leading edge with mechanisms for cooling.

A parametric characterization of transpiration cooling is useful for hypersonic vehicle design, as it allows for an assessment of the feasibility of this technology relative to mission and vehicle requirements. Cost and time investment limit flight testing and experimental testing to a tight parameter space. Further, experimental facilities face challenges in replicating transpiration cooling in non-equilibrium hypersonic conditions. Wind tunnels struggle to simultaneously produce flight-relevant enthalpies and Reynolds numbers. Impulse facilities often cannot achieve long enough test times to capture steady measurements for surface temperature and blowing. An accurate description of injectant impact on heat and mass transfer can reduce the need for vehicle-scale numerical simulation to only a baseline non-blowing case. The leading-edge heat transfer is critical, as it governs material selection and TPS design. By systematically analyzing the TC problem applied to stagnation points, vehicles designers can evaluate possible implementation across a wide range of operating conditions. Heat and mass transfer, often expressed as Stanton numbers, provide essential metrics for evaluating transpiration cooling performance. Additionally, understanding surface effects reduces the decision time and development cost for surface materials. Finally, understanding the fundamental effects of mass injection on the shock layer has broader engineering value, including applications to ablative cooling systems.

The method used in this work, originally presented by Brody *et al.* [2], follows the extension by Blottner [3] of Cheng's [4] thin shock layer work for stagnation line flows. The solver employs a unified domain, inclusive of the freestream, shock layer, and porous regions. By focusing on the dominant physical phenomena and limiting focus to the area of peak heating, the method is suitably accurate while remaining computationally efficient. The resulting solver is a useful engineering tool capable of accurately modeling the major effects of transpiration cooling.

Characterizations for heat and mass transfer at the stagnation point in the presence of mass injection have been investigated across various aerospace applications. Early efforts to develop predictive correlations for these phenomena often focused on more constrained problems, assuming conditions such as equilibrium chemistry and uniform surface

properties. The literature includes important foundational work. Swann and Pittman [5] and Howe and Scheaffer [6] investigated mass injection primarily in the context of ablative materials, though their studies considered air injection. Experimental characterizations under equilibrium conditions were conducted in works by Pappas and Lee [7], Kaatari [8], and more recently Naved *et al.* [9]. The experimental results of Kaatari were later validated by Thompson and Gnoffo [10] using computational methods. Other notable contributions include the work of Sreekanth and Reddy [11] and Mills and Wortman [12]. The latter presented correlations for both heat and mass transfer reduction.

Many studies either relied on computationally expensive simulations, which were often narrow in scope, or made simplifying assumptions that may not hold for complex non-equilibrium hypersonic flows. A common technique, as seen in the work of Rocher [13] and Mills and Wortman [12], is to assume the binary problem of a single injectant species diffusing into a bulk flow described simply as air.

Given the complexity of high-enthalpy shock layers, it is desirable to develop correlations that require minimal detailed knowledge of the shock layer composition or state. Thus, correlations that primarily utilize features of the freestream conditions and injectant properties (such as mass flux, molecular weight, and transport properties) are generally considered most practical for engineering applications. The generic forms of many heat and mass transfer correlations with injection often originate from simplified flow analysis, such as similar solutions for Couette flow [12] or film theory [13, 14]. Polynomial functions, including quadratic forms often seen in the literature [15], can be viewed as empirical fits or expansions of these more fundamental theoretical forms. More recent work, such as the mass Stanton number correlations presented by Rocher *et al.* [13], utilize self-similar boundary layer solutions specifically derived with equilibrium chemistry and specified injection boundary conditions. It is important to note that while these external flow correlations are valuable, they often omit the detailed physics of mass, momentum, and energy transport within the porous layer itself. Although not the primary focus of the external flow correlations discussed here, understanding transport within the porous structure is crucial for predicting non-isothermal surface temperatures and overall cooling system performance. Some results and discussion on this topic are presented by Brody *et al.* [2].

The contribution of this paper is the characterization of transpiration cooling for stagnation line flows in thermo-chemical non-equilibrium, including wall catalysis, varying wall temperature, and the diffusive mixing of shock layer and injectant species near the wall. The objective is to clearly assess the impact on transpiration cooled leading edges of the following parameters: mass flux, injectant, surface characteristics, free-stream conditions, and leading edge radius. The paper is organized into three additional sections. Section II describes the solution methodology and modes of analysis for TC. Section III presents results from a wide range of simulations. Section IV presents conclusions.

II. Methodology and Analysis

A. Method

Results in this study come from the method presented by Brody *et al.* [2]. The main elements are reiterated, but a detailed description of the treatment of the unified domain with surface injectant and wall effects, grid refinement studies, and validation against numerical results and experimental data have been previously presented. The results of this study apply to stagnation flows over spherical leading edges. Two-dimensional effects are incorporated via a tangential pressure gradient, as developed by Cheng [4]. The solution domain extends from the freestream to the plenum wall, resolving the shock structure and explicitly modeling the fluid-solid interaction. The solution methodology follows analytical solutions presented by Homann [16] and Herring [17]. Application to chemically reacting and multi-temperature gas mixtures mimic the solution presented by Blottner [3]. The specific formulation for the conservation equations applied to continuum, two-temperature reacting flows are taken from Gnoffo *et al.* [18]. The solid-fluid interaction is taken from Hermann *et al.* [19]. A Darcy penalization term is included in the momentum equation to account for porous flow, as presented by Cimolin and Discacciati [20]. The pore-diameter Reynolds number remains low enough to exclude the Forchheimer term [21, 22]. These are the resulting conservation equations:

$$0 = -\nabla \cdot (\rho_s \vec{u}) - \nabla \cdot (\rho_s D_s \nabla y_s) + \dot{w}_s \tag{1}$$

$$0 = -\nabla \cdot (\rho \vec{u} \otimes \vec{u}) - \nabla p + \nabla \cdot \tau - \alpha \frac{\mu}{k_D} \vec{u} \tag{2}$$

$$0 = -\nabla \cdot (\rho e_v \vec{u}) + \nabla \cdot ((k_e + k_v) \nabla T_v) + \nabla \cdot \left(\sum_{s=1}^{n_s} h_{v,s} (\rho_s D_s \nabla y_s) \right) - p_e \nabla \cdot \vec{u} - S - Q_{rad} \tag{3}$$

$$0 = -\nabla \cdot (\rho H \vec{u}) + \nabla \cdot q_c + \nabla \cdot q_d + \nabla \cdot (\tau \cdot \vec{u}) - H_v (T_s - T_t) \tag{4}$$

$$0 = k_s (1 - \varepsilon) \nabla \cdot \left(\frac{\partial T_s}{\partial y} \right) - Q_{rad} + H_v (T_s - T_t) \tag{5}$$

The mass production rate, $\dot{w}_s$, the source terms, S, and radiation loss term, Q_{rad}, are taken directly from Gnoffo *et al.*. The conductive heat flux, q_c, and diffusive enthalpy flux, q_d, are defined using Fourier's law and Fick's law with multicomponent diffusion mass flux, respectively.

The conservation equations are discretized along a one-dimensional computational grid. A staggered grid, as presented by Harlow and Welch [23], allows for the treatment of coupled pressure and normal velocity fields (required due to the wide Mach number variance along the domain). Due to varying flow direction resulting from mass injection, upwind formulation of derivatives are required for numerical stability. The resulting system of equations can be represented using a block-tridiagonal residual Jacobian matrix and is solved using Newton-Raphson iterations. Determination of the shock standoff distance and evaluation of the absorbed state at the surface are handled by incorporating additional equations as Schur complements. This maintains the efficiency of the block-tridiagonal Jacobian

while incorporating the complexity of the unified domain. Wall catalycity is handled by the definition of wall reaction rates. Fully catalytic (FC) and non-catalytic (NC) conditions are considered in this work. Park's two temperature model [24, 25] is used to model the non-equilibrium thermochemistry of the shock layer gas.

B. Heat transfer and transport properties

Heat and mass transfer are largely dependent on the conductive and diffusive qualities of the near wall gas mixture. The solver employs rigorous multicomponent definitions for transport property coefficients following the framework of Hirschfelder *et al.* [26]. Transport coefficients represent statistical averages of changes in trajectories of the gas molecules following collisions. The values of the transport properties depend on translational temperature, electron temperature (for the electron-heavy collisions), molecular masses, specific heats, and collision integrals. These are coupled, as higher temperature flows will result in dissociation and ionization (changing chemical compositions). In the context of transpiration cooling, the injectant has the most important effect on transport properties. Lighter gases are both more conductive and more diffusive than heavier species. The surface heat transfer in hypersonic flows with mass injection is primarily composed of conductive and diffusive components. Gas-surface radiative heat flux is negligible for the conditions considered in this study (the freestream velocity is too low), and the shock layer is treated as optically thin. Conductive heat flux, q_c, arises from temperature gradients within the gas mixture. According to Fourier's law of heat conduction, this flux is directly proportional to the local temperature gradient, ∇T, and the thermal conductivity of the gas mixture, k:

$$q_c = -k\nabla T \tag{6}$$

The diffusive heat flux, q_d, arises from the transport of individual species within the gas mixture, each carrying its specific enthalpy. It is defined using Fick's law with multicomponent diffusion:

$$q_d = \sum_{s=1}^{n_s} h_s J_s \tag{7}$$

where h_s is the specific enthalpy of species s, and J_s is the diffusive mass flux of species s.

Multicomponent diffusion was implemented to understand the interaction between the injectant and shock layer and how these mechanisms affect diffusive mass and heat flux. The diffusive mass flux is evaluated using the Stephan-Maxwell equation [27]:

$$J_i = \frac{\rho M_i}{M^2} \sum_{j \neq i} M_j D_{ij} \nabla y_j \tag{8}$$

Definitions for coefficients of multicomponent diffusion come from Hirschfelder *et al.* [26]. The coefficient of diffusion

in a binary mixture is defined:

$$\mathscr{D}_{ij} = 2.6 \times 10^{-7} \frac{\sqrt{T^3(M_i + M_j)/2M_iM_j}}{p\sigma_{ij}^2 \Omega_{ij}^{(1,1)}(kT/\varepsilon_{ij})} \tag{9}$$

The binary coefficients of diffusion in a multicomponent mixture are then constructed, as presented by Sutton and Gnoffo [27]:

$$D_{ij} = \frac{M}{M_j} \frac{F^{ji} - F^{ii}}{|F|} \tag{10}$$

$$F_{ij} = \frac{y_i}{\mathscr{D}_{ij}} + \frac{M_j}{M_i} \sum_{k \neq i} \frac{(y_k)}{\mathscr{D}_{ik}} \quad \text{for } i \neq j \tag{11}$$

$$F_{ii} = 0 \tag{12}$$

The denominator $|F|$ is the determinant of the matrix F, F^{ji} are the transposed cofactors of the matrix F, which can be defined for n species:

$$F^{ji} = (-1)^{i+j} \begin{vmatrix} 0 & F_{12} & \cdots & F_{1n} \\ F_{12} & F_{22} & \cdots & F_{2n} \\ \vdots & \vdots & & \vdots \\ F_{1n} & F_{2n} & \cdots & F_{nn} \end{vmatrix} \tag{13}$$

Thus, while the pure binary diffusion coefficients are not dependent on concentration, the coefficients of diffusion that define diffusive mass flux are.

Fairbanks and Wilke [28] provide a definition for effective diffusion coefficient that describes the ability of a given species to diffuse into a gas mixture. This definition is useful for the analysis of diffusive processes. The effective diffusion of coefficient for species i into a mixture is given:

$$D'_{i,mix} = \frac{1 - y_A}{\sum_{j \neq i} \frac{y_j}{D_{ij}}} \tag{14}$$

C. Heat and mass Stanton numbers

Transpiration cooling is typically assessed by its ability to reduce both surface heat transfer and surface mass transfer. The non-equilibrium solution method presented above provides an accurate description of the approaching shock layer gas, capturing the thermochemical state and flow properties near the surface. Additionally, multi-component transport

property evaluations enable accurate modeling of the injectant-shock layer interaction near the surface. It is useful to employ dimensionless parameters. The blowing ratio, F, normalizes the injected mass flux against the freestream mass flux.

$$F = \frac{\rho_{inj} u_{inj}}{\rho_\infty u_\infty} \tag{15}$$

The heat transfer Stanton number, St, is the heat flux, $\dot{q}_w$, normalized by the external flow enthalpy flux. The heat Stanton number comprises the conductive and diffusive components of heat flux.

$$B_h = \frac{F}{St_{h0}} \tag{16}$$

$$St = \frac{\dot{q}_w}{\rho_\infty u_\infty (H_0 - h_w)} \tag{17}$$

$$H_0 = h_\infty + \frac{1}{2} u_\infty^2 \tag{18}$$

The mass Stanton number, St_m, is the diffusive mass flux of the injectant normalized by the product of the freestream mass flux and the injectant concentration difference.

$$B_m = \frac{F}{St_{m0}} \tag{19}$$

$$St_m = \frac{\rho_s D_s \nabla y_{inj}}{\rho_\infty u_\infty \Delta y_{inj, w-\infty}} \tag{20}$$

A reduction in the mass Stanton number indicates the injectant's ability to impede the diffusion of shock layer species towards the wall. The definition of mass Stanton number with the injectant simplifies the description of the transport of shock layer species to the wall, as the net diffusive flux of the shock layer species must equal that of the injectant.

There exist several approaches for determining the no-blowing Stanton number. The porous section can be removed altogether, using the heat flux for an impermeable plate, as is often done for stagnation flow experiments. The mass flux at the plenum can be set to zero, which results in flow permeating within the porous section. This is often done for flat plate experiments where in-flow to the porous section is minimal. Finally, a condition that the mass flux at the surface is zero can be enforced. This describes a scenario where the radial flow velocity is zero at the surface. This is only meaningfully different for stagnation line flow when the porous medium is of moderate to high permeability (significant transport of shock layer into porous section) and/or the leading edge is considerably curved (tangential mass loss). In this work, the latter method is used but is not found to appreciably affect results.

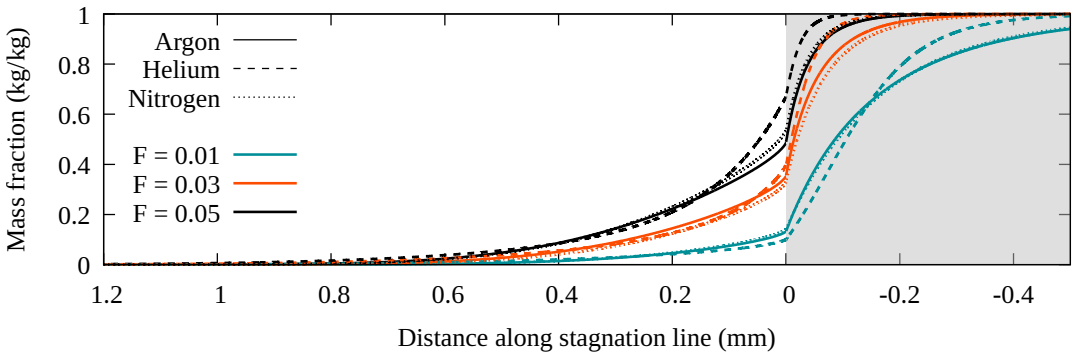

Fig. 2 Injectant mass fraction profiles for varying blowing ratios with different injectants for 50 km, 5 km/s, 25 mm nose radius, NC, and T_w = 300 K case.

III. Results and Discussion

The efficacy of transpiration cooling is evaluated through its impact on both surface heat and mass transfer. Understanding the effect of mass injection for cooling applications requires analysis across a wide parameter space, where thermochemical and flow properties are appreciably altered. In this section, results from transpiration cooling simulations are presented and analyzed. The discussion explores the influence of key parameters such as injectant composition, surface properties, freestream conditions, and leading-edge radius. The breakdown of heat flux components, the formation of the coolant barrier, and the role of transport properties are examined to provide a comprehensive understanding of the mechanisms driving cooling performance. Additionally, correlations for heat and mass Stanton number reduction are presented, offering insights into the effectiveness of transpiration cooling across a wide parameter space.

A. Injectant

The choice of injectant influences heat and mass transfer. Transport properties of the injectant impact the near wall temperature gradient as well as the ability of the shock layer gas to reach the surface. Generally, injectants with smaller molecular weights are more conductive and diffuse through mixtures more easily. Further, specific heat increases for lighter gases. Thus, mixing of a light injectant with the hot shock layer mixture generally reduces the temperature gradient at the mixture interface. This can generally be considered where the radial velocity is reduced to zero, and the interaction between the injectant and shock layer is described by diffusive mixing. The diffusive effects, however, complicate cooling effectiveness at low blowing. Figure 2 shows the concentration profiles of different injectants for varying blowing ratios. While helium is able to diffuse furthest into the shock layer, its concentration at the wall is lowest for the low blowing case. This indicates that the helium is able to diffuse into the shock layer but not block the transport of shock layer species to the wall as effectively as heavier injectants. The trend reverses at moderate to high blowing ratios, where the helium concentration at the wall is significantly higher than that of nitrogen, while

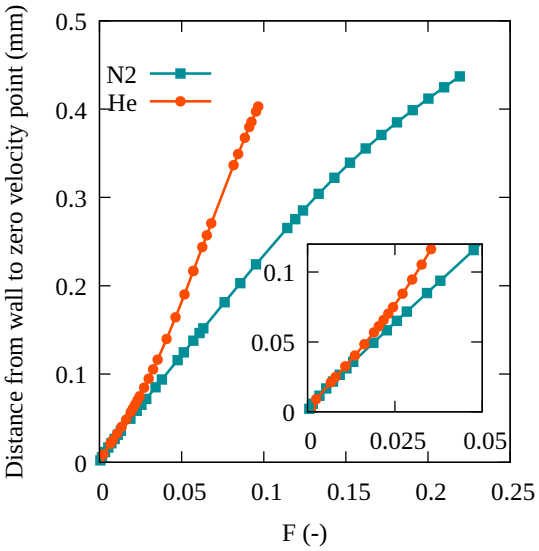

Fig. 3 Distance from wall to zero radial velocity point (where u = 0 m/s) for varying blowing ratios with He and N2 injection for 50 km, 5 km/s, 25 mm nose radius, NC, and Tw = 300 K case.

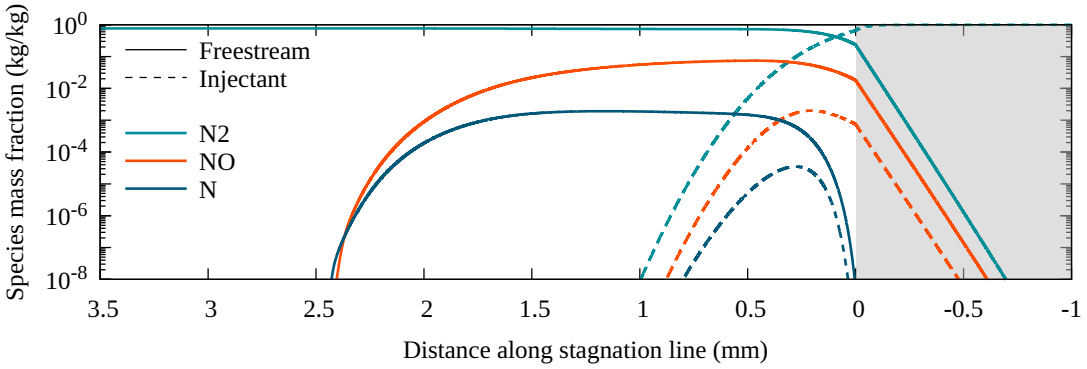

Fig. 4 Nitrogen species profiles for 50 km, 5 km/s, 25 mm nose radius, NC, T_w = 1000 K, N2 injectant, and F = 0.04 .

simultaneously pushing the edge of the coolant barrier farther away from the wall. For heavy injectants, this location grows consistently from low blowing. However, for lighter injectants, the widening of the coolant barrier is relatively similar at low blowing, until it outpaces heavy injectants at some critical amount of blowing. This effect is shown in Figure 3, where the distance from the wall to the zero radial velocity point is shown to be significantly larger for helium than nitrogen at moderate to high blowing.

Inert injectants are often prioritized, especially when oxidation is relevant. Figure 4 displays the relative concentrations of nitrogen-containing species whose nitrogen atoms are provided by either the freestream gas mixture or the injectant. For this conservative case, with elevated wall temperature of 1,000 K, the proportion of atomic nitrogen and nitric oxide generated through the provision of nitrogen atoms from the injectant is never greater than 1% of the total mass fraction of the species. Thus, so long as the injectant inside and near the wall is below reaction temperatures, the injectant will not appreciably contribute to near wall chemistry. This has implications for the choice of injectant, as the cooling effectiveness (under these conditions) is not necessarily altered by the chemical properties of the injectant.

B. Surface properties

The surface properties of the leading edge alter the near-wall environment and thus impact the effectiveness of transpiration cooling. The surface properties considered in this study are wall catalycity and isothermal wall temperature. While the solver is capable of handing non-isothermal wall conditions, such cases are beyond the scope of this paper. Figure 5 demonstrates the effects of surface properties on heat Stanton number. Although the local enthalpy of the flow is increased with higher wall temperature, the temperature gradient at the wall is reduced. This reduction in the gradient decreases the conductive component of heat flux, leading to an overall reduction in heat transfer and, consequently, a lower Stanton number. Conversely, a fully catalytic wall increases the diffusive component of heat flux. This results from the forced recombination of dissociated species which diffuse to the wall. For the cases studied here, atomic oxygen is the major contributor. As a result, the overall heat transfer increases due to the additional energy contributed by the enthalpy of formation of the recombined species. At low blowing, significant concentrations of shock layer species reach the surface and undergo recombination on the catalytic wall, altering the near-wall chemical composition and increasing the molecular weight of the gas mixture. At moderate to high blowing, the coolant barrier prevents most shock layer species from reaching the wall, resulting in similar near-wall gas compositions for both catalytic and non-catalytic conditions. Thus, the catalytic effects are most pronounced at low blowing ratios, where the coolant barrier is not yet fully developed.

Figure 6 provides a comparison of the distance to the zero velocity point for varying blowing ratios with N2 injection for 50 km, 5 km/s, and varying surface properties. Higher wall temperatures reduce the local density of the gas mixture, allowing for easier diffusion of the injectant into the shock layer. This effect persists regardless of blowing ratio. Conversely, the catalytic and non-catalytic cases show divergence only at low blowing ratios. At moderate to high

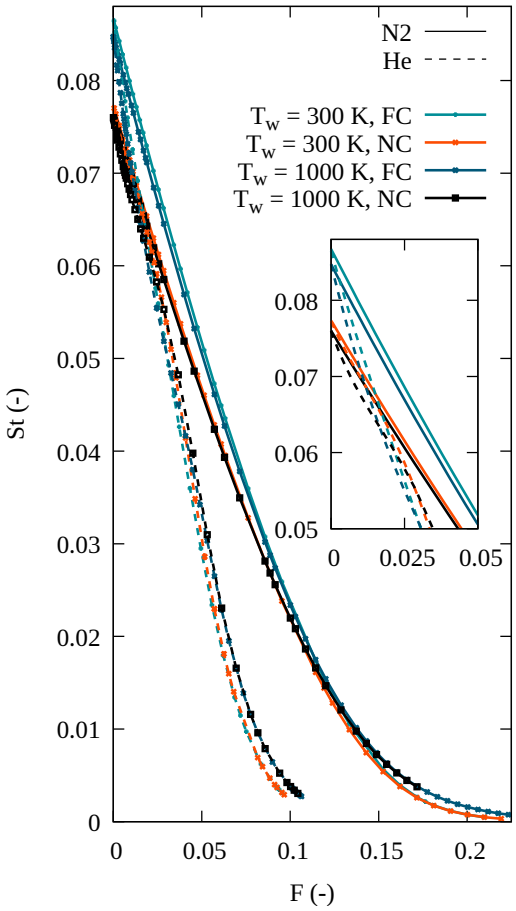

Fig. 5 Stanton number for varying blowing ratios with varying surface properties and He and N2 injection for 50 km, 5 km/s, and 25 mm nose radius case.

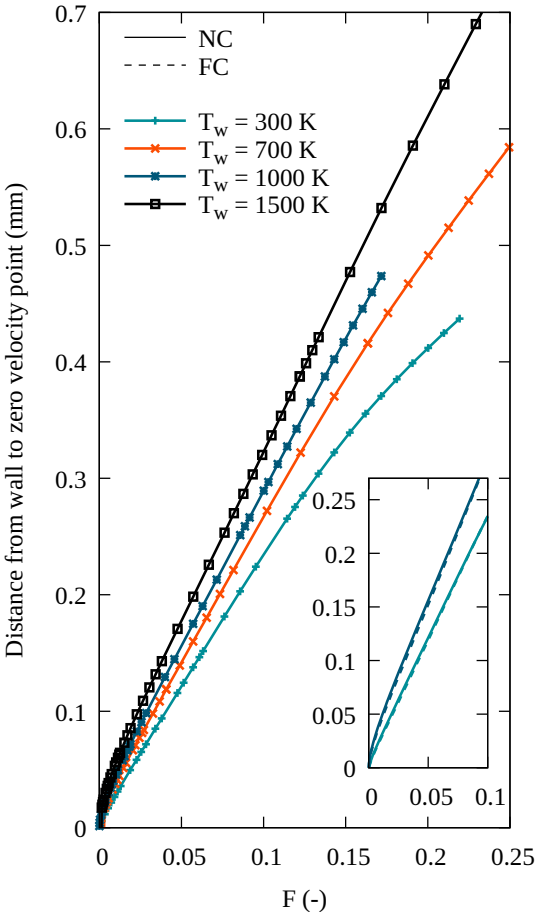

Fig. 6 Distance to zero velocity point for varying blowing ratios with varying surface properties for 50 km, 5 km/s, 25 mm nose radius, and N2 injection case.

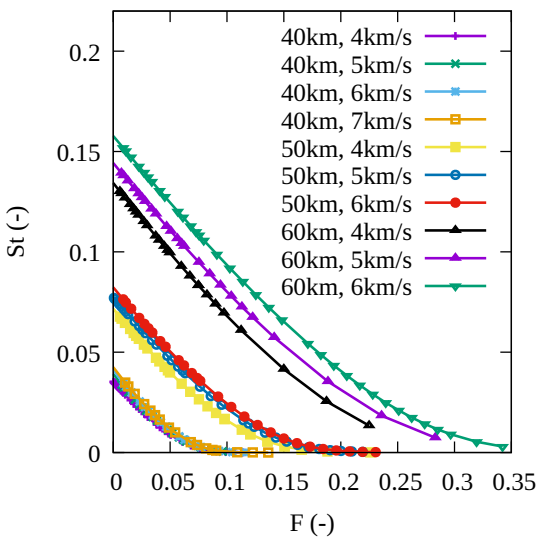

Fig. 7 Stanton number for varying blowing ratios with different freestream conditions for 25 mm nose radius, NC, T_w = 300 K, and N2 injection case.

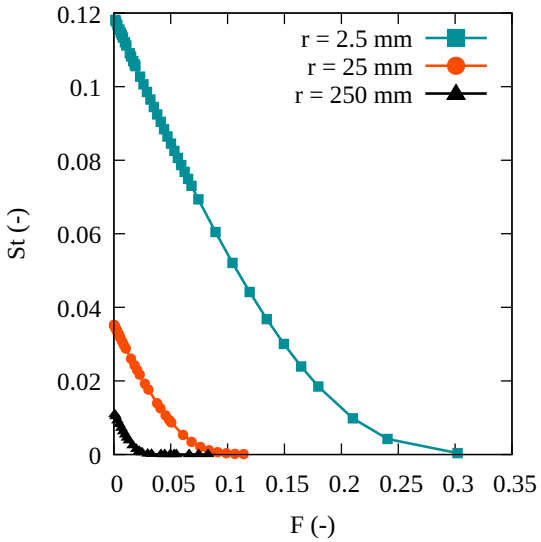

Fig. 8 Stanton number for varying blowing ratios with different nose radii for 40km, 4km/s, NC, T_w = 300 K, and N2 injection case.

blowing ratios, the coolant barrier becomes sufficiently robust that recombining species no longer reach the wall in significant concentrations. These trends highlight the more significant importance of wall temperature in controlling cooling performance. The implications of wall catalycity are mitigated with increased blowing ratios.

C. Freestream conditions and radius

Freestream conditions affect the total enthalpy and chemical properties of the shock layer flow. Figure 7 displays heat Stanton number variation with blowing ratio for nitrogen injection across different altitudes and velocities. Increasing altitude has a more pronounced effect on Stanton number than increasing velocity. The impact of velocity becomes more pronounced at higher altitudes due to the coupling between density and velocity effects. Velocity primarily affects the total enthalpy and degree of dissociation through the shock. At lower altitudes (higher densities), frequent collisions drive the gas mixture toward equilibrium regardless of the initial shock conditions. However, at higher altitudes, the reduced collision frequency allows non-equilibrium effects to persist through the shock layer to the wall, which generally increases Stanton number through heat transfer by dissociated species. Varying freestream conditions do not significantly change the form of the Stanton number reduction with increased blowing, indicating that differences between cases are consistent across blowing.

For given freestream conditions, the radius impacts the thermochemical state of the gas arriving at the wall by affecting the thickness of the shock layer. Figure 8 displays heat Stanton number variation with blowing ratio with varying nose radii. Generally, a small nose radius reduces the shock standoff distance, allowing the shock layer gas to reach the wall with a higher temperature and a larger degree of dissociation. Even high-enthalpy flows with significant

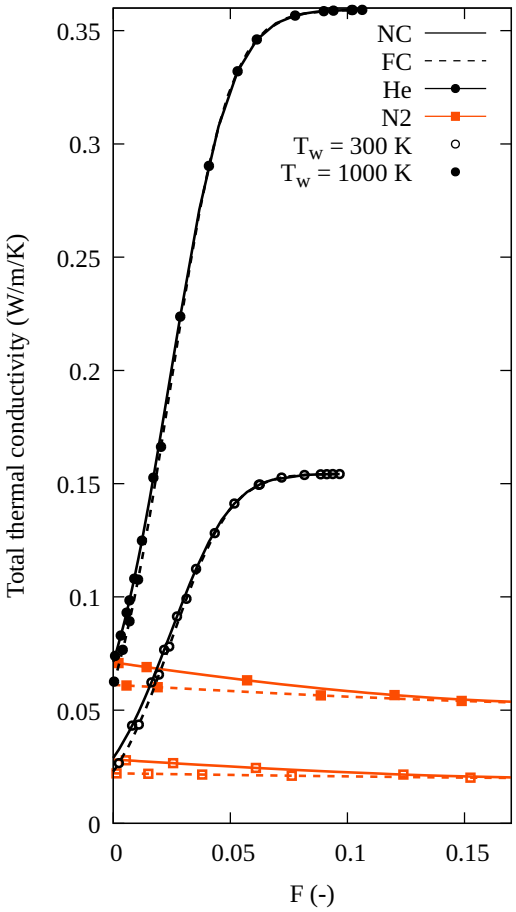

Fig. 9 Total thermal conductivity for varying blowing ratios with He and N2 injection for 50 km, 5 km/s, 25 mm nose radius case.

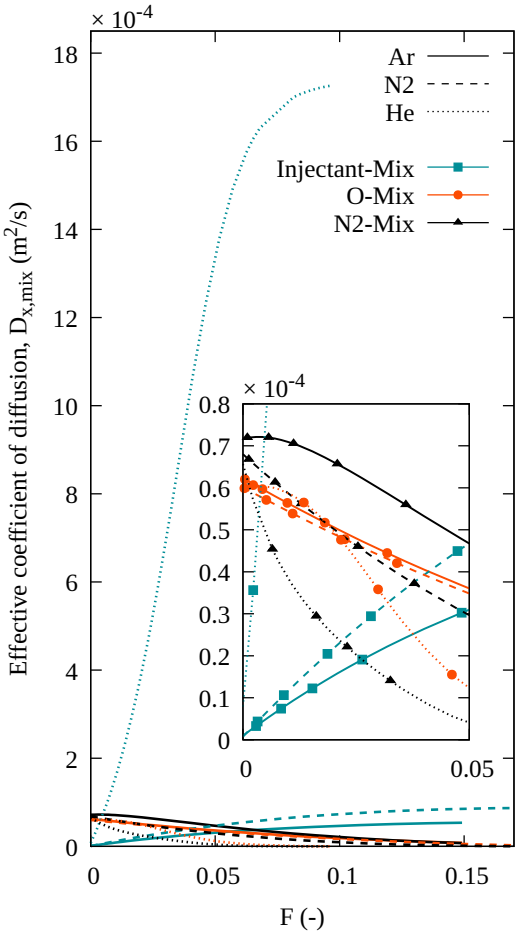

Fig. 10 Effective coefficient of diffusion for varying blowing ratios and different injectants for 50 km, 5 km/s, 25 mm nose radius, NC, and T_w = 300 K case.

regions of non-equilibrium may relax to equilibrium near the wall if the leading edge radius is large enough. Conversely, for very small radii, the leading edge may experience a frozen shock layer gas. Profiles displaying this effect can be found in the work by Brody *et al.* [2].

D. Transport properties and heat flux components

This section presents an analysis of the transport properties and heat flux components that govern the effectiveness of transpiration cooling. The interplay between conduction, diffusion, and injectant and surface properties is explored to provide insights into the mechanisms driving cooling performance.

For the diffusive fluxes, individual species' ability to penetrate through the wall (carrying energy through its specific enthalpy) is mainly controlled by the size of the injectant molecules. It is worth considering the individual behavior of component species present in the shock layer. Implications for oxidation indicate that injectants should be additionally

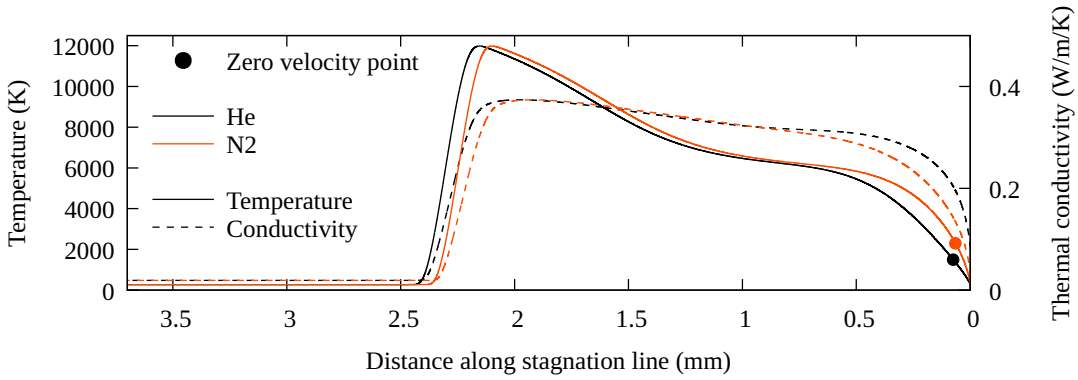

Fig. 11 Temperature and total thermal conductivity profiles with He and N2 injection for 50 km, 5 km/s, NC, T_w = 300 K, and F = 0.023 (B_h = 0.3) case.

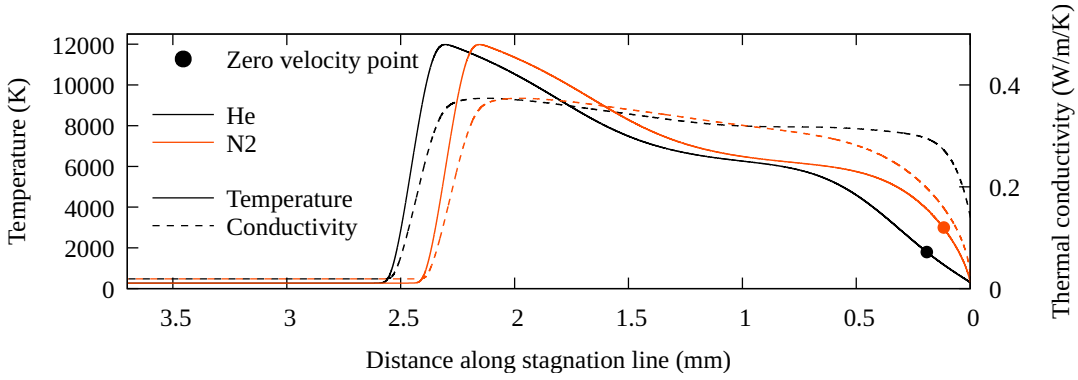

Fig. 12 Temperature and total thermal conductivity profiles with He and N2 injection for 50 km, 5 km/s, NC, Tw = 300 K, and F = 0.046 (B_h = 0.6) case.

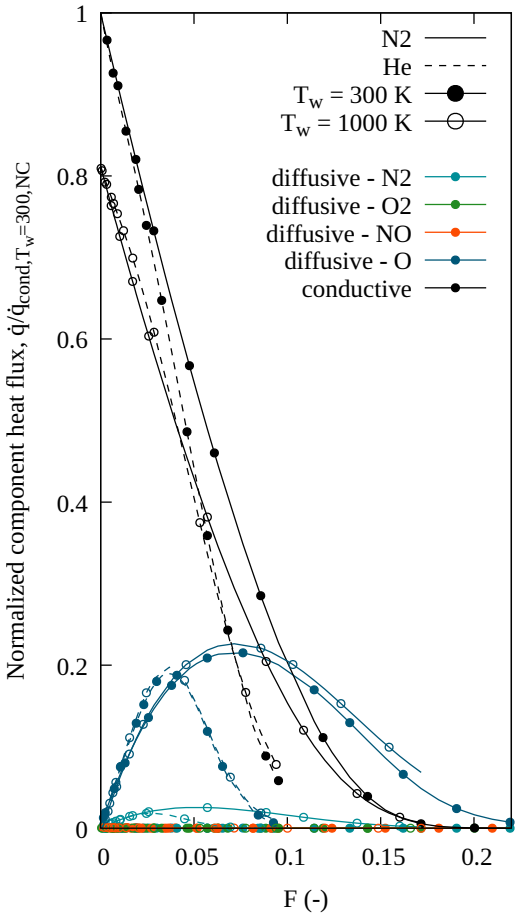

Fig. 13 Conductive and diffusive components of heat flux for varying blowing ratios, different wall temperatures, and He and N2 injection for 50 km, 5 km/s, 25 mm nose radius, and NC case.

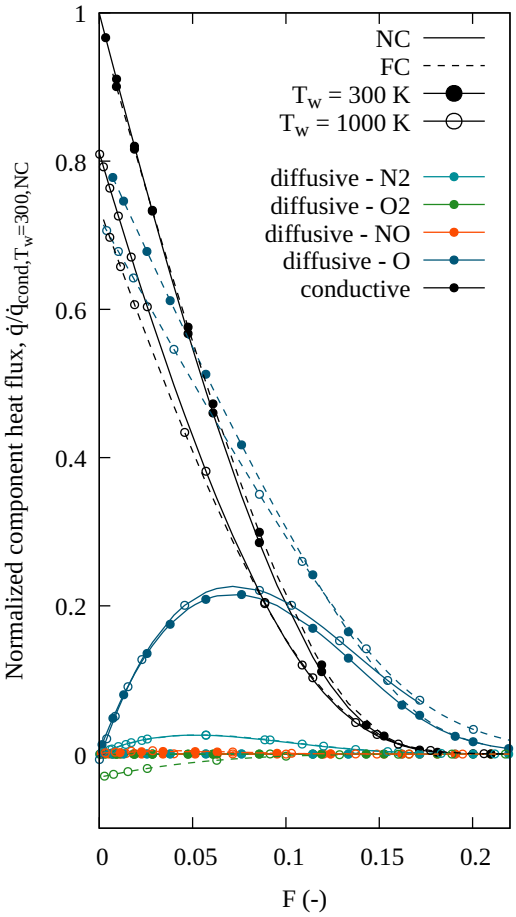

Fig. 14 Conductive and diffusive components of heat flux for varying blowing ratios and different surface properties for 50 km, 5 km/s, 25 mm nose radius, and N2 injection case.

inspected on their ability to block detrimental species. As is the case for the diffusive contribution to heat flux, molecular weight controls a molecule's ability to penetrate through the thermal barrier to the surface. As concentration gradients dominate diffusion processes, profiles for diffusive flux allow a visualization of thermal barrier creation. With no blowing, the shock layer gas reaches the wall unimpeded, and steady state simulations enforce zero net diffusive flux. As blowing increases, penetration of the injectant into the shock layer begins to impede molecules in the shock layer, resulting in a concentration gradient near the wall. Eventually, the injectant is able to completely block diffusive flux of all shock layer species.

Figure 9 shows the total thermal conductivity for varying blowing ratios with He and N2 injection for 50 km, 5 km/s, and a 25 mm nose radius. The total thermal conductivity increases dramatically with low blowing for the helium injectant case, before stabilizing at the pure helium value for the given wall temperature. The change with in total thermal conductivity is much smaller with low blowing for the nitrogen injection case and even smaller when a catalytic wall is enforced (as the surface chemical composition is more stable). Figure 10 shows the effective coefficient of diffusion for varying blowing ratios at 50 km, 5 km/s, and 25 mm nose radius. As expected, the effective diffusion coefficient is significantly larger for helium than for nitrogen. However, at low blowing, the effective diffusion coefficient of atomic oxygen is also larger for helium than for argon and nitrogen. Helium's effect on the ability of shock layer species to diffuse to the wall is muted compared to its effect on conductivity, indicating that cooling at low blowing for helium is possibly mitigated by the immediate conductive detriment and delayed diffusive benefit. Thus, while helium easily diffuses into the shock layer, it also allows for the lighter shock layer species to diffuse to the wall. This demonstrates the counteracting elements of helium injection relative to cooling at relatively low blowing ratios. It should be noted that the catalytic cases experience a smaller initial conductivity but align with their non-catalytic counterpart at moderate to high blowing.

Figures 11 and 12 present translational temperature and thermal conductivity profiles for low and moderate blowing, respectively. These profiles demonstrate the immediate impact of a light gas on conductivity. The development of the coolant barrier is more delayed, as evidenced by the location of the zero velocity point near that of the nitrogen case for low blowing. The zero velocity point is 14% farther into the shock layer for helium injectant in the low blowing case, whereas it is 49% farther for the high blowing case. While a light gas (with a larger specific heat) is better able to convect heat away from the surface, the generation of the coolant barrier and impact on the mixture conductivity are interconnected. At the interaction between the coolant and the shock layer, a light gas will reduce the temperature gradient, as thermal conductivity will be higher. When this interaction (the zero velocity point) is relatively far from the wall, the reduced thermal gradient augments the pre-wall cooling, as seen by the concave up temperature profile near the wall in Figure 12. However, if this point is near the wall, the increased conductivity of helium is exclusively detrimental.

Figure 13 illustrates the conductive and diffusive components of heat flux for varying blowing ratios with a non-catalytic wall. At low blowing ratios, the conductive component dominates the total heat flux due to the steep

temperature gradient near the wall. As blowing increases, the injectant displaces the hot shock layer gas near the wall, reducing the temperature gradient and, consequently, the conductive heat flux. This reduction in the conductive component is a key mechanism of transpiration cooling.

The diffusive component is influenced by both the transport properties of the gas mixture and the specific enthalpy of the species diffusing to the wall. The largest contributor to the diffusive heat flux is atomic oxygen, which has a high specific enthalpy. The diffusive component is relatively small at low blowing ratios but becomes more significant as blowing increases. The maximum magnitude of the diffusive heat flux relative to the conductive heat flux is similar across injectants, indicating the strength of light injectants is more dependent on the quick development of a coolant barrier rather than an enhanced ability to specifically stop transport of atomic oxygen.

Figure 14 compares the conductive and diffusive heat flux components for fully catalytic and non-catalytic wall conditions. The catalytic wall forces the recombination of dissociated species, such as atomic oxygen, at the surface. This recombination releases additional energy, increasing the diffusive heat flux. As a result, the total heat flux is higher for catalytic walls compared to non-catalytic walls, particularly at low blowing ratios where dissociated species can still reach the wall in significant concentrations.

The results indicate that the relative contributions of conductive and diffusive heat flux depend strongly on the blowing ratio, wall catalycity, and injectant properties. At low blowing ratios, the conductive component dominates, while at higher blowing ratios, the diffusive component becomes more significant. For catalytic walls, the diffusive component is enhanced due to the recombination of dissociated species, which increases the overall heat flux to the surface. Further, helium injection results in a conductive heat flux component that is non-monotonic in curvature, whereas the heavier injectants are uniformly concave up. This is not true for the diffusive components, which show no meaningful shape difference between the injectants. These trends highlight the importance of understanding the interplay between conduction and diffusion in designing effective transpiration cooling systems.

E. Stanton number reduction

This section presents the reduction in heat and mass Stanton number across a wide parameter space relevant to transpiration cooling. A global correlation is provided, and freestream conditions, leading-edge radius, and surface effects are considered. The correlation is compared to existing correlations in the literature from Marvin and Pope [15], Yoshikawa [29], and Mills and Wortman [12]. It should be noted that accuracy of these correlations should be prioritized at low blowing ratios, as high blowing ratios are unrealistic for applications due to complications to boundary layer structure [30, 31].

It is useful to present a correlation that is accurate across a wide parameter space and does not require case-specific values. Based on the results and analysis presented in this study, the following correlation was determined for the reduction in Stanton number with blowing ratio:

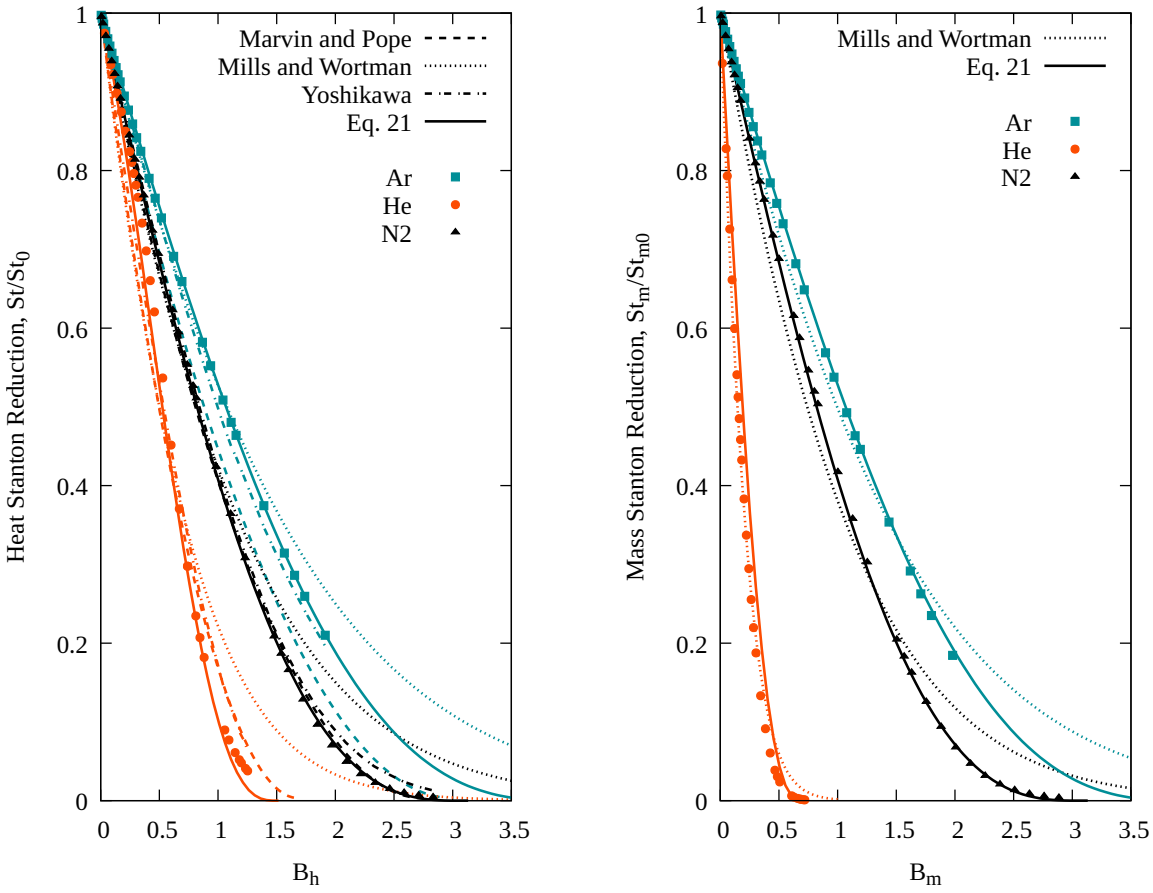

(a) Heat transfer

(b) Mass transfer

Fig. 15 Stanton number reduction for varying blowing parameter and different injectants for 50 km, 5 km/s, 25 mm nose radius, NC, and T_w = 300 K case with comparisons to existing correlations.

$$\frac{St}{St_0} = \frac{St_m}{St_{m0}} = (1 - B_*)^3 (1 + B_*)^{c_2} \tag{21}$$

$$B_* = \frac{B}{c_1} \left(\frac{M_\infty}{M_{inj}} \right)^{0.75/c_2} \tag{22}$$

The exponent 0.75 is similar to the coefficient n presented by Marvin and Pope [15]. The coefficient c_1 is the blowing parameter required to completely impede heat and mass transfer for injection by a gas into itself. For air, this value is found to be 3.15. While such large blowing parameters will likely disrupt the consistent behavior of cooling [30, 31], it is useful to ground the correlation to such nominal values. It should be noted that the Swann and Pittman [5] and Marvin and Pope [15] correlations implicitly follow this methodology in the use of a polynomial expression. The coefficient c_2 introduces an inflection point in the heat Stanton reduction curve, seen when helium is used as an injectant. As such, its value is 2 for light gases (helium) and 1 for heavy gases (argon and nitrogen) when considering heat Stanton number. For mass Stanton number, the value of c_2 is always 1. The characterization of the inflection point for helium injection is not considered in previous correlations but is seen in the numerical results of Mills and Wortman [12] as well as the experimental results of Pappas and Lee [7]. Figure 15 displays the presented correlation relative to simulation results as well as correlations from the literature applied to the same test case.

A mass/heat transfer analogy is generally appropriate for heavier injectants. However, for lighter injectants like helium, the analogy breaks down, particularly at low blowing ratios. This divergence is likely due to helium's high thermal conductivity, which diminishes its cooling effectiveness despite its superior diffusive properties. The inflection point in reduction for helium is attributed to the delayed effectiveness of its diffusive barrier coupled with its increased conductivity.

Results are now presented across a wide range of conditions. The presented correlation performs reasonably well and better than those from literature for the simulation results. It is useful to understand how this correlation may underpredict or overpredict cooling effectiveness. Figure 16 illustrates the reduction in heat and mass Stanton numbers for varying freestream conditions. Subfigure (a) Heat transfer shows the heat Stanton number reduction, while subfigure (b) Mass transfer presents the mass Stanton number reduction. The no-blowing Stanton number effectively normalizes freestream effects, allowing for consistent trends across different altitudes and velocities. At low blowing ratios, the reduction is primarily influenced by the wall conditions and the chemical composition of the near-wall shock layer gas. At higher blowing ratios, the injectant composition becomes the dominant factor, as the coolant constitutes the majority of the near-wall gas mixture.

The influence of leading-edge radius on Stanton number reduction is shown in Figure 17. Larger radii allow for greater thermochemical relaxation of the shock layer gas, reducing the heat flux to the wall. Conversely, smaller radii

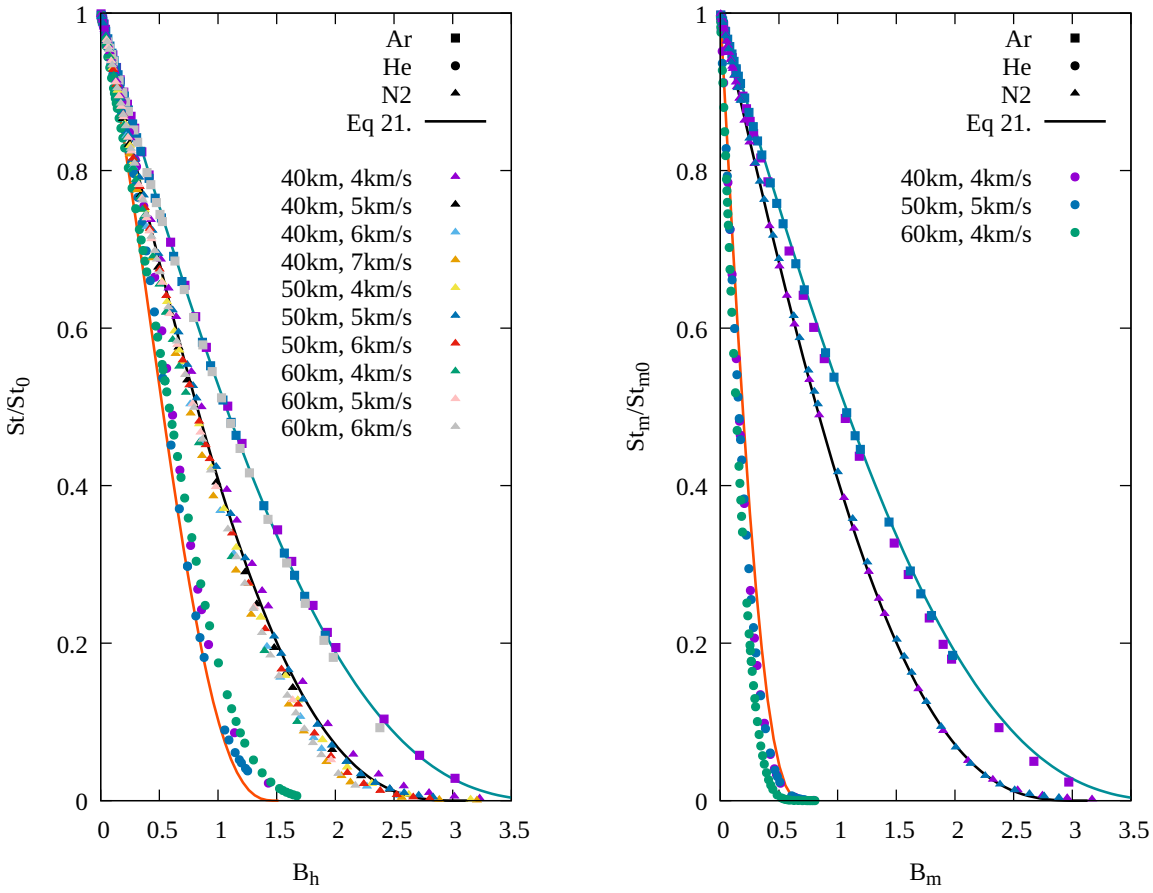

(a) Heat transfer

(b) Mass transfer

Fig. 16 Stanton number reduction for varying blowing parameter and different freestream conditions and injectants for 25 mm nose radius, NC, and T_w = 300 K case.

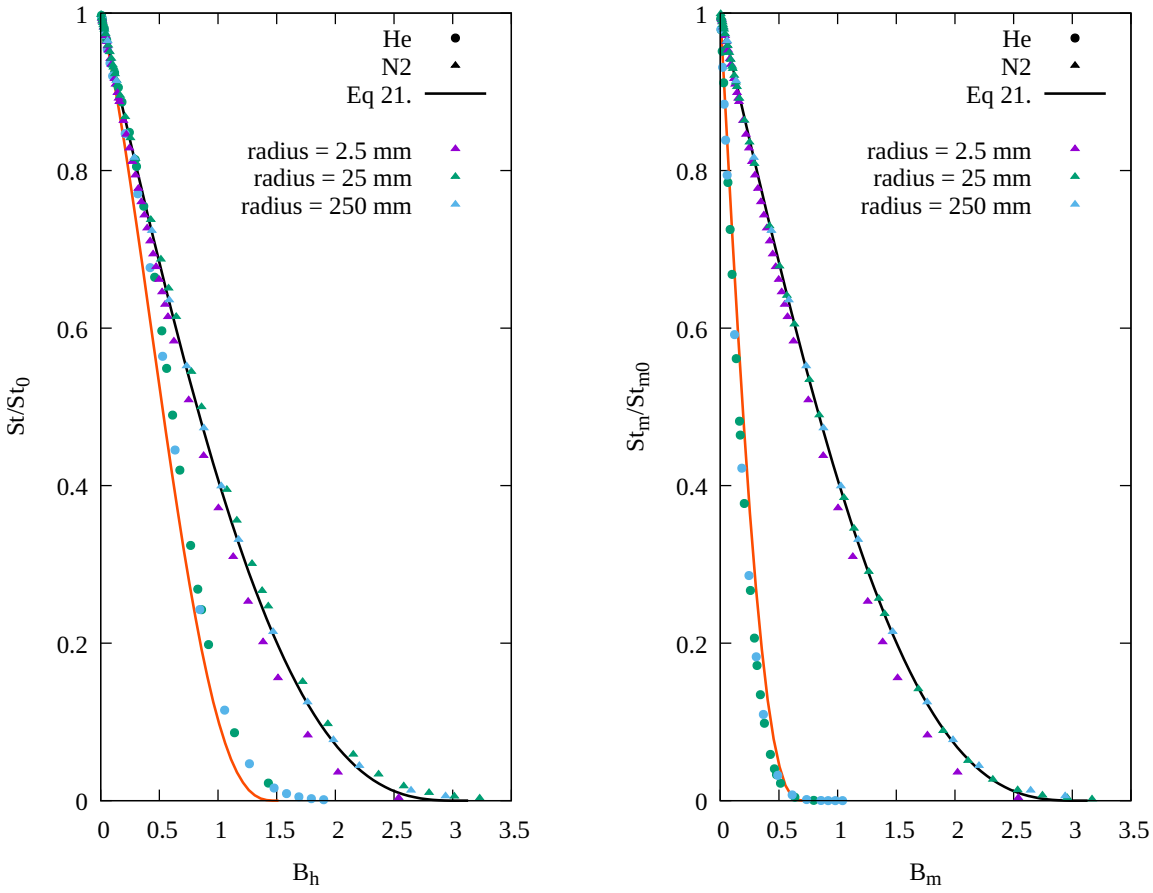

(a) Heat transfer

(b) Mass transfer

Fig. 17 Stanton number reduction for varying blowing parameter and different nose radii and He and N2 injection for 40 km, 4 km/s, NC, and T_w = 300 K case.

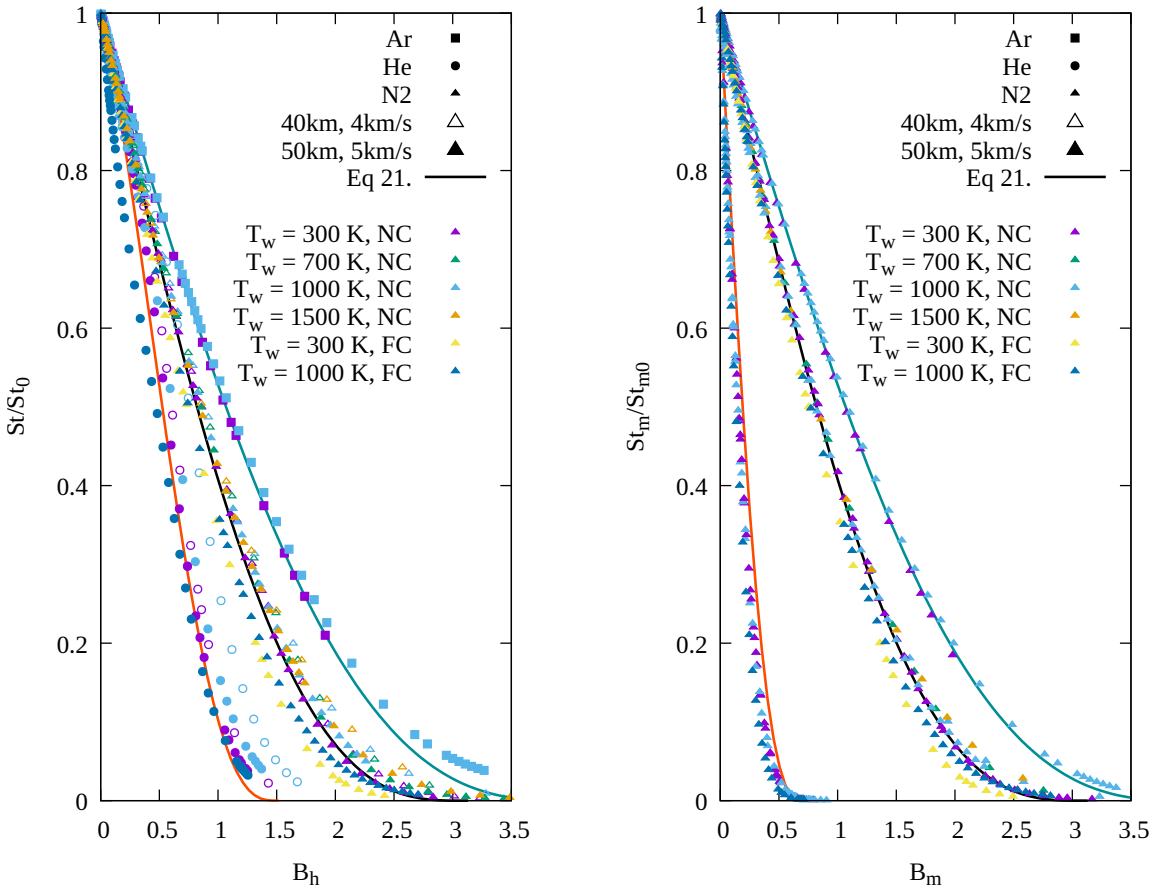

(a) Heat transfer

(b) Mass transfer

Fig. 18 Stanton number reduction for varying blowing parameter and different freestream conditions, surface conditions, and injectants for 25 mm nose radius case.

result in a thinner shock layer and higher heat flux due to a higher thermal gradient. Additionally, larger degrees of non-equilibrium near the wall reduce density and increase the number densities of atomic species that can recombine at the wall, thus increasing surface heat flux further. The trends in reduction with blowing ratio are consistent across radii, but the magnitude of the reduction depends on the initial shock layer conditions.

Surface properties, including wall temperature and catalycity, also play a significant role in Stanton number reduction, as shown in Figure 18. At low blowing ratios, catalytic walls enhance the diffusive heat flux due to the recombination of dissociated species, increasing the overall heat transfer. However, at moderate to high blowing ratios, the coolant barrier becomes sufficiently thick to prevent recombining species from reaching the wall, diminishing the catalytic effects. Wall temperature, on the other hand, affects cooling performance across all blowing levels by altering the thickness of the coolant barrier and the local temperature gradient.

The results presented here highlight the interplay between freestream conditions, surface properties, and injectant characteristics in determining the effectiveness of transpiration cooling. The global correlation developed in this study provides a useful tool for predicting reduction across a wide range of conditions, enabling more efficient design and optimization of transpiration cooling systems.

F. Mars

To extend the analysis beyond Earth's atmosphere, results for a representative Mars entry condition are also considered. For simplicity and convenience in this study, the thermochemical model proposed by Park *et al.* [25] is utilized. While there is reason to believe that this model may not be entirely accurate for all Mars entry conditions [32], it provides a widely referenced framework and serves as a suitable generic test case for evaluating transpiration cooling performance. Validation for the implementation of the thermochemical model was conducted using a test case presented by Park *et al.* [25] and is shown in Figure 19.

Transpiration cooling simulations were then performed for the same Mars atmospheric conditions as the validation case, considering injection of molecular nitrogen. The resulting heat Stanton number reduction as a function of the blowing parameter is displayed in Figures 20 and 21. The correlation presented, including the molecular weight correction, reasonably replicates cooling for these Mars-specific conditions. The value for c_1 is found to be 4.5. It should also be noted that injection with CO2 will not be consistent due to the high reactivity of CO2 at the near-wall temperatures (which will result in a cooling effect from endothermic dissociation reactions). The applicability of the correlation supports the conclusions drawn from work by Marvin and Pope [15] and Yoshikawa [29], which suggested that altering the freestream gas composition does not significantly affect cooling effectiveness for a given blowing parameter, so long as the injectant is similar in molecular weight.

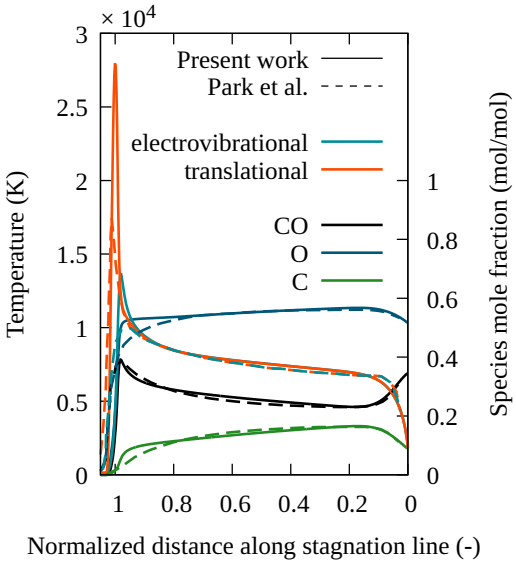

Fig. 19 Temperature and mass fraction profiles on stagnation line for 53 km, 8 km/s, and 1 m nose radius case in Mars atmosphere with comparison to Park *et al.* [25].

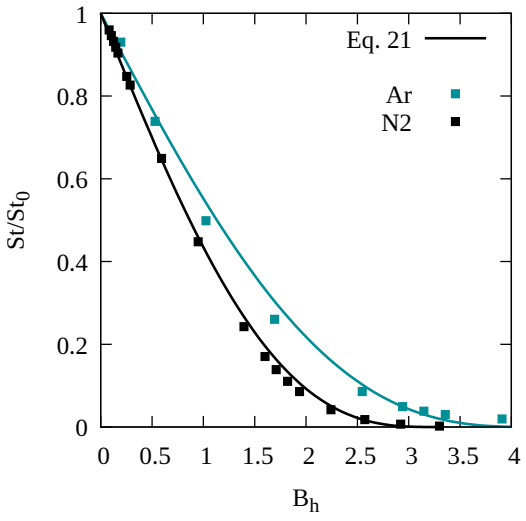

Fig. 20 Stanton number reduction for varying blowing ratios with N2 injectant for 53 km, 8 km/s, and 1 m nose radius case in Mars atmosphere.

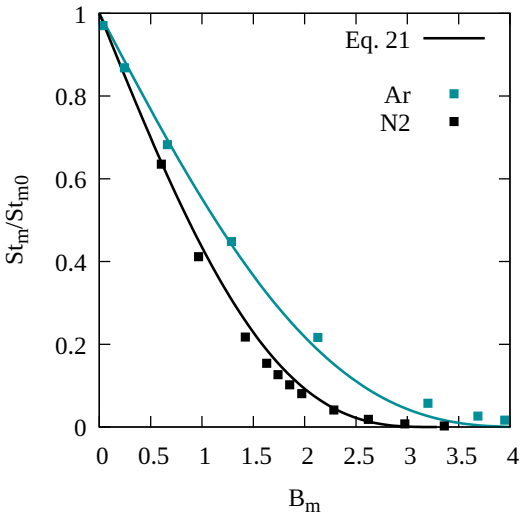

Fig. 21 Mass Stanton number reduction for varying blowing ratios with N2 injectant for 53 km, 8 km/s, and 1 m nose radius case in Mars atmosphere.

IV. Conclusions

This study investigates the effectiveness of transpiration cooling (TC) for stagnation point flows in hypersonic, thermochemical non-equilibrium conditions. The results provide a characterization of the key parameters influencing heat and mass transfer, including freestream conditions, leading-edge radius, injectant composition, and surface properties.

At low blowing ratios, cooling performance is dominated by wall conditions and the chemical composition of the near-wall shock layer gas. The no-blowing Stanton number effectively normalizes freestream effects, enabling consistent trends across varying altitudes and velocities. At higher blowing ratios, the injectant composition becomes the primary driver of cooling behavior, as the coolant constitutes the majority of the near-wall gas mixture. The transition from wall-dominated to injectant-dominated behavior underscores the importance of selecting an appropriate injectant and material for specific flight conditions.

Injectant properties, particularly molecular weight, play a critical role in determining cooling effectiveness. Lighter injectants, such as helium, exhibit superior diffusive properties but suffer from increased thermal conductivity, which diminishes their cooling performance at low blowing ratios. Conversely, heavier injectants, such as nitrogen, provide more consistent cooling performance across a range of blowing ratios. The inflection point in heat Stanton number reduction for helium is attributed to the delayed effectiveness of its diffusive barrier coupled with its increased conductivity. These results emphasize the need to consider transport properties when selecting an injectant. Inert gases are generally preferred due to a perceived benefit in protection against oxidation [9, 13]. However, it appears that low excitation of relatively cool injectant results in low reactivity with shock-layer, meaning reactive species can be employed without increased oxidation risk for some conditions. Low blowing behavior is dominated by the wall conditions and the chemical composition of the near wall shock layer gas.

Surface properties, including wall temperature and catalycity, significantly influence cooling performance. Higher wall temperatures reduce the local temperature gradient, decreasing conductive heat flux but also increasing the coolant barrier by enhancing diffusion into the shock layer. Fully catalytic walls increase the diffusive heat flux by forcing the recombination of dissociated species, such as atomic oxygen, at the surface. However, the catalytic effects are diminished at moderate to high blowing ratios, where the coolant barrier prevents recombining species from reaching the wall.

The study also demonstrates that freestream conditions and leading-edge radius affect the thermochemical state of the shock layer and, consequently, the surface heat and mass transfer. Higher altitudes and smaller radii exacerbate non-equilibrium effects, increasing the heat flux to the wall. Larger radii allow for greater thermochemical relaxation, reducing the heat flux. At very small radii, the frozen shock layer results in a more dissociated gas mixture near the wall. Cooling becomes slightly more effective, as the reduction in recombination reactions and mass transfer of dissociated species greatly reduces heat and mass Stanton number. Cooling performance, however, is relatively consistent across most freestream conditions and radii considered in this work.

Finally, the results validate the use of dimensionless parameters, such as the heat and mass Stanton numbers, for evaluating transpiration cooling performance. A mass/heat transfer analogy is generally appropriate for heavier injectants, but it breaks down for lighter injectants like helium due to their unique transport properties. The global correlation developed in this study provides a useful tool for predicting Stanton number reduction across a wide range of conditions, enabling more efficient design and optimization of transpiration cooling systems.

This work provides a detailed understanding of the mechanisms governing transpiration cooling in hypersonic flows. The findings underscore the importance of tailoring injectant selection, surface properties, and geometric design to specific mission requirements. Future work should focus on extending these results to non-isothermal wall conditions and exploring the coupling between surface material properties and cooling performance.

Acknowledgments

Samuel Brody gratefully acknowledges the Marshall Commission and the University of Oxford for financial support as well as the U.S. Air Force for their support of this effort. Justin Clarke gratefully acknowledges the Rhodes Trust for financial support.

References

[1] Rocher, M. E., Hermann, T., and McGilvray, M., "Oxidation Response of Transpiration-Cooled ZrB2 on a Hypersonic Stagnation Point," *Journal of Spacecraft and Rockets*, Vol. 59, 2022, pp. 1486–1495. https://doi.org/10.2514/1.A35309.

[2] Brody, S., Lau, K. S., Clarke, J., McGilvray, M., and Luca, D. M., "Numerical Simulation of Transpiration Cooling on Stagnation Line in Thermochemical Non-Equilibrium," *Journal of Thermophysics and Heat Transfer*, 2025. Under review.

[3] Blottner, F., "Viscous Shock layer at the Stagnation Point with Nonequilibrium Air Chemistry," *AIAA Journal*, Vol. 7, 1969, pp. 2281–2288. https://doi.org/10.2514/3.5528.

[4] Cheng, H., "The Blunt-Body Problem in Hypersonic Flow at Low Reynolds Numbers," , No. AF-1285-A-10, 1963.

[5] Swann, R. T., and Pittman, C. M., *Numerical analysis of the transient response of advanced thermal protection systems for atmospheric entry*, National Aeronautics and Space Administration, 1962.

[6] Howe, J. T., and Sheaffer, Y. S., "Mass addition in the stagnation region for velocity up to 50,000 feet per second," Tech. Rep. NASA-TR-R-207, 1964.

[7] Pappas, C. C., and Lee, G., "Heat transfer and pressure on a hypersonic blunt cone with mass addition," *AIAA Journal*, Vol. 8, No. 5, 1970, pp. 954–956. https://doi.org/10.2514/3.5801.

[8] Kaattari, G. E., "Effects of mass addition on blunt-body boundary-layer transition and heat transfer," Tech. Rep. NASA-TP-1139, 1978.

[9] Naved, I., Hermann, T., McGilvray, M., Ewenz Rocher, M., Hambidge, C., Doherty, L., Le Page, L., Grossman, M., and Vandeperre, L., "Heat Transfer Measurements of a Transpiration-Cooled Stagnation Point in Transient Hypersonic Flow," *Journal of Thermophysics and Heat Transfer*, Vol. 37, No. 2, 2023, pp. 296–308. https://doi.org/10.2514/1.T6610.

[10] Thompson, R., and Gnoffo, P., *Implementation of a Blowing Boundary Condition in the LAURA Code*, 2008. https://doi.org/10.2514/6.2008-1243.

[11] Sreekanth, S., and Reddy, N., "Correlations for injection cooled surface temperatures in compressible high speed flows," , 1997. https://doi.org/10.2514/6.1997-2577.

[12] Mills, A., and Wortman, A., "Two-dimensional stagnation point flows of binary mixtures," *International Journal of Heat and Mass Transfer*, Vol. 15, No. 5, 1972, pp. 969–987. https://doi.org/https://doi.org/10.1016/0017-9310(72)90234-7.

[13] Rocher, M. E., Hermann, T., McGilvray, M., and Gollan, R., "Correlation for Species Concentration on a Hypersonic Stagnation Point with Mass Injection," *AIAA Journal*, Vol. 60, 2022, pp. 2798–2809. https://doi.org/10.2514/1.J061159.

[14] Moyer, C. B., and Rindal, R. A., "An analysis of the coupled chemically reacting boundary layer and charring ablator. part 2-finite difference solution for the in-depth response of charring materials considering surface chemical and energy balances," Tech. Rep. NASA CR-1061, NASA, 1968.

[15] Marvin, J. G., and Pope, R. B., "Laminar convective heating and ablation in the Mars atmosphere." *AIAA Journal*, Vol. 5, No. 2, 1967, pp. 240–248. https://doi.org/10.2514/3.3948.

[16] Homann, F., "Einfluß großer zähigkeit bei strömung um zylinder," *Forschung auf dem Gebiet des Ingenieurwesens A*, Vol. 7, No. 1, 1936, pp. 1–10.

[17] Herring, T. K., "The boundary layer near the stagnation point in hypersonic flow past a sphere," *Journal of Fluid Mechanics*, Vol. 7, 1960, pp. 257–272. https://doi.org/10.1017/S002211206000147X.

[18] Gnoffo, P. A., Gupta, R. N., and Shinn, J. L., "Conservation equations and physical models for hypersonic air flows in thermal and chemical nonequilibrium," Tech. Rep. NASA TP 2867, 1989.

[19] Hermann, T. A., McGilvray, M., Ifti, H. S., Hufgard, F., and Loehle, S., *Fluid-Solid Heat Exchange in Porous Media for Transpiration Cooling Systems*, 2023. https://doi.org/0.2514/6.2019-0537.

[20] Cimolin, F., and Discacciati, M., "Navier–Stokes/Forchheimer models for filtration through porous media," *Applied Numerical Mathematics*, Vol. 72, 2013, pp. 205–224. https://doi.org/10.1016/j.apnum.2013.07.001.

[21] Ifti, H. S., Hermann, T., McGilvray, M., Larrimbe, L., Hedgecock, R., and Vandeperre, L., "Flow Characterization of Porous Ultra-High-Temperature Ceramics for Transpiration Cooling," *AIAA Journal*, Vol. 60, No. 5, 2022, pp. 3286–3297. https://doi.org/10.2514/1.J061009.

[22] Sobieski, W., and Trykozko, A., "Darcy's and Forchheimer's laws in practice. Part 1. The experiment," *Technical Sciences/University of Warmia and Mazury in Olsztyn*, 2014.

[23] Harlow, F. H., and Welch, J. E., "Numerical Calculation of Time-Dependent Viscous Incompressible Flow of Fluid with Free Surface," *The Physics of Fluids*, Vol. 8, No. 12, 1965, pp. 2182–2189. https://doi.org/10.1063/1.1761178.

[24] Park, C., "Review of chemical-kinetic problems of future NASA missions. I - Earth entries," *Journal of Thermophysics and Heat Transfer*, Vol. 7, No. 3, 1993, pp. 385–398. https://doi.org/10.2514/3.431.

[25] Park, C., Howe, J. T., Jaffe, R. L., and Candler, G. V., "Review of chemical-kinetic problems of future NASA missions. II - Mars entries," *Journal of Thermophysics and Heat Transfer*, Vol. 8, No. 1, 1994, pp. 9–23. https://doi.org/10.2514/3.496.

[26] Hirschfelder, J. O., Curtiss, C. F., and Bird, R. B., *Molecular Theory of Gases and Liquids*, John Wiley & Sons, Inc., 1954.

[27] Sutton, K., and Gnoffo, P. A., "Multi-component diffusion with application to computational aerothermodynamics," *7th AIAA/ASME Joint Thermophysics and Heat Transfer Conference*, 1998. https://doi.org/10.2514/6.1998-2575.

[28] Fairbanks, D. F., and Wilke, C. R., "Diffusion coefficients in multicomponent gas mixtures," *Industrial & Engineering Chemistry*, Vol. 42, No. 3, 1950, pp. 471–475.

[29] Yoshikawa, K. K., "Linearized Theory of Stagnation Point Heat and Mass Transfer at Hypersonic Speeds," Tech. Rep. NASA TN D-5246, 1969.

[30] Holden, M., *An experimental study of massive blowing from a nosetip during Jovian entry*, American Institute of Aeronautics and Astronautics, 1981. https://doi.org/10.2514/6.1981-1070.

[31] Löhle, S., Auweter-Kurtz, M., and Eberhart, M., "Local Enthalpy Measurements in a Supersonic Arcjet Facility," *Journal of Thermophysics and Heat Transfer*, Vol. 21, No. 4, 2007, pp. 790–795. https://doi.org/10.2514/1.30543.

[32] Wright, M., Edquist, K., Tang, C., Hollis, B., Krasa, P., and Campbell, C., *A Review of Aerothermal Modeling for Mars Entry Missions*, 2010. https://doi.org/10.2514/6.2010-443.

Chapter 6
Conclusions and future work

"[B]y making intelligent use of analysis, CFD, ground-based test, and flight tests (both research and development flight tests as well as flights of the prototype), one can determine the aerothermodynamic environment for hypersonic vehicles subjected to diverse requirements."

John J. Bertin [67]

Hypersonic flight vehicles are increasingly sought after for military, commercial, and exploratory applications. The main technical challenge in the development and operation of hypersonic vehicles is the management of the large heat loads caused by aerodynamic heating. All hypersonic vehicles operating to date solve this problem by featuring blunt leading edges and in some instances ablative thermal protection systems. Bluntness and ablation alleviate aerodynamic heating, albeit at the cost of aerodynamic performance. The aerodynamic performance and maneuverability required by vehicles capable of long range, sustained hypersonic flight is only possible with sharp leading edges. The feasibility of these vehicles and their mission is therefore predicated on the ability to manage thermal loads on sharp leading edges. Transpiration cooling (TC), which involves injecting a coolant gas through a porous surface, is a promising active TPS technology offering reusability, adaptability, and shape preservation compared to traditional ablative systems. The focus of this thesis is to study, numerically, transpiration cooling of sharp tips and with a view to resolve knowledge gaps in this promising technology and its application to hypersonic flight.

Accurate computational modeling is crucial for developing effective thermal protection systems due to the high costs and technical difficulties of experimental and flight testing. Several questions remain open for vehicle designers, including:

- the efficacy of various injection compositions and rates to mitigate heat loads
- the impact of mass injection on stagnation and surface flows
- the mitigation of oxidation
- the effect on catalytic heating
- the volume and mass requirements of such systems

Numerical research into this domain provides value in pointing experimentalists and vehicle designers to worthwhile paths of effort and technology development. As described in the Literature review, the value of a stagnation line solver extends past its contribution for leading edge heating analysis.

The use of the Parabolized Navier-Stokes equations allows for the subsequent analysis of the flow around an entire vehicle. The nature of missions proposed for high-atmospheric and extra-atmospheric

vehicles will guarantee encountering non-equilibrium phenomena. When considering such flows with diverse gas mixtures, the methodology must feature appropriate thermochemical modeling as well as a detailed description of the diffusive fluxes, including multicomponent diffusion.

6.1 Research Aims and Contributions

The goal of this project is to develop a computationally accurate and inexpensive numerical methodology for modeling transpiration cooled stagnation points. The resulting solver has the ability to model the following phenomena: non-equilibrium thermochemistry, wall catalycity, solid temperature, and species transport to and inside the porous medium. The solver's modular framework allows for the inclusion of diverse thermochemical models, such as those representing the Martian atmosphere, enabling the investigation of non-terrestrial mission scenarios. Furthermore, improved correlations for heat flux and species diffusive flux around stagnation point in non-equilibrium flow over a sphere have been presented, extending equilibrium-based correlations by several sources [166, 165, 125, 163, 164].

The method is based on the axisymmetric, viscous, two-dimensional Navier-Stokes equations applied to thermochemical non-equilibrium. A center-line expansion applied to a spherical leading edge is used to model the stagnation line region. Park's two temperature model is used to model local thermal non-equilibrium, with forward and backward reaction rates used for chemical non-equilibrium. Transport properties are evaluated using rigorous kinetic theory, as presented by Hirschfelder *et al.* [58]. Lastly, a unified domain is employed to allow for continued development of the porous interface and interaction between the porous medium and boundary layer.

The research was structured around three interconnected objectives, presented in Chapters 3, 4, and 5. Chapter 3 focused on the fundamental requirement of accurate thermochemical modeling by expanding the OCEAN thermochemistry database and library. This was specifically directed towards supporting rigorous calculations of transport properties, which are crucial for accurately describing the behavior of high-temperature gas mixtures. A key aspect of this work involved the detailed analysis of collision integrals for polar species like NO and CO, which are relevant to both atmospheric entry and potential injectant compositions. This foundational thermochemical capability, enabling the accurate computation of transport properties for complex, non-equilibrium gas mixtures, was a necessary prerequisite for the development of the numerical solver. Chapter 4 detailed the development and validation of a stagnation line numerical solver designed to accurately model the coupled shock layer and porous medium. This solver harnesses thermochemical conclusions developed in Chapter 3 and was validated against existing data for non-equilibrium flow with and without mass injection. Its efficiency stems from the quasi-one-dimensional assumption while retaining essential physics. Chapter 5 presented the utilization of this validated and efficient solver as a tool to conduct parametric investigations of transpiration cooled spherical tips. This allowed for a systematic characterization of the transpiration cooling problem, exploring the sensitivity of cooling performance to various parameters such as injectant type, blowing rate, free stream conditions, and wall properties across a

large operational parameter space.

The contributions of this thesis represent novel and valuable advancements within the field of hypersonic thermal protection systems. The main contributions of the thesis can be summarized in the following list:

- This solver provides an efficient yet accurate tool specifically tailored for analyzing transpiration cooling at hypersonic stagnation points under realistic non-equilibrium conditions, crucially including the explicit modeling of coupled flow and species transport within the porous cooling medium. This capability offers a distinct advantage over many previous studies that either employed simplifying assumptions regarding the porous layer or required computationally expensive higher-dimensional simulations to capture these effects.
- Specifically, the validation efforts demonstrated that the developed solver accurately reproduces key flow parameters such as stagnation profiles, surface heat flux, and shock standoff distance in non-equilibrium flow when compared against existing simulation results and experimental data. The method developed in this thesis is capable of determining the full profiles of species concentration, temperature, velocity, and pressure along the stagnation line (for the shock layer and the porous medium) within 10 minutes for air atmosphere cases, requiring only 10-20,000 cells for mesh convergence of the entire domain. State-of-the-art simulation methods used in the validation of the solver employ two-dimensional formulations, requiring on the order of 100,000 cells (excluding consideration of a porous section with injection) [27, 25, 80].
- The detailed analysis of collision integrals for polar species and their incorporation into the thermochemical framework contributes to a more refined and accurate understanding and modeling of transport properties in relevant high-temperature gas mixtures. In the context of the TC problem, this is essential for precise thermochemical modeling not only in the shock layer (especially for Mars applications) but also within the porous medium when foreign injectants, potentially including polar molecules, are used. Non-equilibrium conditions specifically may result in large concentrations of polar species such as NO or CO, depending on the atmosphere.
- The solver's ability to handle duplicated species as pseudospecies allows for investigation of complex injectant/shock layer chemical mixing phenomena. For example, in air, the nitric oxide in the shock layer contains nitrogen atoms from the free stream and the coolant plays only a marginal role in the atomic nitrogen balance. This has important implication for injectant selection, where traditionally inert coolants are favored.
- Parametric studies, made feasible by the efficiency and capabilities of the developed methodology, yield valuable quantitative data and illuminate the complex interactions between various factors influencing transpiration cooling performance.

- These results provide specific insights into the effectiveness of different injectants and the impact of parameters like wall catalycity and blowing rate, contributing directly to the development of more accurate predictive correlations (shown to be applicable in both air and Martian atmospheres) and informed design guidelines for engineering applications.
- If the injectant has similar molecular weight to the shock layer gas, then its cooling action is due mainly to the direct removal of heat from the porous material and through shielding the wall. This is the standard view of the transpiration cooling mechanism. However, if the injectant has a much lower molecular weight than the shock layer gas, the standard cooling mechanism is opposed by the injectants highly conductive and diffusive nature. The parametric studies confirmed that lighter gases like helium are generally more effective primarily due to better surface shielding, although their effectiveness can be diminished at very low blowing rates where diffusion of shock layer species towards the wall becomes more dominant.
- The investigation into wall conditions demonstrated that while surface characteristics like catalycity and thermal boundary conditions exert a noticeable localized influence on surface heat flux and temperature, particularly at low blowing rates, the impact of these surface properties is substantially reduced at high blowing rates. This is because significant mass injection effectively displaces reactive species away from the wall and reduces near-wall temperature gradients, thus dominating the thermal response regardless of the specific surface properties.
- Consideration of a wide range of Reynolds numbers, via parametric sweep of radius and free stream pressure and velocity, confirmed that Stanton number reduction is not hugely affected by Reynolds number. However, certain cases appreciably altered the non-equilibrium state reaching the wall.

6.2 Future Work

The research conducted in this thesis provides a robust foundation and valuable preliminary insights for continued exploration and development of transpiration cooling as a viable and effective thermal protection strategy for future hypersonic vehicles. Building upon the capabilities and findings already presented, several avenues for future work are identified to further enhance the solver's fidelity and expand the characterization of the TC problem. These comprise both developments of the solver and directed simulations to provide useful results to experimentalists and vehicle designers.

6.2.1 Material properties and gas-surface interaction

The current study primarily utilized material properties for porous alumina, largely for consistency with available validation cases. A crucial next step involves conducting a comprehensive parametric

investigation using realistic and representative material properties for a wider range of candidate porous TPS materials, such as Carbon-Carbon composites or other Ultra-High Temperature Ceramics (UHTCs). This would entail analyzing the impact of variations in thermal conductivity, porosity, and permeability (e.g., using Darcy or Forchheimer coefficients relevant to specific materials) on critical performance metrics such as cooling effectiveness, solid temperature distribution, and potential thermal stresses within the material. The solver's existing capability to model non-isothermal walls and account for fluid-solid heat exchange within the porous medium, as demonstrated by the preliminary non-isothermal results, makes it well suited for this detailed analysis.

Furthermore, extending the solver to incorporate models for gas-surface interaction would enable the consideration of ablative and pyrolysis cooling mechanisms. Surface recession, high-temperature surface chemistry phenomena, and gas-surface collision behavior would provide a more comprehensive tool for evaluating the performance of TPS materials under hypersonic conditions. The unified coupling of the shock layer and porous section potentially allows for the analysis of coupled active-passive TPS concepts, which are relevant for long-duration hypersonic missions.

6.2.2 Investigation of diverse atmosphere and complex injectants

The current research primarily focused on atmospheric entry conditions representative of Earth, employing relatively simple injectants. Future work should expand this scope to investigate the efficacy of transpiration cooling in diverse atmospheric environments. Analyzing TC performance in non-terrestrial atmospheres is crucial for the design of TPS for future planetary exploration missions. Additionally, the inclusion of more complex coolants, including potential pyrolysis gases that might evolve from ablative materials (e.g., containing hydrocarbons) or alternative advanced cooling fluids (e.g., alkaline metals), would enhance the solver's versatility and applicability to a broader range of TPS concepts. The modular framework established in Chapter 4 for incorporating different thermochemical models facilitates the integration of these new species and mixtures by adding their relevant collision integrals and thermochemical data.

6.2.3 Porous Medium and Interface

Refinement of the flow and characteristics of the porous medium as well as more robust treatment of the interface are important areas of development. Currently, the porous interface models a catalytic boundary and gas-metal conduction and enforces the same property conservation as throughout the shock layer. In this form, the solver uses the porosity to define "open" and "walled" portions of the domain. Refining the model to account for pores would offer greater physical accuracy. Improving the treatment of this interface to include more detailed surface phenomena, such as surface roughness effects or more complex chemical processes, and ensuring more rigorous conservation of properties across the boundary would also contribute to higher predictive accuracy. The current implementation

provides a strong foundation for incorporating these more detailed models within the overall solver framework.

6.2.4 Catalycity and Catalytic Heating

Another area of future development in the solver concerns the porous medium. Alongside the benefits noted above to refining the domain for the porous medium, this also offers the capability to better model the catalytic surface and interior of the porous medium. Understanding the impact of catalytic heating on hypersonic vehicles is of paramount importance. As early as 1959, analysis by Chung [174] determined that injection can appreciably diminish catalytic heating, which can be equal in magnitude to convective heating in certain flight conditions. The solver is capable of taking finite catalytic rates at the surface. Varying rates could be investigated to better mimic true material properties. Additionally, future work could extend this capability to include the effects of catalycity occurring within the porous section itself. The solver could be expanded to include effects of catalycity throughout the porous section. This is particularly relevant because reactive species from the shock layer, such as atomic oxygen or nitrogen, can penetrate into the porous material, especially at lower blowing rates, leading to exothermic reactions within the bulk material that contribute to the overall heat load and potentially damage the material. Implementing an "absorbed state" or similar mechanism within each porous cell to track species and model internal catalytic reactions could enable this capability. Given that catalytic heating can be a significant contributor to the total heat flux to the surface, particularly for highly catalytic TPS materials, a more detailed and comprehensive understanding of its interaction with the transpiration cooling process, both at the surface and within the porous medium, is critical for accurate TPS design and material selection.

6.2.5 Oxidation and Injectant Composition

Choice of injectant composition has been an important area of research for several decades, such as the analysis of nitrogen, helium, and freon by Holden *et al.* [175]. Inert and air injectants have been favored for simplicity. As shown in Chapter 5, with the extension of TC to other planetary missions, there is opportunity for analysis of foreign injection in non-air atmospheres. Specifically, injection of carbon dioxide might provide effective cooling do to its endothermic reactivity with a high-temperature Martian gas mixture. More generally, the ability to model various injectants is essential to creating a useful tool for preliminary design choices.

Further, building upon the analysis of how injectant composition influences species transport, future work should specifically focus on the role of transpiration cooling in mitigating oxidation at the surface of carbon-based or other oxidizing TPS materials. The ability of mass injection to limit the transport of highly oxidizing species, such as atomic oxygen and molecular oxygen, towards the wall is a key benefit of TC for protecting underlying structural materials from degradation. Quantitative

characterization of this oxidation mitigation effect for different injectants (e.g., comparing inert gases like Ar and He with potentially reducing gases like H2 or CH4) and a wide range of flow conditions would be useful for designing TC systems for surface materials. The results presented in Chapter 5, which already show the impact of blowing rate on the atomic oxygen mass fraction at the wall, provide a clear starting point for this focused investigation by allowing for the calculation of oxidation rates based on the predicted near-wall species concentrations and temperatures.

6.2.6 Extension to Vehicle Geometries

The current solver is specifically focused on the leading stagnation point, which represents the region of peak heat flux on a sharp body and is a critical design point. While this is a vital area to analyze, assessing the overall heat load distribution over more generic hypersonic vehicle leading edge geometries (e.g., cylindrical swept leading edges) is essential for practical TPS design across the entire vehicle surface. The current implementation for spherical leading edges could be extended through the modification of metric coefficients and analysis of the momentum equation for the differing geometry.

6.2.7 Correlations between cold wall facilities and hot wall flight in non-equilibrium plasma

The observed discrepancies between experimental results obtained from cold wall ground facilities (e.g., shock tunnels operating at room temperature wall conditions) and predictions for hot wall flight conditions in a non-equilibrium plasma environment highlight a significant challenge in validating computational models and applying ground test data to real-world scenarios. Future work could pursue the development of improved correlations that can effectively bridge this gap. This could involve using the developed solver to simulate a wide range of conditions relevant to both cold wall experiments and hot wall flight in non-equilibrium plasma, systematically varying parameters like wall temperature, free stream enthalpy, and pressure. By comparing the solver's predictions under these varying conditions to available experimental data, improved correlations could be developed to extrapolate ground test results to relevant flight conditions with greater confidence. This would enhance the applicability and trustworthiness of ground testing data for predicting flight performance and validating computational models.

6.3 Final remarks

In summary, the research presented in this thesis has successfully developed a valuable computational tool and provided fundamental quantitative and qualitative insights into the complex physics governing transpiration cooling at hypersonic stagnation points under non-equilibrium conditions. The outlined future work represents a logical progression building upon this foundation, aiming to further refine the

modeling capabilities, expand the understanding of the phenomenon across a wider range of conditions and materials, and ultimately contribute to the successful design and implementation of transpiration cooling systems for future hypersonic vehicles.

Appendix A
Rigorous definition for transport properties

In the subsequent description of computing transport properties from collision integrals, it is useful to define the following ratios:

$$A^*_{ij} = \frac{\Omega^{(2,2)*}_{ij}}{\Omega^{(1,1)*}_{ij}} \tag{A.1}$$

$$B^*_{ij} = \frac{5\Omega^{(1,2)*}_{ij} - 4\Omega^{(1,3)*}_{ij}}{\Omega^{(1,1)*}_{ij}} \tag{A.2}$$

$$C^*_{ij} = \frac{\Omega^{(1,2)*}_{ij}}{\Omega^{(1,1)*}_{ij}} \tag{A.3}$$

Collision Integrals

The transport Boltzmann equation, below, is a tool that can used to determine transport properties for a thermodynamics system experiencing equilibrium or non-equilbrium conditions [58]. The Boltzmann equation can be defined as follows:

$$\frac{\partial f}{\partial t} + \left(v\frac{\partial f}{\partial r}\right) + \left(\frac{1}{m}X\frac{\partial f}{\partial v}\right) = \left(\frac{df}{dt}\right)_{coll} \tag{A.4}$$

X is an external force. f is the distribution function. The solution of the Boltzmann equation describes this distribution function which can then be used to determine transport properties for given flow conditions. Thus, the Boltzmann equation describes the behavior of a thermodynamic system not in equilibrium by analyzing the probability distribution for the position and momentum of a typical particle. It should be noted that this equation is valid only at low densities such that the effects of collisions involving more than two particles are negligible. A more detailed description of the Boltzmann equation can be found in the work of Hirschfelder *et al.* [58]. It should be noted that the standard recommended solutions by Hirschfelder *et al.* employ only the first term of the Sonine polynomial equation, which reduces the thermal diffusion (accounting for Soret effects) to zero [176]

This comes from the special definition of the right-hand side of the equation with “collision integrals”. The computation of collision integrals allows for the evaluation of the transport properties such as thermal conductivity, thermal diffusivity, and viscosity for a gas mixture. Collision integrals

are defined using the following non-dimensionalized parameters:

$$r = \frac{r'}{\sigma} \tag{A.5}$$

$$b = \frac{b'}{\sigma} \tag{A.6}$$

$$\varphi = \frac{\varphi'}{\varepsilon_0} \tag{A.7}$$

$$\varepsilon = \frac{\varepsilon'}{\varepsilon_0} \tag{A.8}$$

$$T^* = \frac{kT}{\varepsilon_0} \tag{A.9}$$

$$\mu = \frac{\mu'}{(\varepsilon_0 \sigma^3)^{\frac{1}{2}}} \tag{A.10}$$

It should be noted that Hirschfelder *et al.* [58] ε explicitly as $\frac{1}{2}\mu g^2$ where μ is the reduced mass and g is the initial relative speed of the colliding molecules.

The three parameters that define a two-particle collision should be discussed. These are: impact parameter (b), initial kinetic energy (ε), and the radial distance (r) used in the intermolecular potential function ($\varphi(r)$). The impact parameter is defined as the distance of closest approach in the absence of the intermolecular potential. The intermolecular potential is a function of the radial distance between particles but may also include other parameters.

The solution process begins with the analysis of the deflection angle, computed for a given impact parameter and temperature (i.e. kinetic energy). The angle of deflection depends primarily on the intermolecular potential, $\varphi(r)$. This angle describes the difference in the relative velocity vectors of both interacting particle before and after the collision. This deflection angles is defined [58]:

$$\chi(\varepsilon, b) = \pi - 2b \int_{r_c}^{\infty} \frac{dr}{r^2 F(b, \varepsilon, r)^{\frac{1}{2}}} \tag{A.11}$$

Where $F(b, \varepsilon, r)$ is defined by:

$$F(b, \varepsilon, r) = 1 - \frac{\varphi(r)}{\varepsilon} - \frac{b^2}{r^2} \tag{A.12}$$

r_m is the radius (the intermolecular separation) with the minimum value. This is called the distance of closest approach, which is found by solving the equation $F(b, \varepsilon, r) = 0$.

Determination of the deflection angle is required when calculating a theoretical cross section $Q^{(l)}(\varepsilon)$. If assuming an intermolecular potential φ, the non-dimensional cross sections can be calculated with the deflection angle, integrated across all initial approach distances. A non-dimensional form can be attained

$$Q^{(l)}(\varepsilon) = \frac{2}{\left[1 - \frac{1}{2}\frac{1+(-1)^l}{1+l}\right]} \int_0^{\infty} (1 - \cos^l \chi(\varepsilon, b, \delta) b db \tag{A.13}$$

Finally, the normalized collision integral $\Omega_{ij}^{(l,s)*}$ can be calculated using:

$$\Omega_{ij}^{(l,s)*}(T^*) = \frac{2}{(s+1)!T^{*s+2}} \int_0^\infty x^{2s+3} e^{-x^2} Q^{(l)}(xT^*) dx \tag{A.14}$$

Viscosity

Hirschfelder *et al.* [58] present a rigorous method for evaluation viscosity of gas mixtures. The coefficient for pure viscosity and the first approximation for a binary mixture are defined:

$$[\eta_i]_1 = 2.6693 \times 10^{-8} \frac{\sqrt{MT}}{\sigma^2 \Omega^{(2,2)*}(T^*)} \tag{A.15}$$

$$[\eta_{ij}]_1 = 2.6693 \times 10^{-8} \frac{\sqrt{2M_1M_2T/(M_1+M_2)}}{\sigma_{ij}^2 \Omega^{(2,2)*}(T_{12}^*)} \tag{A.16}$$

From these terms, the rigorous definition for viscosity of multicomponent gas mixtures is:

$$[\eta_{mix}]_1 = -\frac{\begin{vmatrix} H_{11} & H_{12} & H_{13} & \cdots & H_{1n} & x_1 \\ H_{12} & H_{22} & H_{23} & \cdots & H_{2n} & x_2 \\ H_{13} & H_{23} & H_{33} & \cdots & H_{3n} & x_3 \\ . & . & . & & . & . \\ . & . & . & & . & . \\ . & . & . & & . & . \\ H_{1n} & H_{2n} & H_{3n} & \cdots & H_{nn} & x_n \\ x_1 & x_2 & x_3 & \cdots & x_n & 0 \end{vmatrix}}{\begin{vmatrix} H_{11} & H_{12} & H_{13} & \cdots & H_{1n} \\ H_{12} & H_{22} & H_{23} & \cdots & H_{2n} \\ H_{13} & H_{23} & H_{33} & \cdots & H_{3n} \\ . & . & . & & . \\ . & . & . & & . \\ . & . & . & & . \\ H_{1n} & H_{2n} & H_{3n} & \cdots & H_{nn} \end{vmatrix}} \tag{A.17}$$

$$H_{ii} = \frac{x_i^2}{[\eta_i]_1} + \sum_{k=1}^{n} \frac{2x_i x_k}{[\eta_i k]_1} \frac{M_i M_k}{(M_i+M_k)^2} \left[\frac{5}{3A_{ik}^*} + \frac{M_k}{M_i} \right], \qquad k \neq i \tag{A.18}$$

$$H_{ij} = -\frac{2x_i x_j}{[\eta_{ij}]_1} \frac{M_i M_j}{(M_i+M_j)^2} \left[\frac{5}{3A_{ij}^*} - 1 \right], \qquad i \neq j \tag{A.19}$$

Conductivity

Under Park's two temperature model, conductivity can be defined as the sum of the electrovibrational conductivity, here defined as λ_1 and evaluated at the electrovibrational temperature, as the transrotational conductivity, here defined as λ_2 and evaluated at the translation temperature. λ_2 is often defined simply as λ_h or the conductivity contribution from the heavy species, whereas as λ_1 comprises the contributions from the electron excitation and vibrational modes and from the free electrons.

$$\lambda = \lambda_1 + \lambda_2 \tag{A.20}$$

$$\lambda_1 = \lambda_{e,v} + \lambda_e \tag{A.21}$$

Unfortunately, rigorous derivations for all components have not been presented. However, empirical methods have been presented that mimic the form of the rigorous definition for viscosity and offer better accuracy over mixing rules [58, 64]. The heavy particle contribution is defined the following expressions given by Hirschfelder.

$$L_{ii} = -4\frac{x_i^2}{\lambda_{ii}} - \sum_{k=1}^{n-1} \frac{2x_i x_k (7.5M_i^2 + 6.25M_k^2 - 3B_{ik}^* M_k^2 + 4A_{ik}^* M_i M_k}{(M_i + M_k)^2 A_{ik}^* \lambda_{ik}}, \qquad k \neq i \tag{A.22}$$

$$L_{ij} = \frac{2x_i x_j M_i M_j}{(M_i + M_j)^2 A_{ij}^* \lambda_{ij}} (11.25 - 3B_{ij}^* - 4A_{ij}^*), \qquad i \neq j \tag{A.23}$$

$$\lambda_h = 4\frac{\begin{vmatrix} L_{11} & L_{12} & L_{13} & \cdots & L_{1n} & x_1 \\ L_{12} & L_{22} & L_{23} & \cdots & L_{2n} & x_2 \\ L_{13} & L_{23} & L_{33} & \cdots & L_{3n} & x_3 \\ . & . & . & & . & . \\ . & . & . & & . & . \\ . & . & . & & . & . \\ L_{1n} & L_{2n} & L_{3n} & \cdots & L_{nn} & x_n \\ x_1 & x_2 & x_3 & \cdots & x_n & 0 \end{vmatrix}}{\begin{vmatrix} L_{11} & L_{12} & L_{13} & \cdots & L_{1n} \\ L_{12} & L_{22} & L_{23} & \cdots & L_{2n} \\ L_{13} & L_{23} & L_{33} & \cdots & L_{3n} \\ . & . & . & & . \\ . & . & . & & . \\ . & . & . & & . \\ L_{1n} & L_{2n} & L_{3n} & \cdots & L_{nn} \end{vmatrix}} \tag{A.24}$$

The electron contribution to conductivity is adapted from Capitelli *et al.* [64].

$$\lambda_e = \frac{75 n_e^2 k}{8}\left(\frac{2\pi kT}{m_e}\right)\frac{1}{q^{11}-(q^{12})^2/q^{22}} \tag{A.25}$$

$$q^{11} = 8\sqrt{2}n_e^2 Q_{ee}^{(2,2)} + 8\sum_{j=1}^{\nu-1} n_j n_e\left[\frac{25}{4}Q_{ej}^{(1,1)} - 15Q_{ej}^{(1,2)} + 12Q_{ej}^{(2,2)}\right] \tag{A.26}$$

$$q^{12} = 8\sqrt{2}n_e^2\left[\frac{7}{4}Q_{ee}^{(2,2)} - 2Q_{ee}^{(2,3)}\right] + 8\sum_{j=1}^{\nu-1} n_j n_e\left[\frac{175}{16}Q_{ej}^{(1,1)} - \frac{315}{8}Q_{ej}^{(1,2)} + 57Q_{ej}^{(1,3)} - 30Q_{ej}^{(1,4)}\right] \tag{A.27}$$

$$q^{22} = 8\sqrt{2}n_e^2\left[\frac{77}{16}Q_{ee}^{(2,2)} - 7Q_{ee}^{(2,3)} + 5Q_{ee}^{(2,4)}\right] + 8\sum_{j=1}^{\nu-1} n_j n_e\left[\frac{1225}{64}Q_{ej}^{(1,1)} - \frac{735}{8}Q_{ej}^{(1,2)} + \frac{399}{2}Q_{ej}^{(1,3)} - 210Q_{ej}^{(1,4)} + 90Q_{ej}^{(1,5)}\right] \tag{A.28}$$

The electrovibrational contribution to conductivity is again taken from Capitelli *et al.* [64]. It must be noted that this derivation follows from analysis for local thermodynamic equilibrium. However, the internal contribution defined by Capitelli *et al.* can be treated as the contribution due to the electrovibrational modes in thermal non-equilibrium when assessed at the electrovibrational temperature.

$$\lambda_{e,v} = \frac{1}{T}\sum_{j=1}^{\nu}\frac{x_j\frac{c_{p_{e,v,j}}}{R}}{\sum_{i=1}^{\nu}\frac{x_i}{pD_{ij}(1)}} \tag{A.29}$$

Electrical Conductivity

Electrical Conductivity is assessed at the electrovibrational temperature and is described by Capitelli *et al.* [64]

$$\sigma = \frac{3e^2 n_e^2}{2}\frac{\sqrt{2\pi k m_e T}}{|q|}\begin{vmatrix} q^{11} & q^{12} \\ q^{21} & q^{22}\end{vmatrix} \tag{A.30}$$

$$|q| = \begin{vmatrix} q^{00} & q^{01} & q^{02} \\ 1^{10} & q^{11} & q^{12} \\ q^{20} & q^{21} & q^{22}\end{vmatrix} \tag{A.31}$$

$$q^{00} = 8n_e\sum_{j=1}^{\nu-1} n_j Q_{ej}^{(1,1)} \tag{A.32}$$

$$q^{01} = 8n_e\sum_{j=1}^{\nu-1} n_j\left[\frac{5}{2}Q_{ej}^{(1,1)} - 3Q_{ej}^{(1,2)}\right] \tag{A.33}$$

$$q^{02} = 8n_e\sum_{j=1}^{\nu-1} n_j\left[\frac{35}{8}Q_{ej}^{(1,1)} - \frac{21}{2}ej^{(1,2)} + 6Q_{ej}^{(1,3)}\right] \tag{A.34}$$

Species Diffusivity

The diffusive mass flux can be described using the Stephan-Maxwell equation, as defined by Sutton and Gnoffo [36].

$$J_i = \frac{\rho M_i}{M^2} \sum_{j \neq i} M_j D_{ij} \nabla x_j \tag{A.35}$$

Their definition for coefficients of multicomponent diffusion follow those presented by Hirschfelder *et al.* [58]. The first approximation (first term of the Sonine polynomial expansion) for the coefficient of diffusion in a binary mixture:

$$\mathcal{D}_{ij} = 2.6 \times 10^{-7} \frac{\sqrt{T^3 (M_i + M_j)/2 M_i M_j}}{p \sigma_{ij}^2 \Omega_{ij}^{(1,1)} (kT/\varepsilon_{ij})} \tag{A.36}$$

The coefficient of diffusion in a multicomponent mixture is defined:

$$D_{ij} = \frac{M}{M_j} \frac{F^{ji} - F^{ii}}{|F|} \tag{A.37}$$

$$F_{ij} = \frac{x_i}{\mathcal{D}_{ij}} + \frac{M_j}{M_i} \sum_{k \neq i} \frac{(x_k)}{\mathcal{D}_{ik}} \qquad \text{for} \quad i \neq j \tag{A.38}$$

$$F_{ii} = 0 \tag{A.39}$$

The denominator $|F|$ is the determinant of the matrix F. The values F^{ji} are the transposed cofactors of the matrix F, which can be defined:

$$F^{ji} = (-1)^{i+j} \begin{vmatrix} 0 & F_{12} & F_{13} & \cdots & F_{1n} \\ F_{12} & F_{22} & F_{23} & \cdots & F_{2n} \\ F_{13} & F_{23} & F_{33} & \cdots & F_{3n} \\ . & . & . & & . \\ . & . & . & & . \\ . & . & . & & . \\ F_{1n} & F_{2n} & F_{3n} & \cdots & F_{nn} \end{vmatrix} \tag{A.40}$$

Bibliography

[1] M. Satchell, *Numerical Simulation and Modeling of Shock Tube Experiments*. PhD thesis, University of Oxford, 2021.

[2] L. Pollock and G. Wild, "An examination of high-speed aircraft – part 1: Past, present, and future," *Transportation Engineering*, vol. 18, 2024.

[3] W. Zhang, Z. Zhang, X. Wang, and T. Su, "A review of the mathematical modeling of equilibrium and nonequilibrium hypersonic flows," *Advances in Aerodynamics*, vol. 4, no. 1, p. 38, 2022.

[4] S. Nonaka, H. Mizuno, K. Takayama, and C. Park, "Measurement of shock standoff distance for sphere in ballistic range," *Journal of Thermophysics and Heat Transfer*, vol. 14, no. 2, pp. 225–229, 2000.

[5] G. Colonna, F. Bonelli, and G. Pascazio, "Impact of fundamental molecular kinetics on macroscopic properties of high-enthalpy flows: The case of hypersonic atmospheric entry," *Phys. Rev. Fluids*, vol. 4, p. 033404, Mar 2019.

[6] M. Ewenz Rocher, *Application of transpiration cooling on hypersonic vehicles to mitigate material oxidation*. PhD thesis, University of Oxford, 2021.

[7] H. N. Kelly and M. L. Blosser, "Active cooling from the sixties to nasp," 1994.

[8] A. Laganelli, "A comparison between film cooling and transpiration cooling systems in high speed flow," American Institute of Aeronautics and Astronautics (AIAA), 1 1970.

[9] D. F. Potter, *modeling of radiating shock layers for atmospheric entry at Earth and Mars*. PhD thesis, University of Queensland, 2011.

[10] H. Cheng, "The blunt-body problem in hypesnic flow at low reynolds numbers," 1963.

[11] T. A. Heppenheimer, *Facing the Heat Barrier: A History of Hypersonics*. National Aeronautics and Space Administration, NASA History Division, Office of External Relations, 2007.

[12] R. M. Cummings, W. H. Mason, S. A. Morton, and D. R. McDaniel, *Applied Computational Aerodynamics: A Modern Engineering Approach*. Cambridge Aerospace Series, Cambridge University Press, 2015.

[13] T. von Karman, "Aerodynamics selected topics in the light of their historical development," 1954.

[14] J. T. Howe, "Hypervelocity atmospheric flight: real gas flow fields," Tech. Rep. NASA RP-1249, 1990.

[15] M. E. Tauber, G. P. Menees, and H. G. Adelman, "Aerothermodynamics of transatmospheric vehicles," *Journal of Aircraft*, vol. 24, pp. 594–602, 1987.

[16] J. J. Bertin and R. M. Cummings, "Fifty years of hypersonics: where we've been, where we're going," *Progress in Aerospace Sciences*, vol. 39, no. 6, pp. 511–536, 2003.

[17] M. D. Kim, S. Swaminathan, and C. H. Lewis, "Viscous shock-layer predictions of three-dimensional nonequilibrium flows past the space shuttle at high angle of attack," 1983.

[18] I. Boyd and J. Padilla, *Simulation of Sharp Leading Edge Aerothermodynamics*.

[19] W. F. Santos, "Bluntness impact on lift-to-drag ratio of hypersonic wedge flow," *Journal of Spacecraft and Rockets*, vol. 46, pp. 329–339, 2009.

[20] C. Park, *Nonequilbrium Hypersonic Aerothermodynamics*. John Wiley & Sons, Inc., 1990.

[21] C. Park, "Review of chemical-kinetic problems of future nasa missions. i - earth entries," *Journal of Thermophysics and Heat Transfer*, vol. 7, no. 3, pp. 385–398, 1993.

[22] R. S. Chaudhry and G. V. Candler, *Statistical Analyses of Quasiclassical Trajectory Data for Air Dissociation*.

[23] R. S. Chaudhry, *Modeling and Analysis of Chemical Kinetics for Hypersonic Flows in Air*. PhD thesis, University of Minnesota, 2018.

[24] C. Park, J. T. Howe, R. L. Jaffe, and G. V. Candler, "Review of chemical-kinetic problems of future nasa missions. ii - mars entries," *Journal of Thermophysics and Heat Transfer*, vol. 8, no. 1, pp. 9–23, 1994.

[25] J. G. Kim and S. M. Jo, "Modification of chemical-kinetic parameters for 11-air species in re-entry flows," *International Journal of Heat and Mass Transfer*, vol. 169, p. 120950, 2021.

[26] R. S. Chaudhry and I. D. Boyd, *Parametric Comparison of the Park and MMT Chemical Kinetics Models for Hypersonic Blunt Cones*.

[27] R. S. Chaudhry, I. D. Boyd, and G. V. Candler, *Vehicle-Scale Simulations of Hypersonic Flows using the MMT Chemical Kinetics Model*. 2020.

[28] G. Pascazio, D. Ninni, F. Bonelli, and G. Colonna, "Hypersonic flows with detailed state-to-state kinetics using a gpu cluster," in *Plasma Modeling (Second Edition)*, 2053-2563, pp. 10–1 to 10–41, IOP Publishing, 2022.

[29] M. Capitelli, G. Colonna, and A. D'Angola, *Fundamental aspects of plasma chemical physics*, vol. 66. Springer, 2012.

[30] G. Colonna, M. Tuttafesta, M. Capitelli, and D. Giordano, "Non-arrhenius no formation rate in one-dimensional nozzle airflow," *Journal of Thermophysics and Heat Transfer*, vol. 13, no. 3, pp. 372–375, 1999.

[31] I. Armenise, M. Capitelli, G. Colonna, and G. Gorse, "Nonequilibrium vibrational kinetics in the boundary layer of re-entering bodies," *Journal of Thermophysics and Heat Transfer*, vol. 10, no. 3, pp. 397–405, 1996.

[32] F. Bonelli, G. Pascazio, and G. Colonna, "Effect of finite-rate catalysis on wall heat flux prediction in hypersonic flow," *Phys. Rev. Fluids*, vol. 6, p. 033201, Mar 2021.

[33] F. P. Incropera, D. P. DeWitt, T. L. Bergman, and A. S. Lavine, *Fundamentals of Heat and Mass Transfer*. John Wiley & Sons, 6th ed., 2007.

[34] J. Anderson Jr., *Hypersonic and High-Temperature Gas Dynamics*. American Insitute of Aeronautics and Astronautics, second ed., 2006.

[35] M. E. Tauber and K. Sutton, "Stagnation-point radiative heating relations for earth and mars entries," *Journal of Spacecraft and Rockets*, vol. 28, no. 1, pp. 40–42, 1991.

[36] K. Sutton and P. A. Gnoffo, "Multi-component diffusion with application to computational aerothermodynamics," *7th AIAA/ASME Joint Thermophysics and Heat Transfer Conference*, 1998.

[37] J. A. Fay and F. R. Riddell, "Theory of stagnation point heat transfer in dissociated air," *Journal of the Aerospace Sciences*, vol. 25, no. 2, pp. 73–85, 1958.

[38] A. M. Brandis and C. O. Johnston, *Characterization of Stagnation-Point Heat Flux for Earth Entry*. 2014.

[39] S. Gai and N. Mudford, "Stagnation point heat flux in hypersonic high enthalpy flow," *Shock Waves*, vol. 2, no. 1, pp. 43–47, 1992.

[40] R. B. Pope, "Stagnation-point convective heat transfer in frozen boundary layers.," *AIAA Journal*, vol. 6, no. 4, pp. 619–626, 1968.

[41] L. A. Anderson, "Effect of surface catalytic activity on stagnation heat-transfer rates.," *AIAA Journal*, vol. 11, no. 5, pp. 649–656, 1973.

[42] R. A. East, R. J. Stalker, and J. P. Baird, "Measurements of heat transfer to a flat plate in a dissociated high-enthalpy laminar air flow," *Journal of Fluid Mechanics*, vol. 97, no. 4, p. 673–699, 1980.

[43] T. A. Parthasarathy, R. A. Rapp, M. Opeka, and R. J. Kerans, "A model for the oxidation of zrb2, hfb2 and tib2," *Acta Materialia*, vol. 55, pp. 5999–6010, 10 2007.

[44] H. G. Timmer, C. L. Arne, T. R. Stokes, and H. H. Tang, "Aerothermodynamic characteristics of slender ablating re-entry vehicles," *Journal of Spacecraft and Rockets*, vol. 8, pp. 373–374, 1971.

[45] P. F. Holloway and E. L. Morrisette, "Roughness effects on boundary-layer transition for blunt-leading-edge plates at mach 6," Tech. Rep. NASA TN D-3517, 1966.

[46] E. R. G. Eckert and N. B. Livingood, "Comparison of effectiveness of convection-, transpiration-, and film-cooling methods with air as coolant," 1954.

[47] M. Rocher, M. McGilvray, T. Hermann, H. S. Ifti, F. Hufgard, M. Eberhart, A. Meindl, S. Lohle, T. Giovannini, and L. Vandeperre, "Correction: Testing a transpiration cooled zirconium-di-boride sample in the plasma tunnel at irs," 01 2019.

[48] E. Van Driest, "Investigation of laminar boundary layer in compressible fluids using the crocco method," Tech. Rep. NACA TN-2497, 1952.

[49] W. G. Vincenti and C. H. Kruger, *Introduction to Physical Gas Dynamics*. New York: John Wiley & Sons, 1965.

[50] R. C. Millikan and D. R. White, "Systematics of vibrational relaxation," *The Journal of Chemical Physics*, vol. 39, pp. 3209–3213, 12 1963.

[51] J.-H. Lee, "Basic Governing Equations for the Flight Regimes of Aeroassisted Orbital Transfer Vehicles," in *19th Thermophysics Conference*, (Reston, Virigina), American Institute of Aeronautics and Astronautics, 6 1984.

[52] J.-H. Lee, "Electron-Impact Vibrational Excitation Rates in the Flowfield of Aeroassisted Orbital Transfer Vehicles.," *Progress in Astronautics and Aeronautics*, vol. 103, pp. 197–224, 1986.

[53] S. Gordon and B. J. McBride, "Computer Program for Calculation of Complex Chemical Equilibrium," Tech. Rep. NASA-RP-1311, 1994.

[54] P. A. Gnoffo, R. N. Gupta, and J. L. Shinn, "Conservation equations and physical models for hypersonic air flows in thermal and chemical nonequilibrium," 2 1989.

[55] R. N. Gupta, J. M. Yos, and R. A. Thompson, "A review of reaction rates and thermodynamic and transport properties for the 11-species air model for chemical and thermal nonequilibrium calculations to 30000 k," Tech. Rep. NASA RP-1232, NASA, 1989.

[56] F. Blottner, "Viscous shock layer at the stagnation point with nonequilibrium air chemistry," *AIAA Journal*, vol. 7, pp. 2281–2288, 1969.

[57] M. G. Dunn and S. W. Kang, "Theoretical and Experimental Studies of Reentry Plasmas.," *NASA Contractor Reports*, no. April, 1973.

[58] J. O. Hirschfelder, C. F. Curtiss, and R. B. Bird, *Molecular Theory of Gases and Liquids*. New York: John Wiley & Sons, Inc., 1954.

[59] J. M. Yos, "Transport properties of nitrogen, hydrogen, oxygen, and air to 30,000 k," tech. rep., Avco Corp Wilmington MA Research and Advanced Development Division, 1963.

[60] C. R. Wilke, "A viscosity equation for gas mixtures," *The Journal of Chemical Physics*, vol. 18, no. 4, pp. 517–519, 1950.

[61] G. E. Palmer and M. J. Wright, "Comparison of methods to compute high-temperature gas viscosity," *Journal of Thermophysics and Heat Transfer*, vol. 17, pp. 232–239, 2003.

[62] T. E. Magin and G. Degrez, "Transport algorithms for partially ionized and unmagnetized plasmas," *Journal of Computational Physics*, vol. 198, no. 2, pp. 424–449, 2004.

[63] C. Muckenfuss and C. F. Curtiss, "Thermal conductivity of multicomponent gas mixtures," *The Journal of Chemical Physics*, vol. 29, pp. 1273–1277, 1958.

[64] M. Capitelli, G. Colonna, C. Gorse, and A. D'angola, "Transport properties of high temperature air in local thermodynamic equilibrium," *The European Physical Journal D*, vol. 11, pp. 279–289, 2000.

[65] A. Murphy and C. Arundelli, "Transport coefficients of argon, nitrogen, oxygen, argon-nitrogen, and argon-oxygen plasmas," *Plasma Chemistry and Plasma Processing*, vol. 14, pp. 451–490, 12 1994.

[66] J. N. Moss, "Reacting viscous-shock-layer solutions with multicomponent diffusion and mass injection," Tech. Rep. NASA-TR-R-411, NASA, 1974.

[67] J. J. Bertin, *Hypersonic Aerothermodynamics*. Washington, D.C.: American Institue of Aeronautics and Astronautics, Inc., 1994.

[68] P. V. Marrone and C. E. Treanor, "Chemical relaxation with preferential dissociation from excited vibrational levels," *The Physics of Fluids*, vol. 6, pp. 1215–1221, 09 1963.

[69] S. P. Sharma, W. M. Huo, and C. Park, "Rate parameters for coupled vibration-dissociation in a generalized ssh approximation," *Journal of Thermophysics and Heat Transfer*, vol. 6, no. 1, pp. 9–21, 1992.

[70] T. Gokcen, "N2-ch4-ar chemical kinetic model for simulations of atmospheric entry to titan," *Journal of Thermophysics and Heat Transfer*, vol. 21, no. 1, pp. 9–18, 2007.

[71] L. P. Leibowitz and T.-J. Kuo, "Ionizational nonequilibrium heating during outer planetary entries," *AIAA Journal*, vol. 14, no. 9, pp. 1324–1329, 1976.

[72] L. Landau and E. Teller, "On the theory of the dispersion of sound phys," *Z. Sowjetunion*, vol. 10, p. 34, 1936.

[73] D. A. Andrienko and I. D. Boyd, "Vibrational energy transfer and dissociation in o2–n2 collisions at hyperthermal temperatures," *The Journal of Chemical Physics*, vol. 148, p. 084309, 02 2018.

[74] F. Homann, "Einfluß großer zähigkeit bei strömung um zylinder," *Forschung auf dem Gebiet des Ingenieurwesens A*, vol. 7, no. 1, pp. 1–10, 1936.

[75] M. J. Lighthill, "The fundamental solution for small steady three-dimensional disturbances to a two-dimensional parallel shear flow," *Journal of Fluid Mechanics*, vol. 3, no. 2, pp. 113–144, 1957.

[76] T. K. Herring, "The boundary layer near the stagnation point in hypersonic flow past a sphere," *Journal of Fluid Mechanics*, vol. 7, pp. 257–272, 1960.

[77] C. D. Scott, "Wall catalytic recombination and boundary conditions in nonequilibrium hypersonic flows—with applications," in *Advances in Hypersonics: Modeling Hypersonic Flows*, pp. 176–250, Springer, 1992.

[78] A. Bourdon and A. Bultel, "Numerical simulation of stagnation line nonequilibrium airflows for reentry applications," *Journal of Thermophysics and Heat Transfer*, vol. 22, no. 2, pp. 168–177, 2008.

[79] G. V. Candler, "Rate effects in hypersonic flows," *Annual Review of Fluid Mechanics*, vol. 51, no. Volume 51, 2019, pp. 379–402, 2019.

[80] Y. Yang, S. Lee, and J. G. Kim, "Influence of catalytic wall on the effective radius of a blunt body geometry in a nonequilibrium hypersonic flow," *Case Studies in Thermal Engineering*, vol. 35, p. 102085, 2022.

[81] S. Chen and Q. Sun, "A quasi-one-dimensional model for hypersonic reactive flow along the stagnation streamline," *Chinese Journal of Aeronautics*, vol. 29, no. 6, pp. 1517–1526, 2016.

[82] C.-Y. Wen and H. G. Hornung, "Non-equilibrium dissociating flow over spheres," *Journal of Fluid Mechanics*, vol. 299, p. 389–405, 1995.

[83] M. Panesi, A. Munafò, T. E. Magin, and R. L. Jaffe, "Nonequilibrium shock-heated nitrogen flows using a rovibrational state-to-state method," *Phys. Rev. E*, vol. 90, p. 013009, Jul 2014.

[84] A. Munafò and T. E. Magin, "Modeling of stagnation-line nonequilibrium flows by means of quantum based collisional models," *Physics of Fluids*, vol. 26, p. 097102, 09 2014.

[85] Q. Hong, X. Wang, Y. Hu, and Q. Sun, "Development of a stagnation streamline model for thermochemical nonequilibrium flow," *Physics of Fluids*, vol. 32, p. 046102, 04 2020.

[86] M. Fey, R. Jeltsch, and S. Müller, "Stagnation point computations of nonequilibrium inviscid blunt body flow," *Computers & Fluids*, vol. 22, no. 4, pp. 501–515, 1993. Special Issue Egon Krause Honour Issue.

[87] A. Klomfass and S. Müller, "Calculation of stagnation streamline quantities in hypersonic blunt body flows," *Shock Waves*, vol. 7, no. 1, pp. 13–23, 1997.

[88] D. A. Nield and A. Bejan, *Convection in porous media*, vol. 3. Springer, 2006.

[89] H. Darcy, *Les fontaines publiques de la ville de Dijon: exposition et application des principes à suivre et des formules à employer dans les questions de distribution d'eau*, vol. 1. Victor dalmont, 1856.

[90] S. Whitaker, "Flow in porous media i: A theoretical derivation of darcy's law," *Transport in porous media*, vol. 1, pp. 3–25, 1986.

[91] P. Forchheimer, "Wasserbewegung durch boden," *Zeitschrift des Vereines Deutscher Ingenieure*, vol. 45, pp. 1782–1788, 1901.

[92] H. S. Ifti, T. Hermann, M. McGilvray, L. Larrimbe, R. Hedgecock, and L. Vandeperre, "Flow characterization of porous ultra-high-temperature ceramics for transpiration cooling," *AIAA Journal*, vol. 60, no. 5, pp. 3286–3297, 2022.

[93] W. Sobieski and A. Trykozko, "Darcy's and forchheimer's laws in practice. part 1. the experiment," *Technical Sciences/University of Warmia and Mazury in Olsztyn*, 2014.

[94] W. Jäger and A. Mikelić, "On the boundary conditions at the contact interface between a porous medium and a free fluid," *Annali della Scuola Normale Superiore di Pisa-Classe di Scienze*, vol. 23, no. 3, pp. 403–465, 1996.

[95] V. Nassehi, "Modelling of combined navier–stokes and darcy flows in crossflow membrane filtration," *Chemical Engineering Science*, vol. 53, no. 6, pp. 1253–1265, 1998.

[96] P. Angot, "Analysis of singular perturbations on the brinkman problem for fictitious domain models of viscous flows," *Mathematical Methods in the Applied Sciences*, vol. 22, no. 16, pp. 1395–1412, 1999.

[97] W. J. Layton, F. Schieweck, and I. Yotov, "Coupling fluid flow with porous media flow," *SIAM Journal on Numerical Analysis*, vol. 40, no. 6, pp. 2195–2218, 2002.

[98] C.-H. Bruneau and I. Mortazavi, "Passive control of the flow around a square cylinder using porous media," *International Journal for Numerical Methods in Fluids*, vol. 46, no. 4, pp. 415–433, 2004.

[99] O. Iliev and V. Laptev, "On numerical simulation of flow through oil filters," *Computing and Visualization in Science*, vol. 6, pp. 139–146, 2004.

[100] C.-H. Bruneau and I. Mortazavi, "Numerical modeling and passive flow control using porous media," *Computers & Fluids*, vol. 37, no. 5, pp. 488–498, 2008. Special Issue Dedicated to Professor M.M. Hafez on the Occasion of his 60th Birthday.

[101] A. Cerminara, R. Deiterding, and N. Sandham, "Direct numerical simulations of coolant injection through a porous layer for transpiration cooling in hypersonic flow," 2019.

[102] A. Cerminara, R. Deiterding, and N. D. Sandham, "Transpiration cooling using porous material for hypersonic applications," in *Convective Heat Transfer in Porous Media*, pp. 263–286, CRC Press, 2019.

[103] Y.-K. Chen, F. S. Milos, and T. Gokcen, "Loosely coupled simulation for two-dimensional ablation and shape change," *Journal of Spacecraft and Rockets*, vol. 47, no. 5, pp. 775–785, 2010.

[104] J. de Mûelenaere, T. Magin, J. Lachaud, and N. Mansour, *Stagnation line approximation for ablation thermochemistry*. 2011.

[105] A. Martin and I. D. Boyd, "Strongly coupled computation of material response and nonequilibrium flow for hypersonic ablation," *Journal of Spacecraft and Rockets*, vol. 52, no. 1, pp. 89–104, 2015.

[106] M. Rom and S. Müller, "Derivation and analysis of a 1d porous medium flow solver embedded in a two-domain model for 2d and 3d transpiration cooling," *International Journal of Heat and Mass Transfer*, vol. 195, p. 123127, 2022.

[107] H. Weng and A. Martin, *Development of a Universal Solver and Its Application to Ablation Problems*. 2017.

[108] H. Weng and A. Martin, *Modeling FiberForm Oxidation in a Flow Tube using a Universal Solver*. 2019.

[109] U. Duzel and A. Martin, *Modeling High Velocity Flow Through Porous Media*. 2020.

[110] S. Baeg, R. Davuluri, and A. Martin, *Development of two-temperature model in unified solver*. 2024.

[111] F. Cimolin and M. Discacciati, "Navier–stokes/forchheimer models for filtration through porous media," *Applied Numerical Mathematics*, vol. 72, pp. 205–224, 2013.

[112] H. C. Brinkman, "A calculation of the viscous force exerted by a flowing fluid on a dense swarm of particles," *Flow, Turbulence and Combustion*, vol. 1, no. 1, pp. 27–34, 1949.

[113] J. Yao and H. Zhang, "Comparing darcy's law and the brinkman equation for numerical simulations of saltwater intrusion," *Sustainability*, vol. 15, no. 18, 2023.

[114] T. Lévy, "Fluid flow through an array of fixed particles," *International Journal of Engineering Science*, vol. 21, no. 1, pp. 11–23, 1983.

[115] J.-L. Auriault, C. Geindreau, and C. Boutin, "Filtration law in porous media with poor separation of scales," *Transport in porous media*, vol. 60, no. 1, pp. 89–108, 2005.

[116] J.-L. Auriault, "On the domain of validity of brinkman's equation," *Transport in Porous Media*, vol. 79, pp. 215–223, 09 2009.

[117] T. A. Hermann, M. McGilvray, H. S. Ifti, F. Hufgard, and S. Loehle, *Fluid-Solid Heat Exchange in Porous Media for Transpiration Cooling Systems*. 2023.

[118] V. D. Rannie, "A simplified theory of porous wall cooling," 1947.

[119] E. A. Barber, "An experimental investigation of stagnation- point injection," *Journal of Spacecraft and Rockets*, vol. 2, no. 5, pp. 770–774, 1965.

[120] L. W. Woodruff and G. C. Lorenz, "Hypersonic turbulent transpiration cooling including downstream effects," *AIAA Journal*, vol. 4, pp. 969–975, 1966.

[121] R. N. Meroney and W. H. Giedt, "The effect of mass injection on heat transfer from a partially dissociated gas stream," *Journal of Heat Transfer*, vol. 89, pp. 205–213, 08 1967.

[122] R. J. Moffat and W. M. Kays, "The turbulent boundary layer on a porous plate : Experimental heat transfer with uniform blowing and suction," 1968.

[123] R. L. Simpson, R. J. Moffat, and W. M. Kays, "The turbulent boundary layer on a porous plate: Experimental skin friction with variable injection and suction," 1969.

[124] C. C. Pappas and G. Lee, "Heat transfer and pressure on a hypersonic blunt cone with mass addition," *AIAA Journal*, vol. 8, no. 5, pp. 954–956, 1970.

[125] K. K. Yoshikawa, "Linearized theory of stagnation point heat and mass transfer at hypersonic speeds," 1969.

[126] M. Holden, *An experimental study of massive blowing from a nosetip during Jovian entry*.

[127] S. Löhle, M. Auweter-Kurtz, and M. Eberhart, "Local enthalpy measurements in a supersonic arcjet facility," *Journal of Thermophysics and Heat Transfer*, vol. 21, no. 4, pp. 790–795, 2007.

[128] R. Feldhuhn, *Heat transfer from a turbulent boundary layer on a porous hemisphere*. 1976.

[129] G. E. Kaattari, "Effects of mass addition on blunt-body boundary-layer transition and heat transfer," Tech. Rep. NASA-TP-1139, 1978.

[130] P. A. Libby and M. Pierucci, "Laminar boundary layer with hydrogen injection including multicomponent diffusion," *AIAA Journal*, vol. 2, no. 12, pp. 2118–2126, 1964.

[131] L. F. Hearne, J. H. Chin, and L. W. Woodruff, "Final report study of aerothermodynamic phenomena associated with reentry of manned spacecraft," 1966.

[132] J. T. Howe and Y. S. Sheaffer, "Mass addition in the stagnation region for velocity up to 50,000 feet per second," Tech. Rep. NASA-TR-R-207, 1964.

[133] V. V. Riabov, "Heat transfer on a hypersonic sphere with diffuse rarefied-gas injection," *Journal of Spacecraft and Rockets*, vol. 41, no. 4, pp. 698–698, 2004.

[134] J. Meinert, J. Huhn, E. Serbest, and O. J. Haidn, "Turbulent boundary layers with foreign gas transpiration," *Journal of Spacecraft and Rockets*, vol. 38, pp. 191–198, 2001.

[135] M. Holden, K. Rodriguez, and R. Nowak, *Studies of shock/shock interaction on smooth and transpiration-cooled hemispherical nosetips in hypersonic flow*. 1991.

[136] M. Holden and S. Sweet, *Studies of transpiration cooling with shock interaction in hypersonic flow*. 1994.

[137] S. Choi, S. Scotti, K. Song, H. Ries, S. Choi, S. Scotti, K. Song, and H. Ries, *Transpiring cooling of a scram-jet engine combustion chamber*. 1997.

[138] T. Langener, J. V. Wolfersdorf, and J. Steelant, "Experimental investigations on transpiration cooling for scramjet applications using different coolants," *AIAA Journal*, vol. 49, pp. 1409–1419, 7 2011.

[139] G. T. Colwell and J. M. Modlin, "Heat pipe and surface mass transfer cooling of hypersonic vehicle structures," *Journal of Thermophysics and Heat Transfer*, vol. 6, no. 3, pp. 492–499, 1992.

[140] M. Arai and T. Suidzu, "Porous ceramic coating for transpiration cooling of gas turbine blade," *Journal of Thermal Spray Technology*, vol. 22, pp. 690–698, 2013.

[141] A. Wambersie, H. Wong, P. Ireland, and I. Mayo, "Experiments of transpiration cooling inspired panel cooling on a turbine blade yielding film effectiveness levels over 95%," *International Journal of Turbomachinery, Propulsion and Power*, vol. 6, no. 2, 2021.

[142] *Low Order Heat & Mass Flow Network modeling for Quasi-Transpiration Cooling Systems*, vol. Volume 6B: Heat Transfer — General Interest/Additive Manufacturing Impacts on Heat Transfer; Internal Air Systems; Internal Cooling of *Turbo Expo*, 06 2022.

[143] Q. Mi, S. Yi, D. Gang, X. Lu, and X. Liu, "Research progress of transpiration cooling for aircraft thermal protection," *Applied Thermal Engineering*, vol. 236, p. 121360, 2024.

[144] S. Mohammed Ibrahim, P. Vivek, and K. P. J. Reddy, "Experimental investigation on transpiration cooling effectiveness for spacecraft entering martian atmosphere," *AIAA Journal*, vol. 54, no. 9, pp. 2922–2926, 2016.

[145] H. S. Ifti, T. Hermann, M. McGilvray, and J. Merrifield, "Numerical simulation of transpiration cooling in a laminar hypersonic boundary layer," *Journal of Spacecraft and Rockets*, vol. 59, no. 5, pp. 1726–1735, 2022.

[146] I. Naved, T. Hermann, C. Hambidge, H. S. Ifti, M. McGilvray, I. S. Tirichenko, and L. Vandeperre, "Quantifying the surface heat transfer on transpiration cooled porous materials in laminar and turbulent hypersonic boundary layers," ESA Conference Bureau/ATPI Corporate Events, 2022.

[147] L. Lees, "Convective heat transfer with mass addition and chemical reactions," in *Combustion and Propulsion. 3rd AGARD Colloquium. NY: Pergamon Press*, 1958.

[148] W. Zhang, Y. Yi, X. Bai, and A. Nakayama, "A local thermal non-equilibrium analysis for convective and radiative heat transfer in gaseous transpiration cooling through a porous wall," *International Journal of Heat and Mass Transfer*, vol. 162, p. 120389, 2020.

[149] Y. Yi, Y. Liu, and A. Nakayama, "A two-domain local thermal non-equilibrium analysis for forced convection in a transpiration-cooled channel filled with a porous medium," *Transport in Porous Media*, vol. 149, pp. 733 – 761, 2023.

[150] H. Mickley, *Heat, mass, and momentum transfer for flow over a flat plate with blowing or suction*, vol. 3208. National Advisory Committee for Aeronautics, 1954.

[151] J. HARTNETT and C. LIU, *Transpiration cooling correlations for air and nonair free streams*. 1968.

[152] H. Yang, X. Liu, Y. Bian, and G. Wang, "Numerical investigation on the mechanism of transpiration cooling for porous struts based on local thermal non-equilibrium model," *Energies*, vol. 15, no. 6, 2022.

[153] Y.-Q. Liu, P.-X. Jiang, Y.-B. Xiong, and Y.-P. Wang, "Experimental and numerical investigation of transpiration cooling for sintered porous flat plates," *Applied Thermal Engineering*, vol. 50, no. 1, pp. 997–1007, 2013.

[154] M. A. Keller, M. J. Kloker, and H. Olivier, "Influence of cooling-gas properties on film-cooling effectiveness in supersonic flow," *Journal of Spacecraft and Rockets*, vol. 52, no. 5, pp. 1443–1455, 2015.

[155] M. Hombsch and H. Olivier, "Film cooling in laminar and turbulent supersonic flows," *Journal of Spacecraft and Rockets*, vol. 50, no. 4, pp. 742–753, 2013.

[156] V. I. Lysenko, S. A. Gaponov, B. V. Smorodsky, Y. G. Yermolaev, and A. D. Kosinov, "Influence of distributed heavy-gas injection on stability and transition of supersonic boundary-layer flow," *Physics of Fluids*, vol. 31, p. 104103, 10 2019.

[157] A. van Foreest, M. Sippel, A. Gülhan, B. Esser, B. Ambrosius, and K. Sudmeijer, "Transpiration cooling using liquid water," *Journal of Thermophysics and Heat Transfer*, vol. 23, no. 4, pp. 693–702, 2009.

[158] A. Gülhan and S. Braun, "An experimental study on the efficiency of transpiration cooling in laminar and turbulent hypersonic flows," *Experiments in fluids*, vol. 50, pp. 509–525, 2011.

[159] D. Glass, A. Dilley, and H. Kelly, *Numerical analysis of convection/transpiration cooling*. 1999.

[160] W. D. Henline, "Transpiration cooling of hypersonic blunt bodies with finite rate surface reactions," Tech. Rep. NASA CR-177516, 1989.

[161] M. Ewenz Rocher, T. Hermann, M. McGilvray, M. Grossman, and L. Vandeperre, "Measuring the concentration of freestream species on a hypersonic transpiration-cooled stagnation point," *Journal of Spacecraft and Rockets*, vol. 59, no. 4, pp. 1380–1387, 2022.

[162] M. E. Rocher, T. Hermann, and M. McGilvray, "Oxidation response of transpiration-cooled zrb2 on a hypersonic stagnation point," *Journal of Spacecraft and Rockets*, vol. 59, pp. 1486–1495, 9 2022.

[163] M. E. Rocher, T. Hermann, M. McGilvray, and R. Gollan, "Correlation for species concentration on a hypersonic stagnation point with mass injection," *AIAA Journal*, vol. 60, pp. 2798–2809, 2022.

[164] A. Mills and A. Wortman, "Two-dimensional stagnation point flows of binary mixtures," *International Journal of Heat and Mass Transfer*, vol. 15, no. 5, pp. 969–987, 1972.

[165] J. G. Marvin and R. B. Pope, "Laminar convective heating and ablation in the mars atmosphere.," *AIAA Journal*, vol. 5, no. 2, pp. 240–248, 1967.

[166] R. T. Swann and C. M. Pittman, *Numerical analysis of the transient response of advanced thermal protection systems for atmospheric entry*. National Aeronautics and Space Administration, 1962.

[167] S. Sreekanth and N. Reddy, *Correlations for injection cooled surface temperatures in compressible high speed flows*. 1997.

[168] R. Thompson and P. Gnoffo, *Implementation of a Blowing Boundary Condition in the LAURA Code*. 2008.

[169] I. Naved, T. Hermann, M. McGilvray, M. Ewenz Rocher, C. Hambidge, L. Doherty, L. Le Page, M. Grossman, and L. Vandeperre, "Heat transfer measurements of a transpiration-cooled stagnation point in transient hypersonic flow," *Journal of Thermophysics and Heat Transfer*, vol. 37, no. 2, pp. 296–308, 2023.

[170] R. Swigart, W. Shih, J. Wang, R. Snow, and J. Trolier, *Hypersonic film cooling effectiveness and aero-optical effects*. 1988.

[171] W. Kays, "Heat transfer to the transpired turbulent boundary layer," *International Journal of Heat and Mass Transfer*, vol. 15, no. 5, pp. 1023–1044, 1972.

[172] W. M. Kays, M. E. Crawford, and B. Weigand, *Convective heat and mass transfer*, vol. 2. McGraw-Hill New York, 1980.

[173] C. B. Moyer and R. A. Rindal, "An analysis of the coupled chemically reacting boundary layer and charring ablator. part 2-finite difference solution for the in-depth response of charring materials considering surface chemical and energy balances," Tech. Rep. NASA CR-1061, NASA, 1968.

[174] B. M. P. Chung, "Shielding stagnation surfaces of finite catalytic activity by air injection in hypersonic flight," 1959.

[175] M. Holden, R. Neumann, G. Burke, and K. Rodriguez, "An experimental study of the effects of injectant properties on the aerothermal characteristics of transpiration-cooled cones in hypersonic flow," in *21st Fluid Dynamics, Plasma Dynamics and Lasers Conference*, 1990.

[176] R. Taylor and R. Krishna, *Multicomponent mass transfer*. John Wiley & Sons, 1993.